STUDY OF SEMICONDUCTOR NANOCOMPOSITES USING RAMAN AND AFM MAPPING

By

Ekta Rani

Enrolment Number: PHYS03201004008

Raja Ramanna Centre for Advanced Technology

Indore-452013, India

A thesis submitted to the

Board of Studies in Physical Sciences

In partial fulfillment of requirements for the Degree of

DOCTOR OF PHILOSOPHY

of

HOMI BHABHA NATIONAL INSTITUTE

January 2016

Homi Bhabha National Institute

Recommendations of the Viva Voce Committee

As members of the Viva Voce Committee, we certify that we have read the dissertation prepared by Miss Ekta Rani titled **"Study of semiconductor nanocomposites using Raman and AFM mapping"** and recommend that it may be accepted as fulfilling the thesis requirement for the award of Degree of Doctor of Philosophy.

Chairman – **Dr. P. K. Gupta**		**Date:** 20/06/16
Guide / Convener – **Dr. Alka Ingale**		**Date:** 20/06/16
External Member – **Dr. V. Sathe**	Vasant Sathe	**Date:** 20/06/16
Examiner – **Prof. C. Narayana**	Chandrabhas	**Date:** 20/06/2016
Member 1- **Dr. D. K. Palit**	Palit	**Date:** 20/06/2016
Member 2- **Dr. K. I. Priyadarshini**	K. Indira Priyadarsini	**Date:** 20.6.2016
Member 3- **Dr. S. R. Mishra**	SR Mishra	**Date:** 20-6-2016
Member 4- **Dr. A. Dubey**		**Date:** 20/6/2016
Member 5- **Dr. K. Das**	Kaustuv Das	**Date:** 20/6/2016

Final approval and acceptance of this thesis is contingent upon the candidate's submission of the final copies of the thesis to HBNI.

I hereby certify that I have read this thesis prepared under my direction and recommend that it may be accepted as fulfilling the thesis requirement.

Date: 20/06/16

Place: RRCAT, Indore

Alka Ingale
Guide

STATEMENT BY AUTHOR

This dissertation has been submitted in partial fulfillment of requirements for an advanced degree at Homi Bhabha National Institute (HBNI) and is deposited in the Library to be made available to borrowers under rules of the HBNI.

Brief quotations from this dissertation are allowable without special permission, provided that accurate acknowledgement of source is made. Requests for permission for extended quotation from or reproduction of this manuscript in whole or in part may be granted by the Competent Authority of HBNI when in her judgment the proposed use of the material is in the interests of scholarship. In all other instances, however, permission must be obtained from the author.

Ekta Rani

Ekta Rani

DECLARATION

I, hereby declare that the investigation presented in the thesis has been carried out by me. The work is original and has not been submitted earlier as a whole or in part for a degree/diploma at this or any other Institution/University.

Ekta Rani

Ekta Rani

List of Publications arising from the thesis

a) Published

i) In journals:

1. On red-shift of UV Photoluminescence with decreasing size of Si nanoparticles embedded in SiO_2 matrix grown by pulsed laser deposition;
   Amita Chaturvedi, M. P. Joshi, **Ekta Rani**, Alka Ingale, L. M. Kukreja and A. K. Srivastava, **J. of Luminescence** (2014) **154**, 178–184.
2. Correlation of size and oxygen bonding at the interface of Si nanocrystal in Si-SiO_2 nanocomposite: A Raman mapping study;
   Ekta Rani, Alka A. Ingale, A. Chaturvedi, C. Kamal, D. M. Phase, M. P. Joshi, A. Chakrabarti, A. Banerjee and L. M. Kukreja, **J. of Raman Spectroscopy** (2016) **47**, 457-467
3. Insight into one-step growth of nearly monodispersive CdS nanocrystals embedded in polyvinyl pyrrolidone spheres;
   Ekta Rani, Rahul Aggarwal, Alka A Ingale, K. Bapna, C. Mukherjee, M. K. Singh, P. Tiwari and A. K. Srivastava, **J. of Materials Science** (2016) **51**, 1581-1590.
4. Resonance Raman mapping as a tool to monitor and manipulate Si nanocrystals in Si-SiO_2 nanocomposite;
   Ekta Rani, Alka A. Ingale, A. Chaturvedi, M. P. Joshi and L. M. Kukreja, **Appl. Phys. Lett.** (2015) **107**, 163112.
5. Corroboration of Raman and AFM mapping to study Si nanocrystals embedded in SiO_2;
   Ekta Rani, Alka A. Ingale, A. Chaturvedi, M. P. Joshi and L. M. Kukreja
   J. of Alloys and Compounds (2016) **672**, 403-412

b) Presented in International Conferences:

1. Insight into growth of CdS-PVP NCps using Raman and PL mapping.
   Ekta Rani, Alka A. Ingale, Rahul Aggarwal,
   Proc. of International conference on Raman spectroscopy (ICORS) India, August 2012.

2. Probing interface of Si nanocrystals in Si-SiO_2 NCp using Raman mapping.
   Ekta Rani, Alka A. Ingale, A. Chaturvedi, M. P. Joshi and L. M. Kukreja,
   Proc. of International conference on nano science and technology (ICONSAT) India, March 2014 **has received Best poster Award.**

I dedicate this thesis to

My family

Acknowledgements

This thesis work is the part of research that has been done since I came to RRCAT. First of all, I would like to thank God for all the blessings he has showered onto me, which has enabled me to complete and write this last note in my research work. Also, when I look back, I realize that there are many people who deserve special mention. I would like to thank them for making my time during my research in the Institute a period, I will treasure.

It is my great honor and privilege to express my deep sense of gratitude to my Ph.D. guide Dr. Alka A. Ingale, at the successful completion of this thesis work. Words can never be enough in expressing how grateful I am to her. She has infused enthusiasm at every step of research work. Each meeting with her added invaluable aspects to the implementation and broadened my perspective. I feel invigorated at every moment on recalling the words of inspirations received from her. She taught me to think at basic level for every problem. I thank her for his expertise shown in guiding my work and the willingness to share her knowledge and experience. From her, I have learned how to select problems, to solve them and to present their solutions. Her profound practical skills, immense knowledge and critical but valuable remarks led me to do a good research. She has infused many ideas that helped me a lot in growing up in the field of science. I am greatly indebted to her for her support, trust, guidance and encouragement throughout these years. She pushed me to develop my weaknesses and exploit my strengths. Her courage and the way to tackle new and difficult problems is admirable. She owns a great quality to sort out the experimental difficulties with many exciting ideas that eventually helped me in reaching the targets. She has a great ability to keep the person motivated. She is keen for a chat about interesting things in physics as well as philosophy and is always very encouraging. One of the best thing is that she has made me realized my potential and passion for research. Sometimes, we are just lucky!

I am thankful to Smt. Amita Chaturvedi and Dr. K. Bapna for the growth of Si-SiO_2 nanocomposites and CdS-PVP nanocomposites, respectively. I am thankful to Smt. Amita Chaturvedi for helping me out in the growth of new Si-SiO_2 nanocomposites as per requirement. I am also thankful to Dr. M. P. Joshi and Dr. L. M. Kukreja for help provided during the course of this work and growth of new Si-SiO_2 samples. I am also thankful to Smt. Amita Chaturvedi, Dr. M. P. Joshi and Dr. L. M. Kukreja for reading and discussion on the manuscripts. I am very grateful l to Dr. L. M. Kukreja for being very supportive throughout my Ph.D work.

I specially thank Mr. Rahul Aggarwal for teaching me how to perform atomic force microscopy measurements and discussion with him was always fruitful for me. I also thank Shri. H. S. Patel and Dr. Mahesh K. Swami for their support provided while working in the Raman lab.

I thank Dr. C. Kamal, Dr. Arup Banerjee and Dr. Aparna Chakrabarti for DFT/TDDFT calculations to support our experimental observations, which has also enhanced my understanding. I am very grateful to Dr. C. Mukherjee for showing trust and allowing to me to use their set-up for absorption and reflectance measurements on both nanocomposites studied. I am thankful to Mr. Rajiv Kamparath for the help provided during these measurements. I am extremely thankful to Dr. V. K. Dixit for being encouraging and always very supportive. I also thank Dr. Dixit and Miss Geetanjali for performing ATR-FTIR measurements on CdS-PVP nanocomposites. Thanks are due to Dr. D. M. Phase, UGC DAE CSR Indore for their help provide for XPS measurements and data analysis on various Si-SiO_2 nanocomposites. I am thankful to Mr. A. D. Wadikar, UGC DAE CSR Indore for performing the XPS measurements on these nanocomposites. I would like to thank Mr. M. K. Singh, Smt. Rashmi Singh and Smt. Pragaya Tiwari for performing SEM measurements on various CdS-PVP nanocomposites. Thanks are due to Kum. Sushmita Bhartiya for teaching me sample preparation for SEM measurements. I am thankful to Smt. Rachna Selvamani for performing gold coating for SEM measurements. I am thankful to Dr. A. K. Sinha and Mr. M. N. Singh for XRD measurements on CdS-PVP nanocomposites. I am thankful to Dr. Tarun K. Sharma for the help provided during photoluminescence measurements on various Si-SiO$_2$ nanocomposites. I also thank Miss Disha, Mr. Dipankar Jana and Shri Sanjay Porwal for performing these measurements. I am thankful to Dr. Sanjay Rai for his help provided during the reflectivity measurements. I am thankful to Dr. Mrinalini Sharma and Dr. T. S. Dhami for allowing me to use their centrifuge, ultra-sonicator and spin coater for isolation of nanostructures. I am also thankful to Mr. Viresh Nayak and Mr. Arijit Chakraborty for the help provided in Matlab programming. I thank Smt. Sapana Rege for the help provided in the office during the Ph.D course.

I am thankful to Dr. P. K. Gupta for his support during the SEM measurements on CdS-PVP nanocomposites. I am also thankful to Shri S. V. Nakhe for his support during the absorption and diffuse reflectance spectroscopy measurements on Si-SiO$_2$ and CdS-PVP nanocomposites. Thank are due to Dr. P. A. Naik, Dr. G. S. Lodha and Dr. S. K. Deb for support provided to use Indus facility in RRCAT. I am extremely thankful to Dr. H. S. Rawat, Head LPAS for his constant support during my Ph.D.

I specially thank Dr. P. K. Gupta (Chairman-C1) for his constructive motivation and guidance during the course of this work. I also thank Dr. Gupta for his valuable suggestion on the annual reposts as well as synopsis. I am very grateful to Dr. D. K. Aswal (External member-C1) for being very supportive during the course of this work. I also thank him for his valuable suggestions on the synopsis. I thank Dr. D. K. Aswal and his team for allowing me to learn and perform gas sensing measurements on CdS-PVP nanocomposites and thin film of CdS.

I am thankful to Prof. C. Narayana, JNCASR, Bengaluru, India and Prof. O. Pages, University of Lorraine, France for examining this thesis work. I would like to thank Dr. V. Sathe, UGC DAE CSR, Indore for attending my viva-voce examination as an external member of Ph.D committee.

I sincerely thank our Dean HBNI Dr. Arup Banerjee and Ph.D. coordination committee members specially Dr. G. S. Lodha, Dr. P. A. Naik and Dr. S. B. Roy for their continuous care and help provided during the Ph. D. course. I also thank our HBNI cell at RRCAT to provide all the necessary support during my Ph. D. course work. I also thank HBNI, RRCAT for celebrating Ph.D day.

I am very grateful to Dr. P. D. Gupta, Director RRCAT for his continual help provided to all Ph.D. students. I am also grateful to members of C1-Doctoral Committee.

My time at RRCAT was made enjoyable in large part due to my batch-mates and friends who have become a part of my life. We had valuable research discussions. We together had enjoyed small trips and parties. They have also taught me how to play volleyball. Playing with them was quite refreshing after spending whole day in the lab. I thank Dr. Aparna Chakrabarti for inviting us for dinner on several occasions at her home. We all had really enjoyed that time.

Above all, it would have not been possible for me to achieve this milestone in my research career without encouragement and support from my all family members who have prayed for my success.

Contents

Chapter 1: Introduction

Chapter 2: Experimental techniques

Chapter 3: Si-SiO_2 nanocomposites

Chapter 4: CdS-PVP Nanocomposite

4.2. Insight into one-step growth of nearly monodispersive CdS nanocrystals embedded in PVP spheres

4.3. Effect of relative concentration of Cd/S ion source and PVP on the morphology

4.4. Effect of preheating of chemical bath on the morphology

Annexure

References

Synopsis

Materials at nanoscale show unique properties due to their large surface-to-volume ratio and or quantum size effects. In addition, studies at nanoscale are important for miniaturization of devices with improved performances. Recently, there have been large number of studies on a new class of materials - known as nanocomposites (NCps) in which nanostructures are embedded into a processable matrix that can be either ceramic or polymer [1,2]. These NCps find applications in variety of devices e.g. photovoltaic [3,4], optoelectronic [5], etc. It is therefore essential to synthesize and characterize the NCps, to ensure the reproducibility of the process that can be scaled-up. The properties of NCps depend not only on the individual components, but also on their interaction and morphology [2]. Therefore, to have desired control on growth of a NCp, it is imperative to understand the characteristic of individual component in the presence of other and the formation mechanism(s) of NCps. Raman spectroscopy is an excellent non-contact, non-destructive optical tool to study size, crystalline quality, stress, surface/interface, structure, phase transition, effect of doping etc. of a semiconductor nanostructure. Therefore, spatial variation of local bonding environment of semiconductor nanocrystals (NCs) in a matrix can be effectively probed using Raman mapping.

The motivation of this thesis work was to use Raman spectroscopy for the investigation of two specially chosen class of NCps: (i) Si-SiO_2 (ceramic matrix) and ii) CdS-polyvinyl pyrrolidone (PVP: polymer matrix) NCps. In the first case, an inorganic ceramic matrix is an oxide of the same semiconductor, whereas in the second case, organic matrix provides a completely heterogeneous NCp. The interactions between the semiconductor NCs and a matrix are expected to be quite different in these two cases. The results obtained using Raman spectroscopy had been supported by other techniques, such as, atomic force microscopy (AFM), X-ray diffraction and X-ray photoelectron spectroscopy (XPS).

This thesis is organized into five chapters.

Chapter 1: Introduction

In this chapter, we begin with a brief history of semiconductors and it's ever increasing presence in various fields [3-5] like electronics, optoelectronics, photovoltaics, etc. The importance of semiconductor NCs and the relevance of semiconductor NCps are discussed. A brief overview of the literature on some special class of NCps is presented. In particularly, Si-SiO_2 (semiconductor-semiconductor oxide) and CdS-PVP (inorganic-organic) NCps are discussed in detail. Use of Raman spectroscopy/mapping, which is our main research tool to study both the NCps, is described. Finally, the motivation of the thesis work is presented.

Chapter 2: Experimental techniques

This chapter describes experimental techniques used for the study of Si-SiO_2 and CdS-PVP NCps. Si-SiO_2 single and multilayer NCps were grown on crystalline Al_2O_3 substrate using pulsed laser deposition (PLD). Si and SiO_2 targets were ablated alternatively in the chamber by varying the deposition time of silicon, while keeping the SiO_2 deposition time constant. CdS-PVP NCps were grown on glass substrate using chemical bath deposition. The bath parameters like concentration of Cadmium acetate (Cd ion source: Cd-A), Thiourea (S ion source: ThU) and PVP, deposition time, heating/cooling cycles were varied to study growth of this NCp.

Working principles of Raman spectroscopy/mapping and AFM are presented. Theoretical background for Raman spectroscopy is also discussed. Basic optical techniques like absorption, photoluminescence and diffuse reflectance spectroscopy, which were used to get information about band gap, are described. X-ray diffraction (XRD), XPS and electron microscopies like scanning electron microscopy (SEM), transmission electron microscopy (TEM) and its variants are also described.

Chapter 3: Si-SiO$_2$ nanocomposites

In Si-SiO$_2$ NCps, large variation in Si optical phonon from 495 - 519 cm^{-1} has been reported over a decade in different NCps [6-8]. In this Chapter, Raman mapping of Si-SiO$_2$ NCps grown using PLD, was used to elucidate the origin of this variation reported in literature and also observed by us in each of these NCps. This allowed us to perform systematic investigation of the whole range of Si phonon frequencies under same experimental conditions. Raman spectroscopy monitored local laser irradiation experiment was performed on desired frequencies located using Raman mapping. In this five step experiment, changes in Raman spectra were measured, while laser irradiation was kept ON and OFF for certain durations. The understanding developed along with Raman and AFM mapping on same sites were further used to get unique information about the morphology of these NCps grown using PLD.

i) Correlation of size and oxygen bonding at the surface/interface of Si nanocrystals in Si-SiO$_2$ nanocomposites

Based on the difference in line shapes of Si phonons and their behavior during the laser irradiation experiment, low frequency (LF: 495 - 510 cm^{-1}) and high frequency (HF: 515 - 519 cm^{-1}) phonons were attributed to the surface/interface of Si NCs and SiO$_2$ matrix and core of Si NCs, respectively. Unusual Stokes/anti-Stokes Raman intensity ratio for LF phonons indicated that LF phonons may be observable due to resonance enhancement of Raman signal. This understanding was also found to be consistent with the observation of such a strong signal coming from surface/interface of Si NCs in Si-SiO$_2$ NCp. Density functional and time dependent density functional theory based calculations of Raman spectra (C. Kamal, ISUD, RRCAT) for Si cluster (Si$_{41}$) terminated by oxygen (Si$_{41}$O$_{42}$H$_{24}$) had shown strongest Raman mode ~512 cm^{-1} to be originating from vibrations of surface atoms. This can be considered to be analogous to LF phonons. Further, XPS measurements of two Si-SiO_2 NCps containing contrasting content of LF phonons, was well corroborated with the observation of LF phonons from smaller size Si NCs. With the understanding that LF and HF phonons originate at surface (smaller size) and core (larger size) of Si NCs, respectively, origin of intermediate frequency (IF: 511 - 514 cm^{-1}) phonons is discussed in the next section.

ii) Resonance Raman mapping of Si-SiO_2 nanocomposite : Monitoring and manipulation of Si nanocrystals

Mainly two types of IF phonons, IF1 and IF2 with very different asymmetric line shape as well as intensities were observed in Raman mapping. It was found that both IF phonons can be explained using superposition of LF and HF phonons, considering that these phonons originate from intermediate size Si NCs and thus have contributions from both surface/interface and core phonons in different proportion. Observed blue shift and increase and decrease in the intensity for IF1 and IF2 phonons during the laser irradiation experiment can both be correlated to increase in size of Si NC and thereby leading to a dominant contribution of core phonons. Further, Stokes/anti-Stokes Raman measurements in corroboration with results of wavelength dependent Raman mapping showed that resonance Raman scattering is crucial for the observance of surface/interface phonons. These results were further supported using absorption spectroscopy. It is also important to note that during laser irradiation at low power, we found that if enough time is given, Si NCs grow in size to give larger core phonon contribution i.e. LF phonon gets converted to IF phonon and IF phonons gets converted to HF phonon further confirming our attributions of these phonons. This can allow Raman spectroscopy monitored, controlled manipulation of the Si-SiO_2 device properties using laser.

The correlation of our understanding and data from literature showed that LF, IF and HF phonons originate from smaller size (< ~ 4 nm), intermediate size (~ 4 nm to ~ 6 nm) and larger size (> ~ 6 nm) Si NCs, respectively. Further, we established that resonance Raman scattering is crucial for the observance of surface/interface phonons. Thus, occurrence of surface/interface phonons depends on two factors 1) size of Si NC (optical band gap) and 2) excitation wavelength. This study showed that the effect of surface/interface for Si NCs is due to interaction of surface atoms of Si NC with Si and Oxygen atoms in the matrix. Our study, thus explained the variation of Raman data reported in the literature over the years for Si-SiO_2 NCps. Further, presence of multiple optical gaps in Si-SiO_2 NCps makes it a good candidate for third generation photovoltaic devices. Our understanding developed for Si-SiO_2 NCp can be gainfully used to manipulate and characterize the NCp, simultaneously for photovoltaic device applications using laser.

iii) Understanding the morphology of nanocomposites from correlation of Raman and AFM mapping

Raman and AFM mapping together showed formation of clusters of Si NCs embedded in SiO_2, although the growth was carried out to be multilayer. Further, Raman mapping showed two types of clusters with i) Gaussian and ii) non Gaussian intensity patterns of Si phonons. Correlation of phonon intensity patterns with observed AFM data on the same selected area, indicated that clusters of Si NCs, small in size ~ 100 nm (organized in two dimension) and large in size ~ 2 μm (three dimension (3D)) are formed. Further, Raman mapping performed with varying focal spot along the depth confirmed this observation and revealed that some of the 3D clusters are stacked with smaller Si NCs at the top and larger Si NCs at the bottom. Raman and AFM mapping of a single layer indicated that Si NCs are formed in the plume itself and cluster formation occurs by rupturing SiO_2 buffer layer. Annealing at 800 ^{0}C in Si rich SiO_2 was found to be the cause of stacking of smallest size Si NCs at the top layer of the cluster. Thus, understanding of Si phonons in SiO_2 matrix led to an important information of the morphology and thereby growth mechanism of Si-SiO_2 NCps, which was difficult to obtain by any other conventional technique.

iv) Size dependent interface bonding of Si nanocrystals in Si-SiO_2 nanocomposite: corroboration of Raman and XPS study

In the previous sections, we have discussed the use of Raman mapping to study surface/interface of Si-SiO_2 NCps. In this section, we discuss one to one corroboration between size dependence of surface/interface of Si-SiO_2 NCps using Raman mapping and XPS. The beam size in XPS (~ 1 cm x 1 cm) covers the full NCp; therefore, an average signal from XPS measurement needs to be corroborated with the statistical information obtained from the Raman data. XPS measurements showed observance of Si^{1+}, Si^{2+} and Si^{3+} suboxide states with higher intensity in the NCps corresponding to higher content of HF, IF and LF phonons in Raman mapping, respectively. Thus, quantitative corroboration between Raman mapping and XPS had been established for all NCps studied. Observed one to one corroboration was understood as due to formation of smaller Si NCs in Si excess SiO_2 (top layer) during annealing at 800 ^oC.

Chapter 4: CdS-PVP nanocomposites

CdS-PVP NCps was chosen to study, as monomers of PVP prefers to complex with many inorganic compounds and thus provide surface passivation. In the literature, most of the reports showed that CdS-PVP NCps are grown using two-step growth processes, wherein NCs capped with polymer are grown separately and are incorporated in polymer matrix [9-11]. We had chosen one-step growth process, wherein CdS NCs and PVP matrix were being grown simultaneously using chemical bath deposition (CBD).

i) Insight into one-step growth of nearly monodispersive CdS nanocrystals embedded in polyvinyl pyrrolidone spheres

In this section, we discuss the optimization study of CdS NCs embedded in PVP, grown using one-step CBD. Systematic study of variation in Cadmium acetate (Cd ion source: Cd-A), Thiourea (S ion source: ThU) and PVP concentration, deposition time, heating/cooling cycles; elucidated co-operative growth mechanism for CdS-PVP NCp. This results in different optimum growth conditions for the formation of CdS-PVP NCp than that for CdS thin film. Absorption, scanning and transmission electron microscopy together, showed that nearly monodispersive CdS NCs with sizes ~ 6 to 10 nm for different NCps are embedded in PVP sphere (sizes ~ 100 - 900 nm). Diffuse reflectance spectra was used as a guide to separate scattering contribution from absorption spectra. The scattering contribution was understood to be occurring due to Rayleigh and Mie scattering due to PVP spheres/structures seen in SEM micrographs. Our observations and understanding suggested that formation of PVP spheres led to inclusion of nearly monodispersive CdS NCs with better passivation. Further, decrease in size of CdS NCs with higher molar concentration of Cd-A & ThU and formation of nearly monodispersive CdS NCs embedded in PVP spheres were corroborated qualitatively with existing growth modeling studies of NCps. Co-operative nature of growth for CdS-PVP NCp using CBD was further investigated using Raman and AFM mapping.

ii) Effect of relative concentration of Cd/S ion source and PVP content on the morphology of CdS-PVP nanocomposite: Raman, PL and AFM mapping study

Raman and AFM mapping investigation of CdS-PVP NCps on same selected sites showed two different morphologies of CdS-PVP NCps, wherein CdS NCs are embedded in i) PVP sphere and ii) thin film of PVP for different relative concentration of Cd-A/ThU to PVP, as a result of co-operative growth mechanism. It has been predicted that the morphology depends on the density of NCs, if the strength of interaction is same [12]. We found that larger concentration of Cd/S ion source (larger density of CdS NCs) led to formation of PVP sphere, whereas, thin film of PVP was observed in case of lower concentration of Cd/S ion source, which is consistent with the theoretical prediction [12]. Further, formation of PVP spheres led to inclusion of nearly monodispersive CdS NCs of better crystalline quality. In addition, we found that smaller CdS NCs of better crystalline quality with better passivation were embedded in smaller PVP spheres, which was found to be a minimum energy configuration [13].

iii) Effect of growth temperature on the morphology of CdS - PVP nanocomposites: Raman and AFM mapping with XRD

Three dimensional intensity profile in Raman image of isolated PVP sphere indicated volume absorption of CdS NCs, which is driven by attractive interaction between NCs-polymer and high density of NCs, leading to the collapse of polymer [13]. Further, it was found that this collapse transition of PVP is not favored at 70 ^{o}C and thus it led to opening (at 70 ^{o}C) and reformation (room temperature) of CdS-PVP NCp. Grazing incidence XRD (INDUS, BL-12) data showed formation of both cubic and hexagonal phases for NCps grown at room temperature, whereas, chemical bath heated at 70 ^{o}C leads to NCps with purely hexagonal phase. Further, Raman, PL and AFM mapping in corroboration with XRD data showed that there exist residual tensile stress in CdS NCs embedded in single PVP sphere as compared to the dimer, which led to observance of resonance Raman scattering of CdS NCs due to stress related band gap tuning.

To summarize, one-step growth of CdS-PVP NCp using CBD was found to be co-operative in nature. While, this method eliminates an additional step for growth of NCps, we found that complexity of the process actually led to better control on the growth i.e. formation of nearly monodispersive CdS NCs of better crystalline quality and with better passivation. This is expected to enhance the non-linear optical properties of CdS NCs, which are useful for optical limiting devices.

Chapter 5: Conclusion

This chapter summarizes results of work presented in the earlier chapters. In Si-SiO_2 nanocomposites grown by pulsed laser deposition, large variation (495 - 519 cm^{-1}) in Si phonon frequencies was shown to arise from surface/interface of smaller Si nanocrystal and core of larger Si nanocrystals dispersed in SiO_2 matrix. The large size distribution of Si nanocrystals in these nanocomposites was used advantageously to probe similarity and differences in them under certain experimental conditions. This Raman spectroscopy/mapping study showed that the extended interface generated due to interaction between surface atoms of Si NC and Oxygen in the matrix plays an important role in Raman spectra, contribution of which depends on the size of a Si nanocrystal. Further, it was found that the resonance Raman scattering is crucial for the observance of these surface/interface phonons. This understanding can now be well correlated to variation of Si optical phonon frequency reported in literature. Further, this understanding in corroboration with atomic force microscopy revealed stacking of different size Si nanocrystals in clusters of Si-SiO_2. This unique information about morphology of Si nanocrystals embedded in

SiO_2 is difficult to obtain by any other conventional technique. Similarly, in CdS-PVP nanocomposites grown using chemical bath deposition, the interaction between CdS nanocrystal surface and PVP monomers gave rise to collapse of polymer, which in turn led to formation of nearly monodispersive CdS nanocrystals embedded in PVP spheres. The complexity of one-step growth process actually allowed desired control on growth of CdS-PVP nanocomposite using a simple growth technique of chemical bath deposition.

In both nanocomposites studied, it was found that interaction between constituent parts i.e. semiconductor nanocrystal and matrix plays an important role in determining the morphology as well as properties of nanocomposites. The Chapter is concluded by bringing out the future scope of work.

References

[1] L. L. Beecroft and C. K. Ober *Chem. Mater.***,** **9**, (1997) 1302.
[2] A. Du , Y. H. Ng, N. J. Bell, Z. Zhu, R. Amal and S. C. Smith *J. Phys. Chem. Lett.*, **2**(8), (2011) 894.
[3] S.Xiao and S. Xu *Crit. Rev. Solid State Mater. Sci.*, **39**, (2014) 277.
[4] J. N. Freitas, A. S. Gonçalve and A. F. Nogueira *Nanoscal*e, **6**, (2014) 6371.
[5] B.Hamilton *Semicond. Sci. Technol.*, **10**, (1995) 1187.
[6] G. Faraci, S. Gibilisco, P. Russo, A. R. Pennisi, G. Compagnini, S. Battiato, R. Puglisi and S. L. Rosa *Eur. Phys. J. B*, **46**, (2005) 457 and references therein.
[7] I. F. Crowe, M. P. Halsall, O. Hulko, A. P. Knights, R. M. Gwilliam, M. Wojdak and A. J. Kenyon *J. App. Phys.*, **109**, (2011) 083534 and references therein.
[8] G. H. Li, K. Ding, Y. Chen, H. X. Han and Z. P. Wang *J. Appl. Phys.*, **88**, (2000) 1439
[9] M. Pattabi, B. Saraswathi and A. K. Manzoor *Mater. Res. Bull.*, **42**, (2007) 828.
[10] S. Peretz, B. Sava, M. Elisa and G. Stanciu *J. Optoelectron. Adv. M.*, **11**, (2009) 2108.
[11] F. Antolini, M. Pentimalli, T. Di Luccio, R. Terzi and M. Schioppa *Mater. Lett.*, **59**, (2005) 3181.
[12] M. G. Opferman, R. D. Coalson, D. Jasnow and A. Zilman *Phys. Rev. E*, **86**, (2012) 031806.
[13] D. Antypov, J. A. Elliott *Macromolecules*, **41**, (2008) 7243.

List of Figure Captions

List of Table captions

Chapter 1

Introduction

“I am not afraid to consider the final question as to whether, ultimately in the great future we can arrange atoms the way we want; the very atoms, all the way down! …The principles of physics, as far as I can see, do not speak against the possibility of maneuvering things atom by atom. It is not an attempt to violate any laws … but in practice, it has not been done because we are too big. The problems of chemistry and biology can be greatly helped if our ability to see what we are doing, and to do things on an atomic level, is ultimately developed, a development which I think cannot be avoided".

Feynman,1960

Materials at nanoscale show unique properties due to quantum size effects and or their large surface to volume ratio. Specially, semiconductor nanostructures are studied extensively as they form the basis for many modern electronic [1] and optoelectronic [2] devices. Further, the thrust for long-term stability, reproducibility and synthesis on a large scale with a control on the structure, has branched nanoscale research towards semiconductor nanocomposites. Semiconductor nanocomposites are composites, wherein functional semiconductor nanostructures are embedded in a passive matrix. Properties of nanocomposites mainly depend on the functional component used; however, the interaction between constituent components although weak may influence formation and properties of these nanocomposites. Thus, it is important to understand the characteristic of a functional component in the presence of the matrix. Raman spectroscopy is an excellent non-contact, non-destructive optical tool to study semiconductors and semiconductor nanostructures, as their band gap lies in the visible region. It can be used to obtain information regarding size, crystalline quality, stress, structure, etc. of a semiconductor nanostructure. Further, Raman spectroscopy being a local probe, it can also be used to study the effect of surrounding environment on nanostructure and thus can give information regarding the interaction between semiconductor nanostructure and matrix.

In this chapter, we start with the brief history of semiconductors and it’s ever increasing presence in various fields. Further, importance of semiconductor nanostructures is briefly described. Taking from here we discuss, the need of forming semiconductor nanocomposites and their relevance. Utility to study nanocomposites using Raman spectroscopy and the necessity of Raman mapping is also discussed. Materials chosen for this study are also discussed in this light.

1.1. Semiconductors

A semiconductor is defined as a material with electrical resistivity lying in the range of 10^{-2} to 10^{9} Ω cm [3]. It is also defined as a material whose band gap lies between 0 and 4 electron volts (eV). Materials with zero band gap are recognized as metals, while those with band gap larger than ~ 4 eV are known as insulators.

1.1.1. History of semiconductors

Alessandro Volta was the first person who introduced the word *semiconductor* or *materials* of *semiconducting nature* [4] in 18th century. Later on, first significant observation in the field of semiconductor was made by Faraday [5] in 1833, when he found that Silver Sulfide have a negative temperature coefficient of resistance, a characteristic which is different from metals. The observation that a photo-voltage could be produced by shining light on the surface of one electrode in an electrolyte by Becquerel [6] in 1839 was another contribution. Later on, Smith [7] in 1873 showed that the resistance of Selenium could be reduced by shining light on it (photo-conductivity). Further, in 1874, it was found out that the contact resistance between certain materials does not obey Ohm's law, but depends on the magnitude and sign of the applied voltage [8,9]. Thus, by 1885, fundamental properties of semiconductors were discovered, although, not all on the same material [10].

1.1.2. Applications of semiconductors and recent trends

Semiconductors are core of modern electronic [1] and optoelectronic [2] industries. In optoelectronics devices, optics and electronics are brought together within a single material i.e. the material should allow the manipulation of light, the manipulation of electrical current and their interaction. Metals are excellent electrical conductors, however, do not allow light to travel inside, whereas, dielectric materials can accommodate and guide light waves, but they are electrical insulators. Semiconductors are in between these two, as they can carry current and can be designed to allow for the transformation of light into current and vice versa and thus, quite useful in optoelectronic devices. Semiconductors are also enormously used in photovoltaic devices since the development of first practical photovoltaic cell in 1954 [11]. This is because renewable energies have attracted attention in recent decades as they have shown real potential for addressing issues such as increasing energy requirements, climate change and global warming problems that obstruct the sustainable development of human society. Among various kinds of renewable energies that have been developed, solar power [12] is regarded as the most appealing clean energy.

As solar cells are practical source of sustainable energy, the challenge that photovoltaic research community is facing, is to improve the efficiency and reduce the cost of these devices. Therefore, the drive to miniaturization has been rapidly pushing industry into atomic and nanometer scale devices. In this regard, development of advanced synthesis techniques [13], which can facilitate growth of highly crystalline quality materials, is an enabling step toward making such devices a reality.

1.2. Nanostructures

Nanostructures are defined as the structures with at least one characteristics dimension measured in the nanometer range (1-100 nm) [14]. Today, interest is focused on Nanotechnology, which can be broadly defined as, ‘‘creation, processing, characterization, and utilization of devices with dimension on the order of 1-100 nm, which exhibits novel physical and chemical properties due to their nano-scale size’’ [15]. Thus, the word “nano” does not just denote “miniaturization”; such miniaturization must lead to novel properties. The interest in nanostructures stems from the fact that their properties change with their size or shape [15-17]. This is because properties of a system are determined by the type of motion allowed for its electrons, which is determined by the space in which the electrons are allowed to move [16]. In bulk materials, electrons are free to move, whereas, in atoms and molecules, electrons are confined to much smaller dimensions. Once bound in nanostructures i.e. when size is smaller than critical length that characterizes many phenomena, motion of electron becomes strongly confined and thus quantization sets in. Therefore, novel properties of nanostructures, which are not observed in bulk and in isolated atoms, arise owing to their nano size and have their origins in quantum mechanics. Further, in case of bulk materials, a relatively small percentage of atoms are present near the surface. However, surfaces are very important for nanostructures, wherein the small size ensures large number of atoms near the surface [18-19]. Since, atoms present at the surface are loosely bounded as compared to atoms present inside, surface properties such as electronic structure, reactivity can be quite different from the inside. This can leads to different chemical and physical interactions, which are governed mainly by surfaces. Thus, when the size of materials is reduced to nanoscale, their physical and chemical properties change, resulting in unique properties due to their large surface to volume ratio and or quantum size effect. Research in this area is a fascinating branch of science. The size [20, 21] and shape [22,23] dependent properties of nanostructures lead to surprising discoveries. Unique behavior of nanostructures not only shows great potential for innovative applications, but also poses challenges. In order to use nanostructures, one has to develop highly controllable, simple and cheap growth techniques, high resolution characterization tools and new theories/modifications to theories to explain experimental observations. All this together will facilitate use of nanostructures in various applications [24,25]. Nanotechnology thus, has captured the imaginations of scientists and engineers not only because of the explosion of discoveries at the nanometer scale, but also because of the potential implications.

1.2.1. Classification of Nanostructures

Nanostructure is defined as the structure with at least one dimension d is less or equal to a critical length d*, $d \leqslant d^* \approx 100$ nm [26]. The value of d* have no certain magnitude because it is determined physically by a critical characteristic of some phenomena (free path length of electrons or phonons, de Broglie wavelength, diffusion length, etc.) giving rise to the size (quantum confinements) effects. Reduction in the spatial dimension or one can say confinement of particles in particular direction within a structure leads change in electronic density of states in that direction. Hence, classification of nanostructure materials depends on the number of dimension/dimensions that is/are confined to nanometer range. Accordingly, one can have three types of system:

i) System confined in three-dimension (Quantum dots): This includes nanoparticles in which electron are confined in all the three directions. Nanoparticles could be either amorphous or crystalline.

ii) System confined in two-dimension (nanowire/nanotubes): Here electrons are confined in two directions and are free to move in third direction. This includes nanowires, nanotubes, nanorods having diameter and thickness in the range of nanometer e.g. semiconductor nanowires, carbon nanotubes.

iii) System confined in one-dimension (Quantum well): In these systems, confinement occurs in one direction. This includes films on a substrate having thickness in the range of nanometer and remaining two dimensions (length and width) are large.

Difference in their properties due to confinement in different dimensions and surface to volume ratio they find applications in different fields [27-32]. Some representative examples are cited in the following.

Quantum dots are extensively used for in photovoltaic devices [27] and gas sensors [28]. Third generation photovoltaic devices employ multi band gap in a single device, which can be achieved using quantum dots of same material but with varying sizes, which in turn control light emission properties. Easy band gap tuning can be achieved using quantum dots because of quantum confinement in all the directions. Further, the most important parameter that determines the sensitivity of gas sensors is the specific surface-to-volume ratio of a material, which is highest for spherical quantum dots. The higher detection area of the nanoparticles leads to greater adsorption of gas species and thus increased sensing capability.

Nanowires/nanotubes show high electrical conductivity/mechanical strength [29]. Confinement in radial direction and large aspect ratio leads to directional flow of electron, phonons, and photons. Because of the nearly one-dimensional electronic structure, electronic transport in metallic carbon nanotubes occurs ballistically (i.e. without scattering) over long lengths, enabling them to carry high currents. Further, their high modulus and strength make them ideal functional material for polymer composites. Further, the large dielectric mismatch between the nanowires and it's surrounding environment causes photon confinement in sub-wavelength sized nanowires, and light can be guided over large distances with very little loss [30]. In addition to their function as active device elements nanowires/nanotubes can also be used as interconnects in micro-nano electronics [31].

Quantum wells are thin layered nanostructures, which derive most of their properties from the quantum confinement of charge carriers (electrons and "holes") in thin layers of one semiconductor "well (low band gap)" material sandwiched between other semiconductor "barrier (large band gap)" layers. Quantum wells are used to fabricate cascade lasers [32]. The change in the refractive index at the hetero-interface between the large band gap and low band gap material provides waveguide effect which confines emitted light from the well. This confinement enhances stimulated emission and substantially reduces the threshold current as compared to that required for bulk laser. Further, confinement of charge carriers in well (2 dimensional electron gas) leads to enhanced recombination of electron hole pairs to emit laser light [32].

Nanostructures were not necessarily produced in laboratories over many years, but have always existed in nature as discussed briefly in the following.

1.2.2. Natural nanostructures

Our body is the perfect example of a nanostructured material. DNA in our body is a long double strand molecule with thickness of single strand is ~ 0.34 nm, diameter of double helix is 2 nm (very small as compared to length of strand) and thus it can be termed as nanowire. Other examples of natural nanostructures are i) milk, ii) lotus leaf, iii) butterfly wings etc.

i) Milk is a colloid, which contains lipids and proteins. White appearance of milk is due to the presence of nanostructure proteins called casein micelles (50-300 nm).

ii) Lotus leaf shows the water repelling property. Surface of leaf is covered with micrometer-sized papillae. The roughness of the hydrophobic papillae reduces the contact area between the surface and a liquid drop, with droplets residing only on the tips of the epicuticular wax crystals on the tops of papillose epidermal cells.

iii) Beautiful colors of butterfly wings are usually contributed by two sources: pigments and periodical sub micrometer structures, which are also referred to as “chemical” and “physical” colors, respectively.

Naturally occurring nanostructures also include organic (proteins, polysaccharides, viruses, among others) as well as inorganic compounds (iron oxy-hydroxides, alumino silicates, metals, among others) and are produced by weathering, volcano eruptions, wildfires or microbial processes. In addition to naturally occurring nanostructures, there is a long history of using synthetically prepared nanostructures in various applications, although science of the same was not well known.

1.2.3. History of man-made Nanostructures

One of the oldest questions in natural philosophy and science is the subject of intense research presently. The ancient philosopher Democritos in 400 BC posed the question: “What happens if a macroscopic material is split in two over and over again? Democritos said that eventually the microscopic parts derived from multiple divisions would be distinct from the starting material; indeed, at some point the process of successive division would lead to the individual atom” [14]. Spectacular effects were obtained with metal nanoparticles as color pigments in luster and glass technology [33-36]. Metallic luster decorations of glazed ceramics appeared in Mesopotamia during the 9th century [34]. These decorations showed amazing optical properties due to the presence of separate silver and/or copper nanoparticles dispersed within the outermost layer of the glaze. Silver nanoparticles also have a very long and diverse history [36]. Products containing silver nanoparticles have been commercially available for more than 100 years and are used in applications as diverse as pigments, photographic, wound treatment, catalysts, as a biocide etc [36]. From a scientific point of view, the big step in nanoscale research was made by Michael Faraday approximately 155 years ago [37]. His systematic studies on the interaction of light with metal nanoparticles can be regarded as the emergence of Nanoscience and Nanotechnology. The concept of man-made nanostructures and their potential use in technology was again raised over 60 years ago. Feynman said that there are no fundamental physical reasons why materials could not be obtained by manipulating individual atoms. However, due to the absence of instrument, which can probe at nano scale, people were not much involved in working on nanostructures. In 1981, the emergence of scanning probe microscopy (SPM) followed by the arrival of atomic force microscopy five years later was crucial for nano-science [38] and opened the door to the nano-world. Emergence of these techniques and systematic work done on the photo-catalytic properties of colloidal CdS nanoparticles [39-41] led to the exciting possibility of tailoring the chemical and physical properties of a material by controlling crystallite size and shape on a nanometer scale rather than by altering the composition [42]. This has changed the semiconductor applications significantly.

1.2.4. Applications of semiconductor nanostructures and Recent trends

Semiconductor nanostructures are made from a variety of different compounds. They are referred to as II-VI, III-V or IV semiconductor nanostructures, based on the periodic table groups into which these elements are formed [43]. For example, Si and Ge are group IV, GaN, GaP, GaAs, InP and InAs are III-V, while those of ZnO, ZnS, CdS, CdSe and CdTe are II-VI semiconductors. Semiconductor nanostructures possess unique and useful chemical and physical properties and therefore they have attracted significant interest in research and applications in diverse disciplines such as in optoelectronic devices [10], solar cells [44, 45], biomedical imaging and therapy [46,47], sensors [48], hydrogen production [49,50], etc. We have already discussed above, the importance of semiconductors and the need for nanostructures for optoelectronic devices and solar cells. Further, because of superior optical properties compared to the traditional organic dyes and fluorescent proteins [51-53], semiconductors nanostructures/nanocrystals (NCs) have shown potential for bio-sensing applications [46,47]. Their relatively long fluorescent lifetimes allow the distinction between signal and the fluorescence of the background [51, 54, 55]. Gas sensing methods based on bulk semiconductor crystals rely on the interactions between their surface atoms and the gas which need to be detected [56]. This implies that NCs should be ideal candidates for sensing purposes because of their extremely large surface to volume ratio. Semiconductor NCs are also used for hydrogen production, which is a promising alternative fuel rather than fossil fuels, since it is completely pollution free and can readily be produced from renewable energy resources, thus eliminating the net production of greenhouse gases. Photo-catalytic hydrogen production from water in one of the promising techniques and the electronic properties of semiconductor NCs makes them good photo-catalyst [57,58].

Above examples suggest that semiconductor NCs have shown encouraging success in various applications. However, most of the properties exhibited by NCs are size dependent due to quantum confinement effect and/or increase in surface to volume ratio. Due to large surface to volume ratio in NCs, two possibilities can arise, 1) Agglomeration of particles to form larger particles due to Ostwald ripening and Vander Waals interactions and 2) large number of surface defect states which can suppress their luminescence properties. This may wipe out benefits associated with NCs/nanostructures [59-61]. This suggests that work was still needed to address issues of long-term stability, reproducibility and synthesis on a large scale such as thin films, with a control on the structure at the atomic level. Thus, in order to surpass the limitations associated with nanostructures, advanced materials such as their nanocomposites with improved properties and functionalities, have been proposed [62-67].

1.3. Nanocomposites

Nanocomposite (NCp) is grown by embedding NCs into a processable, transparent matrix material, which can be ceramic (inorganic) or polymer (organic) [68-70]. With this process, optical properties of NCs can be utilized in more technologically important forms such as films. Further, the ability to control the location of NCs within a matrix would result in tailored and enhanced properties of hybrid materials. NCps combine the properties of each component and show enhanced functionality.

1.3.1. Importance of nanocomposites

NCps provide stability and processibility to nanostructures. NCps have been shown variety of applications in various fields such as in gas sensors [71,72], energy storage [73], optoelectronics [74], photovoltaic [75], biomedical [76] and other systems due to the stability provided by matrix to semiconductor NCs. Combining the tunable optical properties of NCs with it's oxide matrix, which is transparent, these NCps have shown applications in ultrafast optical switching, ultrafast imaging, optical telecommunication, signal processing [77]. Besides, these NCps are chemically and thermally stable. Another class of NCps prepared by mixing of NCs with polymers has been practiced for decades. For example, the clay-reinforced resin known as Bakelite was introduced in the early 1900's as one of the first mass-produced polymer-NCs composite [78], which fundamentally transformed the nature of practical household materials. In addition, nature has always combined inorganic and organic components at the nanoscale to construct smart materials with remarkable properties. Bone is considered to be a composite material consisting of a high elastic modulus mineral 'fibres' embedded in a low elastic modulus organic matrix permeated with pores filled with liquids.

1.3.2. Semiconductor nanocomposites

NCps can be described as a combination of two or more components which may have been thoroughly researched; however, there may still be a need to get insight into the NCps. Although, interactions between matrix and semiconductor NCs are expected to be weak in NCps, it may be interesting to see, if they can have far reaching consequences in formation and properties of NCps. Further, the interaction at the interface, between semiconductor NCs and matrix will be very different depending on whether matrix is a oxide of the same semiconductor (Si NCs in SiO_2, Ge NCs in GeO_2 etc.) or completely heterogeneous matrix (semiconductor NCs in polymer matrix) and hence, can give rise very different manifestations in formation and properties of these NCps. In case of semiconductor-semiconductor oxide NCp, experimentally there were some observations (UV-Vis photoluminescence (PL)), which could not be attributed to quantum confinement effects. Further, theory was suggestive that the interaction between Si, Ge atoms in NC with the oxygen atoms in matrix can play an important role in electronic and optical properties of semiconductor NCs embedded in oxide matrix [79-83]. However, it needs to be established experimentally. Also in case of inorganic-organic NCps, experimentally as well theoretically it was recently found that interactions between nanostructures and flexible block-copolymer chains play crucial role in deciding the final structure of the NCp [84-89]. However, for NCs-homopolymers NCps, it is yet to be explored, whether and how the interaction between NCs and polymers affect the structure of NCps. Thus, there is indeed a need to enhance the understanding of the fundamental interaction and intricate interfaces between NCs and the corresponding matrix to achieve control on the growth process and thereby properties of NCps. In an attempt to study possible effects of interactions within constituent components of the semiconductor NCps, we have chosen to study two NCps 1) Si-SiO_2 NCp and 2) CdS-polyvinyl pyrrolidone (PVP) NCp, which has potential photovoltaic and optoelectronic applications.

Raman spectroscopy being sensitive to local bonding environment, it is expected to give us information about interaction between constituent semiconductor NCs and matrix and it's effect on formation and properties of these NCps.

1.4. Raman spectroscopy

Raman spectroscopy [90] is an inelastic light scattering of low level excitations of the medium/material. In solids, we mainly study quantized lattice vibrations (phonon) of the materials. Since, light interacts with lattice via electrons; it also gives information about electronic band structure. Raman spectroscopy is an excellent non-contact, non-destructive optical tool to study materials. It is particularly suitable to study semiconductor nanostructures/NCs (band gap in the range 2 - 3 eV), as it allows resonance Raman scattering in the visible region giving rise to reasonable signal for semiconductor NCs. Raman spectroscopy is a local probe and lattice vibrations are sensitive to composition, structure, stress, crystalline quality, local environment etc. Thus, it can be used to obtain the information regarding size, crystalline quality, stress, surface/interface, structure, phase transition, effect of doping etc. in nanostructures/NCps locally. Low level carrier excitations can additionally predict type of carriers, carrier concentration etc. In all, Raman spectroscopy is capable of giving information about material’s structural, optical and electronic properties. Raman spectroscopy has many advantages among many characterization techniques. Typically, the samples need little or no preparation before characterization. In addition, Raman Spectroscopy is typically a fast characterization tool. In the following, we discuss the history of Raman spectroscopy.

1.4.1. History and relevance today

Interaction of photon with the matter mainly leads to absorption, reflection and transmission of light [91]. However, some photons interact with the material and scatter from it. For example, Rayleigh scattering of light is a familiar phenomenon that is responsible for the blue color of the sky. In 1928, C.V. Raman discovered inelastic light scattering [90]. In the original experiment, sunlight was focused by a telescope onto a sample which was either a purified liquid or a dust-free vapor. A second lens was placed by the sample to collect the scattered radiation. A system of optical filters was used to show the existence of scattered radiation with an altered frequency from the incident light - the basic characteristic of Raman scattering. Thus, Raman scattering is an inelastic scattering of light by the material, leading to change in energy of incident photon. Since then, phenomenon has been referred to as Raman scattering and study of the same as Raman spectroscopy.

Since, Raman spectroscopy is inherently weak scattering process, invention of laser in 1960's revolutioned the applicability of Raman spectroscopy due to increase in the sensitivity of the measurements. This led to it's increased importance in the field of physical, chemical, biological sciences, archaeology, history of arts, etc. Raman spectroscopy is one the most important and simple spectroscopic technique for analysis in basic and applied sciences. Further, Raman mapping can be used effectively to study NCps, as it combines Raman spectroscopy and imaging to provide detailed variation in phonon parameters at spatially different position in the sample as described below.

1.4.2. Raman mapping

A possibility to not only probe locally, but visualize a chemical structure, composition, conformational state and effect of matrix on nanostructures has stimulated the development of imaging techniques [92]. High sensitivity of Raman spectroscopy to change in size, crystalline quality, stress, surface/interface, structure, phase transition, effect of doping, disorder, etc. of a semiconductor nanostructure and the need for little or no sample preparation make Raman mapping a highly attractive analytical technique. Raman mapping is a method for generating detailed images based on the sample's Raman spectrum. Therefore, change in Raman spectra at spatially different position can be studied. The sample stage is raster-scanned to record Raman spectrum across a chosen area. Raman image is generally generated using intensity of phonon of a particular material, however, image can also be generated using frequency of a phonon e.g. when one needs mapping of stress. Using Raman mapping, one can study distribution (size, crystalline quality, effect of surface/interface, stress, etc.) within NCp film, which is invisible by standard optical microscopy. Thus, Raman images depict a variation in spectral information at spatially different positions. With them, one can rapidly see how phonon parameter alters within a sample. This makes Raman mapping an ideal technique to study NCps, as it gives information about local bonding environment, which may change within a NCp.

We have developed a methodology to perform Raman and atomic force microscopy (AFM) mapping at same site in a sample. This combined Raman and AFM mapping for chosen NCps gives important information about embedded semiconductor nanocrystals, which is difficult to obtain otherwise.

1.5. Nanocomposites chosen for this study

Two NCps investigated are grown using different growth techniques, which further the understanding of different growth techniques along with NCps. Si-SiO_2 NCps are grown using Pulsed laser deposition (PLD) and CdS-PVP NCps are grown using Chemical bath deposition (CBD).

1.5.1. Si-SiO_2 nanocomposite

Silicon is a promising material as it is non-toxic and abundant in nature. Silicon NCs have innumerable applications which include their use as sensors [93], optoelectronic devices [94], photovoltaic devices [95], electroluminescent displays [96], photo-detectors [97], as a lasing material for photo-pumped tunable lasers [98], as an electrode material for Li-ion battery [99]. In addition, high photoluminescence quantum efficiency [100] and stability against photo-bleaching of Si NCs [101] make them an ideal candidate for replacing fluorescent dyes in imaging techniques.

Interest in Si has started in 1950s, with the publication of a new p-n junction photocell allowing the conversion of solar radiation into electricity. However, bulk Si has indirect band gap ~ 1.1 eV and thus luminescence efficiency is very low. UV-visible PL with increased efficiency was first observed in porous Si (p-Si) [102]. However, there has been a debate on whether, the blue shift of the PL and optical absorption with increasing porosity is due to the quantum confinement [103] or due to the nature of surface localized states of small Si crystallites [104-106]. Further, observation of optical gain in Si NCs embedded in SiO_2 matrix (Si-SiO_2 NCp) [107,108] has stimulated research in this NCp. Different kind of techniques are used to grow Si NCs embedded in SiO_2 matrix [109-150]. A debate, however, continues, over the origin of the light emission from Si-SiO_2 NCp [109-116]. In order to understand the origin of UV-visible PL of Si-SiO_2 NCp, theoretical work was done on oxygen and hydrogen passivated Si cluster [151-152] as well as Si-SiO_2 NCp [80], which predict that the presence of oxygen at the surface affects their emission properties.

We find similar debate on Raman spectra of Si-SiO_2 NCps. Unlike other inorganic NCs, large variation (495 - 522 cm^{-1}) in Si phonon frequencies embedded in SiO_2 has been reported by different groups for different samples. This is found to be true, irrespective of the growth technique used for growth of Si-SiO_2 NCp [117-150]. We believe that the two issues are interconnected and higher specificity of Raman spectroscopy can be advantageously used to resolve it. In the extensive literature survey, we find that, in the range noted above, origin of higher frequency phonon ~ 516 cm^{-1} and above has been attributed to phonon confinement [153] in Si NCs and is well understood. However, it has been found that PCM is inadequate to give correct red shift and line shape fitting simultaneously for lower phonon frequencies ~ 500 cm^{-1} [117-118, 131-132, 134, 136, 141, 144-146, 154-157]. Several groups have addressed this discrepancy and different solutions e.g. size distribution [117, 145], bond polarizability model [155,156] and laser heating at low power density [154, 157] have been proposed to obtain correct red shift along with correct line shape fitting. However, no present models give understanding of the line shape and frequency for low frequency Si phonons.

Aim of this work is to investigate the origin of large variation obtained in frequencies of Si optical phonon in the Si-SiO_2 NCp and understand the correlation between this variation and nanostructure – matrix interaction, if any. Si-SiO_2 NCps studied are grown on crystalline Al_2O_3 substrate using PLD [158]. In these NCps, the whole range of Si phonon frequencies (495-519 cm^{-1}) is observed in each NCp using Raman mapping. This is the first time that the whole variation is reported on a single NCp. This allowed us to do systematic investigation of these Si phonon frequencies, as we could now access/monitor their behavior with respect to each other under certain experimental conditions. This is expected to give us a clue to the origin of this variation. Understanding the origin of these phonons is further used in corroboration with AFM to gain insight into morphology of these Si-SiO_2 NCps. This has allowed us to understand the growth mechanism of PLD grown Si-SiO_2 NCps.

1.5.2. CdS-Polyvinyl pyrrolidone (PVP) nanocomposite

Inorganic-organic NCps represent a merger between traditional inorganic and organic materials, resulting in hybrid composition [159], wherein inorganic NCs show optoelectronic properties and polymers provides numerous advantages such as facile and reliable manufacturing methods, broad compatibility with other materials, flexible, low cost etc [160]. Therefore, inorganic-organic NCps are of growing interest because of their numerous potential applications such as enhancement of conductivity [161,162], toughness [163], optical activity [164,165], catalytic activity [166] and chemical selectivity [167,168], gas sensors [169], etc. Thus, polymers provide processibility, keeping intact the optoelectronic properties of semiconductor NCs.

CdS is an important semiconducting material, as it is possible to engineer the band gap of CdS nanostructure over a wide spectral range (visible to UV). CdS NCs show promising applications in biological labeling [170], photo-catalysis [171], optoelectronic and photovoltaic devices [172]. CdS NCs also show good sensitivity to NO_2 gas and thus can be used as efficient gas sensor [173]. Further, different polymer matrices such as polyvinyl pyrrolidone (PVP) [174], polydiacetylene [175] and polystyrene [176] have been used to grown CdS-polymer NCps. PVP is preferably chosen as a matrix for the composites because of the two important characteristics [177, 178], i) different group of PVP forms complex with many inorganic compounds and thus provide surface passivation and ii) PVP has good film-forming and adhesive behaviour on many substrates and it’s films exhibit good optical quality.

Further, finding new routes for driving inorganic NCs and organic polymers to self-assemble into NCps is one of the challenges. In this quest, combining theoretical work [84-89] and experimental observation can guide optimization of several routes for incorporating semiconductor NCs in polymer matrix. Several chemical methods are used for the fabrication of semiconductor NCs embedded in polymer matrix [179-193]. Chemical methods are preferred route for growth of inorganic-organic NCp to avoid decomposition of organic matrix at higher temperatures generally involved in physical methods. Further, using physical growth technique for NCs and chemical growth technique for organic matrix will be costly in terms of both time and money. The CdS-PVP NCps studied are grown using CBD.

CBD is one simple, low cost and versatile route to grow NCs embedded in polymer [184-193]. In the literature, most of the reports show that NCps are grown using two-step CBD growth process [184-190]. In this two-step growth process, NCs are grown separately and are incorporated in polymer matrix. However, to the best of our knowledge, no systematic study has been performed for one-step growth of CdS-PVP NCp grown using CBD. Thus, it is important to do systematic study of CdS-PVP NCp, grown using one-step growth process, to get insight into the growth mechanism and it’s correlation to nanostructure–matrix interaction. Further, Raman and AFM mapping are used together to correlate the observed difference in morphology of NCps grown using different growth parameters.

Raman mapping is used to probe the effect of interaction between NCs and matrix on the formation and properties of semiconductor NCps. Further, by combining this understanding of NCps with topography obtained from AFM mapping, unique information about morphology and growth mechanisms of NCps is obtained.

Chapter 2

Experimental techniques

In this chapter, growth of NCps studied and characterization techniques used for the study are described. Si-SiO$_2$ NCps and CdS-PVP NCp are grown using pulsed laser deposition (PLD) and chemical bath deposition (CBD), respectively by collaborators. Basic process and details of growth parameters/conditions used in PLD and CBD are described at the beginning of the chapter.

In this work, Raman spectroscopy/mapping and AFM mapping are used as main research tools to study Si-SiO$_2$ and CdS-PVP NCps. Working principle of these methods along with the theoretical background for Raman spectroscopy is developed. Importance and the use of Raman mapping to study NCps is also discussed. We also describe the methodology developed to perform Raman and AFM mapping at same selected area in these NCps to establish correlation between Raman spectroscopy and morphology. Basic optical techniques like absorption, diffuse reflectance and photoluminescence spectroscopy used to get information about band gap of the NCps are also described. X-ray diffraction and electron microscopies like scanning electron microscopy (SEM), transmission electron microscopy (TEM) and it's variants, used to support the understanding developed are also discussed.

2.1. Growth

Si-SiO$_2$ NCps are grown using PLD and CdS-PVP NCps are grown using CBD. Both these techniques and relevant growth parameters/conditions are discussed in the following.

2.1.1. Pulsed laser deposition

In PLD [194], a pulsed laser beam is focused onto the surface of a solid target. The absorption of electromagnetic radiation by the solid surface leads to rapid evaporation of the target material. The evaporated material consist of ionized species i.e. plasma plume, which gets deposited on the substrate either in vacuum or in the presence of background gas as required. In PLD growth, parameters such as wavelength of laser, it's peak power/energy, pulse repetition rate, target-substrate distance, substrate temperature needs to be optimized. It is also feasible to produce multilayer films of different materials by sequential ablation of assorted targets. Si-SiO_2 multilayer NCps are grown using PLD by collaborators (LMPD, RRCAT).

Laser parameters used for multilayer growth of Si-SiO_2 NCps are, i) KrF laser (248 nm, pulse duration- 20 ns), ii) pulse repetition rate - 10 Hz and iii) energy density ~ 2 J/cm^2. A multi target deposition chamber is utilized for the growth purpose [158]. Single crystal Si wafer and SiO_2 pellet are used as the targets and crystalline Al_2O_3 is used as the substrate. Initially, deposition chamber is evacuated to a base pressure of ~ 5 x 10^{-7} mbar using a turbo molecular pump. For the growth of multilayer, Si and SiO_2 targets are ablated alternatively and the plasma plume is collected over the substrate. Growth is carried out in helium background pressure of ~ 10^{-1} mbar. Targets are continuously rotated to avoid any pit formation and to ensure uniform ablation of the material. Deposition time of Si is varied from 45 s to 210 s in order to achieve variable mean sizes, keeping deposition time of SiO_2 (thickness ~ 20 nm) constant. Expected thickness of Si layer per second is ~ 0.06 nm. Thus, thickness for E1 to E6 is expected to vary from ~ 360 nm to ~ 560 nm. In this way, 15 multilayers of Si/SiO_2 are grown on buffer layer of SiO_2 (thickness ~ 20 nm) deposited on crystalline Al_2O_3 substrate. All the depositions are carried out at room temperature. To improve the crystalline quality of the particles after the growth, samples are annealed in nitrogen ambience at 800 ^{0}C in the same chamber without exposing them to the atmosphere. We have studied six such NCps with varying deposition time of Si, 1) E1 (45 s), 2) E2 (90 s), 3) E3 (120 s), 4) E4 (150 s), 5) E5 (180 s) and 6) E6 (210 s) with numbers appearing in the parenthesis denote the deposition time in seconds. We have also studied one unannealed NCp with deposition time of Si as 90 s. Rest of the growth conditions are same. This NCp is designated as E2U.

In order to support the result observed for NCps noted above and to understand the observed morphology of multilayer Si-SiO_2 NCps, we have grown another set of Si-SiO_2 NCps with similar laser parameters. For this new set, deposition time of Si (45 s) and SiO_2 (3 min) is kept constant. In this set, we have studied, 1) E7 - 10 ML of Si/SiO_2 with additional SiO_2 layer at the top, 2) E8 - 10 multilayers of Si/SiO_2 (top layer - Si), 3) E9 - single layer of Si/SiO_2 with additional SiO_2 layer at the top, 4) E10 - single layer of Si/SiO_2 (top layer - Si). All these NCps are annealed at 800 ^{o}C. Further, to study the effect of annealing on Si-SiO_2 NCps, we have prepared a set of NCp - 10 multilayers of Si/SiO_2 with additional SiO_2 layer at the top. This NCp is kept unannealed (E11) and annealed at 200 ^{o}C (E12), 400 ^{o}C (E13), 600 ^{o}C (E14). Rest of the growth parameters are kept same as mentioned above.

2.1.2. Chemical bath deposition

CBD is a simple growth technique, which is used to grow thin film or NCs onto a desired substrate [195]. This process involves reaction between precursors, nucleation followed by growth. In CBD, film formation may take place from two distinct mechanisms. The first growth mechanism involves the reaction of atomic species at the surface. It corresponds to an atom-by-atom process, also called “ion-by-ion”. The second deposition mechanism is associated to the agglomeration of colloids formed in the solution. It can be considered as “cluster-by-cluster” growth. In practical situations both processes may interact, leading to films where colloids are included in the growing film. In other words, the formation of nuclei can occur by heterogeneous nucleation on the substrate or by homogeneous nucleation in the bulk solution. The deposition parameters such as relative concentration of reactants, temperature, pH of the bath, duration of deposition etc. affect the deposited film. CBD technique has many advantages such as simplicity i.e. no requirement for sophisticated instruments, no vacuum requirements, minimum material wastage, economical way of large area deposition and no need of handling poisonous gases. Growth of CdS-PVP NCps using CBD is described in the following.

Avoiding the separate growth of CdS NCs, one-step growth of NCps is attempted. Ingredients used for growth of CdS-PVP NCp are Cadmium acetate (Loba Chemie, AR grade, 99 %) as Cd ion source, Thiourea (Loba Chemie, AR grade, 99 %) as S ion source and PVP (Loba Chemie, 99 %, 40,000 grams/mole) as an organic matrix. All the required beakers and glass slides are dipped in aqua-regia and left for one hour before deposition. Later, all the equipments are washed in water and cleaned ultrasonically in ethanol followed by de-ionized water for four minutes. Glass slides are kept vertically in the chemical bath as per the experimental requirement. Water bath is prepared for heating the chemical bath by filling tap water in a large beaker and a smaller beaker is used for the chemical bath. The heating and stirring arrangements are accordingly made in the large and small beaker, respectively. A stirrer is kept in the solution, which can rotate about its axis. 100 ml of chemical bath containing aqueous solution of PVP, Cadmium acetate (Cd-A: Cd^{+2} source) and Thiourea (ThU: S^{-2} source) is prepared in the following manner. PVP solution is prepared by adding measured amount of PVP to 80 ml of deionized water. Appropriate weight of Cd-A and ThU is added to each of two beakers containing 10 ml of deionized water. These aqueous solutions of PVP, Cd-A and ThU are mixed in the chemical bath. It is important to note here that for all depositions, molarity of Cd-A and ThU is taken to be same. For convenience of writing, concentration of Cd-A &ThU is written in molar (M) and content of PVP is written in grams (g) for 100 ml of aqueous chemical bath, except where otherwise noted. Sample grown with Cd-A & ThU concentration of 1 M and PVP content of 2 g will be described hereafter as 1M, 2g. To study the growth of CdS NCs in PVP matrix from various angles, we have investigated,

i) The effect of different molarities of Cd-A & ThU: Three different Cd-A & ThU concentrations 0.01, 0.5 and 1 M are used to study the growth.

ii) The effect of different quantity of PVP: quantity of PVP is varied from 0.05 g to 10 g (1.25 $*10^{-2}$ mM to 2.5 mM) in discrete steps for 0.5 M Cd-A & ThU.

iii) The effect of heating/cooling process and deposition time on the growth.

2.2. Raman and Atomic force microscopy mapping

Raman spectroscopy/mapping is used as a main research tool to study both semiconductor NCps. Further, the understating developed using Raman spectroscopy is used in corroboration with AFM to get insight into the morphology of these NCps as described below.

2.2.1. Raman spectroscopy

Interaction of photons with the matter leads to absorption, reflection and transmission of light. However, it is also possible for the photon to interact with the material and scatter from it. In this case, there is no need for the photon to have an energy which matches the difference between two energy levels of the material. This scattering process is regarded as inelastic scattering (Raman scattering: frequency of scattered light is different from incident) [196]. In this thesis, we will talk about inelastic light scattering mediated by optical phonons i.e. scattering of visible light (2-3 eV) by optical phonons (2-3 meV). In the following, we will discuss the quantum theory of Raman spectroscopy.

2.2.1.1. Quantum theory of Raman spectroscopy

When a monochromatic light of frequency ω falls on a system, most of the light passes as such but in addition, scattering of light occurs [196]. It was found that scattered light consists of a very strong line in the spectrum at the frequency ω (elastic scattering- Rayleigh scattering) as well as series of weaker lines at frequency $\omega \pm \omega(\mathbf{q})$, which is due to inelastic scattering and is called Raman scattering. Here, $\omega(\mathbf{q})$ is the frequency of optical phonon. Frequencies $\omega - \omega(\mathbf{q})$ corresponds to Stokes lines and $\omega + \omega(\mathbf{q})$ corresponds to anti-Stokes lines. The interaction of radiation with matter is treated as a problem of time dependent perturbation in quantum mechanics. When a photon is incident on a crystal, it sets up a perturbation of its electronic wave function, as only electron can follow the fast changing electric field of visible radiation. Thus, wave function of perturbed crystal acquires a mixed character and becomes linear combination of all possible wave function of unperturbed crystal with time dependent coefficient. Hamiltonian of this system is given by,

$$\hat{\mathrm{H}}_{\mathrm{s}} = \hat{\mathrm{H}}_{\mathrm{R}} + \hat{\mathrm{H}}_{\mathrm{m}} + \hat{\mathrm{H}}_{\mathrm{eR}} \qquad 2.1$$

Where $\hat{\mathrm{H}}_{R}$ = Hamiltonian of radiation in absence of medium,

$\hat{\mathrm{H}}_{\mathrm{eR}}$ = Interaction Hamiltonian of radiation and medium,

$\hat{\mathrm{H}}_{m}$ = Hamiltonian of medium in absence of radiation and is given by,

$$\hat{\mathrm{H}}_{\mathrm{m}} = \hat{\mathrm{H}}_0 + \hat{\mathrm{H}}_{\mathrm{I}} \tag{2.2}$$

$\hat{\mathrm{H}}_0$ is the total Hamiltonian of electronic level,

$\hat{\mathrm{H}}_{\mathrm{I}}$ is the interaction Hamiltonian between electronic and vibration level.

Thus, $\hat{\mathrm{H}}_{\mathrm{eR}}$ and $\hat{\mathrm{H}}_{\mathrm{I}}$ are treated as perturbation Hamiltonian and $\hat{\mathrm{H}}_0$ and $\hat{\mathrm{H}}_R$ are unperturbed Hamiltonians. Thus, electrons mediate the scattering of phonons, although they remain unchanged after the process. Each scattering event in the quantum mechanical theory corresponds to a transition between initial states $|i\rangle$ and final states $|f\rangle$ of the scattering medium, these being Eigen states of $\hat{\mathrm{H}}_0$.

$$\hat{\mathrm{H}}_0|i\rangle = \hbar\omega_I\,|i\rangle \tag{2.3}$$

$$\hat{\mathrm{H}}_0|f\rangle = \hbar\omega_f\,|f\rangle \tag{2.4}$$

The radiation field simultaneously undergoes transition from an initial state with n_I and n_s to final state with n_I-1 and n_s+1.

$$\hat{\mathrm{H}}_R\,|n_I, n_s\rangle = (n_I\hbar\omega_I + n_s\hbar\omega_s)|n_I, n_s\rangle \tag{2.5}$$

$$\hat{\mathrm{H}}_R\,|n_I{-}1, n_s + 1\rangle = \{(n_I - 1)\hbar\omega_I + (n_s + 1)\hbar\omega_s\}|n_I - 1, n_s + 1\rangle \tag{2.6}$$

These transitions in the system are due to perturbation $\hat{\mathrm{H}}_{eR}$. The energy lost/gained by the scattering medium in the process is $\left|\hbar\omega_f - \hbar\omega_I\right|$, the energy that is equal to energy gained/lost by photon $|\hbar\omega_I - \hbar\omega_s|$. In second quantization, wherein physical quantities (e.g. momentum) as well as fields are quantized and vector potential/electric field operators are given by,

$$\hat{A}(\vec{r}) = \sum_k \left(\frac{2\pi\hbar c^2}{\eta_k^2 V\omega_k}\right)^{1/2} \hat{e}_k.\left(\hat{a}_k e^{i\vec{k}.\vec{r}} + \hat{a}_k^+ e^{-i\vec{k}.\vec{r}}\right) \qquad 2.7$$

$$\hat{E}(\vec{r}) = \sum_k \left(\frac{2\pi\hbar\omega_k}{\eta_k^2 V}\right)^{1/2} \hat{e}_k.\left(\hat{a}_k e^{i\vec{k}.\vec{r}} - \hat{a}_k^+ e^{-i\vec{k}.\vec{r}}\right) \qquad 2.8$$

V is sample volume, $\hat{e}_k$ is polarization of the mode k, η_k is refractive index of the medium at frequency ω_k. $\hat{a}_k$ and $\hat{a}_k^+$ are annihilation and creation operator of photon of wave vector k and frequency ω_k, respectively. n_k is number of photons in mode k.

Hamiltonian of electron in crystal field V(r) is given by,

$$\hat{H}_0 = \sum_j \frac{\hat{p}_j^2}{2m} + V(\vec{r}_j) \qquad 2.9$$

here, $\vec{r}_j$ is the position vector of j^{th} electron in the crystal. Radiation interaction field is involved in the electron Hamiltonian by replacing.

$$\hat{p}_j \rightarrow \hat{p}_j - \left(\frac{-e.\hat{A}(\vec{r}_j)}{c}\right) \qquad 2.10$$

$$\hat{H}_0 + \hat{H}_{eR} = \sum_j \frac{1}{2m}\left(\hat{p}_j + \frac{e.\hat{A}(\vec{r}_j)}{c}\right)^2 + \hat{V}(\vec{r}_j) \qquad 2.11$$

This expression satisfy coulomb gauge condition $\nabla.\hat{A} = 0$

$$\hat{H}_{eR} = \frac{e^2}{2mc^2}.\hat{A}(\vec{r}_j).\hat{A}(\vec{r}_j) + \frac{e}{mc}.\hat{A}(\vec{r}_j).\hat{p}_j \qquad 2.12$$

$$\hat{H}_{eR} = \hat{H}'_{eR} + \hat{H}''_{eR} \qquad 2.13$$

Here,

$$\hat{H}'_{eR} = \frac{e^2}{2mc^2}.\hat{A}(\vec{r}_j).\hat{A}(\vec{r}_j) \qquad 2.14$$

$$\hat{\mathrm{H}}''_{eR} = \frac{e}{mc} \cdot \hat{\mathrm{A}}(\vec{r}_j).\hat{p}_j \qquad 2.15$$

In this scattering experiment, scattering cross-section is defined as the rate of removal energy from incident beam to scattering medium by the scattering process into solid angle dΩ, in volume V,

$$\frac{d^2\sigma}{d\omega_s \mathrm{d}\Omega} = \frac{1}{\tau}\frac{\hbar\omega_I}{\bar{\mathrm{I}}_I} \qquad 2.16$$

$\frac{1}{\tau}$ is the transition rate between initial and final state of medium in event of scattering. $\bar{\mathrm{I}}_I$ is mean intensity of incident beam.

The transition rate is given by Fermi golden rule [197]. Transition rate in terms of Raman susceptibility $\Delta\chi_R$ is given by [196],

$$\frac{1}{\tau} = \frac{8\pi^3}{\hbar^2}\frac{n_I}{\eta_I^2\eta_s^2}\sum_{i',j'}[\hat{e}_s \,.\, \Delta\chi_R . \hat{e}_I\,]^2 \;\delta(\omega_{i'} - \omega_{f'}).\mathrm{P}(i') \qquad 2.17$$

Raman scattering process includes electron-radiation interaction and electron-phonon interaction. To write phonon state explicitly one has to introduce electron-phonon Hamiltonian too. In the Raman scattering process, phonon is created (Stokes) or annihilated (anti-Stokes) and thus electronic state will not change. Under the adiabatic approximation, electronic and nuclear wave functions can be separated out. Raman scattering involves annihilation of photon, creation or annihilation of phonon and creation of photon. All the three steps in scattering can take place in any time order and thus one can have six terms in Raman susceptibility for the Stokes process. In this case Raman susceptibility will be of the form,

$$\Delta\chi_R = \frac{e^2}{m^2 V \hbar^2 \omega_s^2} *$$

$$\Big(\sum_{u_1 u_2} \frac{\left\langle 0|p(-\vec{k}_s)|u_2\right\rangle \langle u_2, n+1|\hat{H}_{eL}|u_1, n\rangle \left\langle u_1|p(\vec{k}_l)|0\right\rangle}{(\omega_{u_2}-\omega_s)(\omega_{u_1}-\omega_l)} + \frac{\left\langle 0|p(\vec{k}_l)|u_2\right\rangle \langle u_2, n+1|\hat{H}_{eL}|u_1, n\rangle \left\langle u_1|p(-\vec{k}_s)|0\right\rangle}{(\omega_{u_2}+\omega_l)(\omega_{u_1}+\omega_s)} +$$

$$\frac{\langle 0,\ n+1|\hat{H}_{eL}|u_2, n\rangle \left\langle u_2|p(-\vec{k}_s)|u_1\right\rangle \left\langle u_1|p(\vec{k}_l)|0\right\rangle}{\left(\omega_{u_2-\omega_{ph}}\right)\left(\omega_{u_1-\omega_l}\right)} + \frac{\langle 0, n+1|\hat{H}_{eL}|u_2, n\rangle \left\langle u_2|p(\vec{k}_l)|u_1\right\rangle \left\langle u_1|p(-\vec{k}_s)|0\right\rangle}{(\omega_{u_2}-\omega_{ph})(\omega_{u_1}-\omega_s)} +$$

$$\frac{\left\langle 0|p(-\vec{k}_s)|u_2\right\rangle \left\langle u_2|p(\vec{k}_l)|u_1\right\rangle \langle u_{12}, n+1|\hat{H}_{eL}|0, n\rangle}{(\omega_{u_2}-\omega_s)(\omega_{u_1}+\omega_{ph})} + \frac{\left\langle 0|p(\vec{k}_l)|u_2\right\rangle \left\langle u_2|p(-\vec{k}_s)|u_1\right\rangle \langle u_1, n+1|\hat{H}_{eL}|0, n\rangle}{(\omega_{u_2}+\omega_l)(\omega_{u_1}-\omega_{ph})} \Big) \qquad 2.18$$

Transition from u_1 to u_2 is phonon induced transition. Thus, differential scattering cross section is given by

$$\frac{d\sigma}{d\Omega} = v\frac{\eta_s}{\eta_I} * \frac{1}{c^4} * \frac{\omega_s^5}{\omega_I}\frac{\hbar(n+1)}{2M_r\omega_{ph}a_0^3}\left[\hat{e}_s . \Delta\chi_R . \hat{e}_I\right]^2 \qquad 2.19$$

Here, v is the scattering volume. We define S (scattering efficiency) in angle by dropping v. S is ratio between the scattered and incident power for a path length in solid. Thus,

$$S = n_I\frac{\eta_s}{\eta_I} * \frac{1}{c^4} * \frac{\omega_s^5}{\omega_I}\frac{\hbar(n_{ph}+1)}{2M_r\omega_{ph}a_0^3}\left[\hat{e}_s . \Delta\chi_R . \hat{e}_I\right]^2 \qquad 2.20$$

Here, η_s and η_I depend on scattered and incident frequency, respectively and $[\hat{e}_s . \Delta\chi_R . \hat{e}_I]^2$ gives the microscopic cross section and n_{ph} is the Bose-Einstein occupation factor. Here, S is macroscopic cross section, which depends on the number of incident photon, forth power of scattered frequency ($\omega_s \approx \omega_I$). Thus, Raman cross section is proportional to i) number of incident photons, ii) scattering volume, iii) energy of incident photons (when energy of incident photons is equal to or nearly same as that of real energy levels). Raman scattering is third order scattering process and thus Raman cross section is inherently weak. For nanostructures, scattering volume can be low and thus, Raman cross section will be weaker. Thus, if we want to increase Raman signal for nanostructures, we need to either increase number of incident photons or we can make use resonance Raman scattering, which will depend on excitation wavelength. This can be understood from the Raman susceptibility term (equation 2.18) and scattering efficiency (equation 2.20). Terms 1st, 3rd and 5th suggest that when the excitation wavelength is close to real energy levels, denominator of these terms become vanishingly small to give very large contribution due to resonance enhancement. In the above, we have given scattering efficiency for Stokes process. Similarly, it can be written for anti-Stokes process and is given by,

$$S = n_I \frac{\eta_s}{\eta_I} * \frac{1}{c^4} * \frac{\omega_S^5}{\omega_I} \frac{\hbar(n_{ph})}{2M_r \omega_{ph} a_0^3} [\hat{e}_s \,.\, \Delta\chi_R . \hat{e}_I\,]^2 \qquad 2.21$$

Here, the only difference in anti-Stokes Raman scattering is factor n_{ph}, where it is n_{ph} +1 for Stokes Raman scattering (equation 2.20). This is because in anti-Stokes process, phonon is annihilated. Thus, the intensity of Stokes to anit-Stokes ($\frac{I_{Stokes}}{I_{anit-Stokes}}$) is given by,

$$\frac{I_{Stokes}}{I_{anit-Stokes}} = \frac{(\omega_I - \omega_S)^4}{(\omega_I + \omega_S)^4} \frac{n_{ph}+1}{n_{ph}} \qquad 2.22$$

here, n_{ph} is the given by,

$$n_{ph}(\omega) = \frac{1}{\exp^{\frac{\hbar\omega}{kT}} - 1} \qquad 2.23$$

and therefore,

$$\frac{I_{Stokes}}{I_{anit-Stokes}} = \frac{(\omega_I - \omega_S)^4}{(\omega_I + \omega_S)^4} \exp^{\frac{\hbar\omega}{kT}} \qquad 2.24$$

This suggests that we can calculate the local temperature of the system using intensity (I) ratio of Stokes to anti-Stokes phonon. We have used this ratio to calculate the local temperature for Si-SiO_2 NCps.

2.2.1.2. Instrumentation

Raman scattering (inelastic light scattering) is much weaker ($\sim 10^8$) than Rayleigh scattering (elastic light scattering) [198]. Therefore it is important to filter the Rayleight light, in order to measure Raman scattered signal from any material. The Raman set up generally contains, i) A laser light source for excitation of Raman spectra, ii) Spectrometer to disperse scattered wavelengths and iii) a detector to detect the scattered light at a particular wavelength coming out of the spectrometer: Raman spectra is the intensity of scattering light measured as Raman shift (taking laser light as zero wavenumber) in wavenumbers (cm^{-1}). In conventional Raman scattering set up, suitable external optics is used for focusing the light on the sample to be studied for configuration of interest i.e. 90 ^{0}, 180 ^{0} etc. The collection optics couples scattered light to the spectrometer.

1) Laser light source

Raman scattering is a weak scattering process and thus, coherent and monochromatic laser light source is used to obtain measurable Raman signal. Gas lasers are preferred for the excitation of Raman spectra as, the line width of gas lasers (0.01 cm^{-1}) is much smaller than instrument resolution of spectrometers and they come with many discreet laser lines in one source. This allows us the flexibility to choose appropriate laser line as per requirement of the Raman measurement. Further, one needs to have tightly focused laser beam to achieve spatial resolution in micro Raman spectroscopy/mapping and polarized Raman spectroscopy requires light source with vertical/horizontal polarization. This can be easily achieved using gas lasers.

Different types of gas lasers used are Helium-Neon laser, Helium-Cadmium laser, Argon ion laser, Krypton ion laser etc, which give discreet line in the range 350 nm - 675 nm. To study Si-SiO_2 NCps and CdS-PVP NCps, we have used 448 nm and 514.5 nm line of Ar^+ laser and 441.6 nm line of He-Cd. Since the used lasers are close to E_1 (3.1 eV) and E_0 (2.42 eV) optical gap for Si and CdS, thus Raman mapping can be effectively used to study both these NCps due to resonance enhancement of Raman signal.

2) Spectrometer

A spectrometer is a device which monochromtizes the polychromatic light. A spectrometer has a dispersive element (grating), and collimating and focusing mirrors. The polychromatic light is focused at the entrance and monochromatic light is focused on the exit slit. The spectrometer system can be used in two configurations, i) as a monochromator and ii) as a spectrograph. A monochromator has entrance slit, exit slit and photomultiplier tube (PMT) as detector, whereas, spectrograph has an entrance slit and an open exit slit with charge coupled device (CCD: detector) covering the range of wavelengths. When system is used as a monochromator, grating is rotated around it's axis to scan the wavelength range desired, whereas, intensity of photons for a range of wavelengths can be observed simultaneously in spectrograph configuration i.e. with CCD. The first configuration is called signal channel detection and the later a multichannel detection. Chanel here refers to wavelength. It is obvious to see advantage of multichannel detection over single channel detection in terms of time and sensitivity, as it allows larger acquisition time for improving signal to noise ratio.

In Raman system, monochromator/s are mainly used in three different configurations, i) single monochromator as a spectrograph, ii) double monochromator which has two monochromator in series and iii) triple monochromator, which are used in two different configurations, A) Triple additive and B) Double subtractive + third monochromator as a spectrograph. Three factors decide which configuration to be used for chosen study, i) Stray light rejection, ii) Resolution and iii) Throughput.

The double monochromator used with single channel detection is preferred for high resolution studies. The Triple additive will further increase the spectral resolution at the cost of decreased throughput. Triple stage Raman with double subtractive and third stage as a spectrograph with multichannel detection is suitable for most studies, wherein double subtractive stage acts as a tunable notch filter. Notch filter filters the wavelength in the defined notch which is the Rayleigh light i.e. specific to the excitation laser. However, when throughput is an important point to consider, single stage spectrograph with notch filter is used for Raman studies. This is useful for micro Raman studies of nanostructures. Using micro Raman and nanostructures reduces the scattering volume considerably and hence throughput of the system becomes very important in order to get measurable Raman signal.

3) Detector

Photomultiplier tube: PMTs are light sensitive detectors which gives an output current proportional to intensity of light. PMT consists of input window, photocathode, focusing electrodes, an electron multiplier (dynodes) and as anode. As the photons falls on photocathode of PMT, it emits primary photo-electrons, which are electrostatically accelerated and focused on first dynode of the multiplier. The multiplier is a dynode chain and at the end of the dynode chain an electron emitted at the cathode has multiplied to give ~10^{6} electrons, which is called gain of the PMT. When photon signal is large then collected charge is measured and current and this is called the analog mode of measurement. However, for Raman scattering photon signal is weak and detection is done in photon counting mode wherein one measures an elctron pulse genrated by a single photon. In the photon counting system, the output electron pulses from the PMT are amplified by using pre-amplifier and further discriminator is used to allow a narrow band pass of pulses height to be counted as photon count. This removes pulses genrated at dynodes or due to cosmic radiation which is noise. The other main source of noise that dark current is reduced thermoelectric cooling of PMT to -20 ^{0}C. Quantum efficiency for PMT in visible region is ~ 20 %.

Charged-coupled device: CCD is a silicon-based semiconductor, arranged as an array of photosensitive elements called pixels (potential well), each one of which generates photoelectrons and stores them as a small charge. Charges are stored on each individual pixel as a function of the number of photons striking that pixel. CCD works on the principal of photoelectric effect. Parameters, which need to be considered, are quantum efficiency, noise, sensitivity, dynamic range and gain. Primary source of noise in CCD is 1) Photon noise, 2) Dark noise and 3) Readout noise. Both LN_2 (~ 193 ^{o}C) cooled CCD and thermoelectrically cooled (~ -70 ^{o}C) CCD's are commonly used in Raman systems to reduce thermal/dark noise as per requirement. Higher the quantum efficiency and lower noise leads to higher sensitivity (signal to noise ratio). CCD is used in front illuminated and back illuminated configuration. However, front illuminated CCD are less efficient due to the absorption (UV-Vis) of photons and reflection losses. Back illuminated CCD is preferred, wherein CCD thickness is thinned (~ 10 μm) so that the charges generated near the back side are carried to CCD potential wells before recombination occurs. However, occurrence of interference fringes in near IR region limits the use of back illuminated CCD's in this region. Quantum efficiency for CCD in visible region is ~ 10 % (front illuminated) and 45 % (back illuminated).

2.2.2. Atomic force microscopy (AFM)

AFM is a scanning probe technique, which is used to image surfaces at the nanometer scale [200]. In AFM, a sharp probe attached on cantilever (Fig. 2.4) is brought into close proximity to a sample. Sample is subsequently moved relative to the probe in a raster pattern. AFM operates in constant force mode i.e. force between tip and sample is kept constant as the sample is scanned below the cantilever. Deflection (angular - contact mode and oscillating frequency-non contact mode) in the cantilever is measured by reflection of a laser beam using position sensitive detector, which is used as a feedback signal to move sample stage in z direction. This z movement is measured and noted as topography. Movement of sample stage is controlled by piezoelectric material, which allows movement in very small step size ~ 10 Å. The force between the atoms of the tip and atoms of the sample surface depends on the spring constant of the cantilever and distance between the tip and the sample surface. This force is described using Hooke's Law,

$$F = -k.\, x \qquad 2.28$$

Where, F is the force, k is the spring constant of cantilever, x is the cantilever deflection. Tip is usually made of Si_3N_4 due to it's flexible nature. Depending on the force between atoms of tip and atoms of sample, AFM primarily works in three imaging modes depending on the distance between probe and sample as shown in fig. 2.1.

Contact mode: In contact AFM mode, an AFM tip makes soft "physical contact" with the sample (here the tip sample separation is 5 to 10 Å). The tip is attached to the end of a cantilever with a spring constant lower than the effective spring constant holding the atoms of the sample together. In contact mode, total van der Waals force is positive (repulsive) between atoms of tip and sample. The slope of the van der Waals curve is very steep in the repulsive or contact regime. As a result, the repulsive van der Waals force balances the force that attempts to push the atoms closer together. Thus, as the cantilever tries to push the tip against the sample, the cantilever bends rather than forcing the tip atoms closer to the sample atoms. The magnitude of the total force exerted on the sample varies from 10^{-8} N to the more typical operating range of 10^{-7} to 10^{-6} N. This mode is preferred for hard samples.

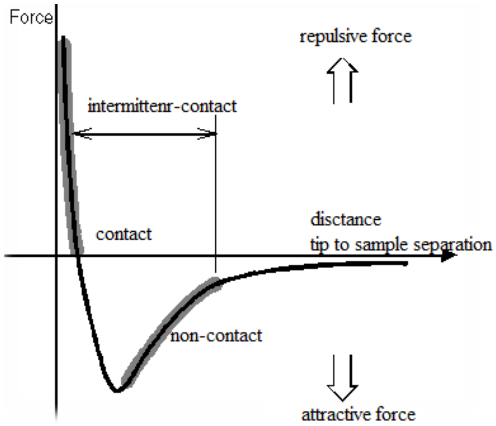

Fig. 2.1. Interatomic force vs. distance curve

Non-contact AFM: In the non-contact AFM (NC-AFM), spacing between the tip and the sample for NC-AFM is on the order of 10 to 100 Å. Here, one measures the sample topography with little or no contact between the tip and the sample. The total force between the tip and the sample in the non-contact regime is very low, generally about 10^{-12} N. Because the force between the tip and the sample in the non-contact regime is low, it is more difficult to measure the force than in the contact regime. The cantilevers used for NC-AFM are stiffer and vibrating at its resonant frequency (typically from 100 to 400 kHz) with amplitude of a few tens of Å. Changes in the resonant frequency or vibration amplitude are detected as the tip scans the sample surface.

Changes in the resonant frequency of a cantilever can be used as a measure of changes in the force gradient, which reflect changes in the tip-to-sample spacing, or sample topography. NC-AFM does not suffer from the tip or sample degradation effects that are sometimes observed after taking numerous scans with contact AFM. Further, NC-AFM is preferred for measuring soft samples.

Intermittent-contact AFM: This operating region is shown in the figure above. In this region tip sample separation varies from 5 Å to 50 Å. In this region the tip on the vibrating cantilever approaches and retracts from the sample periodically. This mode cause less damage to the sample as compared to contact mode in AFM and will be more sensitive than non contact mode.

Resolution: Resolution of AFM is determined by the tip size. In our case tip size is ~ 50 nm.

2.2.3. Raman and AFM mapping

2.2.3.1. Experimental set up used for Raman and AFM mapping

Raman spectroscopy

Micro-Raman spectroscopy/mapping (backscattering geometry) is performed at room temperature using Acton 2500i (single) monochromator with thermoelectric cooled CCD detector. The Raman set up is a part of SPM_integrated Raman system of (WiTec, Germany) (Fig. 2.2). Fig. 2.3 shows enlarged view of microscope showing sample stage, objective, laser line coupler, CCD camera and output optical fiber. Laser line coupler for each laser used (488, 514.5 and 441.6 nm) consists of i) an interference line filter, which allows only laser line to enter and thus removes the plasma line from the laser, ii) a coupler, which allows laser line to enter the microscope objective and backscattered light to pass on to o/p port of microscope and iii) notch filter which attenuates Rayleigh scattered light of the order ~10^6, and thus, allows Raman signal detection with single stage spectrograph. CCD camera noted above is used for observing the microscopic image of the sample and positioning laser for spatially resolved Raman data/mapping. Multimode optical fiber couples scattered light at the o/p port of the microscope to the spectrograph. Herein, single spectrograph with CCD (Fig. 2.1) is used, where spectrograph consist of two concave mirrors and one plane diffraction grating. First mirror collimate the light source and second focus the dispersed light from the grating. Focal length of the system is half meter. This system is equipped with three gratings as, 600 1/mm (window ~ 3600 cm^{-1}), 1200 1/mm (window - 1500 cm^{-1}) and 2400 1/mm (window - 600 cm^{-1}). These windows are noted for 488 nm laser. DV401-BV model of CCD is used, which is back illuminated. Quantum efficiency of CCD is ~ 45 % for laser wavelengths in the range 400 - 500 nm. Pixel size is 26 * 26 μm^2.

We have used 1200 1/mm and 2400 1/mm gratings to perform Raman spectroscopy measurements and 600 1/mm grating for PL spectroscopy. Raman spectroscopy is mostly performed using 2400 1/mm grating, whereas, Raman mapping is performed using 1200 l/mm grating. Microscope objective 50 x and 100 x are used to perform micro Raman measurements depending upon the suitability. Numerical aperture (NA) and working distance (WD) for 50 x and 100 x objectives are 0.55, 0.9 and ~ 8 mm, 0.03 mm; respectively. Microscope objective of 100 x gives better spatial resolution as well as better signal to noise ratio, however, one needs to be careful in using the same as WD is very small. Further, while using Raman spectroscopy as a local probe, it is important to consider i) Spatial resolution, ii) Depth of focus and iii) Spectral resolution as described in the following.

i) Spatial resolution

The spatial resolution R is the smallest distance between two points to still appear distinctively on the microscope image. According to the Rayleigh criterion [199],

$$R_{spatial} = 0.61 * (\lambda / NA) \qquad 2.25$$

here, λ is the excitation wavelength. This relation suggests that higher NA and lower λ will give better spatial resolution (Table 2.1).

1 - Lasers
2 - Power supplies for lasers
3 - Microscope
4 - Vibration isolation stage
5 - Spectrometer
6 - CCD
7 - Computer screen
8 - Electronic controller unit

Fig. 2.2. SPM integrated Raman system set up showing different parts as noted in the figure.

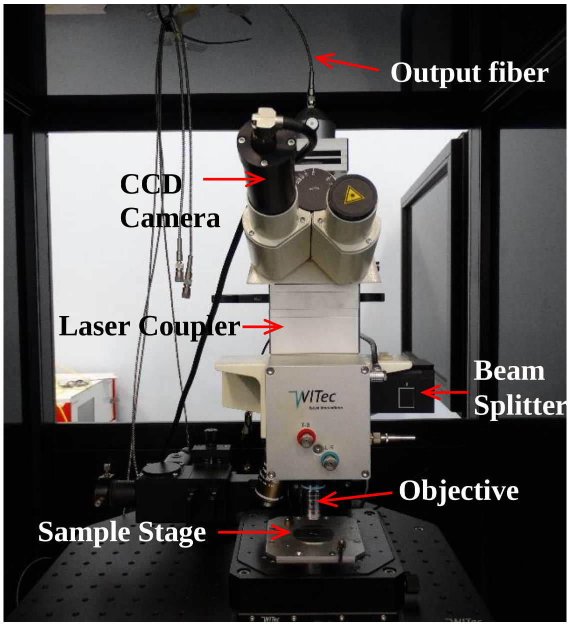

Fig. 2.3. Enlarged view of microscope shows different components as noted in the figure

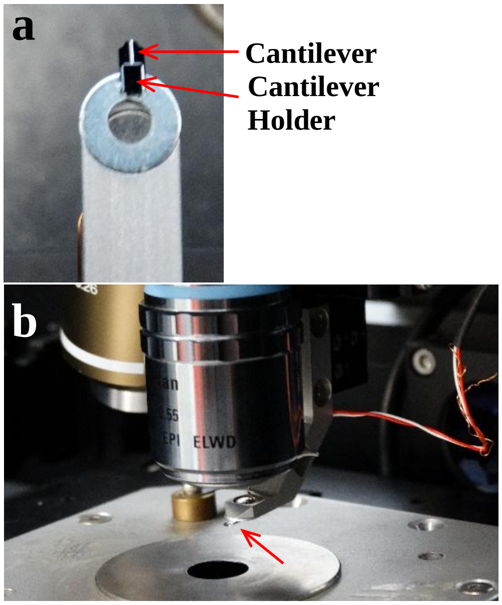

Fig. 2.4. a) Cantilever placed on cantilever holder and b) positioning (makrked with arrow) of cantilever holder.

ii) Depth of focus

Depth of focus refers to as focus tolerance in the image plane of the microscope [199]. This appears due to lens aberration and is given by,

$$z \text{ (in air)} \approx (\lambda/NA^2) \qquad 2.26$$

iii) Spectral resolution

Spectral resolution ($\Delta\lambda$) is the ability of the spectrometer to resolve two closely lying spectral features into separate components and is given by,

$$\Delta\lambda = \text{Slit width} * d * 10^6 / (f * n) \qquad 2.27$$

Here, $\Delta\lambda$ is in units of nm, d is the groove spacing, f is the focal length of the spectrograph (here it is 500 mm) and n is the diffraction order. Slid width is decided by the width of output optical fiber (here it is 100 μm).

Table 2.1. Spatial resolution and depth of focus for different lasers are summarized.

Laser (nm)	Spatial resolution (μm)	Depth of focus (μm)	Spatial resolution (μm)	Depth of focus (μm)
	50x (NA - 0.55)		100x (NA - 0.9)	
441.6	0.49	1.4	0.4	0.5
488	0.54	1.5	0.42	0.6
514.5	0.57	1.6	0.46	0.63

Table 2.2. Spectral resolution

	Spectral resolution (cm^{-1})	
Laser (nm)	1200	2400
441.6	4	2.5
488	3.5	2

Raman mapping

The scan stage is raster-scanned to record Raman spectrum across a chosen area and Raman image is generated using intensity/frequency of a phonon of choice for a particular material. Scan area is chosen with the help of image recorded using CCD camera (Fig. 2.3), which is also used to focus and select positioning of laser.

AFM mapping

We have performed AFM mapping measurements in non-contact mode using 50 x objectives, since the working distance for 100 x objective is very small. Non contact mode is chosen to avoid damage of NCps studied. For 10 * 10 μm^2, we have chosen 300 * 300 steps, which means that obtained step resolution will be around ~ 30 nm. To get high resolution topography image, step resolution is chosen to be at least ten times the size being measured. Further, the scan speed of non contact AFMs is also an important parameter. Scan speed is limited by the speed of the feedback loop that maintains constant amplitude and thus faster scan can lead to observance of noise in the topography image. In our case, used scanning speed ~ 4 s/line gives good topography image.

2.2.3.2. Methodology to perform Raman and AFM mapping on same site

In NSOM-SPM integrated Raman system set up, Witec, one can perform Raman and AFM mapping measurements simultaneously. However, therein we need to use Advantech probe which leads to loss of Raman intensity to some extent and also gives rise to shift between centre of focused laser spot and centre of focused AFM tip (~ 4.0 -7.0 μm). Therefore, we performed these AFM and Raman measurements independently on a selected area by taking visual guidance of an optical image to ensure the data on the same selected area. To ensure that the data is being taken on the same selected area, visual guidance of an optical image is used. When performing, Raman and AFM mapping independently, it is necessary to ensure the position of AFM tip coincide with that of laser spot for Raman mapping. We find that the shift between the laser spot and position of AFM tip is ~ 7 μm, -23 μm. First, we choose particular area with the help of optical image created using microscope and performed Raman mapping on the selected area. After that, we incorporated this shift and performed AFM mapping. Further, we find that even after incorporating this shift, we observed displacement in topography image by ~ 0.2 µm, -0.4 µm as compared to Raman image and thus we always considered large (by ~ 0.5 µm in both the directions) area for performing AFM mapping. Using this method, we performed Raman and AFM mapping on CdS-PVP NCps (Fig. 2.5), as we observed clear structures in these samples in the optical image. This is done number of times and the shift (~ 7.0 µm, -23.0 µm) between the position of AFM tip and laser spot is determined. This shift is incorporated while doing AFM mapping to obtain one to one correspondence between the optical image, Raman image and topography (AFM image) for Si-SiO$_2$ and CdS-PVP NCps.

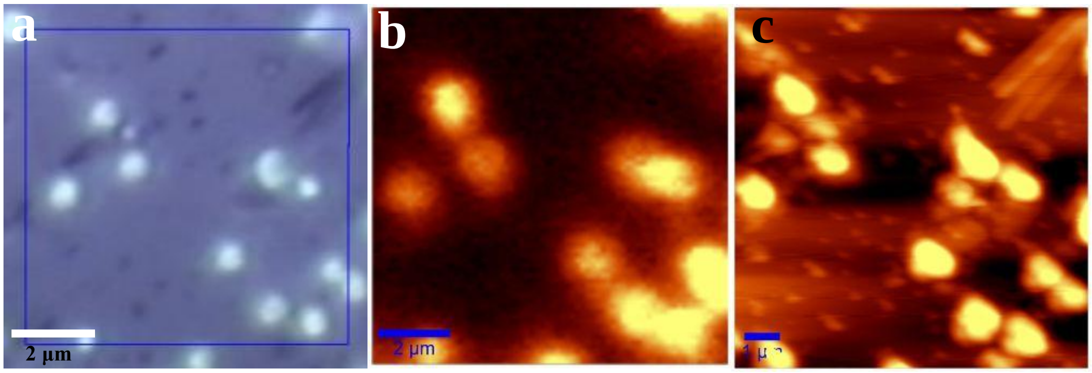

Fig. 2.5. a) Optical image shows isolated strcutres, b) Raman image, c) AFM image showing one to one corresponds between optical, Raman and AFM image.

2.3. Characterization techniques for nanostructures

2.3.1. Absorption and diffuse reflectance spectroscopy

Optical behavior of semiconductors and semiconductor nanostructures in the near infrared, visible, and ultraviolet can be determined by studying the transition between valence and conduction band [201]. Optical absorption spectroscopy is a very useful technique to study this electronic transition in bulk, colloidal, thin film, nanostructures etc. During the measurements, absorbance of a material, which is a logarithmic ratio of the radiation falling upon a material, to the radiation transmitted through a material is measured. Thus, if the energy of an incident photon corresponds to the energy gap between the ground state and an excited state, the photon get absorbed. It is this change which is measured in absorption spectroscopy by the detection of the loss of that energy of radiation from the light. In the direct band gap material, wherein transition take place at **k** = 0, band gap can be obtained from the equation given by,

$$(\alpha h\nu)^2 \propto h\nu \qquad 2.29$$

Band gap is obtained by plotting $(\alpha h\nu)^2$ against hν, where, α is the absorption coefficient and ν is frequency of incident light. The band gap is that energy, where the tangent to this curve intersects energy axis. Absorption coefficient (α) can be obtained from the measured absorbance by,

$$\text{Absorbance} = 0.4343 \times (\alpha \times l) \qquad 2.30$$

Here, l is the thickness of the material (film). We have used this methodology to obtain absorption coefficient for Si NCs using average thickness for Si.

Band gap increases with the reduction in size of nanostructure due to quantum confinement of electrons. Therefore, blue shift [202] observed in band gap can be used to calculate size of NCs. The band gap of a spherical NC is given by,

$$E_{NC} = E_g + \frac{\hbar^2\pi^2}{2R^2}\left(\frac{1}{m_e} + \frac{1}{m_h}\right) - \frac{1.78\, e^2}{4\pi\varepsilon_0 R} \qquad 2.31$$

where, for CdS NCs, Eg is the band gap of bulk CdS (2.42 eV), R is the radius of the NC, m_e is effective mass of the electron (~ 0.19m), m_h is the effective mass of hole (~ 0.53 m), m is the mass of electron, ε_0 is the dielectric constant (~ 5.5) [202].

Interaction of light with matter leads to reflection, transmission, absorption and scattering of light. In general, scattering is negligible and thus during the transmission measurement, one observes mainly optical features in the spectrum. However, quantitative interpretation of absorption spectra in the presence of large scattering is not feasible sometimes. Thus, it is necessary to separate the scattering component from absorption spectra, which can be done using diffuse reflectance spectroscopy.

Reflectance spectroscopy measurements can be performed in diffuse and diffuse + specular mode by keeping the sample at the exit port of integrating sphere. For measuring the diffuse reflectance, the 0^0 configuration is used. In this configuration, the light is incident normally onto the sample surface due to which the specular part of the reflected light goes out through the entrance port, and hence only the diffuse part is measured. In order to measure the total reflectance, the 8^0 configuration of the integrating sphere is used and thus both specular and diffuse reflections are measured collectively by the detector giving the value of total reflectance. Taking diffuse reflectance as a guide, one can separate out the scattering component from absorption spectra of CdS-PVP NCps.

We have performed absorption spectroscopy and diffuse reflectance spectroscopy measurements in the wavelength range 300 - 800 nm using CARY 50 and CARY 5000 UV-Vis spectrophotometer, respectively. Absorption spectroscopy measurements are performed on the both the NCps to obtain information on optical gap of NCs. Further, DRS measurements are performed on CdS-PVP NCps to remove observed scattering contribution from the absorption spectra.

2.3.2. Photoluminescence spectroscopy

Photoluminescence (PL) describes light emission stimulated by exposing the material to light [201]. PL is a non-destructive optical technique used for measuring the band gap of materials and detection of defects. Thus, when a semiconductor absorbs a photon of energy greater than the band gap, an electron is excited from the valence band into the conduction band leaving behind a hole. When the electron de-excite, it may do so in a radiative (release of a photon) manner and thus gives information about the band gap of the material. However, if defect levels are present, electron can non-radiatively relax at the defect center and then radiatively recombine with the hole in the valence band, emitting photon of different energy compared to that for band gap. Thus using PL spectroscopy, one can study the band gap as well as the presence of defects.

We have performed PL mapping of CdS-PVP NCps using 600 1/mm grating with 441.6 nm (2.8 eV) excitation sources as this energy is higher the band gap of CdS. Therefore, using this source, we can study one to one correspondence between absorption and PL spectroscopy to study band gap and thus size of CdS NCs. Further, we have studied the correlation of size of CdS NCs, it’s passivation with the observed morphology of CdS-PVP NCps using PL mapping.

2.3.3. Electron Microscopy

Electron microscopy is based on the concept of wave nature of electrons. There are two types of electron microscopes [203], 1) Scanning electron microscopy (SEM) and 2) Transmission electron microscopy (TEM).

2.3.3.1. Scanning electron microscopy

SEM is used to analyze the surface morphology of material. SEM is a reflection based technique. The electrons are produced from tungsten filament by thermionic emission process. The emitted electrons are accelerated by electric field. The beam is allowed to pass through electromagnetic lenses that condense electron beam. With the help of this arrangement electron beam of high energy is achieved. Interaction of primary electron beam with the sample causes four processes; back scattered electrons, secondary electron, X-rays, auger electron. For each of these, different types of detectors are used. Secondary electrons (SE) have low energy. SE generated in the bulk gets absorbed within the sample. Only those generated in the surface of the sample escape and detected are used for imaging of the surface of sample.

Energy dispersive spectroscopy (EDS) is also used in SEM for knowing chemical composition of elements. A lower energy electron (usually K-shell) is emitted from the atom during the secondary electron emission process leaving a vacancy in this shell. An electron from higher energy level can fall into the lower energy shell to fill this vacancy and it emits energy in the X-ray region. Emitted energy is unique to the element and thus gives information about the elements present in the excited region.

SEM and EDS measurements are performed on CdS-PVP NCps using model XL30CP (30 KV) of Philips, Holland and CARLZEISS SIGMA field emission (FE)-SEM (10 kV) in order to study the morphology of CdS-PVP NCps as well as it’s correlation with the observed scattering contribution in absorption spectra of these NCps.

Resolution: Resolution depends on the beam size and accelerating voltage [203]. Beam with smaller diameter resolve more detailed structure of the sample as compared to beam with larger diameter. Resolution obtained is 35 Å for 30 kV. In case of FE-SEM, the electrons are produced by field emission source, wherein beam diameter is smaller and thus better resolution (20 Å) is achieved using FE-SEM at lower accelerating voltage (~ 5-10 kV).

2.3.3.2. Transmission Electron Microscopy

In TEM, energy of the electrons used is higher as compared to that used for SEM. Source illumination part is same as that in SEM. Here, electron beam has enough energy to travel through the specimen. Some of the electrons get scattered in the specimen and rest get transmitted, which are focused by an intermediate and projector lens onto the fluorescent screen. The beam strikes the screen and light is generated. The darker areas of the image represent those areas of the sample, where scattering is more. The lighter areas of the image represent those areas of the sample that more electrons are transmitted through. Since the scattered electrons have to be transmitted through the sample, sample should be thin enough which not the case is for SEM. The limitation of TEM is that sample thickness should be of the order of 100 nm and hence many a times sample preparation is required and that is very cumbersome. In order to form images in the TEM from transmitted electrons, either the central bright spot, or some or all of the scattered electrons can be used. Electrons scattered at a specific angle can thus be selected by inserting an aperture into the back focal plane of the objective lens. If the direct beam is selected, the resultant image is called bright-field image, and if scattered electrons are selected then the micrograph is called dark-field image.

For the present work, TEM is performed on chosen CdS-PVP NCp using model CM200 of Philips, Holland. Accelerating voltage used in TEM is ~ 200 kV and thus resolution achieved is 2.1 Å [203].

2.3.4. X-Ray Diffraction

Crystal structure is studied through the X-ray diffraction (XRD), which are high-energy electromagnetic radiation [204]. They have energy ranging from 200 eV to 1 MeV. Diffraction depends on the crystal structure and wavelength used. In an atom we have number of electrons and all electrons will scatter beam of X-ray. When we consider atoms in a crystal, each atom will scatter x-rays. Since, atoms are arranged in regular pattern, scattered waves from the atoms will have definite phase relationship and will interfere. If the waves are in phase then there will be constructive interference and when out of phase, there will be destructive interference.

The Bragg's Law: Consider a set of parallel plane with the spacing between the planes is d. Radiation is incident on the planes. The path difference for rays reflected from adjacent planes is $2d\sin\theta$, where θ is the incident angle, measured from the plane. Rays from the adjacent plane will interfere constructively when the scattering angle is equal to the angle of incidence θ of the original beam and when the path difference is an integral multiple n of wavelength λ, so that

$$2d\sin\theta = n\lambda \qquad n = 1, 2, 3... \qquad 2.32$$

This is the Bragg's law. Diffraction occurs only when the wavelength of the wave is of the same order of magnitude as the distance between scattering centers.

Powder diffraction pattern consists of series of peaks with different intensities. Peak intensity is plotted on the ordinate and the measured diffraction angle 2θ, along the abscissa.

Each peak in the diffraction pattern corresponds to X-rays diffracted from a specific set of planes. Our samples are NCs embedded in matrix which are expected to have random orientation. This is expected to give powder XRD pattern. However, one will observe single peak for oriented samples (e.g. single crystal) corresponding to that particular orientation. As we change the angle of diffraction we will get another peak from another set of parallel planes. XRD data can be used to study the crystalline quality, presence of stress, size of NCs, lattice constant, phase transition, etc.

We have performed grazing incidence XRD (GIXRD) using synchrotron source on CdS-PVP NCps for phase identification of CdS NCs. Grazing incidence geometry is used to remove the substrate (glass) contribution because it can obscure the intrinsic feature of the NCp film. GISXRD measurements are performed at angle dispersive X-ray diffraction Beamline -12 on Indus-2 Synchrotron source, RRCAT, India with $\lambda \sim 1.17832$ Å. Resolution of the double crystal monochromator used is ~ 0.04^{o}.

2.3.5. X-ray photoelectron spectroscopy (XPS)

XPS is one of the most important methods to study surfaces/interfaces [205]. In XPS, kinetic energy distribution of the emitted photoelectrons from surface (escape depth ~ 5 - 10 nm) is analyzed to study the composition and electronic state of any sample and is based upon the photoelectric effect. Accordingly, when the sample is irradiated with photons of energy hν, it emits electrons from the sample surface. The kinetic energy of the emitted electron is given by

$$\text{K.E.} = h\nu - \text{B.E.} - \phi \qquad 2.33$$

here, hν is the energy of the incident photon, B.E. is the binding energy of the emitted electron and ϕ is the work function of the spectrometer. The XPS spectrum is the plot of number of emitted electrons per energy interval versus their B.E./kinetic energy. Since, each element produces a characteristic set of XPS peaks; one can identify directly the presence of suboxide stated at the surface/interface of any material. In XPS, the number of detected electrons corresponding to each characteristic B.E. is energy related to the valence state of a particular element present within the area (volume) of the sample being irradiated. In this measurement, high vacuum is required to minimize the contamination of the surface.

In the present work, Omicron XPS system with monochromatic Al-$K_{\alpha1}$ X-ray radiation (1486.6 eV, penetration depth ~ 1 - 10 nm) is used for XPS measurements on Si-SiO_2 NCps to study presence of different suboxide states (Si^{1+-3+}). Survey scans are recorded over 0-1400 eV kinetic energies and then detailed scans are measured to determine the oxidation state of the elements of interest. Resolution of the system is ~ 0.8 eV, which is less than the separation between different suboxide states observed in Si-SiO_2 NCps. Measured spectra is deconvoluted using peakfit [206] software after the removal of linear background. In general, XPS spectra are fitted using Gaussian-Lorentzian line shape, wherein Gaussian part describes instrumental broadening, X-ray line-shape while, the Lorentzian part describes the lifetime broadening.

Chapter 3

Si-SiO_2 nanocomposites

3.1. Introduction

Si NCs have been extensively studied, realizing their potential applications in optoelectronic [207] and photovoltaic [208] devices. Further, it is found highly desirable to have thin film form of Si NCs for most device applications. Therefore, NCps, wherein Si NCs are embedded in an insulating matrix are used to exploit the full potential of Si NCs. Different types of insulating materials such as SiO_2, Al_2O_3, Si_3N_4, and SiC have been used as matrix for Si NCs [209]. Out of these, Si NCs are mainly embedded in SiO_2 due to convenience of it's growth compared to other NCps. Various techniques used to grow Si-SiO_2 NCps are ion implantation [117-124], magnetron sputtering [125-130], cluster beam deposition [131-134], electron gun evaporation [135-136], plasma enhanced chemical vapor deposition [137-141], gas evaporation [143], pulsed laser deposition [148-150], etc. In most of the techniques stated above, the growth of Si NCs is started with amorphous silicon dioxide films (SiO_x) [210,211]. Further, subsequent high temperature annealing (> 1000 ^{0}C) of amorphous SiO_x matrix leads to the formation Si NCs embedded in SiO_2 matrix as a-SiOx is thermodynamically unstable and a chemical reaction takes place upon high temperature annealing [212],

$$SiO_x \rightarrow x/2(SiO_2) + (1-x/2)\ Si$$

It is found in literature that irrespective of growth technique used, Si optical phonons are reported in the range 495 - 519 cm^{-1} in Si-SiO_2 NCps for different NCps [117-150]. Origin of high frequency ($\geq$ 515 cm^{-1}) Si phonons is well understood as due to phonon confinement in Si NCs. However, understanding of origin lower frequencies ~ 500 cm^{-1} is far from satisfactory. Although, there have been few attempts to understand the origin of this variation; this whole range Si phonon is not yet well understood. Similar variations are also found in PL spectra of Si-

SiO_2 and we feel that these two are connected. Thus, the aim of this work is to unravel the reason behind this variation. For this purpose, we have studied PLD grown six Si-SiO_2 NCps [158], wherein Si-SiO_2 multilayers are grown by ablation of Si and SiO_2 targets, alternatively in PLD chamber. It is important to note that Raman spectroscopy and mapping of these Si-SiO_2 NCps shows Si phonon frequencies in the entire range 495 - 519 cm^{-1} in each NCp studied. The observed large distribution in Si phonon frequencies is used advantageously to compare their behavior with respect to each other under same experimental conditions. In section 3.2, we have discussed the use of specially designed Raman spectroscopy monitored laser irradiation (LI) experiment, wherein, Raman spectra is measured under certain experimental conditions for all the frequencies, which are chosen with the help of Raman mapping. From the behaviors of various phonons in this frequency range under LI experiment, low frequency (LF: ~ 495 - 510 cm^{-1}) and high frequency (HF: 515 - 519 cm^{-1}) Si optical phonons are attributed to originate from surface/interface of smaller Si NCs in Si-SiO_2 and core of larger Si NCs, respectively [213]. This result is corroborated with *ab initio* density functional theory (DFT) and time-dependent density functional theory (TDDFT) based calculations of Raman spectra. Using this understanding, the origin of intermediate frequency (IF: 510 - 514 cm^{-1}) phonons is discussed in section 3.3. IF phonons originate from intermediate size Si NCs, wherein both core and surface/interface contribute [214]. Further, it is found that resonance Raman scattering is crucial for the observance of surface/interface phonons [214]. This understanding is also used to explain the Raman data variation reported in literature for Si-SiO_2 NCps. The understating developed using Raman mapping is further used in corroboration with AFM, which reveals stacking of different size Si NCs in clusters of Si-SiO_2 [215] and is discussed in section 3.4. We find that this unique information about morphology of Si NCs embedded in SiO_2 is difficult to obtain by any other conventional technique. Results obtained using Raman spectroscopy/mapping of Si-SiO_2 NCps are also independently checked using XPS, which is an established technique for probing size dependence of surface/interface for Si-SiO_2 NCp [226]. In section 3.5, we have discussed the one to one corroboration between size dependence of surface/interface of Si-SiO_2 NCps using Raman mapping and XPS for single and multilayer NCps and establish Raman mapping as an effective tool to study surface/interface in Si-SiO_2 NCps [216].

3.2. Correlation of size and oxygen bonding at the surface/interface of Si nanocrystals

Raman spectroscopy and mapping data on studied Si-SiO_2 NCps show spatial variation in frequencies ranging from 495 - 519 cm^{-1} in each NCp. This is the first time that the whole range Si phonon frequencies (495 - 519 cm^{-1}) are reported in one sample. This has become feasible due to availability of Raman mapping, as using Raman mapping, detailed Raman images based on the sample's Raman spectrum can be generated and therefore local variation in Raman spectra can be easily studied. This allowed us to do systematic investigation of Si phonon frequency variation for six such Si-SiO_2 NCps by measuring their behavior with respect to each other under same experimental conditions. We have studied six Si-SiO_2 multilayer NCps grown on crystalline Al_2O_3 by ablation of Si and SiO_2 targets, alternatively in PLD chamber by varying the deposition time of silicon as 1) E1: 45 s, 2) E2: 90 s, 3) E3: 120 s, 4) E4: 150 s, 5) E5: 180s, 6) E6: 210 s, while keeping deposition time of SiO_2 constant for all NCps.

3.2.1. Raman spectroscopy

Raman spectrum of bulk Si show first order optical phonon ~ 521 cm^{-1} with full width at half maxima (FWHM) ~ 4 cm^{-1} [217]. Raman spectroscopic measurements performed on four samples (E1, E2, E4 and E6) showed red shift, asymmetric line shape and larger width of Si optical phonons as compared to Raman spectrum of bulk Si [158].

For NCs, quantum confinement of phonons due to size leads to breakdown of Raman selection rule ($\mathbf{q} \sim 0$), leading to contribution from $\mathbf{q} \neq 0$ phonons to the Raman spectrum, where $\mathbf{q}$ is a wave vector of scattered phonon as described by PCM given by Campbell and Fauchet

[153: annexure 3.2.1]. According to this model, first order Raman spectrum of a NC can be calculated as,

$$\mathrm{I}(\omega)\ \alpha \int \frac{|\mathrm{C}(\mathrm{q})|^2}{(\omega - \omega\,(\mathrm{q}))^2 + \left(\frac{\Gamma_0}{2}\right)^2}\, \mathrm{d}^3\mathrm{q} \qquad 3.2.1$$

here, Γ_0 is the natural FWHM of the zone-center optical phonon, C(**q**) is the Fourier coefficient of phonon wave function, which takes into account empirically chosen phonon weighting function (mainly Gaussian weighting function) and is given by,

$$|\mathrm{C}\,(\mathbf{q})|^2 = e^{\frac{-\mathrm{q}^2\mathrm{d}^2}{4}} \qquad 3.2.2$$

here, d is the diameter of Si NC. Phonon dispersion curve (ω(**q**)) has been determined by fitting neutron scattering data obtained for bulk Si [218],

$$\omega(\mathbf{q}) = \left(\mathrm{A} + \mathrm{B}\cos\left(\frac{\mathrm{q}}{2}\right)\right)^{\frac{1}{2}} \qquad 3.2.3$$

where, A = $1.714*10^5\ \mathrm{cm}^{-2}$ and B = $1.00*10^5\ \mathrm{cm}^{-2}$. Negative slope of dispersion curve leads to red shift, broadening and asymmetric line shape of phonons on low frequency side. Here d and Γ_0 are two parameters. Raman spectroscopy measurements performed on these four samples (samples E1, E2, E4 and E6) [158] show: i) the observed red shift (~ 500 cm^{-1}) is not in agreement with the red shift calculated using PCM and ii) TEM performed on monolayer for all these NCps suggests increase in mean size of Si particle (~ 1.4 nm to 5.2 nm) with the increase in deposition time of Si from 45 s (sample E1) to 210 s (sample E6). However, we find that the sizes obtained from the asymmetric line shape fitting of Si optical phonons for these multilayer NCps (~ 4.5 nm to 8.5 nm) are much larger than measured by TEM of a Si-SiO_2 monolayer film.

To investigate the origin of these differences, we performed Raman spectroscopic measurements at spatially different positions in all NCps. This spatially resolved Raman spectroscopic measurements of Si-SiO_2 NCps show variation in the Si phonon frequency from 495 to 519 cm^{-1} in all NCps (E1-E6). It is well known that Raman spectra of NCs show asymmetric line shape of phonon and red shift in its frequency due to phonon confinement effect, which is accounted by PCM. Primarily, PCM has been used to explain Raman spectroscopy results reported for Si NCs grown using various techniques [117-119, 125-140]. Further, it is already noted that PCM alone is inadequate to give correct red shift and line shape fitting simultaneously for Si NCs over a complete range of frequencies observed in these Si-SiO_2 NCps [118, 131-132, 134, 136, 141, 144-146]. Several groups have addressed this discrepancy and different solutions have been proposed as discussed below.

i) Modified PCM model: For Si NCs, wherein significant size distribution is found, the contribution of the same has been explicitly added for calculating the line shape and correct red shift simultaneously [117, 145]. It has been reported that for Si NCs embedded in SiO_2 (crystalline) grown on sapphire via ion implantation [117], PCM works well after including log normal size distribution for phonon frequencies in the range 518 - 522 cm^{-1}. For Si-SiO_2 NCp, fabricated by glow discharge method [145], PCM gives correct result after including Gaussian distribution for phonon frequencies in the range 517 - 519 cm^{-1}. This suggests that the modified PCM i.e. accounting size distribution can describe only the phonon frequencies upto ~ 517 cm^{-1} wherein, Si NCs sizes are in the range ~ 4 - 8 nm.

ii) Laser Heating: While performing Raman spectroscopy measurements, it is important to consider the effect of laser heating on the Raman spectrum. Lot of work has been done to account for red shift due to laser heating in Si NCs at small laser power density (PD) of ~ 5 - 10 kW/cm^2 for visible region [136,141,154,157]. It has been reported that the induced red shift is ~ 1 cm^{-1} for Si NCs embedded in silica on Si substrate at laser PD ~ 5 kW/cm^2 [136]. Whereas, for isolated Si NCs grown on sapphire, induced red shift is ~ 2 cm^{-1} at laser PD ~ 5 kW/cm^2 [154]. This suggest that the red shift induced in our case because of laser heating (if any) can be in between the above two cases, because laser heating depends on the surrounding i.e. substrate and the matrix used. Thus, used laser PD ~ 2 - 5 kW/cm^2 cannot lead to observance of lower (~ 500 cm^{-1}) Si phonons. This indicates that the origin of lower Si phonon frequencies cannot be attributed to laser heating.

iii) Bond Polarizability model (BPL): BPL model is based on the calculation of change in polarizability of each bond considering only nearest neighbor atoms for covalent crystals [155]. Total change in polarizability is calculated by summation of contribution from each bond. Using BPL model, Zi et al. [156] have calculated phonon frequencies for different size of Si NCs and generated an empirical correlation between the size and phonon frequency for Si NCs. This relation is used to calculate sizes of Si NCs (< 5 nm) from the observed red shift [132,135,136,147]. Faraci et al. [132] have reported size of Si NCs ~ 1 nm and 5.5 nm for Si phonon ~ 502 and 517 cm^{-1}, whereas TEM shows size in the range 2 - 12 nm. Long et al. [135] have reported size of Si NC ~ 4.4 nm for red shifted Si phonon frequency ~ 517.7 cm^{-1}, which is in agreement with the size observed in TEM. However, there is no discussion on line shape of this phonon. Stenger et al. [136] have shown that sizes calculated using BPL model (~ 3 and 5.3 nm for Si phonons ~ 515.8 and 518.2 cm^{-1}) are in agreement with the sizes observed using TEM. They have also observed a peak ~ 495 cm^{-1}, however they have mentioned that the origin of this phonon is not clear. Hessel et al. [147] have shown that the sizes calculated using BPL model is ~ 3.26 nm for Si phonon frequency ~ 516 cm^{-1}, whereas, observed sizes using TEM micrographs comes out to be ~ 2.7 nm. Thus, size calculated using BPL is not in agreement with the sizes observed using TEM for very small size Si NCs. Further, Gupta et al. [219] have consolidated the data for Si phonon frequencies in the literature and shown that BPL model also cannot explain the large red shift, especially below 512 cm^{-1}. This suggests that BPL model works well for phonon frequencies in the range 514 - 519 cm^{-1}.

Thus, different groups have reported different Si phonon frequencies in the range noted above for Si-SiO_2 NCps grown with different techniques. Some of the groups have reported the occurrence low frequency phonons, whereas, others have not observed. There have been some attempts to understand this variation reported in the literature, but no satisfactory understanding could be reached for low frequency Si phonons. The question of which conditions of size/shape of Si NCs in SiO_2 matrix leads to these low frequency phonons and why is still remains an unanswered. In the following, we investigate this variation using Raman mapping.

3.2.2. Raman mapping as a local probe to study variation in Si optical phonons

Many sets of Raman mapping (acquisition time 1 s) are performed with step size ~ 0.15 μm on each of the six NCps to generate enough statistical data to make appropriate observations. Since, Raman spectra show phonon frequencies in the range 495 - 519 cm^{-1} for all the NCps, hence Raman images are generated using intensity of phonon with frequencies in the range 490 - 525 cm^{-1}. Representative optical image and Raman image for all the samples is shown in Fig. 3.2.1 - 3.2.6 and Fig. 3.2.1c - 3.2.6c show corresponding Raman spectra for the marked positions in Fig. 3.2.1b - 3.2.6b. These Raman images show presence of different Si phonon frequencies in the range ~ 495 - 519 cm^{-1} over bright region. Further, Raman images show signal from crystalline Si in well separated regions dispersed over the whole film. This suggests that although the growth is carried out to be multilayer, evidence of continuous film of crystalline Si is not observed. Instead, formation of crystalline Si is found only in certain areas of the film with this acquisition time of 1 s. However, optical images show presence of different structures in rest of region too. This is further investigated by performing Raman mapping with acquisition time of 2 s (Fig. 3.2.7), which shows continuous presence of amorphous Si in the remaining region for NCp E1. Similar observation is made for all the NCps and is discussed in detail in section 3.3. Further, while performing Raman mapping, we have observed variation in frequency, FWHM and line shape of Si optical phonon at step size of 0.15 μm. This suggests that the observed spatial resolution is enhanced, because spatial resolution of Raman system is ~ 0.5 μm. Thorough investigation (ref: annexure 3.2.2) suggests that we could observe the effect of individual Si NC as, i) separation between two particles is ~ 100 nm (from TEM data of monolayer) and ii) only central part of Gaussian beam profile gives the significant Raman signal during Raman mapping, which is leading to betterment in observed spatial resolution. It is also important to note that Raman image and corresponding Raman spectra show three different kinds of line shapes for whole range Si optical phonons. Based on the difference in the line shape of Si optical phonons (Fig. 3.2.1c-3.2.6c), these phonons are broadly separated in three different frequency regions as follows, i) 495 - 510 cm^{-1} (LF phonons: Lorentzian line shape), ii) 511 - 514 cm^{-1} (IF phonons: asymmetric line shape which cannot be fitted using PCM) and iii) 515 - 519 cm^{-1} (HF: asymmetric line shape which can be easily explained using PCM).

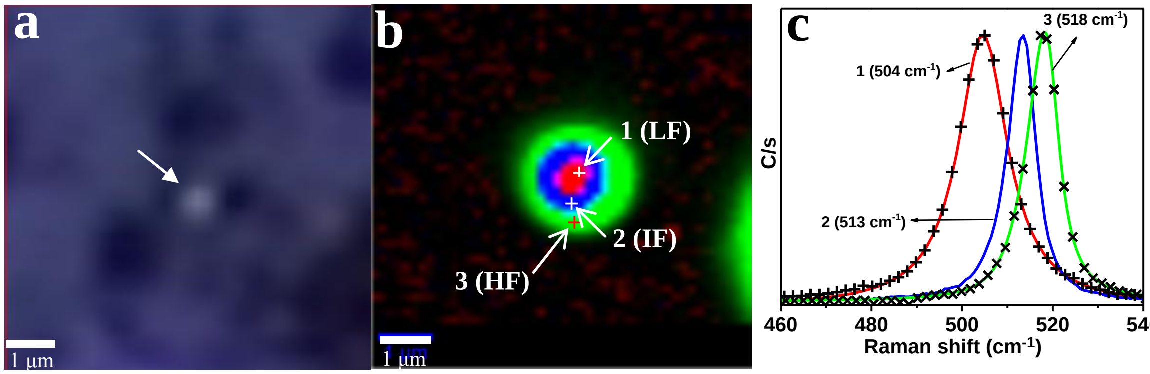

Fig. 3.2.1. a) Optical image of NCp E1, b) corresponding Raman image generated using intensity of phonon in the range 490 - 525 cm^{-1}, where red color shows LF phonons, blue color shows IF phonon and green color shows HF phonons and c) corresponding normalized Raman spectra on positions as marked in Raman image (b). Solid lines show Lorentzian and PCM fit to raw data (+ & ×). Solid line (blue color) shows raw data for IF phonon.

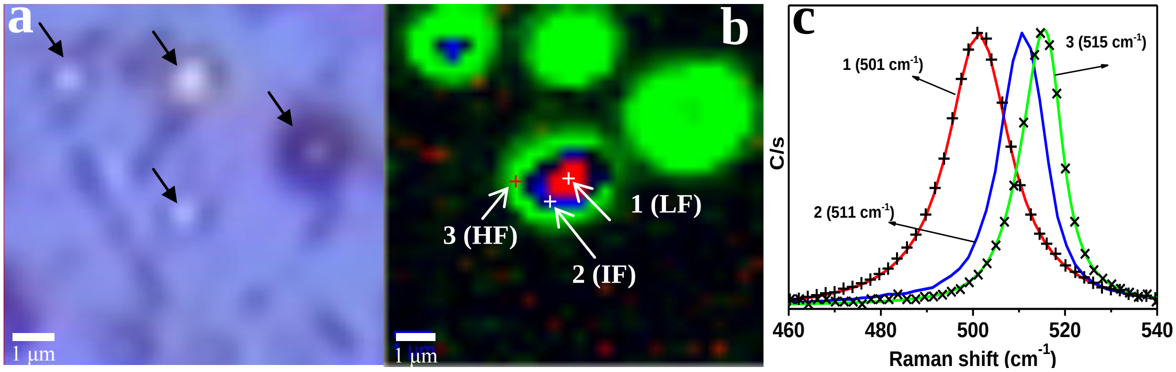

Fig. 3.2.2. a) Optical image of NCp E2, b) corresponding Raman image generated using intensity of phonon in the range 490 - 525 cm^{-1} and c) corresponding normalized Raman spectra on positions as marked in Raman image (b). Solid lines show contribution of LF and HF phonons and fit to raw data (+ & ×). Solid line (blue color) shows raw data for IF phonon.

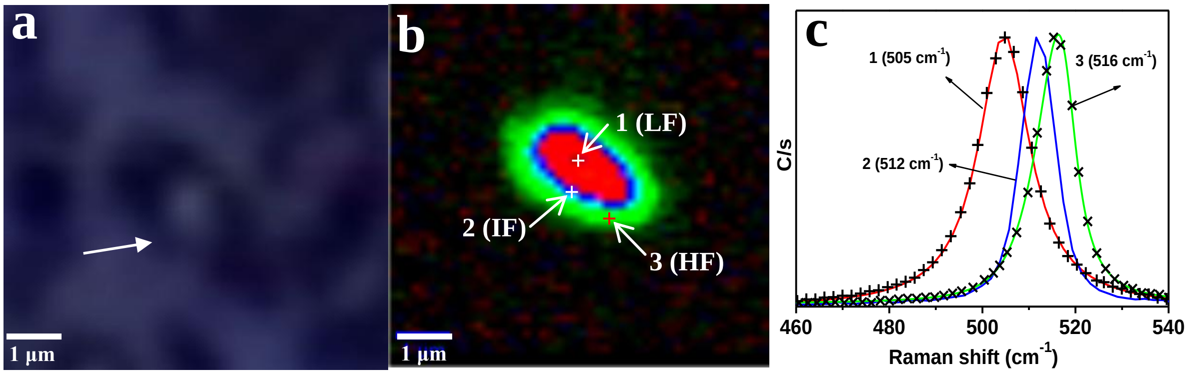

Fig. 3.2.3. a) Optical image of NCp E3, b) corresponding Raman image generated using intensity of phonon in the range 490 - 525 cm^{-1} and c) corresponding normalized Raman spectra on positions as marked in Raman image (b). Solid lines show contribution of LF and HF phonons and fit to raw data (+ & ×). Solid line (blue color) shows raw data for IF phonon.

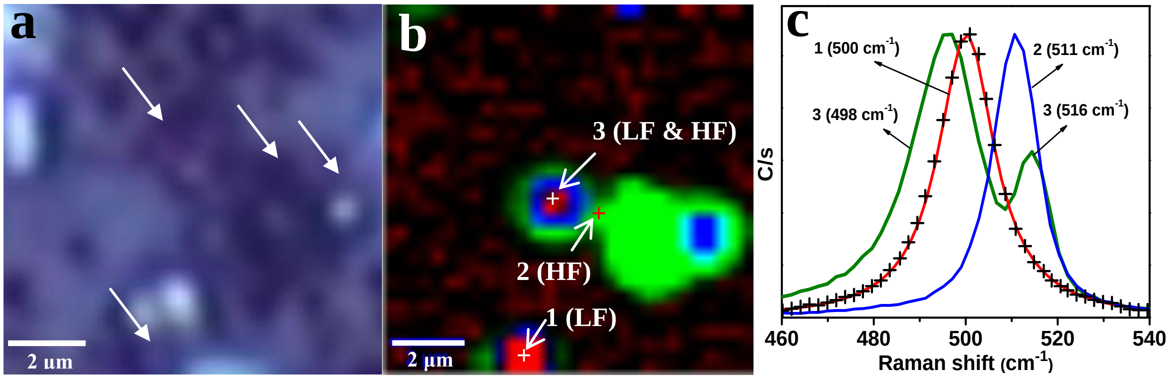

Fig. 3.2.4. a) Optical image of NCp E4, b) corresponding Raman image generated using intensity of phonon in the range 490 - 525 cm^{-1} and c) corresponding normalized Raman spectra on positions as marked in Raman image (b). Raman spectra also show presence of simultaneous LF (~ 498 cm^{-1}) and HF phonon (~ 516 cm^{-1}). Solid lines show contribution of LF fit to raw data (+). Solid line (blue color) shows raw data for HF phonon.

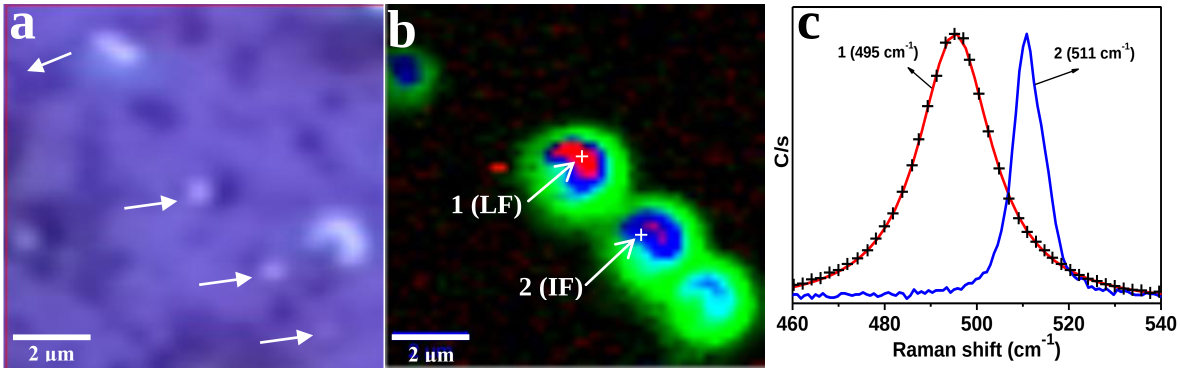

Fig. 3.2.5. a) Optical image of NCp E5, b) corresponding Raman image of marked area, generated using intensity of phonon in the range 495 - 525 cm^{-1} and c) corresponding normalized Raman spectra on positions as marked in Raman image (b). Solid lines show contribution of LF phonon and fit to raw data (+). Solid line (blue color) shows raw data for IF phonon.

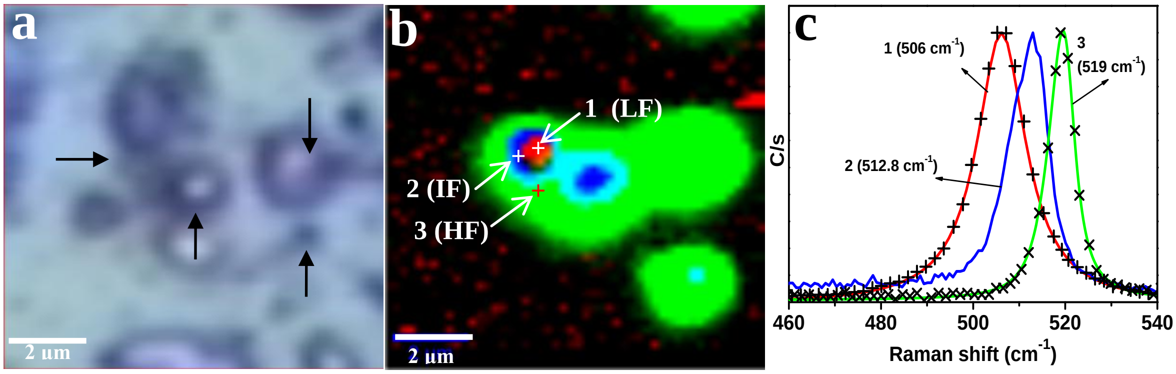

Fig. 3.2.6. a) Optical image of NCp E6, b) corresponding Raman image generated using intensity of phonon in the range 495 - 525 cm^{-1} and c) corresponding normalized Raman spectra on positions as marked in Raman image (b). Solid lines show contribution of LF and HF phonons and fit to raw data (+ & ×). Solid line (blue color) shows raw data for IF phonon.

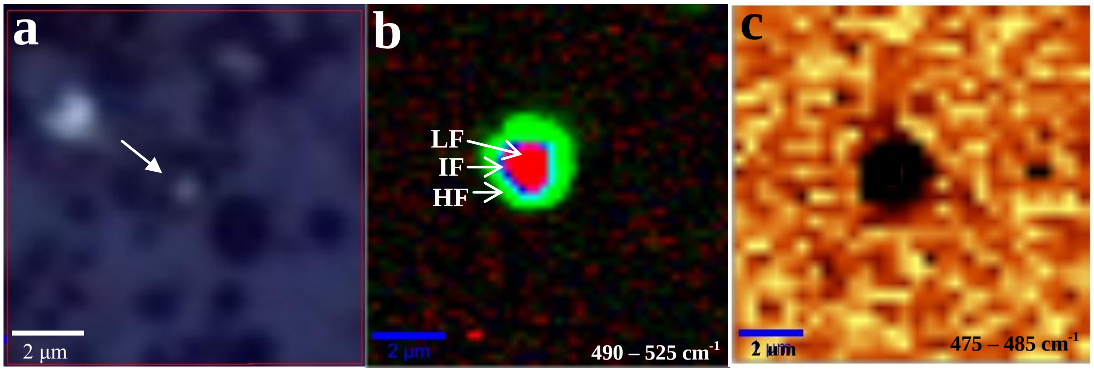

Fig. 3.2.7. a) Optical image of NCp E1, b) corresponding Raman image generated using intensity of phonon in the range 490 - 525 cm^{-1} and c) Similar Raman image generated using intensity of phonon in the range 475 - 485 cm^{-1} showing presence of amorphous Si in the region where crystalline Si is not observed.

Table 3.2.1. Different parameters such as phonon frequency, calculated size, unperturbed width and asymmetry for HF phonons are summarized.

Frequency (cm^{-1})	Size (nm)	Unperturbed width (cm^{-1})	Asymmetry
515	7	9.6	1.27
516	7.6	9	1.19
517	8.1	8.2	1.17
518	8.5	7	1.14
519	9.8	6	1.12

Higher frequency phonons above ~ 515 cm^{-1} show asymmetric line shape, which can be well fitted (Fig. 3.2.1c - 3.2.6c) using PCM. Different parameters such as observed red shift, size calculated from asymmetric line shape, unperturbed width and asymmetry is summarized in Table 3.2.1 for phonon frequencies in the range 515 - 519 cm^{-1}. Fitting shows decrease in red shift and asymmetry in line shape with the increase in size of Si NC from ~ 7 to 10 nm for Si phonon frequencies in the range 515 - 519 cm^{-1}. This clearly shows that these Si phonons originate due to phonon confinement in Si NCs (sizes ~ 7 - 10 nm: Table 3.2.1). Further it shows that larger Si NCs are of better crystalline quality.

The lower phonon frequencies below ~ 510 cm^{-1} shows Lorentzian line shape (Fig. 3.2.1c - 3.2.6c). It is important to note here that at very few places (5%), Raman signal corresponding to amorphous Si is observed, where these lower Si phonon frequencies are measured. In these cases, small asymmetry can be deconvoluted (Fig. 3.2.8) as due to small amorphous Si content and a Lorentzian shape low frequency phonon. We consider three different possibilities for the occurrence of these low frequency phonons. i) The line shape suggests that these phonons are coming from large size Si NCs (nearly bulk > 30 nm), ii) they are originating at amorphous SiO_2 matrix and iii) They originate at surface/interface of Si-SiO_2 NCp. If they are coming from large NCs, than the frequency of the phonons is expected to be ~ 521 cm^{-1}. The lower frequency with large size NC can be explained if there is tensile strain in the Si NC. However, this possibility can be rejected as there are evidences in the literature, which suggests that growth of Si NCs in SiO_2 matrix leads to compressive stress in larger NCs [117, 127]. Presence of compressive stress

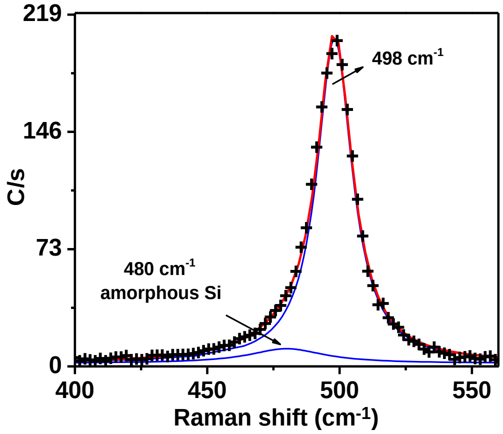

Fig. 3.2.8. Asymmetric line shape of phonon with frequency ~ 498 cm^{-1} fitted using two Lorentzian peaks ~ 480 cm^{-1} and ~ 498 cm^{-1}.

should lead to blue shift in the phonon frequency, which is not observed here and thus the possibility of these phonon coming from larger Si NCs is rejected. Further, Raman spectrum of a-SiO_2 shows broad peak ~ 800 cm^{-1} [220], therefore this possibility is also rejected. This leaves us with the possibility of these phonons originating from surface/interface of Si-SiO_2 NCp. Further, we find that the asymmetric line shape of phonons in the intermediate frequency (IF) range 511 - 514 cm^{-1} (Fig. 3.2.1c - 3.2.6c) cannot be fitted using PCM and hence this frequencies also cannot be said to be originating from confinement due to small size Si NC.

While performing Raman mapping, we have also observed simultaneous occurrence of LF and HF phonons (Fig. 3.2.4c) at some spatial positions. Similar kind of observation is also reported earlier by Faraci et al. [132] in Si-SiO_2 NCp. They have indicated that lower frequencies may be due to Si aggregates having a thin SiO_x (with x = 1 - 2) interface for Si NCs in SiO_2 matrix. In order to obtain a clue to origin of LF and IF phonons, we have designed laser irradiation (LI) experiment. In this experiment, changes in Raman spectra are measured on keeping laser irradiation alternatively ON and OFF for certain duration. We have performed LI experiment on i) simultaneously observed LF and HF phonons, ii) HF phonons, iii) LF phonons and iv) IF phonons. LI experiment is performed at many frequencies in each category stated above in all six NCps studied. It is interesting to note here that low and high frequency range Si phonons behave markedly differently during the LI experiment. Further, it is important to note that observations for LF and HF phonons during LI experiment are same irrespective of their simultaneous or separate occurrence in the Raman spectra as discussed below.

3.2.2.1. Raman spectroscopy monitored Laser irradiation (LI) experiment

Steps of LI experiment are,

1. The desired peak frequency is located using Raman mapping for doing LI experiment on the said frequency ranges.
2. Steps:

1st step: *0 min*; 2nd step : *laser on for 16 mins*; 3rd step : *Laser shutter off for 40 mins*; 4th step : *Again laser on for 16 mins* ; 5th step: *Laser shutter off for 3 hrs.*

At the end of each step (including 1st step: initiation of the experiment: 0 min) Raman spectrum is recorded with acquisition time of 3 s. Laser heating leading to redshift of Si phonon of Si NC is avoided by keeping low laser PD ~ 5 kW/cm^2. This is also confirmed by the fact that all frequencies including LF are observed in one Raman mapping (Fig. 3.2.1 - 3.2.7) at a particular laser PD. This also confirms that red shift of LF and IF phonons cannot be attributed to laser heating and thus, low frequency phonons are intrinsic to Si-SiO$_2$ NCps. While performing this experiment, no mechanical movement is involved. Results are summarized below.

i) Simultaneously observed LF and HF phonons ~ 501 cm^{-1} and ~ 517 cm^{-1}, respectively: The two peaks Raman spectra (Fig. 3.2.9) are approximated using two Lorentzian peaks, for convenience of noting the variation in the frequency. Out of the two peaks LF phonon shows total blue shift by ~ 4 cm^{-1} and decrease in FWHM, whereas, HF phonon does not show any significant change during the experiment. LF and HF Si phonons behave markedly differently during the LI experiment, which suggests that they have different origin.

ii) HF phonons (515 - 519 cm^{-1})**:** In all the measurements performed in this frequency range, phonons show similar behavior i.e. it does not change during the LI experiment. Representative spectra for Si phonon frequency ~ 516 cm^{-1} during the experiment are shown in Fig. 3.2.10. Thus, HF phonons show no change during the LI experiment, whether they are occurring separately or together with LF phonons.

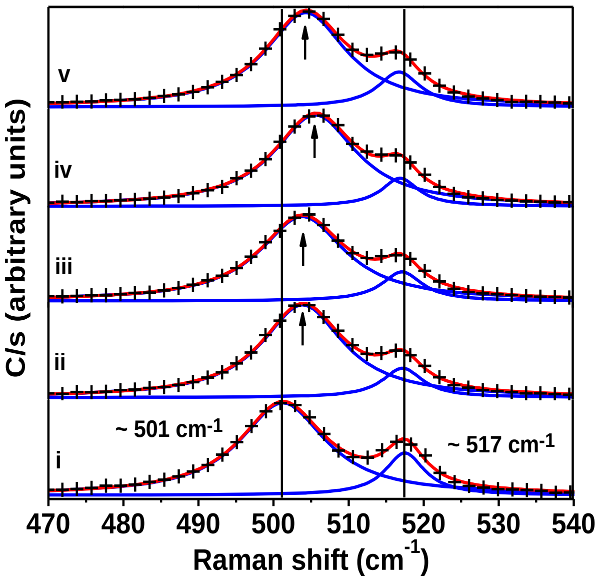

Fig. 3.2.9. Change in Raman spectra for simultaneously occurring LF and HF phonons during the LI experiment. LI steps are i) 0 min, ii) 16 min ON, iii) 40 min OFF, iv) 16 min ON, v) 3 hr OFF. Solid line (red color) is fit to raw data (+). Separate Lorentzian components are shown by dash line (blue color).

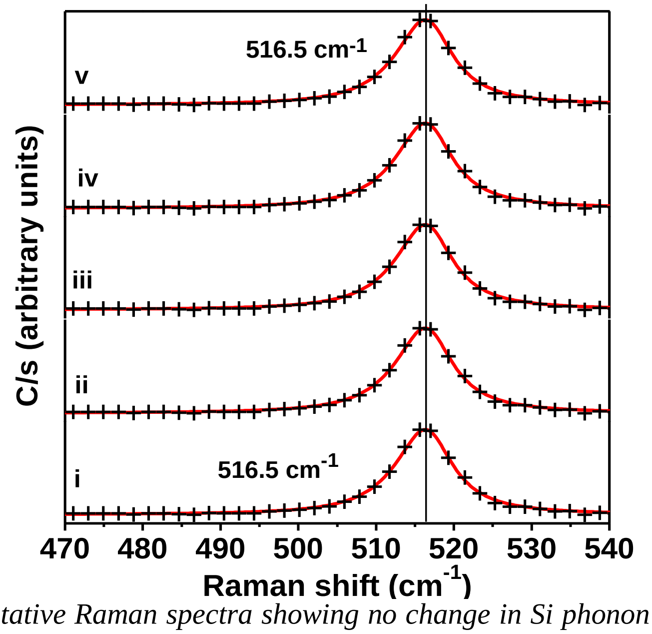

Fig. 3.2.10. Representative Raman spectra showing no change in Si phonon ~ 516 cm^{-1} during the LI experiment. LI steps are i) 0 min, ii) 16 min ON, iii) 40 min OFF, iv) 16 min ON, v) 3 hr OFF. Solid line (red color) is PCM fit to raw data (+).

iii) LF phonons (495 - 510 cm^{-1}): In all the measurements performed in this frequency range, the behavior of peak frequencies is similar i.e. blue shifts of LF phonons with the decrease in FWHM during the LI experiment. Representative Raman spectra (Fig. 3.2.11) for phonon frequency ~ 499, 503, 506, 510 cm^{-1} during the LI experiment.

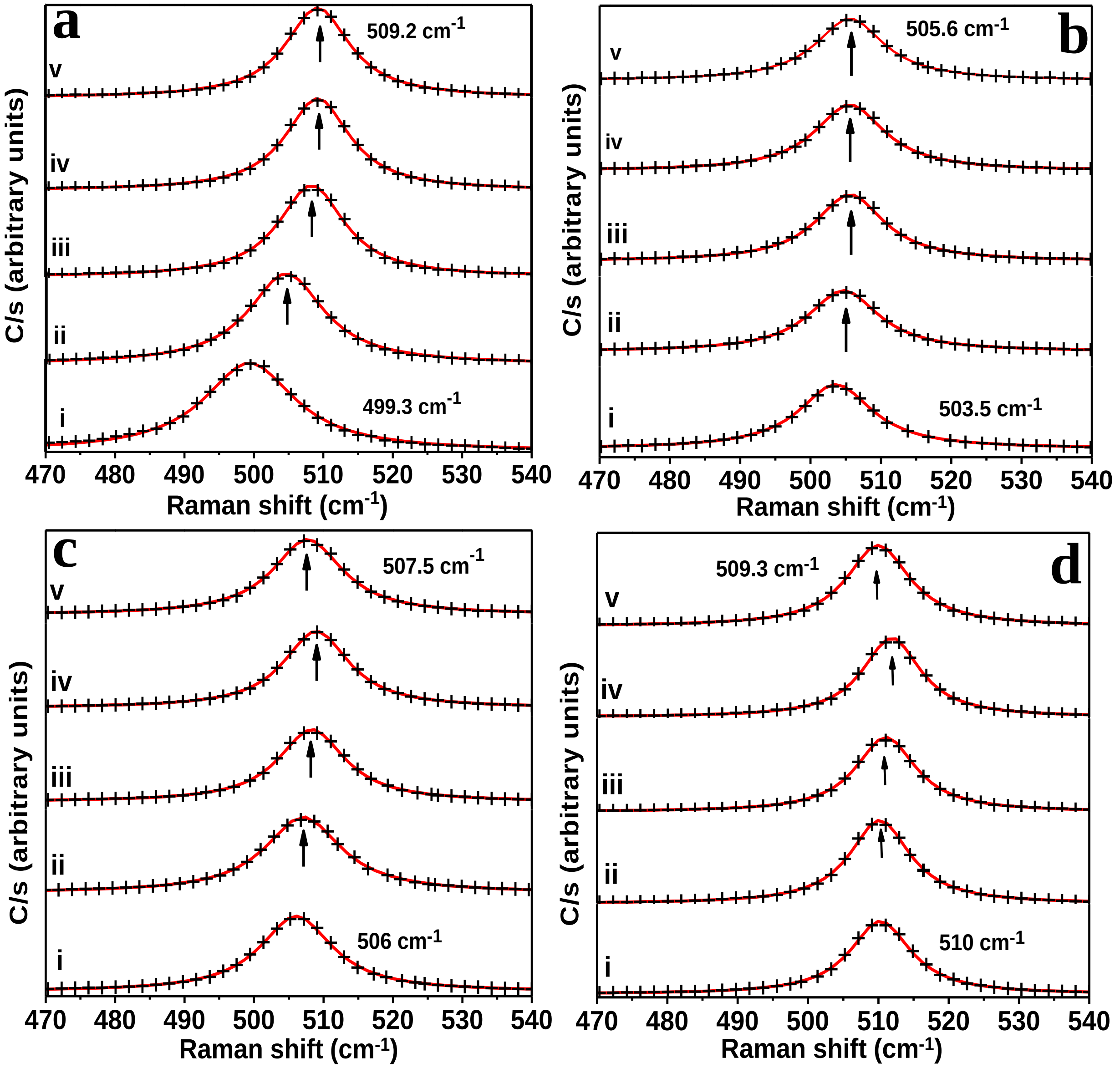

Fig. 3.2.11. Representative Raman spectra for sample E1 showing change in LF phonons during five steps of LI experiment. LI steps are i) 0 min, ii) 16 min ON, iii) 40 min OFF, iv) 16 min ON, v) 3 hr OFF. Solid line (red color) is the Lorentzian fit to raw data (+).

iv) IF phonons: Phonons in this frequency range follows LF behavior during LI experiment i.e. blue shift in frequency with decrease in FWHM. However, IF phonons shows some differences with respect to LF phonons. This will be discussed in next section.

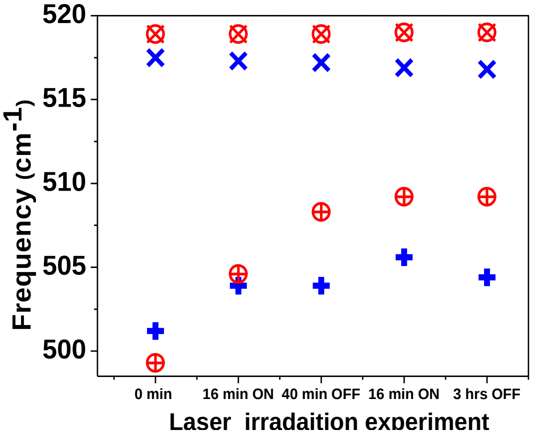

Fig. 3.2.12. Change in LF and HF phonon during LI experiment. Symbols (+) and (×) in circle show phonon frequency ~ 499 cm^{-1} and 517 cm^{-1} occurring separately. Symbol (+) and (×) show two resolvable phonon frequencies ~ 501 cm^{-1} and 507 cm^{-1}, respectively.

Representative variation of peak frequency obtained in five steps of laser irradiation experiment for different range peak frequencies is summarized in Fig. 3.2.12.

The differences noted in the behavior of LF and HF phonons clearly indicate that they have different origin. The manifold reasons as given below and consistencies in the observations noted earlier suggest that LF phonons originate from the surface/interface of Si NC in SiO_2. Molecular dynamics simulation shows that oxidation leads to stretching of Si-Si bonds around the surface only [221] due to presence of different suboxide states at the interface. Presence of different Si sub oxides states (Si^{1+}, Si^{2+}, Si^{3+}) at the surface of Si NC in Si-SiO_2 has been observed experimentally [225] as well as have been theoretically predicted [223-226].

Considering the above and the Lorentzian line shape of a phonon, we attribute LF phonons to stretching vibration of Si-Si bonds at the Surface of Si NC due to Si-SiO_2 interface. Thus, phonon frequency variation in the range from 495 to 510 cm^{-1} can be attributed to variation in local SiO_x environment seen by Si-Si bonds at the surface of the Si NC. This will also lead to a Lorentzian line shape of Si-Si stretching vibration. Further, observed larger width of LF phonons can be understood due to variation in SiO_x environment.

The blue shift in LF phonons (Fig. 3.2.11) accompanied with betterment in crystalline order during LI experiment can be understood in terms of more crystalline Si-Si bonding environment leading to more ordered Si-SiO_2 interface. This will be further discussed later in this section. The attribution of HF phonons observed in the range 515 - 519 cm^{-1} to the core phonon of Si NCs is consistent with observation that no change in frequency, width & line shape is observed during the LI experiment. Below, we will discuss the variation in blue shift of different LF phonons during the LI experiment.

3.2.2.2. Variation in surface/interface (LF) phonons during the LI experiment

Variation in blue shift of various LF phonons in the range 495 - 510 cm^{-1} is plotted in Fig. 3.2.13a during five steps of LI experiment. We have performed the same experiment at many such sites in the said frequency range in all the NCps. It is interesting to note that primarily two types of patterns are observed during the LI experiment, i) In one pattern (type I), initially blue shift and freezing of phonon frequency at the end of the experiment is observed and ii) In another pattern (type II), freezing of phonon frequency is observed in initial steps and thereafter, blue shift on heating and redshift on cooling. There is another important point to note here that

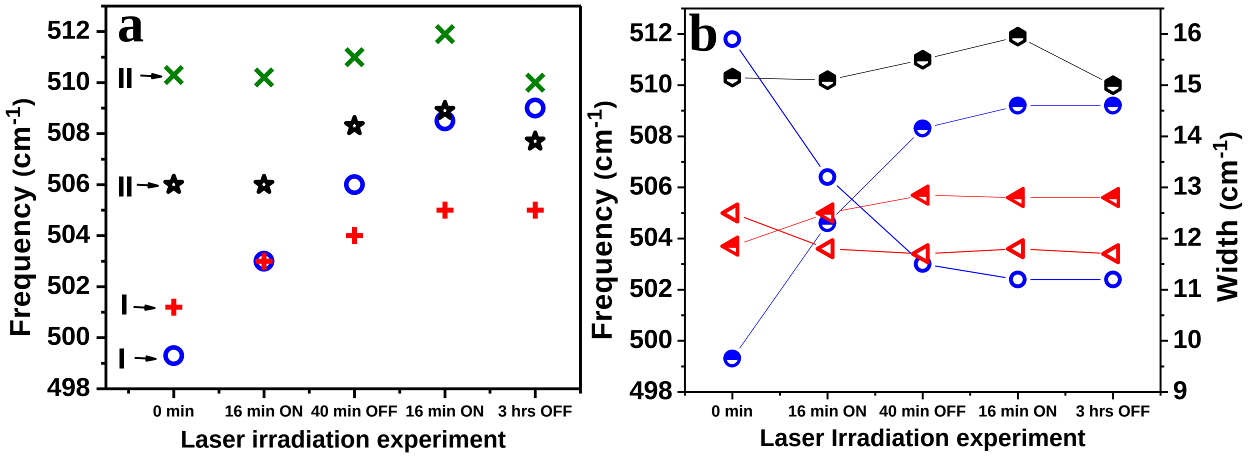

Fig. 3.2.13. a) Change in phonon frequency during LI experiment for LF phonons in the range ~ 495 to 510 cm^{-1} showing two patterns: I and II and b) Change in phonon frequency and corresponding FWHM during LI experiment for LF phonons. Half filled symbols show frequency and open symbols show corresponding FWHM.

change in phonon frequency and FWHM are mirror images of each other (Fig. 3.2.13b) during the LI experiment. Further, blue shift in phonon frequency is always accompanied with betterment in crystalline order of the surface/interface for all the frequencies plotted here. This behavior of the phonon frequency and corresponding FWHM is similar as due to change in the temperature of a crystalline material. For bulk and Si NCs, temperature dependent Raman studies show red shift of Si phonon frequency by ~ 10 cm^{-1} [227] and ~ 15 cm^{-1} [228], respectively, for temperature rise from 300 to 800 K. Although, data from literature suggests that the laser PD used is not expected to give rise heating effect, to recheck the same, we measure the local temperature during the LI experiment to negate the possibility. To know the local temperature during the LI experiment, we have performed Stokes/anti-Stokes Raman measurements using 488 nm excitation, as notch filter is not available for 441.6 nm excitation. We find that behavior of LF (Fig. 3.2.14) and HF phonons is similar using 488 nm excitation too.

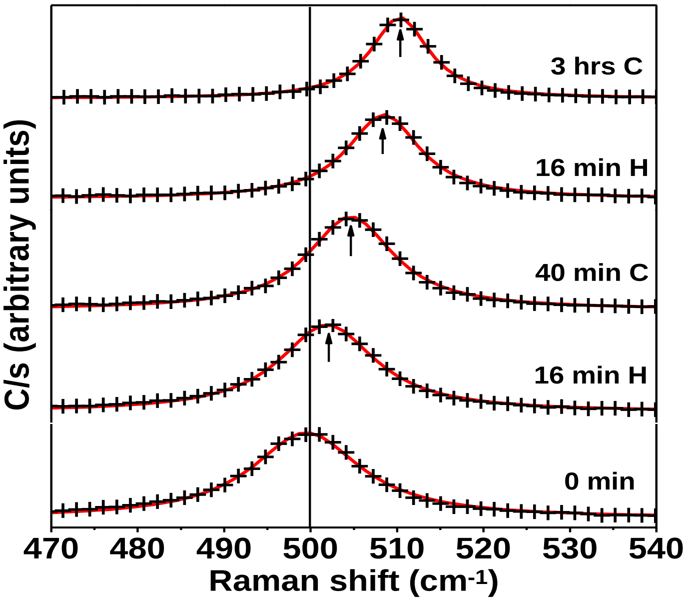

Fig. 3.2.14. Change in Raman spectra of LF phonon ~ 500 cm^{-1} during five steps of LI experiment with 488 nm excitation source. LI steps are i) 0 min, ii) 16 min ON, iii) 40 min OFF, iv) 16 min ON, v) 3 hr OFF. Solid line (red color) is the Lorentzian fit to the raw data (+).

LI experiment for LF and HF phonons, wherein these phonons are observed simultaneously (Fig. 3.2.15) as well as separately (Fig. 3.2.16). Local temperature is calculated using intensity ratio of Stokes to anti-Stokes Raman intensity (I_S/I_{AS}) given by equation (2.24). Local temperature calculated using HF phonon is found to be the room temperature (~ 300 K), which is within the accuracy (± 10 K) of measurements [229]. This is consistent with the fact that no change in HF phonon is observed during the LI experiment. However, local temperature calculated using LF phonon (surface/interface frequencies) is found to be in the range of ~ 550 – 700 K (at spatially different positions). Moreover, continuous blue shift doesn't show a continuous decrease in temperature during LI experiment (Fig. 3.2.17) indicating that there does not exist any correlation between frequency shift of the LF phonon and the temperature obtained from I_S/I_{AS} Raman measurements.

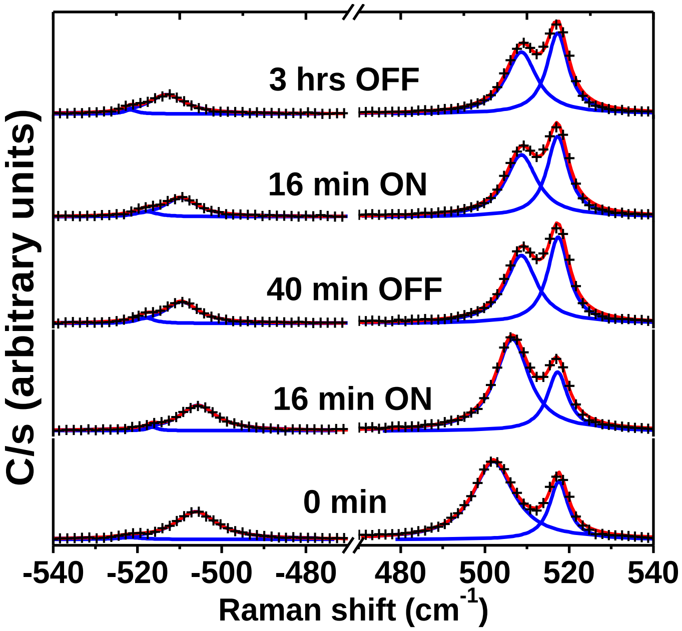

Fig. 3.2.15. Change in Stokes/anti-Stokes Raman spectra for LF and HF phonon ~ 500 and 517 cm^{-1} during five steps of LI experiment as noted in the figure. Solid line (red color) is the fit to raw data (+). Separate components are shown in dash line (blue color).

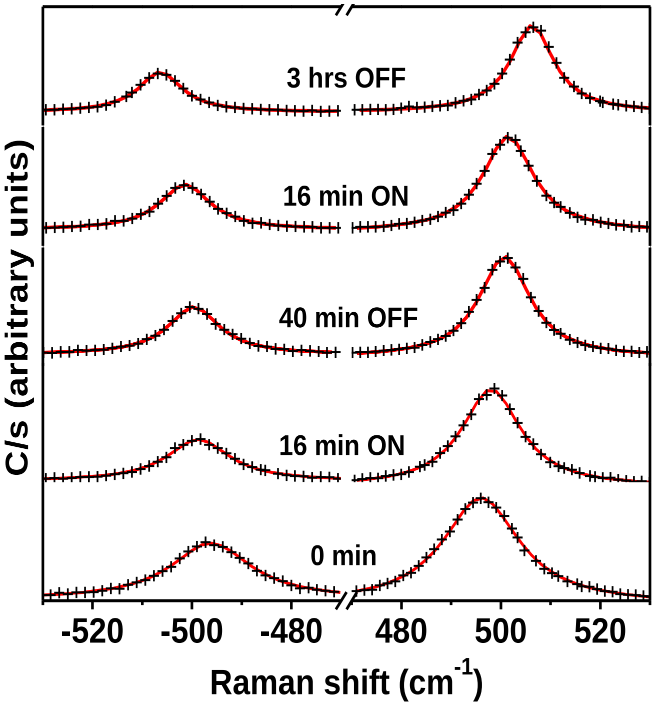

Fig. 3.2.16. Change in Stokes/anti-Stokes Raman spectra for LF phonon ~ 500 cm^{-1} during five steps of LI experiment as noted in the figure. Solid line (red color) is the fit to the raw data (+).

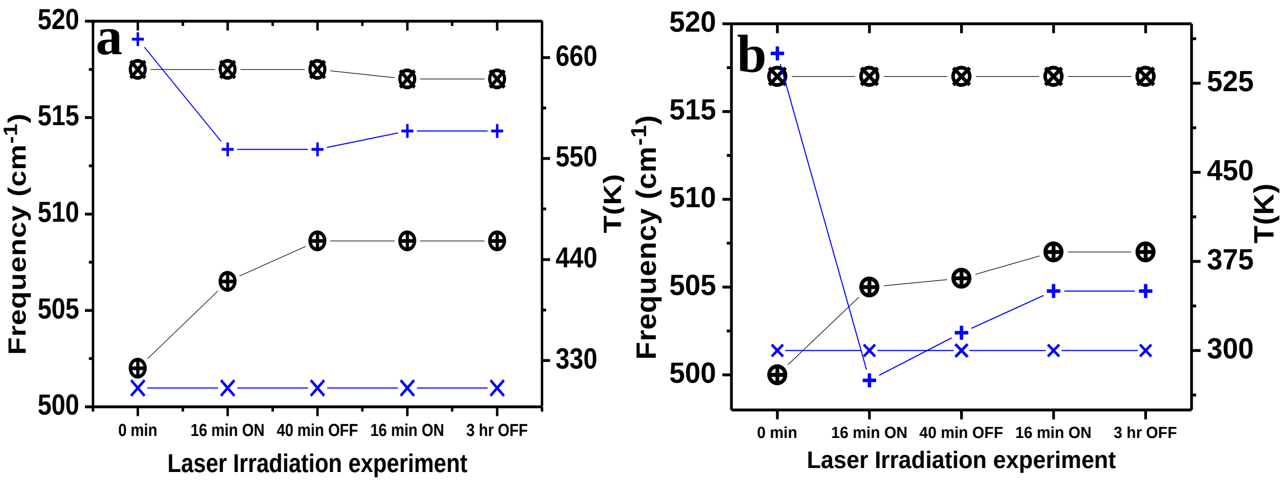

Fig. 3.2.17. Change in phonon frequency and local temperature during LI experiment for a) well resolved LF and HF coming together and b) LF and HF occurring separately. (+) and (×) symbols in circle show LF and HF phonon, respectively. (+) and (×) symbols show corresponding temperature. Line is guide to eye.

It is also important to note that the two different local temperatures at a site, obtained using two different phonons cannot be explained by conventional understanding. Further, after allowing the laser to fall for 16 mins (after 2nd step in Fig. 3.2.17), we observe a decrease in local temperature, suggesting that there are inconsistencies in these results. The plausible explanation for this is that the local temperature calculated from I_S/I_{AS} data using interface/surface phonon (LF phonons) may be incorrect. This can happen, if excitation source is close to one of the real energy levels of the system, leading to resonance Raman scattering. In this case the Raman cross-section is dominated by the resonance term (equations 2.18 and 2.20) and hence the I_S/I_{AS} ratio is no more proportional to phonon occupation number. Therefore, the I_S/I_{AS} ratio can give incorrect value and hence cannot be used to calculate the local temperature. Resonance Raman scattering is indeed observed for LF phonons, whereas HF phonons show non-resonant behavior and detailed study of the same is discussed in next section. This further supports the understanding that LF and HF phonons have different origin.

Study of surface/interface in such dynamic condition (laser irradiation) along with Raman spectroscopy is not feasible using any experimental technique such as XPS [225] and Auger electron spectroscopy [230]. Further, earlier molecular dynamics calculation suggested strong contribution of surface vibrational density of states in the density of phonon states in Si-SiO_2 [79, 226]. To gain insight into surface/interface phonons, Dr. C. Kamal (ISUD, RRCAT) has carried out *ab initio* DFT and TDDFT based calculations of Raman spectra for optimized Si cluster (Si_{41}) terminated by O and H atoms as discussed in the following.

3.2.2.3. Calculation of Raman spectra of Si cluster (Si_{41})

In order to support our experimental results as well as to gain microscopic understanding, DFT [231] based electronic structure calculations for a medium size silicon cluster (Si_{41}) with bulk-like tetrahedral coordination, using Amsterdam Density Functional (ADF) code [232] has been carried out (anneaxure-3.2.2.). Two possible terminations for Silicon atoms present at the surface of the cluster, namely (a) oxygen and (b) hydrogen atoms are considered, in order to avoid the dangling bonds. The former termination is used to mimic the Si cluster/SiO_2 interface. The fully optimized geometric structures of Si_{41} cluster with (a) oxygen ($Si_{41}O_{42}H_{24}$) and (b) hydrogen atoms ($Si_{41}H_{60}$) terminations are shown in Fig. 3.2.18. Hydrogen atoms are used to passivate dangling bonds of Si/oxygen atoms at the surface, where Si cluster is passivated with hydrogen/oxygen. The results of our detailed geometric analysis are summarized in Table 3.2.2.

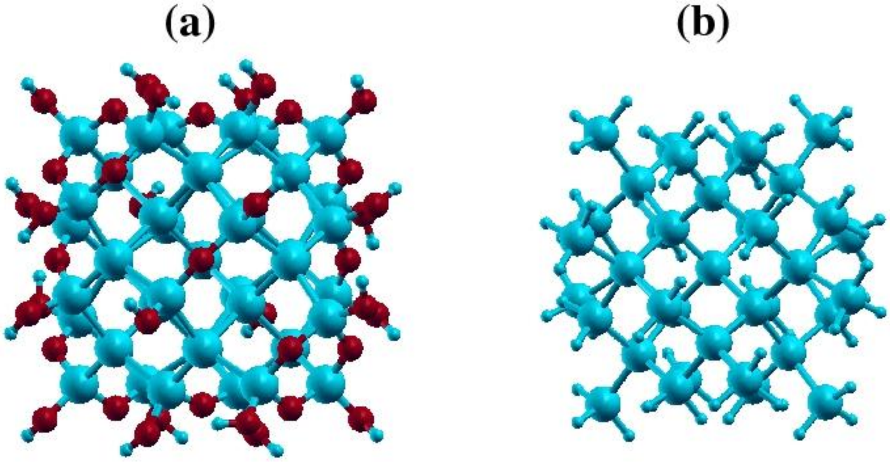

Fig. 3.2.18. Ball and stick model for the optimized geometric structures of Si_{41} cluster with a) oxygen ($Si_{41}O_{42}H_{24}$) and b) hydrogen atoms ($Si_{41}H_{60}$) terminations which are obtained by DFT based electronic structure calculation with PBE XC functional and TZ2P basis set. The balls with colors cyan (large), red (medium) and cyan (small) represent Si, O and H atoms respectively.

Table 3.2.2. The results for the bond lengths and bond angles of Si_{41} cluster with (a) oxygen ($Si_{41}O_{42}H_{24}$) and (b) hydrogen atoms ($Si_{41}H_{60}$) terminations obtained by DFT based electronic structure calculation with PBE XC functional and TZ2P basis set.

System	**Bond length (Å)**			**Bond angle (°)**					
$Si_{41}O_{42}H_{24}$	**Si-Si Core**	**Si-Si Surf.**	**Si-O**	**Si-Si-Si Core**	**Si-Si-Si Core/Surf.**	**Si-Si-Si Core/Surf.**	**O-Si-O**	**Si-O-Si**	**Si-O-Si**
Mean	2.38	2.39	1.66	109.23	100.23	117.10	107.79	126.32	147.18
SD	0.007	0.014	0.009	1.05	1.53	2.87	2.07	0.46	0.50
$Si_{41}H_{60}$	**Si-Si Core**	**Si-Si Surf.**	**Si-H**	**Si-Si-Si Core**	**Si-Si-Si Core/Surf.**	**Si-Si-Si Core/Surf**	**H-Si-H**	**-**	**-**
Mean	2.39	2.36	1.504	107.64	103.06	117.40	107.78	-	-
SD	0.008	.004	0.005	1.07	1.15	0.11	0.60	-	-

We observe from this table that the mean values for Si-Si bond lengths in the core region of the cluster (2.38 in $Si_{41}O_{42}H_{24}$ and 2.39 Å in $Si_{41}H_{60}$) are slightly higher than its corresponding value of 2.34 Å in bulk silicon. Further, for oxygen passivated cluster, bond length increases from core to surface of the cluster. This indicates that the interaction between Si atoms in the cluster is little weaker than that in the bulk form. The maximum variation in the values of bond length with respect to its bulk value is 0.01 Å. The trend of increase in the mean values for these angles is given in 4th - 6th columns of Table 3.2.2. The standard deviations (SD) for both bond lengths and bond angles are also given in Table 3.2.2. The calculated mean values (109.23º and 107.64º for $Si_{41}O_{42}H_{24}$ and $Si_{41}H_{60}$, respectively) of bond angles in the core region indicate that the local environment of Si atom in this region is bulk-like since these values are close to the corresponding bond angle (109.47º) between the Si atoms in bulk. However, we observe large modifications in the mean values of the bond angles between Si atoms as we go to the surface region. Our results show that there exist two different types of bond angles in the surface region: one value is much lower and another being higher than that of in the core region. The former bond angles involve the Si atoms which lie on the surface and below the surface where as the latter ones involve the Si atoms on the surface of the cluster which are terminated by hydrogen/oxygen atoms respectively.

In order to gain more insight into the experimental results these optimized structures are employed to perform calculations (annexure- 3.2.3) of Raman spectra. The calculated Raman spectra of Si_{41} cluster with (a) oxygen ($Si_{41}O_{42}H_{24}$) and (b) hydrogen atoms ($Si_{41}H_{60}$) terminations are presented in Fig. 3.2.19. We expect that the results obtained from the calculations of Raman spectra of Si_{41} cluster with two different types of terminations will help us to get better insight into the effect of environment on the Raman spectra of Si NC in the Si-SiO_2

NCp. Raman spectra of Si_{41} cluster with oxygen and hydrogen terminations show strong peaks at 512 cm^{-1} and 499 cm^{-1}, respectively (Fig. 3.2.19). The frequencies of these two strong peaks observed in Si_{41} cluster with oxygen and hydrogen atoms terminations are different and they are much lower than the corresponding experimental value of Raman peak ~ 521 cm^{-1} in bulk silicon. Furthermore, our detailed analysis shows that the normal modes of vibrations corresponding to these strong peaks, contain motions of Si atoms lying on the surface of Si_{41} cluster, whereas, modes lying in the high wavenumber region with lower intensities arise from the vibrations of all Si atoms in the clusters. Thus, our calculated vibrational wavenumber (~ 512 cm^{-1}) of the strong peak in oxygen terminated cluster can be considered to be analogous to the observed phonon wavenumbers (495 - 510 cm^{-1}) which has been shown to be originating from the surface of Si NCs in the presence of SiO_2 matrix. We wish to emphasize that the results obtained from theoretical calculations of Raman spectra clearly elucidate dominant contribution of Si atoms located at the surface. This further supports the interpretation that LF phonons originate from surface/interface of smaller Si NCs, whereas, HF phonons originate from core of

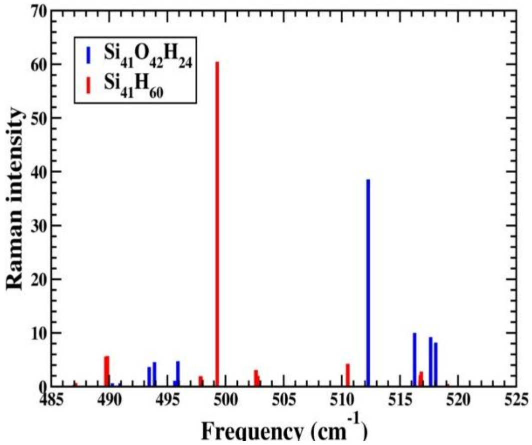

Fig. 3.2.19. Raman spectra of Si_{41} *cluster with a) oxygen (*$Si_{41}O_{42}H_{24}$*) and b) hydrogen (*$Si_{41}H_{60}$*) terminations obtained by employing DFT/TDDFT based response property calculation.*

larger Si NCs. Further, variation found in bond angle and bond length (Table 3.2.2) due to sp^3 and sp^2 hybridization at the surface can well be correlated to large width of LF phonons (Fig. Fig. 3.2.13b) originating at the surface/interface. Similar experimental observations have been reported by Nikitin et al. [234]. They observed that Si phonons in the Raman spectra of smaller (1 - 2 nm) and larger (> 4 nm) Si NCs lie in the ranges 490 - 500 cm^{-1} and 518 - 519 cm^{-1} respectively, which further supports our interpretation.

On the other hand, the calculated frequency of a strong peak in Raman spectra of hydrogen terminated cluster is much lower (~ 499 cm^{-1}) than the corresponding frequencies in oxygen terminated cluster. These results are also consistent with the experimental data reported in the literature. In hydrogen passivated Si NCs (NCs Si: H), Raman spectra show phonon frequencies in the range 500 - 517 cm^{-1} with 514.5 nm as excitation laser [235-236]. Whereas, Raman spectrum of NCs Si: H shows phonon frequencies ~ 439, 462, 478, 486, 504 cm^{-1}, lower than the observed in Si-SiO_2 NCps with 496.5 nm as excitation laser [237]. This is consistent with results of our calculations. Further, it is relevant to note here that observance of surface/interface phonons (LF) is laser excitation dependent. Calculation of Raman spectrum further shows that surface phonon contribution is dominant in small cluster. This further supports the interpretation that LF phonons originate from interface of smaller Si NCs, whereas HF phonons originate from core of larger Si NCs. Observance of surface optical phonon for smaller size NCs has been reported [238]. With further decrease in size of NCs, surface phonon becomes stronger as compared to core phonon (confined phonon) [238] and it's frequency is sensitive to the surrounding medium.

3.2.2.4. Understanding the origin of LF phonons: correlation of size and interface

LI experiment

During the laser irradiation, laser energy can manifest itself in two ways, i) heating of the material and ii) chemical changes in the material. Heating may also lead to changes in the chemical and or mechanical properties like stress, etc., which will be thermally induced changes. Heating of the Si NCs in SiO_2 in our case will lead to observance of red shift and broadening of FWHM in Si phonons, unlike the blue shift observed for LF phonons and no measurable change for HF phonons. Second effect in our case is considered to be surface/interface rearrangement for smaller Si NCs. Although total surface area is larger for larger NCs, surface to volume ratio is much smaller for larger NCs for this surface/interface effect to be observable for larger NCs. Both effects are considered and are discussed further in the following. Molecular dynamics simulations by Soulairol et al. show that for smaller NCs, the extended interface generated due to interaction of surface atom of small Si NCs with Si and Oxygen atoms in the matrix is porous i.e. incoherent and as the size increases, it's porosity decreases and interface tends to become more coherent for larger NCs embedded in SiO_2 matrix [79]. This can in principle lead to higher

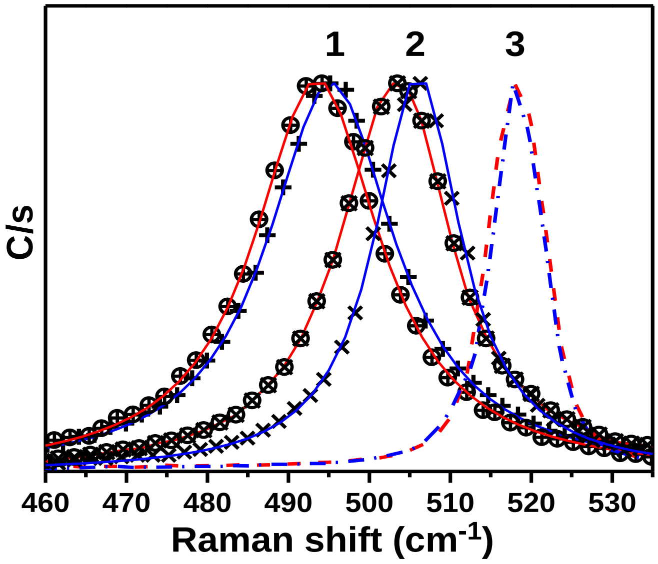

Fig. 3.2.20. Change in LF (1, 2) and HF phonons (3) at laser PD ~ 10 kW/cm^2 and 300 kW/cm^2.

temperature rise for smaller NC at same laser PD due to porosity at the interface compared to that of larger NCs, due to different nature of their interface. Since, local temperature measurement from LF phonons is not feasible as noted above, we have performed power dependent Raman measurements on the site of LF and HF phonons to get further evidence that the observed variation of LF phonons is not related to temperature of a NCp. When, laser PD is increased from 10 kW/cm^2 to 300 kW/cm^2, it is observed that LF phonons red shifts by ~ 1-2 cm^{-1} initially, whereas, HF phonons do not show significant change (red shift ~ 0.2 - 0.4 cm^{-1}) (Fig. 3.2.20). Continuous laser irradiation for half an hour at this power density further shows, blue shift in LF phonons and no change in HF phonons. Initial red shift observed here for LF phonons, may not be due to rise in temperature, as it does not continue, while laser is ON. However, this observed red shift of 1-2 cm^{-1} in LF phonons can be related to relaxation of the compressive stress, which is predicted for small NCs in SiO_2 matrix [79]. Next, the blue shift observed in LF phonons during the LI experiment as well as with continuous laser irradiation, can be correlated to either generation of the compressive stress or correction of Si-O bond to Si-Si bond at the surface/interface. However, betterment in crystalline order during blue shift is suggestive of increase in coherency of interface during laser heating/annealing. The energy provided during LI experiment can lead to the conversion of Si-Ox-Si bonding to Si-Si bonding and in process of filling voids i.e. increases in the coherency of the interface and also leading to blue shift of Si phonon. This further explains the observed blue shift, when the Raman spectra are measured after the laser irradiation was kept OFF for certain duration. This is because if we had observed thermal effects, while the laser irradiation is kept ON, it would show reversible effect in other condition (LI-OFF). However, we have observed permanent change during the laser irradiation experiment. Theoretical investigation by Jiang et al. also shows that temperature recycling improves the sharpness of the interface [239]. This can lead to freezing of value of LF phonons in some cases, as also observed during the LI experiment (Type 1: Fig. 3.2.13a), as once interface is coherent, small energy provided may not be sufficient to change the environment of NC due to presence of matrix. However, when the interface is coherent, this energy is then transferred to the matrix and compressive stress will be generated in Si NCs [127], leading to a small blue shift in LF phonon frequency (~ 1 - 2 cm^{-1}). In this case, therefore, laser OFF condition results in relaxation of this stress, leading to small red shift (1-2 cm^{-1}, Type-II: Fig. 3.2.13a). It may be noted that this observed red shift is only for the higher LF phonons (frequencies ~ 506 - 510 cm^{-1}) during laser OFF condition. In this context, it is important to observe that lower LF phonons (frequencies ~ 495 - 505 cm^{-1}) show larger blue shift (8-10 cm^{-1}) during LI experiment and freezing is observed for these phonons only at the end of LI experiment. Higher frequency LF phonons show freezing at the initial steps of LI. This is consistent with the interpretation of LF phonon originating at the interface and lowering of the Si phonon frequency (leading to LF phonons) is due to higher levels of defects at the interface i.e. variation in the surrounding environment of Si NCs, which gets corrected with the laser energy used, leading to blue shift of the phonon. In general, an irreversible blue shift for lower LF phonons w.r.t. heating is consistent with the understanding developed above that it is occurring due to rearrangement of chemical bonds at the surface of smaller size Si NCs. Thus, our results indicate that this low laser power density is enough to make rearrangements at the interface of Si NCs, however, no measurable changes could be observed in the Raman spectra of larger size NCs. Thus, our results show that the effect of surface/interface depends on size to a large extent, as nature of bonding at the interface changes with size of NCs. For Si-SiO$_2$ NCp, it has been predicted theoretically that Si=O bond forms at the interface leading to the formation of Si^{3+}

suboxides, as the size of Si NCs decreases [222]. This is also later confirmed experimentally using XPS technique by Kim et al. [225]. Increase in size of Si NCs leads to increase in formation of Si-O bonds leading to higher intensities of Si^{2+} suboxides as compared to Si^{3+} suboxides. This is further investigated for our samples using XPS measurements as discussed in the following.

X-ray photoelectron spectroscopy

Two NCps, grown under similar conditions but at different times, wherein laser energy may be different, are studied using Raman mapping. The i) 15 mutilayers (E1) and ii) 10 mutilayers (E7) Si-SiO_2 are grown, which shows abundant presence of LF phonons and very rare presence of LF phonons, respectively. These two NCps are found suitable to check, if XPS data can give corroborative information, as per our interpretation. Since, the beam size in XPS (~ 1 cm x 1 cm), which covers the full sample as noted in the experimental section, average signal from XPS measurement is corroborated with the statistical information obtained from the Raman

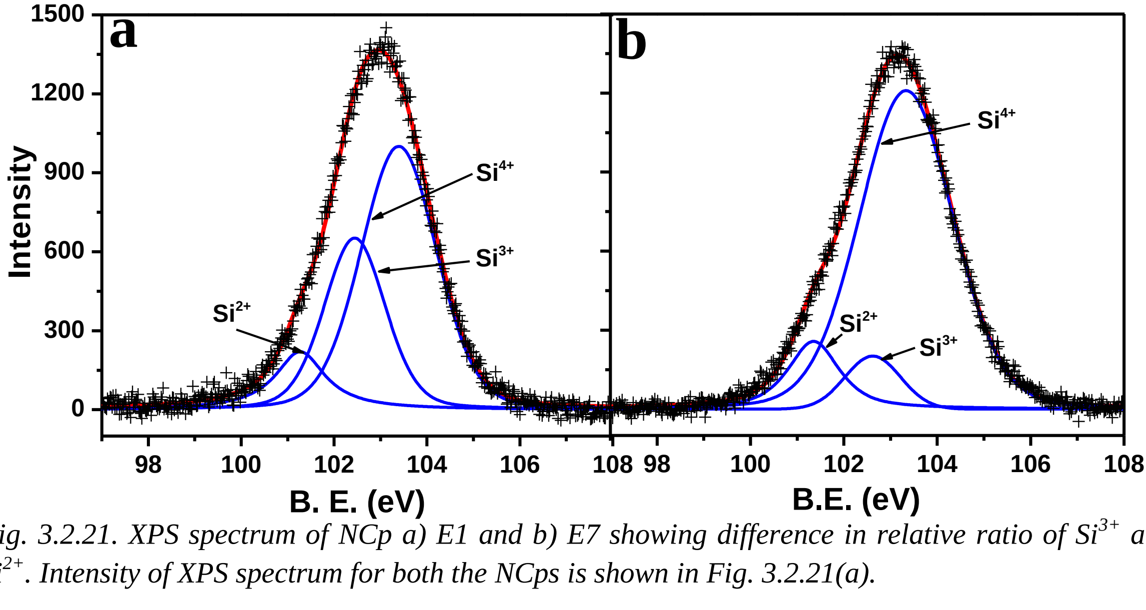

Fig. 3.2.21. XPS spectrum of NCp a) E1 and b) E7 showing difference in relative ratio of Si^{3+} and Si^{2+}. Intensity of XPS spectrum for both the NCps is shown in Fig. 3.2.21(a).

data. The XPS data (Fig. 3.2.21) is fitted using Gaussian-Lorentzian line shapes for the Si 2*p* core-level profile after linear background subtraction using XPS peakfit software [206]. By deconvoluting the spectrum, three chemical structures corresponding to Si^{4+} (B. E. ~ 103.4 eV), Si^{3+} (B. E. ~ 102.3 eV) and Si^{2+} (B.E. ~ 101.2 eV) are observed. XPS gives relative contribution of Si^{4+} with that of Si^{3+} and Si^{2+} in both the samples. Relative intensities (I) of Si^{3+} and Si^{2+} are found to be different in both the samples. $I(Si^{3+})/I(Si^{2+}) = 2.6$ and 0.6 for samples E1 and E7, respectively. As noted above, the $I(Si^{3+})/I(Si^{2+})$ is expected to be > 1 where smaller NCs are more in number and $I(Si^{3+})/I(Si^{2+})$ is expected to be < 1 where larger NCs are more in number. According to our interpretation, E1 should have more number of smaller size NCs and hence should have higher $I(Si^{3+})/I(Si^{2+})$ ratio compared to that of E7. The suboxide peaks corresponding to Si^{3+} and Si^{2+} observed in our sample for E1 and E7 is suggestive of the same i.e. higher number of smaller size NCs in sample E1 as compared to that of sample E7. This independently confirms our attribution of LF phonons as surface/interface phonons of Si NCs in SiO_2 matrix and that variation in the Si phonon wavenumber as due to local variation of Si-SiO_2 interface for LF phonons. It is important to note that the other samples E2-E6, which also shows similar occurrence of LF phonons as E1, show XPS spectra similar to sample E1. This will be discussed in section 3.5 of this chapter.

To summarize, we have performed Raman spectroscopy/mapping study of PLD grown Si-SiO_2 multilayer NCps to elucidate the origin of Si phonon frequencies in the range 495 - 519 cm^{-1}. LF phonons (495-510 cm^{-1}) originate from smaller size Si NCs, where phonon frequency is governed by dominant surface/interface effect and HF phonons (515-519 cm^{-1}) originate from larger size Si NCs, where core phonon is dominant and it’s frequency is governed by the confinement effect. The effect of surface/interface for smaller Si NCs is understood to be due to interaction of surface atoms of Si NC with Oxygen in the matrix. We will use the understanding developed in this work to investigate the origin of IF phonons and establish the corroboration of size and surface/interface phonons using wavelength dependent Raman mapping and literature, as discussed in next section.

3.3. Resonance Raman mapping: Monitoring and manipulation of Si nanocrystals

In the previous section, we show that surface/interface is important in Si-SiO_2 NCps. In this light, we discuss the origin of intermediate frequency (IF: 511 - 514 cm^{-1}) phonons in the present section. Further, wavelength dependent Raman mapping in corroboration with absorption spectroscopy is used to explain the multiple optical gap nature of Si-SiO_2 NCps and it's effect on observation of surface/interface phonons. In the following, we discuss the importance of surface/interface studies of Si-SiO_2 NCps in view of it's application as an efficient material for solar cells.

Research has been mainly focused on increasing the efficiency and reducing the cost of solar cells made of thin films. However, according to Shockley-Quisser limit [240], efficiency of single band gap material cannot be increased more than 30%. To overcome this limit, third generation photovoltaic device have been invented [208], wherein more efficiency can be achieved with the use of multiple optical gaps in a single device. Further, NCs embedded in matrix is also used metal-oxide semiconductor memory devices [209]. One of the most preferred materials for these devices is Si NC embedded in SiO_2 matrix as it is a non-toxic and abundant. For Si-SiO_2 NCps, we have discussed the effect of interaction between Si atoms of NCs and oxygen atoms in the matrix on the Raman spectra. Further, theory is suggestive of the fact that presence of oxygen atoms at the surface plays an important role in affecting the electronic properties of Si NCs ~ 1 - 4 nm in Si-SiO_2 NCps [79-82]. In this regard, the interface of Si-SiO_2 NCps is of intense current interest and has been specifically studied theoretically. Daldosso et al.

show using DFT that the presence of a Si=O at the surface leads to observance of energy gap ~ 2.5 eV [81]. Further, theory is suggestive of the fact that the band-gap region is not only dominated by core but also by sub-oxide interface contribution for small Si NCs (0.8 – 1.4 nm) [80]. However, this embedded surface/interface is difficult to study directly through experiments, although PL spectroscopy [241] has been attempted. In the previous section, we have used the higher sensitivity of Raman spectroscopy to surface/interface and confinement effects in Si NCs due to it's higher specificity as discussed below. Further, we have used this sensitivity of Raman spectroscopy to study the effect of surface/interface on the band gap. Raman spectroscopy/mapping in corroboration with absorption spectroscopy is used to obtain valuable information about the presence of multiple optical gaps in visible range due to dominance of surface/interface for smaller Si NC in SiO_2 matrix as also predicted by simulation studies [79-82].

3.3.1. Raman spectroscopy/mapping: Origin of intermediate frequency (IF) phonons

Representative Raman spectra for some of the IF phonons are shown in Fig. 3.3.1. Raman mapping show mainly two types of IF phonons : i) IF1 with counts/second (C/s) in the range 400 - 600 C/s and frequency ~ 511 - 512 cm^{-1} and ii) IF2 with C/s in the range 50 - 200 C/s and frequency ~ 513 - 514 cm^{-1} in all the NCps studied. Further, Fig. 3.2.1 show asymmetric line shapes for all IF phonons. It is clear that these asymmetric line shapes (Fig. 3.3.1 and 3.3.2) cannot be explained using PCM model. They are suggestive of presence of two phonons. In order to understand the origin of these phonons, laser irradiation experiment has been performed on these two types of phonons in each NCps studied as discussed below.

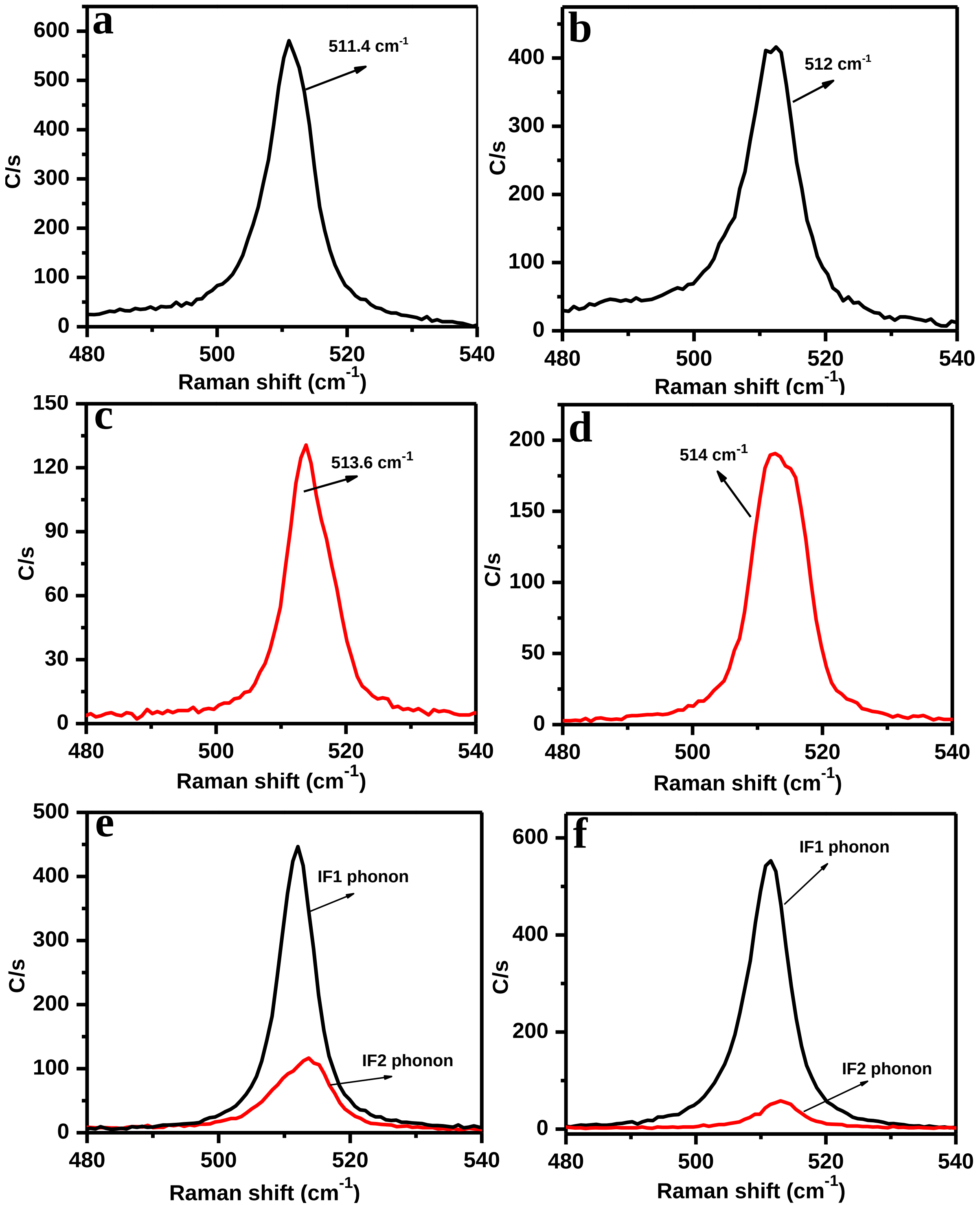

Fig. 3.3.1. a), b), c), d) Raman spectra showing different IF phonons with different line shape and different C/s, e) and f) Raman spectra showing difference in C/s for IF1 and IF2 phonons.

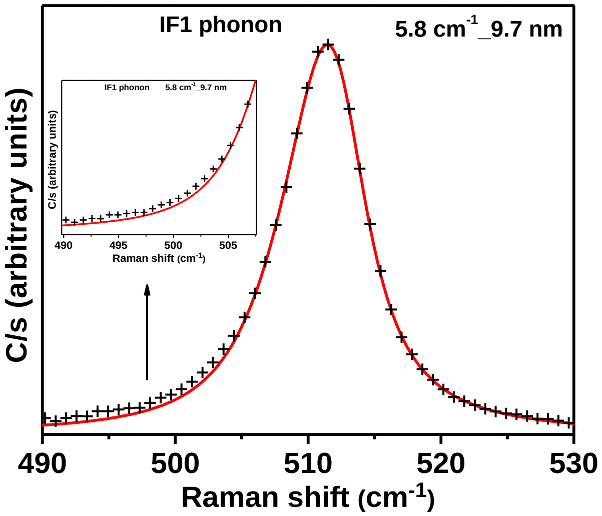

Fig. 3.3.2. PCM fit of IF1 phonon showing mismatch between observed and calculated spectra on the left side of the curve. Theoretical curve is red shifted by ~ 5 cm^{-1} to match the experimental observed Raman spectrum. Inset in show mismatch part clearly.

3.3.1.1. Raman spectroscopy monitored LI experiment

Steps of LI experiment are,

1. The desired peak frequency is located using Raman mapping for doing LI experiment on the said frequency ranges.

2. Steps:

1st step: 0 min; 2nd step : *laser on for 16 mins*; 3rd step : *Laser shutter off for 40 mins*; 4th step : *Again laser on for 16 mins* ; 5th step: *Laser shutter off for 3 hrs.*

Raman spectrum is recorded at the end of each step. The results are summarized in the following. We observe blue shift of both IF1 and IF2 phonons with decrease in FWHM (Fig. 3.3.3a & b). This behavior is similar to behavior of LF phonons during the LI experiment (Fig. 3.2.10). However, there is one major difference in the behavior of these two IF phonons, i.e. IF1 phonons show huge decrease in the intensity (Fig. 3.3.3a & b) whereas, IF2 phonons show increase in the intensity during LI experiment (Fig. 3.3.3c & d). Thus, the asymmetric line shape of IF and change in intensity during the LI experiment suggests that origin of IF phonons cannot be completely related to origin of LF phonons.

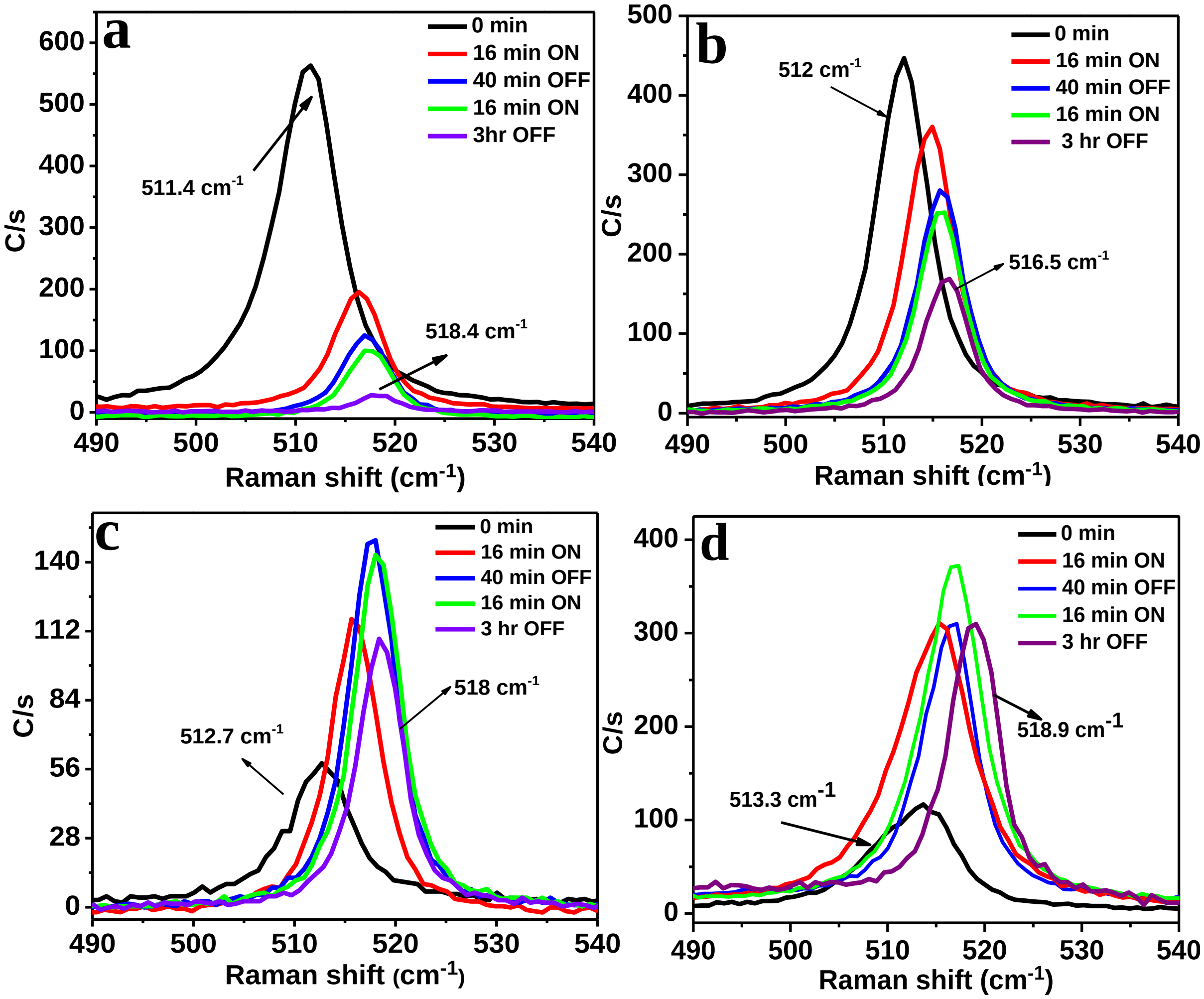

Fig. 3.3.3. Change in a) IF1 phonon ~ 511.4 cm^{-1}, b) IF1 phonon ~ 512 cm^{-1}, c) IF2 phonon ~ 512.7 cm^{-1} and d) IF2 phonon ~ 513.5 cm^{-1} during the LI experiment.

As noted earlier, asymmetry of IF phonons suggest presence of two modes. In previous section, we have seen that LF and HF phonons originate from surface/interface and core of small and large size Si NCs in SiO_2 matrix. Since, IF phonons are intermediate frequency phonons, they can have contributions from both interface and core phonon with an understanding that intermediate sizes can have contributions from both LF and HF phonons. Taking both the above points into consideration, we find that an asymmetric line shape of both IF phonons can be fitted (Fig. 3.3.4a and 3.3.5a) with a Lorentzian and a PCM, accounting for contribution of LF (surface/interface) and HF (core) phonons, respectively. At the initiation of the LI experiment, line shape of IF1 phonon can be fitted with LF phonon ~ 510 cm^{-1} and HF phonon ~ 513 cm^{-1}, assuming both surface/interface and core phonons are contributing simultaneously. Size calculated from asymmetric line shape of HF phonon using PCM comes out to be ~ 6.5 nm (Fig. 3.3.4b). Further, intensity of LF phonon is larger as compared to HF phonon at the initiation of the experiment. During the LI experiment, relative intensity of LF phonon is continuously decreasing and that of HF phonon is increasing. Even after five steps, we are not able to fit the line shape properly with PCM. This suggests that there is still some contribution of surface/interface phonon. Further, after five steps of LI experiment, size calculated using HF phonon comes out be ~ 9.7 nm suggesting increase in size of Si NC. Change in size of NC and relative intensity of LF to HF is shown in Fig. 4b. Further, Fig. 3.3.5a shows that line shape of IF2 phonons after 1st step is approximated with Lorentzian (LF phonon ~ 511 cm^{-1}) and asymmetric line shape (HF phonon ~ 515 cm^{-1}, size calculated from line shape fitting ~ 8.5 nm). Blue shifted IF2 phonon at the 3rd and 4th step could not be well fitted using PCM indicating that still there is some contribution of surface. However, blue shifted IF2 phonon after 5th step of LI experiment can be satisfactorily fitted using PCM. This suggests that there is decrease in interface region with the increase in size of Si NCs during the LI experiment. Change in phonon frequency and corresponding intensity are shown in Fig. 3.3.5b. It shows continuous decrease in intensity for LF phonon and increase in intensity for HF phonon indicating increase in core of Si NC at the expense of surface of NC as is also observed from the increase in size.

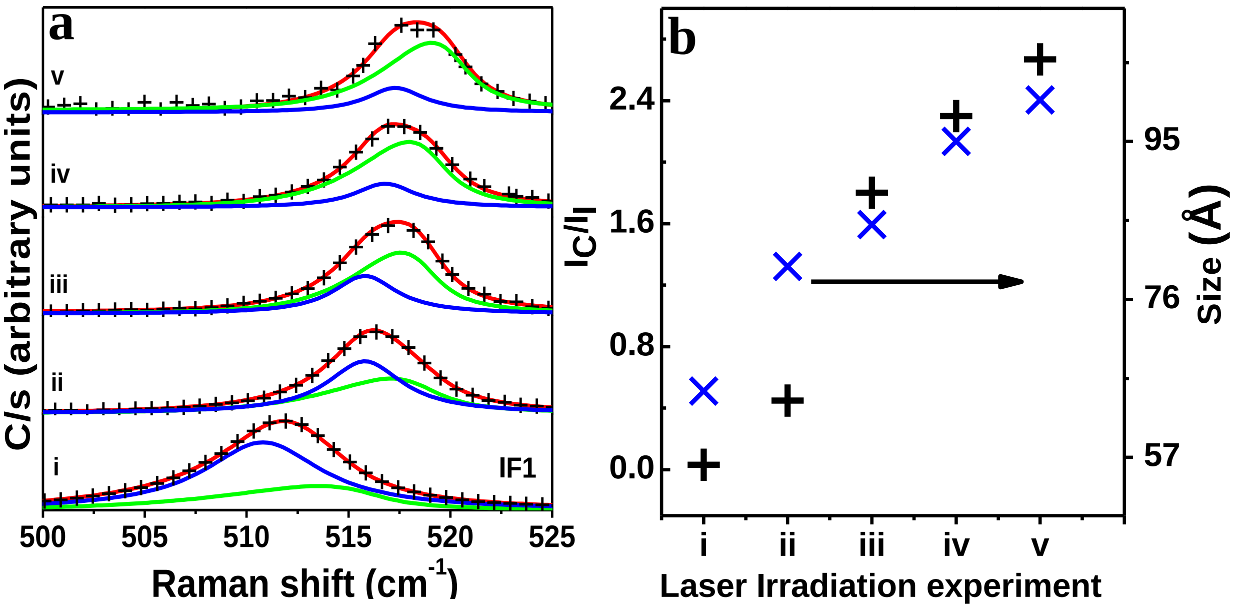

Fig. 3.3.4. Change in a) IF1 phonon, b) ratio of intensity of HF to LF phonon and calculated size during five steps of LI experiment. LI steps are i) 0 min, ii) 16 min ON, iii) 40 min OFF, iv) 16 min ON, v) 3 hr OFF.

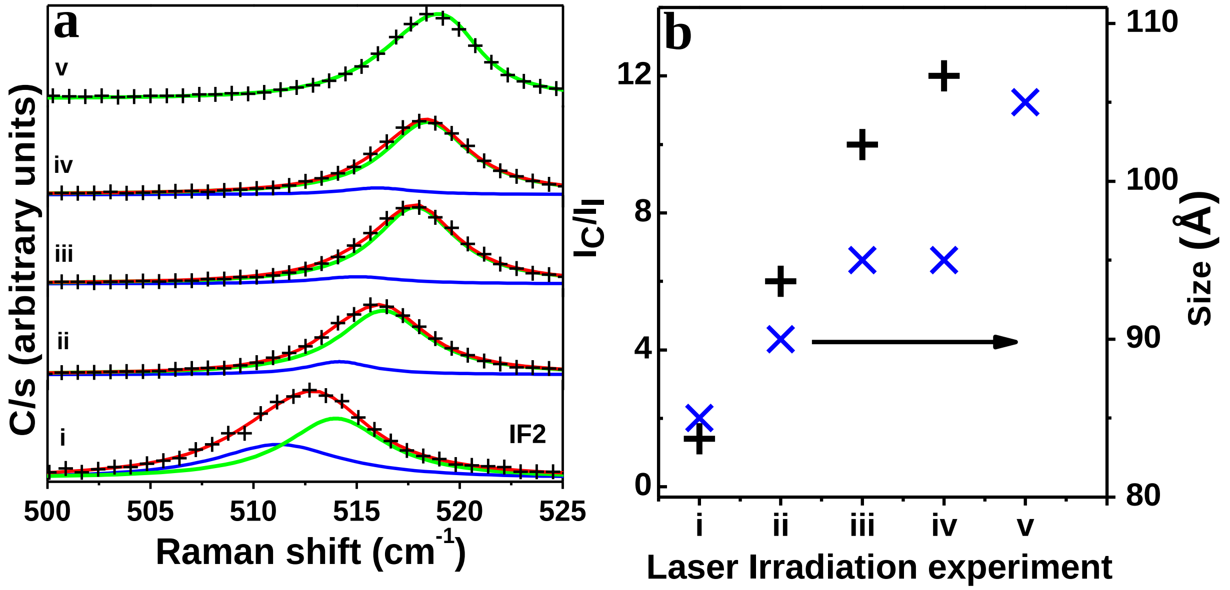

Fig. 3.3.5. Change in a) IF2 phonon, b) ratio of intensity of HF to LF phonon and calculated size during five steps of LI experiment. LI steps are i) 0 min, ii) 16 min ON, iii) 40 min OFF, iv) 16 min ON, v) 3 hr OFF.

Table 3.3.1. Lorentzian peak position and PCM parameters used to fit IF1 phonon

LI steps	LF (width) cm^{-1}	HF (width) cm^{-1}	Size (nm)	Shift included in 521 cm^{-1}
1	510.8 (7)	513.7 (4)	6.5	-1.2 cm^{-1}
2	515.8 (5)	517.7 (3.8)	8.0	-1.2 cm^{-1}
3	515.8 (5)	517.7 (3.6)	8.5	-1.0 cm^{-1}
4	516.9 (4.5)	517.9 (3.6)	9.5	-1.0 cm^{-1}
5	517 (3.5)	518.8 (3)	10	-0.5 cm^{-1}

Table 3.3.2. Lorentzian peak position and PCM parameters used to fit IF2 phonon.

LI steps	LF (width) cm^{-1}	HF (width) cm^{-1}	Size (nm)	Shift included in 521 cm^{-1}
1	511	514.6	85	-4.2 cm^{-1}
2	514	516	90	-1.5 cm^{-1}
3	515	517.7	95	-1.1 cm^{-1}
4	516	518.3	95	-0.6 cm^{-1}
5		518.7	105	-0.6 cm^{-1}
6		518.7	105	-0.6 cm^{-1}

Fig. 3.3.4b and 3.3.5b shows that in case of both IF1 and IF2 phonons, there is increase in size of Si NCs, thereby increasing the core contribution. This suggests that LI experiment has led to more Si-Si like environment and thus increase in size of NC. It may be noted that for PCM fit, bulk frequency (~ 521 cm^{-1}) is allowed to vary to account for generated stress, if any. Indeed, we found that both IF1 and IF2 phonon show decrease in tensile stress for Si NC during the LI experiment (Table 3.3.1. & 3.3.2). Presence of tensile stress is consistent with the molecular dynamics simulation performed on Si NCs embedded in SiO_2 [242]. They have observed tensile stress in the core region of Si NCs due to presence of SiO_2 matrix for Si NCs of size ~ 4 nm. Further, decrease in tensile stress during the LI experiment is expected, because during the experiment size of Si NCs increase due to more and more Si like environment, which makes

interface more coherent. This in turn will lead to compressive stress on Si NCs due to SiO_2 matrix, thus reducing the existing tensile stress in Si NCs. We shall like to note that the observed larger tensile stress for IF2 phonon at the end of first step of LI experiment is due to observed large uncertainty in peak position. However, change in overall intensity for both IF phonons during the LI experiment is still to be understood. To get a clue of the huge change observed in the intensity of these two types of IF phonons during LI experiment, we decided to observe the effect of continuous heating for 2 hrs after the LI experiment as described below.

3.3.1.2. Continuous laser heating after LI experiment

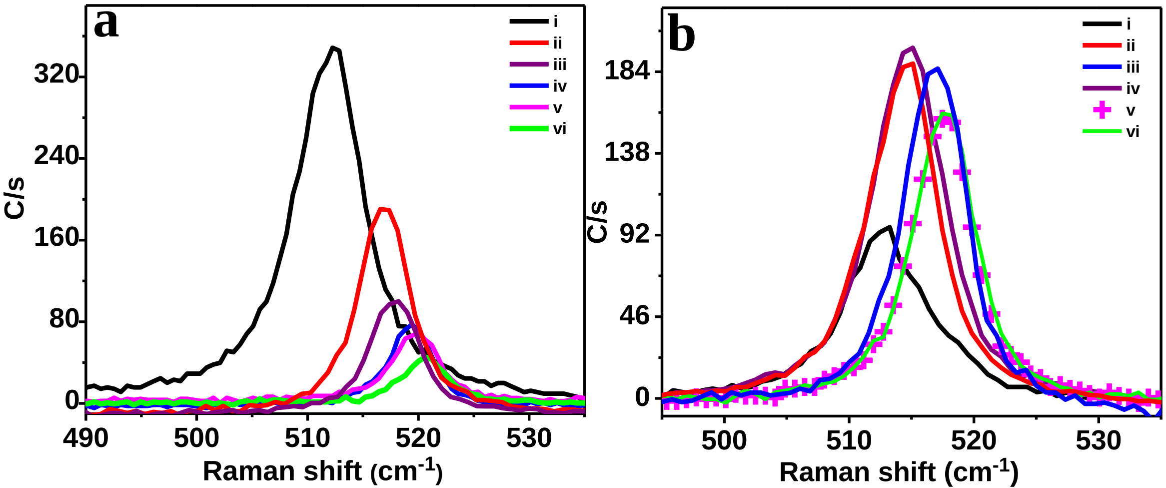

Fig. 3.3.6. Change in a) IF1 phonon and b) IF2 phonon during i) 1st step of LI, ii) 2nd step of LI, iii) 3rd step, iv) 4th step, v) 5th step of LI and vi) 2 hrs continuous Laser heating.

During this experiment, IF2 phonon is not showing any change in frequency, FWHM and intensity (Fig. 3.3.6b) after continuous laser heating for 2 hrs. This behavior is similar to HF phonons and thus confirms our interpretation that this is a core phonon. However, IF1 phonon shows blue shift (Fig. 3.3.6a) after continuous laser heating for 2 hrs. Here, Si phonon frequency observed at 520.8 cm^{-1} shows significant asymmetry (PCM: 10 nm) and smaller contribution of a

Lorentzian. A line shape and C/s of this phonon is similar to IF2 phonon. Both these frequencies seem to be blue shifted and are indicative of generation of compressive stress due to this process. It is only appropriate to measure temperature using stoke/anti-Stoke Raman measurements before we discuss further.

3.3.1.3. Temperature measurements: Stokes/anti-Stokes Raman

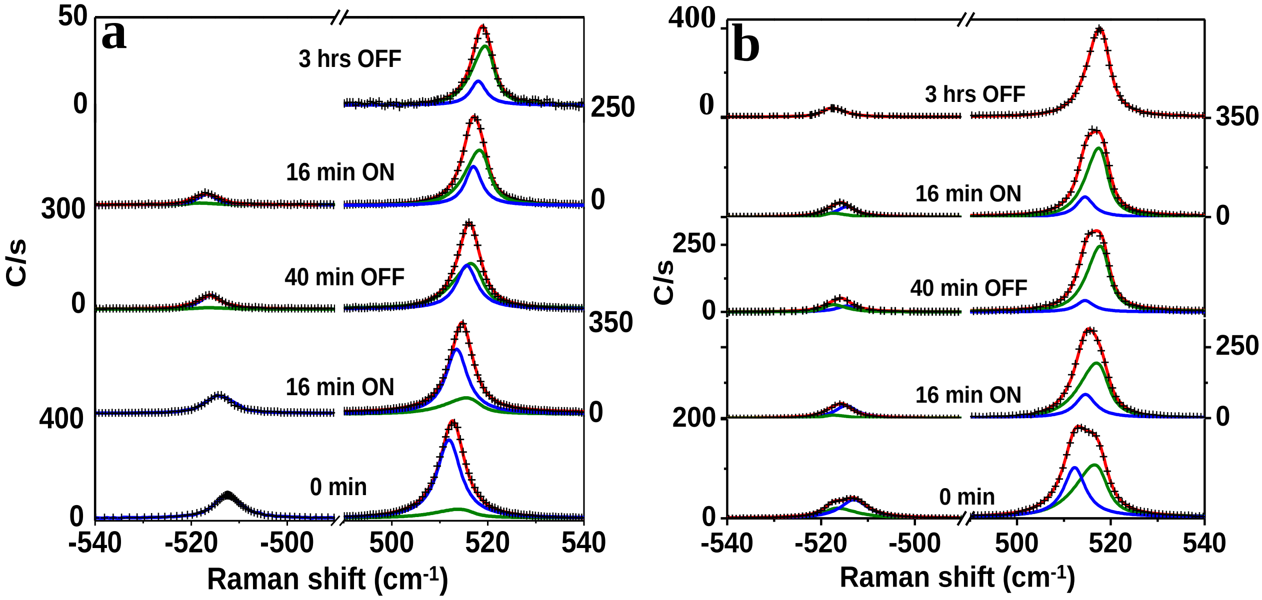

Fig. 3.3.7. Change in Stokes/anti-Stokes Raman spectra for a) IF1 and b) IF2 phonons during five steps of LI experiment. Solid line (red color) is the fit to the data Raw data (+). Lorentzian (blue color) and PCM (olive color) component are shown with solid line. C/s is shown on different sides for the sake of clarity.

In our previous section, we have shown that local temperature calculated using HF phonon comes out to be room temperature, whereas using LF phonons, it gives incorrect temperature. Representative Stokes/anti-Stokes Raman spectra for both IF1 and IF2 phonons are shown in Fig. 3.3.7. We have calculated local temperature using LF and HF phonon, obtained from deconvolution of IF phonons. We find that calculated temperature comes out to be room temperature (~ 290 - 300 K) using HF phonons, however, using interface (LF) phonon, it again comes out to be incorrect (varying from ~ 550 K to 50 K on laser irradiation experiment) for both IF1 (Fig. 3.3.8a) an IF2 phonons (Fig. 3.3.8b), an observation similar to that of LF phonons. This suggests the possibility of Resonance Raman scattering for IF phonons too. Resonance Raman scattering is investigated for LF and IF phonons using wavelength dependent Raman mapping.

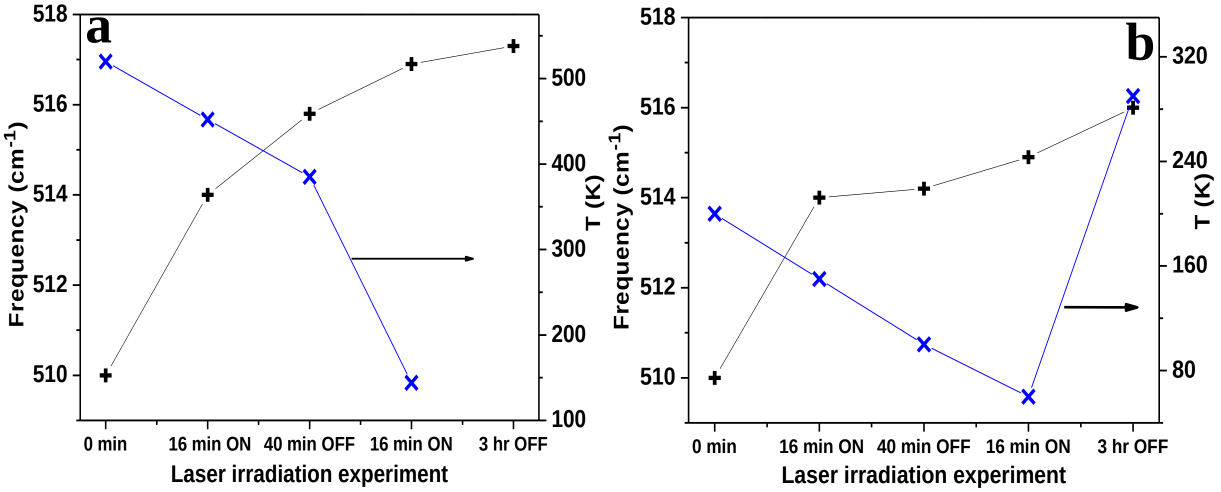

Fig. 3.3.8. Change in phonon frequency and calculated temperature during LI experiment using LF phonon for a) IF1 phonon and b) IF2 phonon. Frequency and corresponding temperature is shown by (+) and (×) symbols, respectively. Line is guide to eye.

3.3.1.4. Wavelength dependent Raman mapping

Wavelength dependent Raman mapping is performed with similar power density ~ 4-5 kW/cm^2 (0.5 s acquisition time) using 441.6 nm, 488 nm and 514.5 nm excitations on same site with the help of visual guidance on all the samples studied. Representative Raman mapping is shown in for sample E4 (Fig. 3.3.9) and sample E1 (Fig. 3.3.10). Raman images are created using LF, IF and HF phonons. Corresponding Raman spectra for sample E4 is shown in Fig. 3.3.9e-g showing maximum intensity for LF, IF and HF phonon for these three lasers lines. It is noteworthy to observe that LF and IF phonons could be observed only using 441.6 and 488 nm excitations, whereas, HF phonons are observed with all three excitations. Further, the ratio of intensities of interface and core phonons (I_{LF}/I_{HF}) is > 1 for all the samples (Table 3.3.3). This is quite surprising knowing that these phonons are coming from much smaller volume (interface ~ 10 Å [222]). This suggests that either there is very large density of very small Si NCs, where from interface phonon contribution is dominant or these phonons are observable due to Resonance Raman scattering. If it is the first case, interface phonons should then be observable with 514.5 nm excitation source also. Excitation dependence of LF and IF phonon's intensity clearly shows that enhancement of Raman signal due to resonance is crucial to the observance of these phonons. Whereas, HF phonons show non resonant behavior like bulk Si phonon and thus these phonons are observable with all the three excitation laser sources with similar intensity.

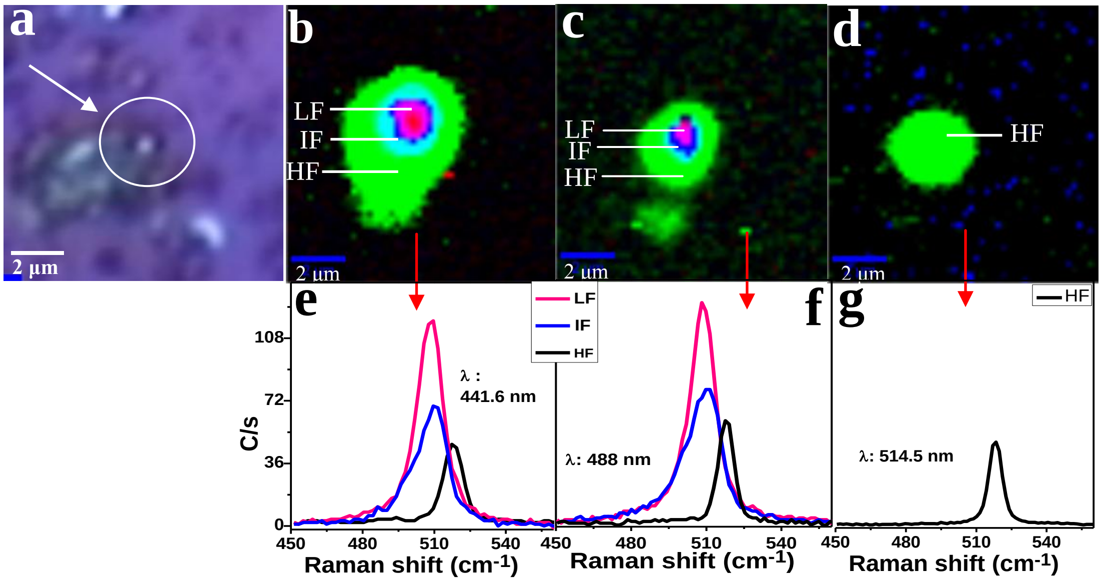

Fig. 3.3.9. a) Optical image of NCp E4, corresponding Raman image of marked region with excitation as b) 441.6 nm , c) 488 nm , d) 514.5 nm showing absence of LF and IF phonons with 514.5 nm as excitation laser and 4e-4g) compares relative intensity of LF and IF to HF phonons for wavelengths noted in the figure. C/s for all three Raman spectra is shown in Fig. 3.3.9e.

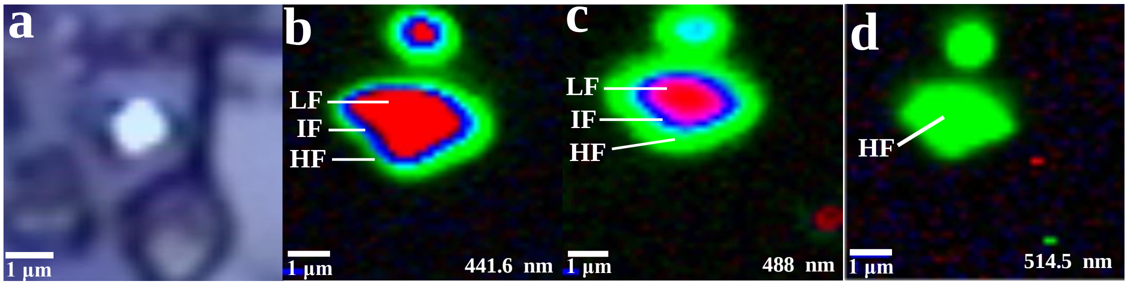

Fig. 3.3.10. a) Optical image of NCp E1, corresponding Raman image of marked region with excitation as b) 441.6 nm, c) 488 nm and d) 514.5 nm showing absence of LF and IF phonons with 514.5 nm as excitation laser.

Table 3.3.3. Ratio of intensity of LF to HF phonon for all NCps with 441.6 nm and 488 nm as excitation sources.

NCp	**$I_{(LF)}/I_{(HF)}$: 441.6 nm**	**$I_{(LF)}/I_{(HF)}$: 488 nm**
E1 (45s)	1.8	1.5
E2(90s)	2.0	1.4
E3(120s)	1.8	1.2
E4(150s)	3.0	2.7
E5(180s)	2.1	1.8
E6(210s)	1.5	No LF

It is important to note that almost similar C/s are observed for HF phonons using these three laser consistent with it's non-resonant behavior. In order to compare absolute intensities of phonons for different laser used, we have calculated different parameters as listed in Table 3.3.4. We find that the penetration depth comes out to be in micron (Table 3.3.4), which is larger than total thickness of NCp film for the three laser used. This suggests that scattering cross section will mainly depend on number of incident photons and $\omega^{4.}$ Taking these two factors into account, intensity of phonon using 441.6 nm as excitation source is expected to be higher ~ 1.16 and 1.2 as compared to 488 nm and 514.5 nm laser, respectively as is observed in our NCps.

Table 3.3.4. Laser parameters, no of photons and ratio of calculated intensity for three wavelengths summarized.

Laser (nm)	Power used (P)	ω^4	No of photons/s $*10^{14}$ (n) = P/hν	Spatial resolution (μm)	Depth of focus (μm)	n * ω^4	
441.6	.4mW	61	8	0.5	1.4	488	1.16
488	.43mW	42	10	0.54	1.6	420	
514.5	.5mW	33	12	0.57	1.7	396	1.2

Wavelength dependent Raman mapping (Fig. 3.3.9 and 3.3.10) shows that i) cluster size reduces as the wavelength changes from 441.6 nm to 514.5 nm and ii) with 514.5 nm excitation, HF phonons are observed in the region, where LF and IF phonons are observed with 488 and 441.6 nm excitations. To understand these observations, Raman spectroscopy is performed by varying the focal spot along the depth (Fig. 3.3.11) at particular spatial position of a cluster. Fig. 3.3.11 shows variation in Si phonon i.e. from LF to HF phonons as we move focal spot downward at that position. This suggests that HF phonons are coming from bottom of the cluster, whereas IF and LF phonons are coming from central and top region of a cluster, respectively. This further suggests that there is stacking of different size Si NCs as HF and LF phonons originate from larger and smaller size NCs. Observance of HF phonons (514.5 nm excitation) in the region where LF and IF phonons are observed (488 and 441.6 nm) can be explained considering different depth of focus for these wavelengths. Depth of focus for these three lasers is given in Table 3.3.4. Highest depth of focus (Table 3.3.4) for 514.5 nm excitation as compared to 488 nm and 441.6 nm, presence of larger size Si NCs at the bottom of the cluster and non resonant nature of HF phonons explains the presence of HF phonons at this excitation, from the region, where LF and IF phonons are observed at 488 and 441.6 nm excitations. Further, spot size, power and power density is given in Table 3.3.4. This shows that power density is nearly similar for all three lasers used. This suggests that difference in size of cluster could be due to difference in scattering efficiency which is proportional to ω^4. Scattering efficiency is calculated for these three wavelengths (Table 3.3.4). This shows that overall decrease in cluster size from 441.6 to 514.5 nm is found to be due to lower scattering efficiency at 514.5 nm leading to observable signal only coming from larger scattering volume region. Details of Raman mapping with varying the focus along the depth will be discussed in next section.

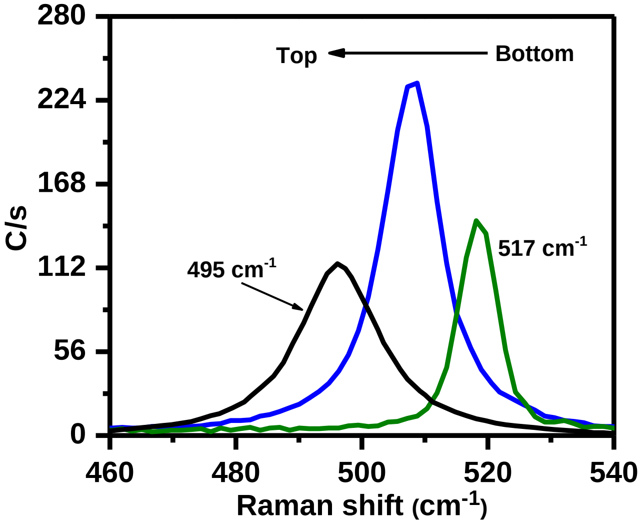

Fig. 3.3.11. Change in Si optical phonon with the change in focus along depth at fixed spatial position.

It is important to note that in particular NCp E6, LF and IF phonons are observable only using 441.6 nm as excitation source (Fig. 3.3.12) which is rather surprising. Further, Table 3.3.3

shows that I_{LF}/I_{HF} for all the samples is ~ 2 (441.6 nm excitation), except NCp E4. For this particular NCp, this ratio is quite higher ~ 3. To understand these two observations, we have performed absorption spectroscopy measurements on these NCps as discussed below.

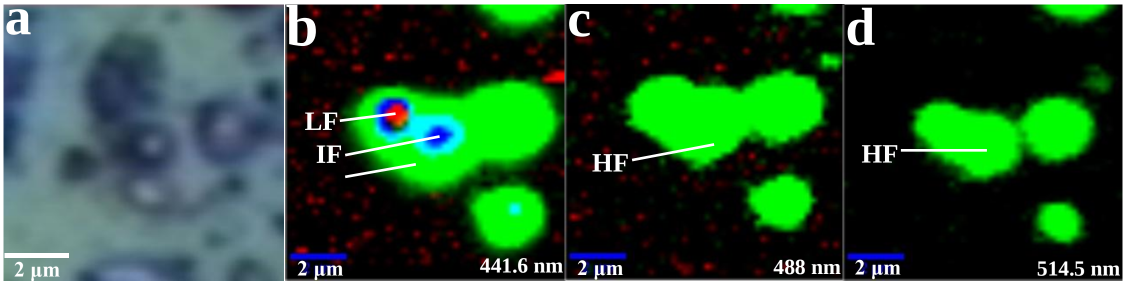

Fig. 3.3.12. a) optical image of NCp E6, corresponding Raman image of marked area with excitation source as b) 441.6 nm, c) 488 nm and d) 514.5 nm. Red and green color shows presence of LF and HF phonons, respectively.

3.3.1.5. Corroboration of absorption spectroscopy with Raman mapping

Absorption spectra of all NCps show interference fringes as shown in Fig. 3.3.13. It is well known that when a beam of light passes through a thin film with the thickness comparable to that of wavelength of light, wave reflected from upper and lower surface interference constructively and destructively leading to observance of interference fringes [243]. Due to presence of interference fringes in the absorption spectra, correlation with resonance Raman scattering is not feasible. Interference fringe free absorption spectra (ref: annexure 3.3.1) are measured by using p-polarized light at Brewster angle [243], wherein, there is no reflected beam and hence no interference fringes.

After the removal of interference fringes, optical band gap can be obtained as per formalism given in chapter 2 (equations - 2.29, 2.30) and are shown in Fig. 3.3.14 and summarized in the Table 3.3.5.

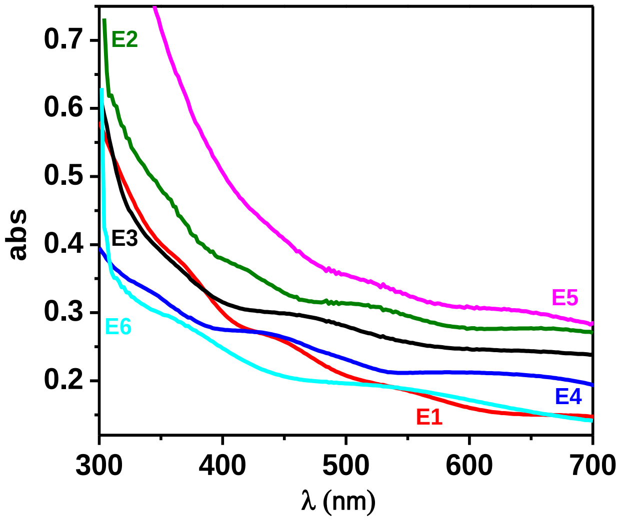

Fig. 3.3.13. Absorption spectra of all NCps showing observance of interference fringes.

Table 3.3.5. Ratio of intensity of LF to HF phonon for all NCps with 441.6 nm and 488 nm as excitation sources. Multiple absorption edges calculated from $(\alpha h\nu)^2$ *vs* $h\nu$ *graph in the range of interest (350 - 520 nm) for all NCps.*

NCp	**$I_{(LF)}/I_{(HF)}$: 441.6 nm**	**$I_{(LF)}/I_{(HF)}$:488 nm**	**Abs edge (eV)**
E1 (45s)	1.8	1.5	2.5, 2.88, 3.2
E2 (90s)	2.0	1.4	2.5, 2.9, 3.1
E3 (120s)	1.8	1.2	2.48, 2.9, 3.2
E4 (150s)	3.0	2.7	2.55, 2.8, 3.3
E5 (180s)	2.1	1.8	2.6, 2.92, 3.1
E6 (210s)	1.5	No LF	2.75, 3.1

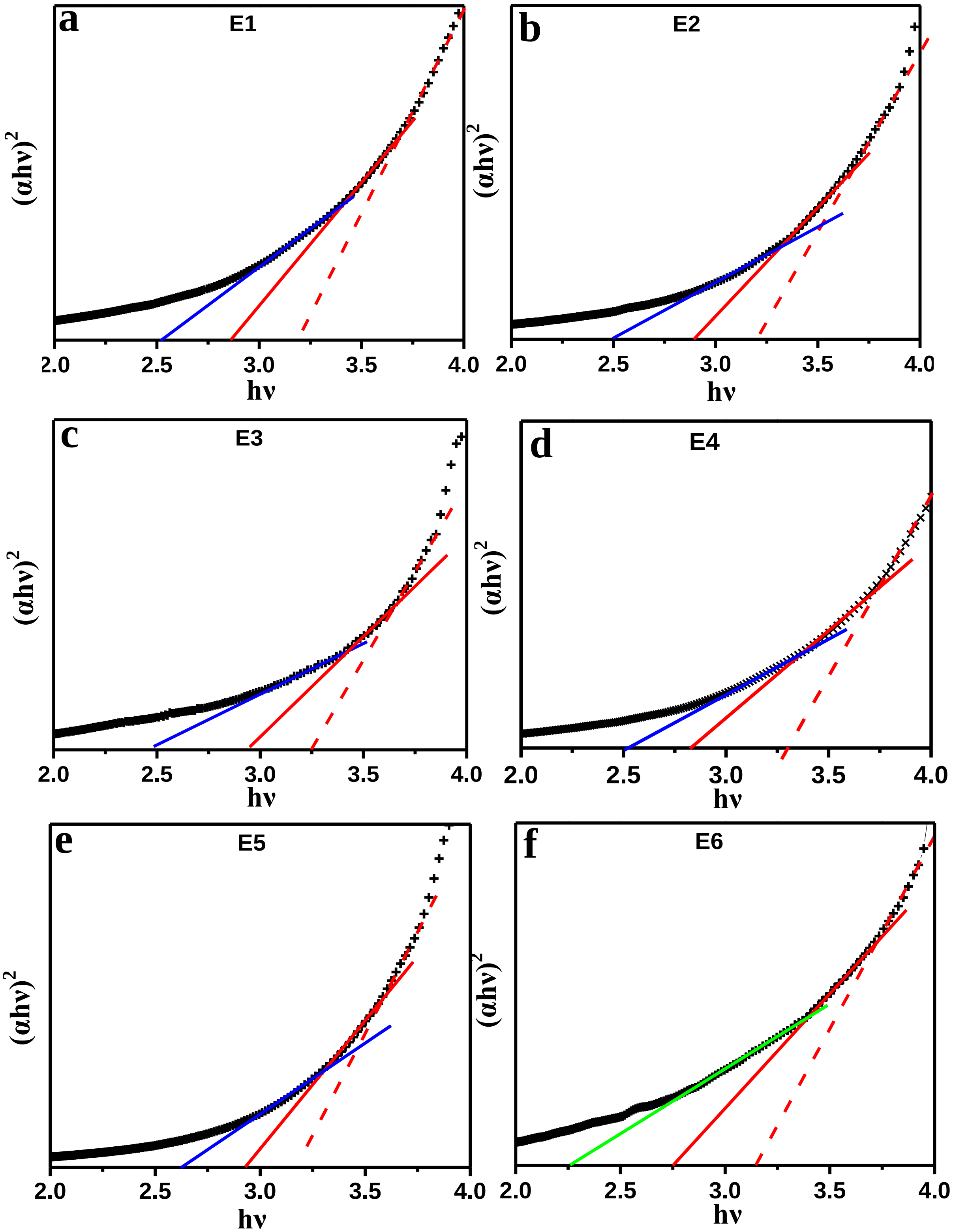

Fig. 3.3.14. $(\alpha h\nu)^2$ vs hν graph of NCp a) E1, b) E2, c) E3, d) E4, e) E5 and f) E6 obtained from absorption spectra.

Absorption spectra show absorption edges ~ 2.50 eV, 2.9 eV and 3.1 eV for all the samples except E6 (Fig. 3.3.14 and Table 3.3.5) where absorption edges ~ 2.3, 2.75 eV and 3.1 eV are observed. In the above, we have discussed the observance of LF and IF phonons using 2.5 and 2.8 eV excitation for all NCps except E6 (Table 3.3.3). Fir this particular NCp, surface/interface phonons are observed using only 2.8 eV excitation. This clearly brings out proximity of real energy level to the laser excitation/s and corresponding Raman signal enhancement due to resonance. This further explains observance of LF and IF phonons only for 441.6 nm (2.8 eV) in case of E6. The results for all samples are summarized in table 3. For sample E4, I_{LF}/I_{HF} is highest for both 441.6 nm and 488 nm excitation source as compared to other samples. This can also be further correlated with observed absorption edges ~ 2.55 eV, 2.8 eV for this sample (Fig. 3.3.14), which almost exactly matches with excitation wavelengths 448 nm (2.54eV) and 441.6 nm (2.8 eV) respectively. Absorption edge ~ 3.1 eV observed in all the NCps corresponds to direct band gap of Si, whereas other absorption edges ~ 2.5 eV and 2.9 eV are related to interface of Si-SiO_2 NCp originating from smaller size NCs [158, 241]. Further, our observation of these band edge are also in agreement with recent eliipsometric study on Si-SiO_2 NCp also shows band edge ~ 2.8 eV and 2.5 eV from smaller size Si NCs [244, 245].

3.3.1.6. Understanding the origin of IF phonons

Results of LI experiment and continuous laser heating for longer time can be explained considering that these two IF1 and IF2 phonons come from two different intermediate size NCs, x_1 and x_2, where $x_1 < x_2$. For smaller size x_1, surface/interface phonon contribution is dominating (Fig. 3.3.4) whereas, for larger size x_2, core and surface/interface phonon contribution is comparable (Fig. 3.3.5). The decrease in the intensity of IF1 phonon on heating can be correlated as due to moving away from the resonance condition for LF phonons due to increase in size and thereby increase in core phonon contribution. Increase in intensity of IF2 phonon on heating can be said to be due to increase in the size of Si NC i.e. scattering volume. The non resonant nature of core phonon further explains the lesser C/s for IF2 phonon as compared IF1 phonon in the beginning of the LI experiment (Fig. 3.3.2).

It is found that during the LI experiment, more and more Si-O bonds are getting converted to Si-Si like environment causing increase in size of Si NC. This increases the intensity of IF2 phonons, which already has comparable core phonon contribution. It is important to note that C/s of IF1 phonons at the end of LI experiment is close to C/s of IF2 phonons at the beginning of the experiment. This further confirms the increase in size x_1 and it is approaching size x_2 on laser irradiation. This clearly suggests conversion of IF1 phonon to IF2 phonon and IF2 phonons to HF phonons. However, as we have discussed in last section, LF phonons did not show conversion of LF phonon to IF phonons during the LI experiment. This is looked into by continuous laser heating for longer time of 3 hrs and 30 mins on LF phonons. It is observed that

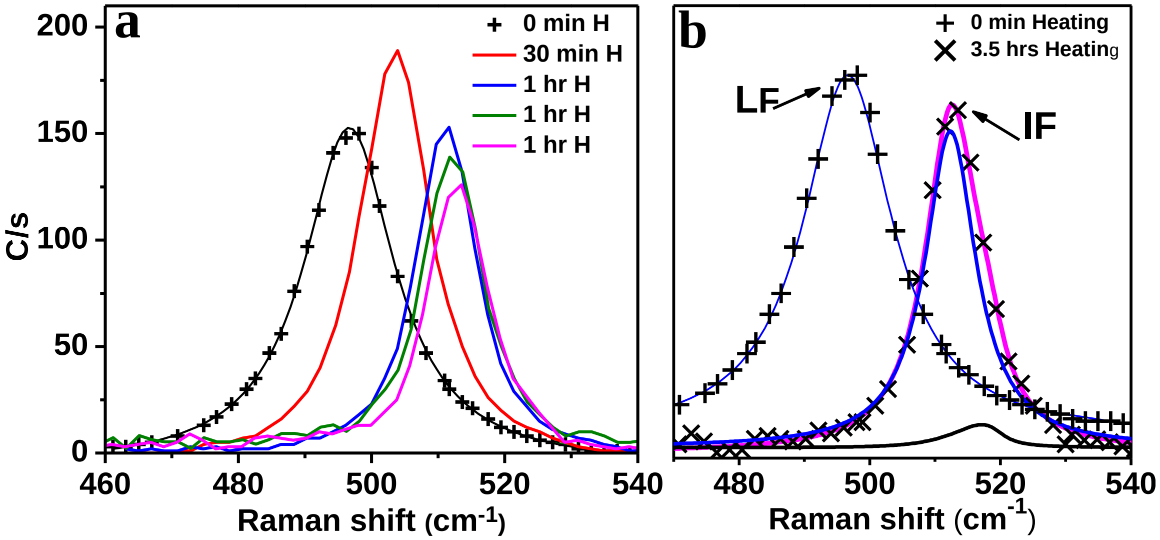

Fig. 3.3.15. a) Change in Raman spectra showing conversion of LF to IF phonon on continuous Laser heating as noted in the figure and b) Solid line is fit to raw data (+ and $^{\times}$). Raman spectrum of LF phonon is shifted in y-axis for the sake of clarity.

LF phonon (~ 497 cm^{-1}: Lorentzian line shape) converted to IF phonon ~ 512.9 cm^{-1} (Fig. 3.3.15) after continuous heating. The asymmetric line shape of this phonon can be fitted with superposition of LF and HF phonon (Fig. 3.3.15b). This shows the conversion of LF to IF phonons and thus further confirming our interpretation of LF phonons, IF and HF phonons originating from interface of smaller, intermediate and core of larger size Si NCs. Understanding developed here for whole range of Si phonons (495 - 519 cm^{-1}) in Si-SiO_2 NCps can be used to explain and understand Raman data reported earlier in the literature.

3.3.2. Corroboration of our results with the literature

It may be interesting to see the correlation of size of NC, wavelength dependent Raman spectra with different interface or passivation of Si NCs reported in literature. Hydrogen passivated Si NCs of sizes ~ 2 - 6 nm excited with 514.5 nm and 496.5 nm show HF [232, 235] and LF phonon [236], respectively. Raman spectra of Si-SiO_2 NCp (size ~ 3 - 5 nm) excited with mainly 514.5 nm laser show mainly observance of core phonons [126, 138]. However, Si NCs of size ~ 2 - 4 nm excited using 488 nm, shows presence of Si phonon frequency ~ 495 cm^{-1} and 517 cm^{-1} simultaneously. Further, peak ~ 495 cm^{-1} disappear for Si NCs of size ~ 6.3 nm [136]. These observations are consistent with our interpretation of LI experiment as noted above. This data further supports that occurrence of surface/interface phonons depends on two factors 1) size of Si NC and 2) excitation wavelength, whether Si NCs are grown in matrix (SiO_2) or passivated by different atoms, as it leads to different electronic band structure [80]. The above mentioned data and our data together suggests that LF, IF and HF phonons are observed from sizes < ~ 4 nm, ~ 4 to 6 nm and > ~ 6 nm, respectively.

In order to support our observation, that is to check whether, presence of oxygen is making significant contribution in observance of range of Si optical phonons, we have performed similar studies on one multilayer NCp film of Si-Al_2O_3 grown on amorphous Al_2O_3 deposited on crystalline Al_2O_3 substrate as described below

3.3.3. Raman mapping of Si-Al_2O_3 nanocomposite

We further performed wavelength dependent Raman mapping on another NCp E1A: Si-Al_2O_3 (amorphous Al_2O_3) NCp, grown on crystalline Al_2O_3 with similar growth conditions. Raman mapping shows formation of clusters of Si NCs as is observed in Si-SiO_2 NCp thin films. Further, phonon frequencies in the range 490 - 519 cm^{-1} are observed with 441.6 and 488 nm excitation (Fig. 3.3.16). However, only HF phonons (515 - 519 cm^{-1}) are observed with 514.5 nm excitation. It is important to note that LF phonon (490 - 510 cm^{-1}) shows Lorentzian line shape, HF phonons (515 - 519 cm^{-1}) show asymmetric line shape which can be fitted using PCM and line shape of IF phonons (511 - 514 cm^{-1}) can be understood using simultaneous contribution of LF and HF phonons similar to that noted in Si-SiO_2 NCps. This confirms that presence of oxygen is making significant contribution in observance of surface/interface phonons due to presence of absorption edges in the visible region and Si-O bonding at the interface. Here, lowest frequency for LF phonons is 490 cm^{-1}.This could be because of difference in matrix that is used to embed Si NCs as change surrounding leads to change in frequency of surface phonons. Result of wavelength dependent Raman mapping corroborates well with absorption spectrum of the same NCp (Fig. 3.3.16). It is interesting to note that for this NCp film, interference fringe free absorption spectrum is observed using un polarized light at normal incidence (Fig. 3.3.16e).

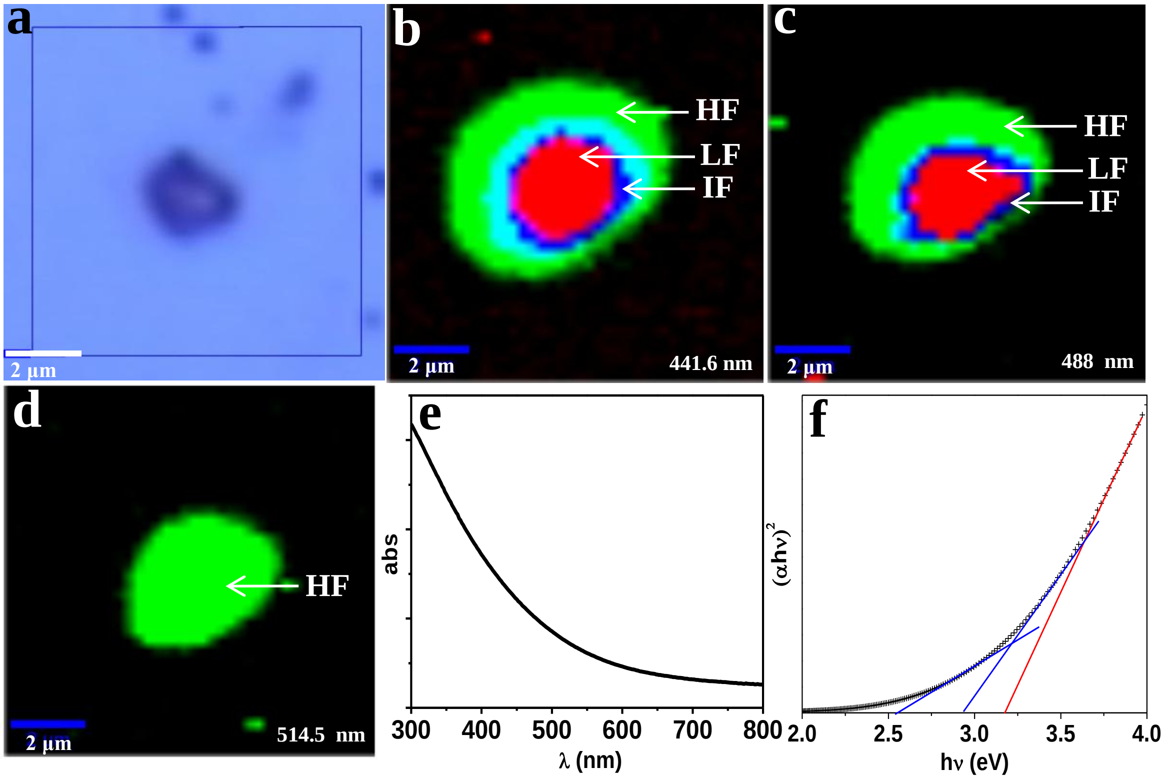

Fig. 3.3.16. a) Optical image of E1A NCp, corresponding Raman image of marked region with excitation as b) 441.6 nm, c) 488 nm, d) 514.5 nm showing absence of LF and IF phonons with 514.5 nm as excitation laser, e) absorption spectra of the same NCp measured with un polarized light showing absence of interference fringes and f) $(\alpha h\nu)^2$ vs $h\nu$ graph for sample E7 obtained from absorption spectra.

This is because buffer layer (Al_2O_3) used in this NCp is same as that of substrate (crystalline Al_2O_3) and therefore there will not be any significant change in refractive index.

To summarize, IF phonons (511 - 514 cm^{-1}) originate from intermediate size NCs where, both surface and core of Si NC contribute simultaneously. Further, temperature obtained from Stoke-antiStokes Raman spectroscopy and results of wavelength dependent Raman mapping in corroboration with absorption measurements show that resonance Raman scattering is crucial for the observance of surface/interface phonons. This also further explains large Raman signal observed from Si NC surface/interface and the Raman data variation observed in the literature for Si phonon frequency in Si-SiO_2 NCps and Si NCs passivated using hydrogen.

The observed sensitivity of Raman spectra to surface/interface and core of Si NCs in SiO_2 matrix in corroboration with AFM is used to understand the observed morphology (clusters of Si NCs - section 3.2). This will be discussed in next section.

3.4. Understanding the morphology of nanocomposites from correlation of Raman and AFM mapping

In PLD grown Si-SiO_2 NCps, Raman mapping shows cluster formation of Si NCs at isolated sites in each NCp, although the growth is carried out to be multilayer as discussed in chapter 2. This is consistent with the cross-sectional TEM data, which does not show any evidence of formation of Si-SiO_2 multilayer. This is investigated by performing Raman and AFM mapping at same sites and further, plausible growth mechanism for the observed morphologies of Si NCs embedded in SiO_2 matrix is elucidated using study of single layer NCp and multilayer NCps annealed at different temperatures as detailed in the following.

3.4.1. Raman and AFM mapping

Raman spectroscopic measurements of Si-SiO_2 NCps (E1-E6) show variation in the Si phonon frequencies from 495 to 519 cm^{-1} in all NCps studied. The observed Si phonon frequencies, i) 495 - 510 cm^{-1} (LF phonons), ii) 511 - 514 cm^{-1} (IF phonons) and iii) 515 - 519 cm^{-1} (HF phonons) are attributed to originate from small (< ~ 4 nm), intermediate (~ 4 - 6 nm) and large (> ~ 6 nm) size Si NCs. Here, LF and HF phonons originate from surface (Si-SiO_2 interface) and core of smaller and larger Si NCs, respectively. IF phonons originate from intermediate size Si NCs where, both surface/interface and core of Si NC contribute simultaneously. In the present section, we will use the understanding developed for in previous section 3.2 and 3.3 for Si phonons to obtain information on morphology of Si-SiO_2 NCps using Raman and AFM mapping on same selected area as described below.

3.4.1.1. Raman mapping

Raman mapping with acquisition time of 1 s and step size ~ 0.15 μm are performed at many sites on each NCp. Raman spectra observed in Raman mapping show phonon frequencies in the range 495 - 519 cm^{-1}, hence Raman image is generated using intensity of frequencies in the range 490 - 525 cm^{-1}. Representative Raman image for NCp E2 is shown in Fig. 3.4.1b. Fig. 3.4.1c shows corresponding normalized Raman spectra for the positions marked in Fig. 3.4.1b.

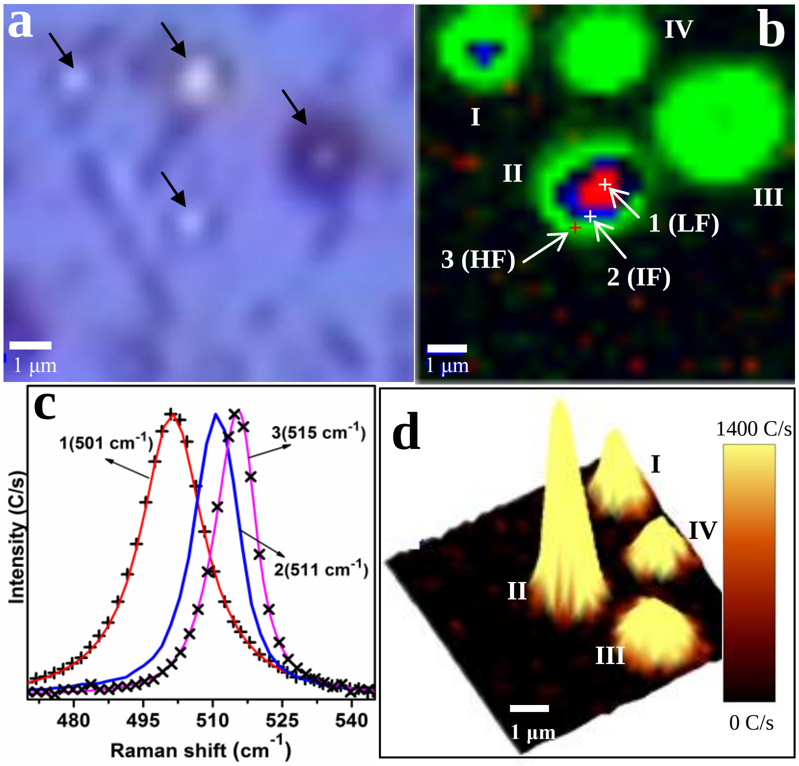

Fig. 3.4.1. a) Representative optical image of NCp E2, b) corresponding Raman image generated using intensity of phonon frequencies in the range 490 - 525 cm^{-1}, c) Corresponding Raman spectra at positions as marked in Raman image and d) intensity profile of Raman image.

Raman images over all NCps indicate presence of clusters of Si NCs, sizes varying from ~ 1 - 4 μm. Fig. 3.4.1c shows that observed red shift and asymmetric line shapes of Si phonon observed in the Raman spectra is well fitted using phonon confinement model for the phonons occurring in the frequency range 515 - 519 cm^{-1}. This suggests formation of Si NCs of different sizes in these clusters. Further, the fact that these Si NCs remained clustered without coalescence to form bigger NCs even after annealing the NCp at 800 ^{o}C, suggests that they are indeed isolated by an insulating matrix of $SiO_{2.}$

Fig. 3.4.2a-c show Raman images created using intensities of LF, IF and HF range phonons for NCp E1. The result of similar measurements on many sites on all NCps is presented as a histogram. Histogram (Fig. 3.4.2d) is created for LF, IF and HF phonons for all NCps, giving the percentage of occurrence of these phonons in these NCps.

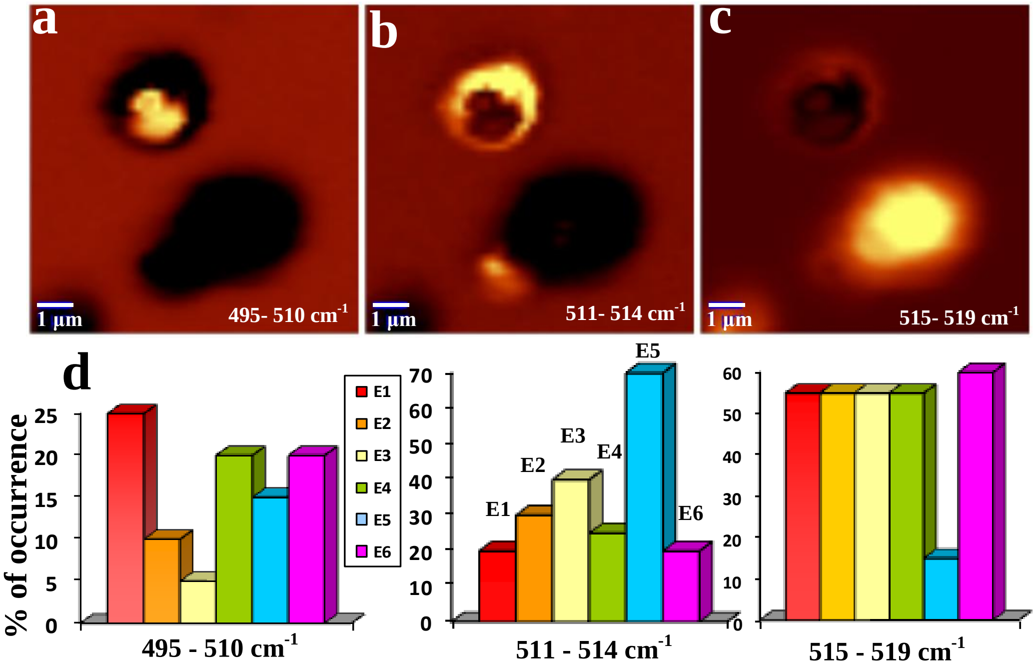

Fig. 3.4.2. Raman image generated using phonon frequency a) ~ 495 - 510 cm^{-1}, b) 511 - 514 cm^{-1}, c) ~ 515 - 519 cm^{-1} and d) Histogram showing variation in percentage of occurrence of these phonon frequencies in the NCps grown with increasing deposition time from left to right.

Histogram shows that large distribution is present in occurrence of these frequencies indicating large size distribution in all NCps studied. However, there is a pattern observed with the deposition time. Occurrence of LF phonons (495 - 510 cm^{-1}) is highest for NCp E1 i.e. NCp grown with lowest time of deposition. This suggests that smaller size Si NCs have formed in large proportion in NCp E1. Occurrence of HF phonons (515 - 519 cm^{-1}) is highest for NCp E6 grown with highest time of deposition suggesting higher presence of larger size Si NCs. Further, the decrease in percentage of LF phonons with the increase in deposition time for NCps E1, E2 and E3 is observed. Whereas, occurrence of IF phonons increases with the increase in deposition time in these three NCps.

It is important to note that we have observed mainly two patterns of intensity profile for Raman images, performed on all NCps, 1) type-1: the intensity profile is nearly Gaussian (Fig. 3.4.1d: Raman image is generated using intensity of frequencies in the range 490 - 525 cm^{-1}) for most of these clusters (~ 60%) and 2) type-2: for some clusters, intensity is not maximum near the center of the cluster, but increases towards the edge (Fig. 3.4.3b). Type-1 intensity profile is noted in the cluster, wherein i) LF, IF, HF phonons and ii) only HF phonons are observed. However, type-2 intensity profile is observed only for HF phonons. Since, HF phonons show non-resonant behavior, intensity of HF phonons mainly reflects density of Si NCs. This suggests that density of clustered Si NCs for type-1 is higher at the center and decreases towards the edge of cluster i.e. of Gaussian nature, whereas, for type-2, density of Si NCs has non Gaussian profile.

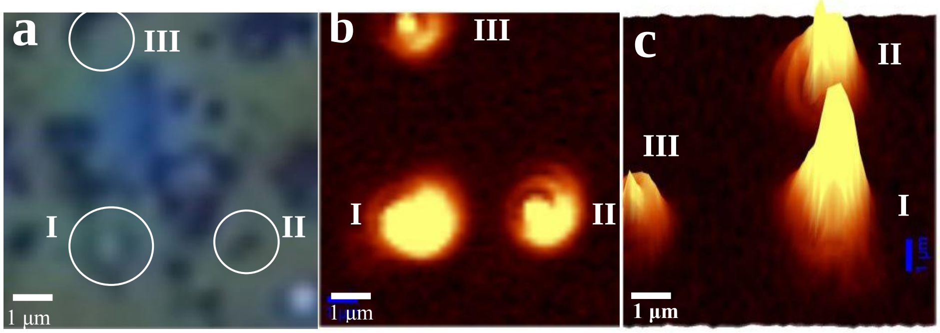

Fig. 3.4.3. a) Representative optical image of NCp E4, b) Raman image of selected area generated using frequency ~ 515 - 519 cm^{-1} and c) intensity profile of Raman image (rotated by 90^{0} showing the non-Gaussian form of intensity).

It is important to note that for type-1 Raman images, one to one correspondence with observable isolated structures in the optical image is seen (Fig. 3.4.1). However, this is not the case for type-2 Raman images, as detailed in the following. Representative optical (Fig. 3.4.3a) and Raman image (of marked area in optical image: Fig. 3.4.3b) shows that cluster I stand out from the background (visible) in the optical image as a white spot, whereas cluster II and III cannot be separated from the background (not visible). It may be noted that black spot observed at cluster II does not represent size and shape of Raman intensity profile and similar observations are made for all such measurements. Therefore, white structures in optical images are only considered as Si-SiO_2 clusters. Thus, one can say that absence of isolated structures in the optical image and non Gaussian intensity profile of a cluster in the corresponding Raman image is indicative of two dimensional (2D) clustering of Si NCs, since, it is difficult to imagine formation of three dimensional (3D) structures with largest density of Si NCs on the edge. AFM measurements are performed on all NCps to obtain further insight into the morphology of these multilayer NCps.

3.4.1.2. AFM mapping

Many sets of AFM and Raman mapping are performed on the same site with the help of visual guidance of the optical image, created using microscope as discussed in chapter 2. Representative data is shown in Fig. 3.4.4 for NCp E5. Fig. 3.4.4, shows the optical image, Raman image (Fig. 3.4.4b) and corresponding AFM image (Fig. 3.4.4c) of the area chosen (Fig. 3.4.4a) for AFM and Raman study. One can observe one to one correspondence in all three images noted above. Raman mapping shows formation of larger Si NCs, as only HF phonons are observed in these clusters. This suggests that the intensity observed in Raman mapping represent density of Si NCs in that particular cluster. The low resolution (300 Å) AFM image (Fig. 3.4.4c), shows presence of structures of height and width varying from 1 - 2 μm and 1 - 4 μm, respectively. Three dimensional intensity patterns observed in the Raman image and three dimensional AFM image shows formation of type-1 cluster that is 3D clustering of Si NCs. It is to be noted that there is one to one correspondence between intensity ratio in the Raman image (Fig. 3.4.4d) of two clusters (I/II ~ 1.08) and height ratio (I/II ~ 1.07) in the AFM image (Fig. 3.4.4e) confirming our interpretation of 3D clustering. Low resolution (300 Å: Fig. 3.4.4c) shows that all the four cluster are quite smooth. We have tried to perform higher resolution (30 Å) AFM mapping on the clusters, wherein, only HF phonons are observed. It does not give any additional information as it shows to be one big cluster with no smaller distinguishable structures.

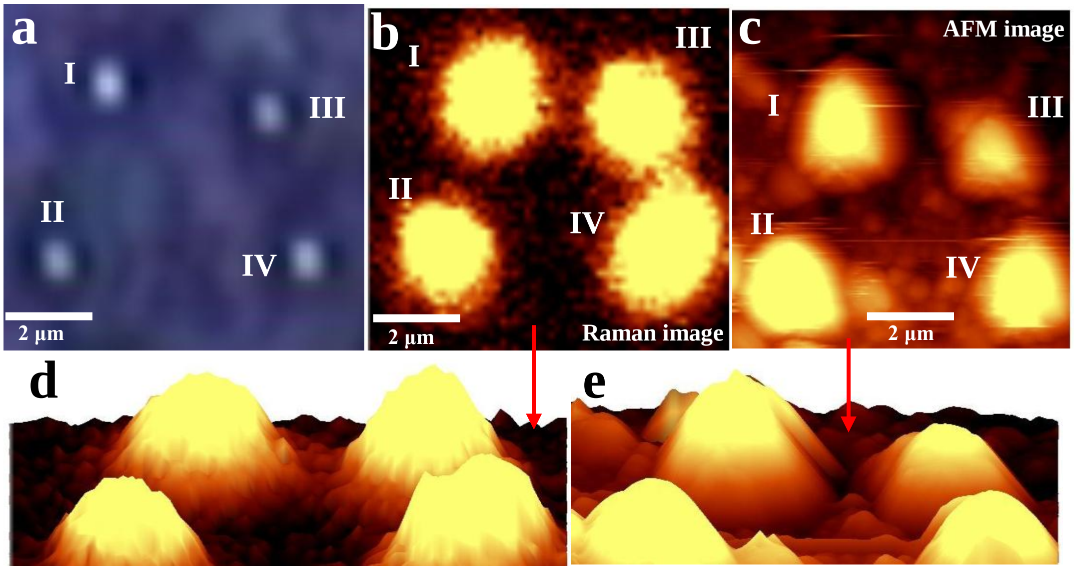

Fig. 3.4.4. a) Representative optical image of NCp E5, b) Raman image of selected area generated using frequency ~ 515 - 519 cm^{-1} and c) Corresponding AFM image, d) intensity profile of Raman image and e) 3D AFM image.

For type-2 clusters, we do not observe one to one correspondence in optical, Raman and AFM imaging (Fig. 3.4.5) in cluster size and intensity as observed for type-1 clusters. Optical image and corresponding Raman image (Fig. 3.4.5) shows that cluster I is of type-1 and cluster II is of type-2. Corresponding Raman spectra show presence of HF phonons in both the clusters

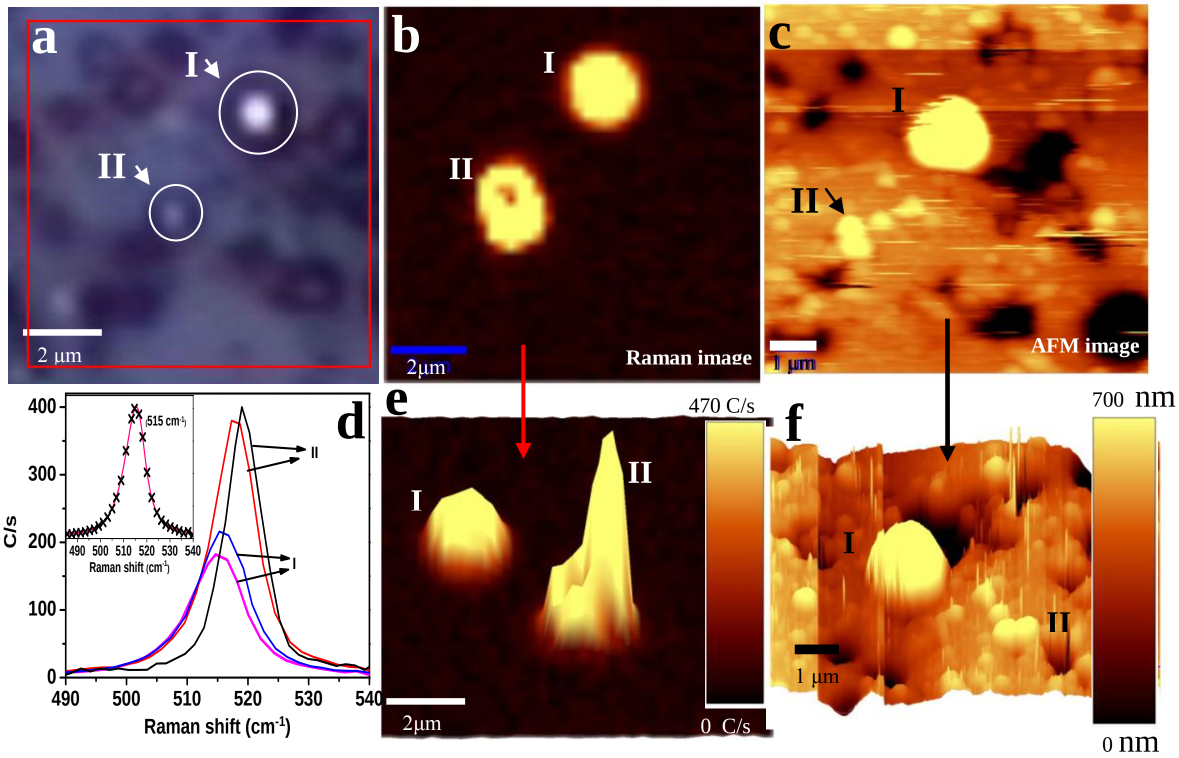

Fig. 3.4.5. a) Optical image of NCp E1, b) Raman image, c) Low resolution AFM image, d) Corresponding Raman spectra showing presence of HF phonons in both clusters, inset show asymmetric line shape fitting for phonon ~ 515 cm^{-1} using PCM, e) intensity profile of Raman image (rotated by 90^{0}) and f) 3D AFM image (rotated by 90^{0}).

(Fig. 3.4.5d). Further, maximum intensity for cluster II is ~ 1.7 times that of maximum intensity for cluster I (Fig. 3.4.5e). The ratio is similar to intensity of maximum intensity phonon of cluster II to cluster 1 ~ 1.65. AFM measurement performed on the similar region shows that cluster I is observable in the topography image, which is a consistent observation. However, for cluster II, intensity in the Raman image (Fig. 3.4.5b & e) is not matching with the topography (height ~ 0.2 μm) observed in the AFM image (Fig. 3.4.5c & f). Instead, segregation of small clusters is observed in that region. This suggests 2D organization of small clusters of Si NCs. Raman mapping in corroboration with AFM shows larger Raman intensity (Fig. 3.4.5e & f) in 2D cluster as compared to 3D cluster. In order to look into this, we have fitted the Raman spectra using phonon confinement model [153]. We find that asymmetric line shape of HF phonon (518 - 519 cm^{-1}) observed in type-2 (2D) cluster can be fitted using size ~ 9.5 nm with unperturbed width is ~ 6 cm^{-1}. Whereas, asymmetric line shape of HF phonon (515 - 516 cm^{-1}) observed in type-1(3D) cluster can be fitted using size ~ 7.5 nm with unperturbed width is ~ 8 cm^{-1}. This suggests presence of larger NCs with better crystalline quality in type-2 cluster leading to larger Raman intensity (Fig. 3.4.5c).

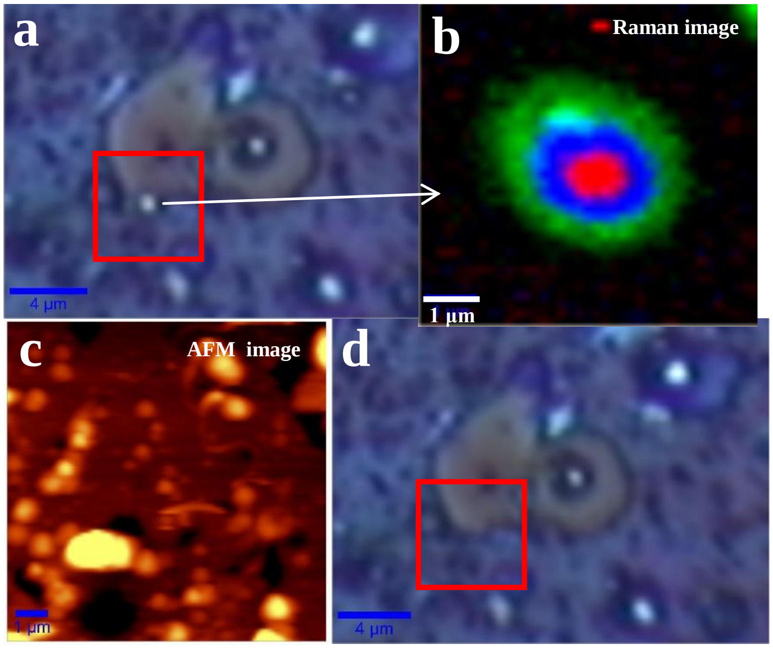

Fig. 3.4.6 a) Optical image, b) Raman image of marked area, c) corresponding AFM image of marked area and d) optical image of same area after performing AFM once showing absence of that cluster.

It is important to note that, we have attempted to perform AFM measurements for several sites on the cluster, wherein LF and IF phonons are also observed (Fig. 3.4.6). However, we find that while AFM measurements in non contact mode are in progress, it never gets completed as cluster gets physically removed from the site, as can be seen in the optical (Fig. 3.4.6a & d) and Raman image after the AFM (Fig. 3.4.6c). All the care has been taken to use fresh AFM tips, non-contact modes etc, but the same observation gets repeated. This indicates that these types of clusters are softer at the top and gets easily attached to the tip. This can happen if thicker part of the top is made up of amorphous SiOx matrix.

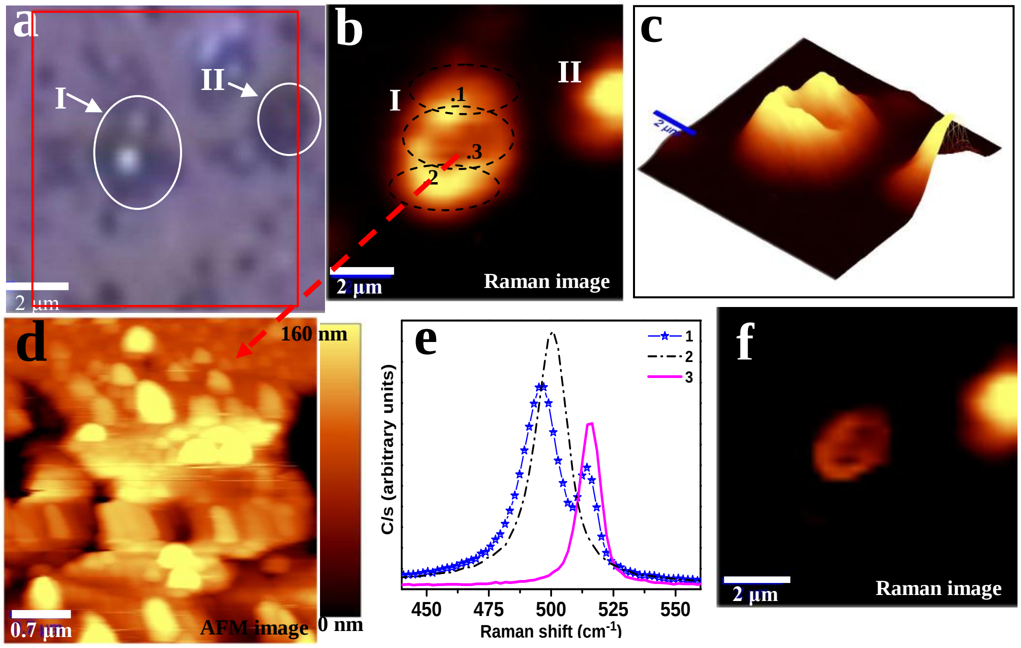

Fig. 3.4.7. a) Optical image of NCp E3, b) Corresponding Raman image, c) intensity profile of Raman image (rotated by 45^o)), d) High resolution AFM image at the center of cluster I (marked with arrow), e) Raman spectra at marked positions and f) Raman image of whole cluster I after performing AFM once.

Since we could not perform AFM on these clusters, wherein LF phonons are observed, we have performed high resolution (30 Å) AFM measurements on the two closely spaced clusters, wherein we have observed HF and simultaneous LF/HF phonons (Fig. 3.4.7a, b & e). This suggests presence of smaller and larger size Si NCs in close proximity. Three dimensional intensity profile in Raman image suggest that this is type-2 cluster (Fig. 3.4.7c). Higher resolution (30 Å) AFM measurement (Fig. 3.4.7d) is performed on this particular cluster, wherein HF phonons are observed (center of the marked cluster I in the Raman and optical image: Fig. 3.4.7 a & b). Topography image shows presence of smaller clusters of height varying from 0.07-0.16 μm. This confirms that this is a type-2 cluster. Further, when we tried to perform AFM in the region, wherein only LF phonons are observed (lower region of the cluster), this cluster gets physically removed except the part which shows presence of HF phonons (Fig. 3.4.7f: Raman image after performing AFM), as per our earlier observations.

Since, AFM could not performed, where LF phonons are observed, we performed Raman mapping with varying focal spot along the depth, which is also expected to confirm 2D and 3D formation of clusters of Si NCs as discussed below.

3.4.2. Understanding the morphology and it's origin

3.4.2.1. Raman mapping by varying focal spot along the depth

In Raman spectroscopic measurements at selected sites, we have noted change in phonon frequency, FWHM, line shape and intensity with change of focus (in z direction: depth), while optimizing the Raman signal. We investigate this in detail by performing Raman mapping by focusing the laser spot along the depth, in step size ~1.5 μm (Fig. 3.4.8 & 3.4.9). Fig. 3.4.8a, shows the optical image, Fig. 3.4.8b - d show Raman image at different focal spot along the depth and corresponding Raman spectra are shown in Fig. 3.4.8e - g. Highest intensity spectra are shown for different phonons (LF, IF and HF) in each image. The positions are marked where highest intensity is obtained and one can note that it changes laterally (in x-y plane) along the depth, suggesting three dimensional organization of Si NCs. In the first step, taking help from visual guidance of optical image, laser is focused at the top region of the film and Raman mapping is performed. Raman image shows presence of LF, IF and HF phonons (Fig. 3.4.8a). We observed that when the focal point is moved deep inside the cluster, i) at focal point ~ 1.5 μm below the surface: only IF and HF phonon are observed, ii) increase in intensity of HF phonon, iii) increasing in area where HF phonons are present and iv) when focal point is moved further below by ~ 1.5 μm, HF phonons are observed at the site of LF and IF phonons (Fig. 3.4.8). The observation that LF phonons (originating from smaller size NCs) are coming from upper region of the cluster, whereas HF phonons (originating from larger size NCs) are coming from deeper region and IF phonons (originating from intermediate size NCs) from the intermediate region of film, suggest stacking of different size of Si NCs, wherein smaller NCs are formed in upper region of the film and larger size NCs are present in deeper region of the film. This is consistent with the observation of higher intensity for HF phonons as we move down in the cluster. Herein, Raman mapping is performed with acquisition time of 0.5 s, where we observe Raman signal from crystalline Si only. However, Raman mapping performed with higher acquisition time of 10 s shows Raman signal from crystalline Al_2O_3 substrate too. This suggests that with lower acquisition time (0.5 s), only higher intensity Raman signal is being picked up, which show significant difference in Si optical phonons along the depth of a cluster. This can happen only if Si NCs are well separated along the depth. Further, our observation suggests that the stacking of large, intermediate and smaller size Si NCs from bottom to top are organized in pyramid like shape i.e. base is broad. Therefore, as the focal spot moves deeper in the cluster, Raman image of HF phonons becomes larger in lateral dimensions, as Raman signal from all larger Si NCs forming a base can be observed, however, for the focal spot at the top, only region consisting of larger scattering volume (high density of larger Si NCs) can give rise to observable Raman signal (HF phonon). Therefore, both focal spot and scattering volume together need to be considered for explaining the intensity profile in the Raman image.

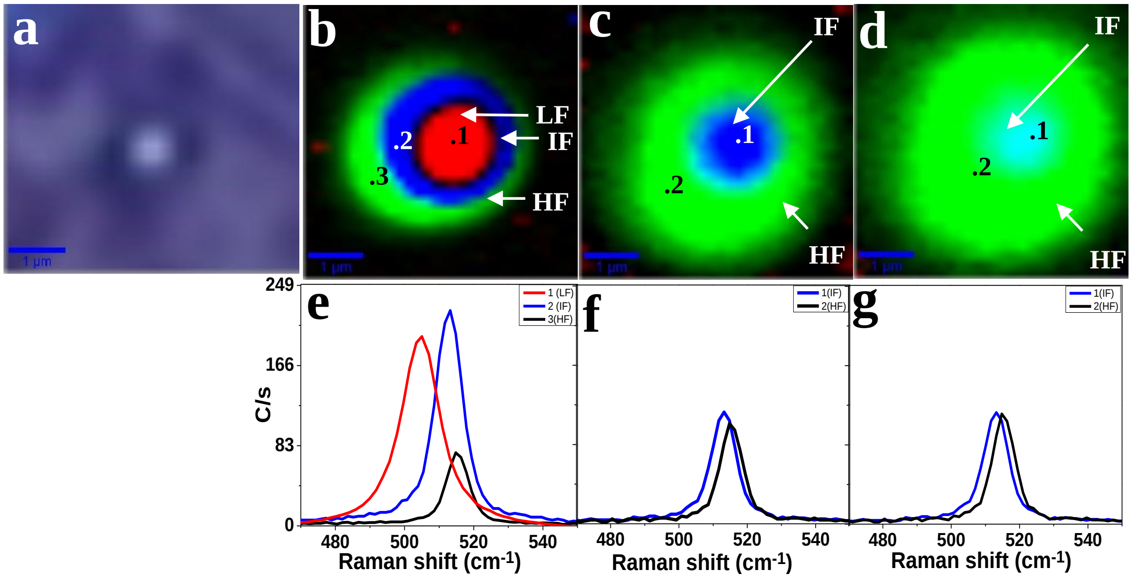

Fig. 3.4.8. a) Optical image of NCp E4, corresponding Raman image of marked area at the b) top, c) middle and d) bottom region of the chosen area observed by varying focal spot along depth. The green region shows HF phonons (515-519 cm^{-1}), Blue color shows IF phonons (511-514 cm^{-1}) and red shows LF region of frequencies (495-510 cm^{-1}). Fig. 3.4.8e-g shows Raman spectra for maximum intensity of observed LF, IF and HF phonons in Raman image b, c and d respectively. C/s for all the three spectra is shown in Fig. 3.4.8e.

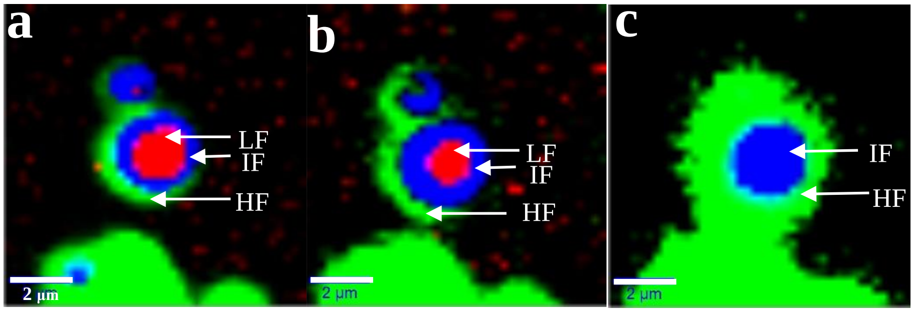

Fig. 3.4.9. Raman mapping, performed by changing focal spot along the depth, a) top, b) middle and c) bottom region of the cluster.

Raman mapping is also performed by changing focal spot along the depth in the region, where we have observed only HF phonons in type-1 clusters. Intensity profile of Raman image shows increase in size of Raman image (Fig. 3.4.10c) when the focal spot is moved to deeper region (1.5 μm) of the cluster (Fig. 3.4.10b), although there is no change in C/s. This suggests that in this case, clusters of larger Si NCs are organized in 3D. Further, moving focal spot deeper in the region, we observed decrease in C/s because of decrease in scattering efficiency.

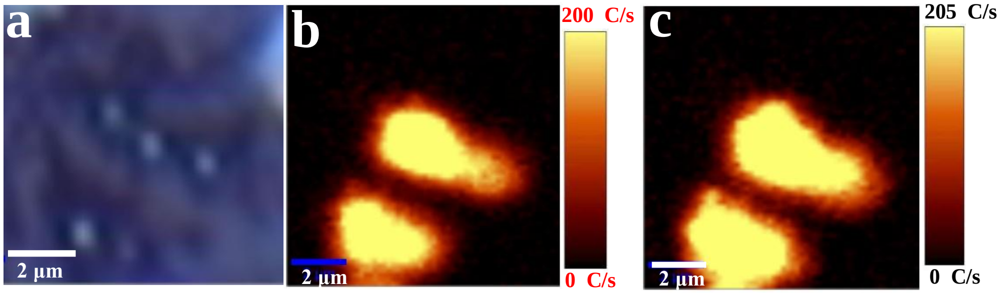

Fig. 3.4.10. a) Representative optical image of NCp E5 with corresponding intensity profile of Raman image b) at top and c) in the deeper region at step size of ~ 1.5 μm.

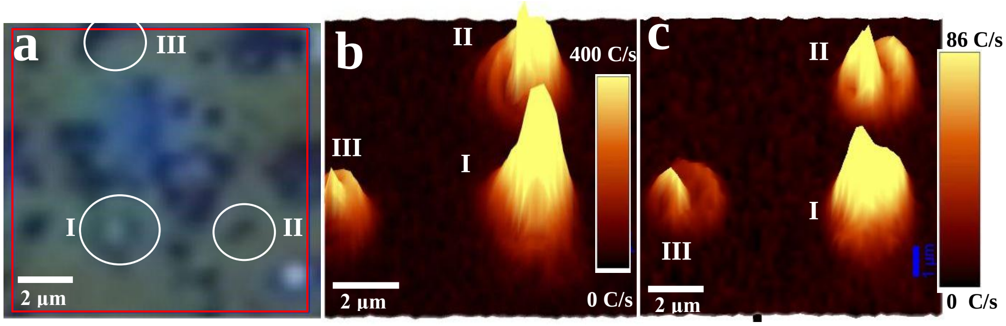

Fig. 3.4.11. a) Representative optical image of NCp E4, b) intensity profile of Raman image (rotated by 90^0) of selected area and c) intensity profile of Raman image (rotated by 90^0) performed at step size of ~ 1.5 μm.

Further, Raman mapping is also performed by changing focal spot along the depth in the region, where we have observed type-2 clusters. Intensity profile of Raman image shows decrease in C/s (Fig. 3.4.11c) when the focal spot is moved to deeper region (1.5 μm) of the cluster (Fig. 3.4.11b). This suggests the formation of small clusters of Si NCs in this case to be organized in two dimensions i.e. in plane.

Results obtained from Raman mapping with varying focal spot are consistent with observations and understanding developed using Raman and AFM mapping. These results show that Si NCs are clustered in i) smaller clusters (~ 100 nm), which are organized closely in two dimensions and ii) a big (~ 2 μm) three dimensional isolated cluster. This can also explain the discrepancy between the size of cluster observed in optical image and it's Raman image, as noted in sub subsection 3.4.2.1. Optical image is the fluorescent image (emission) created in the reflection mode. Thus, it may happen that we are able to observe fluorescence from only the surface of these clusters, whereas, emitted light from the bottom of the film/cluster is getting reabsorbed within the clusters. However, we are able to collect the Raman signal from the bottom of the cluster as well, leading to the larger Raman image (penetration depth ~ 3 - 5 μm, for 441.6 - 514.5 nm). These observations are repeated at several sites on all NCps. However, it is important to note that the size of cluster in Raman image is quite large from optical image for clusters, wherein, LF, IF and HF phonons are observed (Fig. 3.4.8 & 3.4.9) as compared to cluster showing only HF phonons (Fig. 3.4.10). Reason of this is discussed later.

To further understand the region of nanocomposite films, wherein small clusters (height ~ 0.3 - 0.6 μm) are seen in AFM and Raman signal for crystalline silicon could not be obtained (Fig. 3.4.4 & 3.4.5), longer acquisition time (5 s) mapping is performed. These measurements are performed at many sites on all the NCps. Representative Raman mapping is shown in Fig. 3.4.12. Raman image generated using phonon frequency ~ 515 - 525 cm^{-1} (Fig. 3.4.12a) and 465 - 495 cm^{-1} (Fig. 3.4.12b) shows two additional peaks, i) substrate related (crystalline Al_2O_3) phonon peak ~ 415 cm^{-1} over the whole mapping region (Fig. 3.4.12c) and ii) a broad asymmetric Raman spectrum ~ 480 cm^{-1} in the region where crystalline Si phonon peak is not observed (Fig. 3.4.12b), indicating presence of amorphous Si nanoparticles (NPs) in this region. Raman images of Fig. 3.4.12 suggest that there is Si throughout the film either in the form of clustered Si NCs or amorphous Si NPs dispersed in SiO_2 matrix.

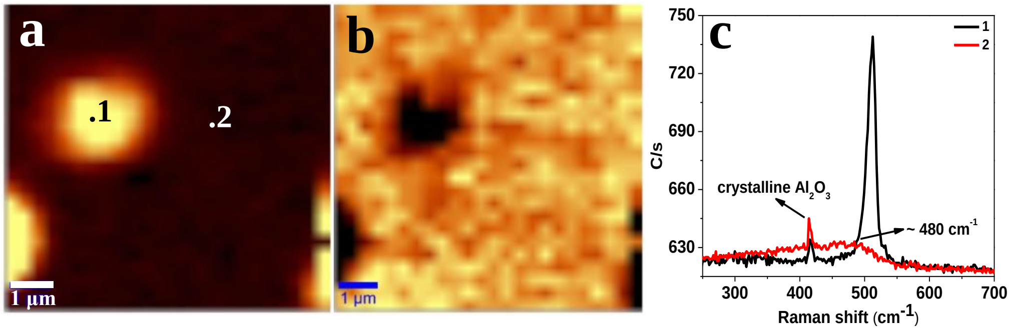

Fig. 3.4.12. Raman image generated using phonon frequency a) ~ 515 - 525 cm-1, b) 465-495 cm^{-1} and c) Raman spectra (acquisition time 5s) showing Si NC (marked as 1), amorphous Si (marked as 2).

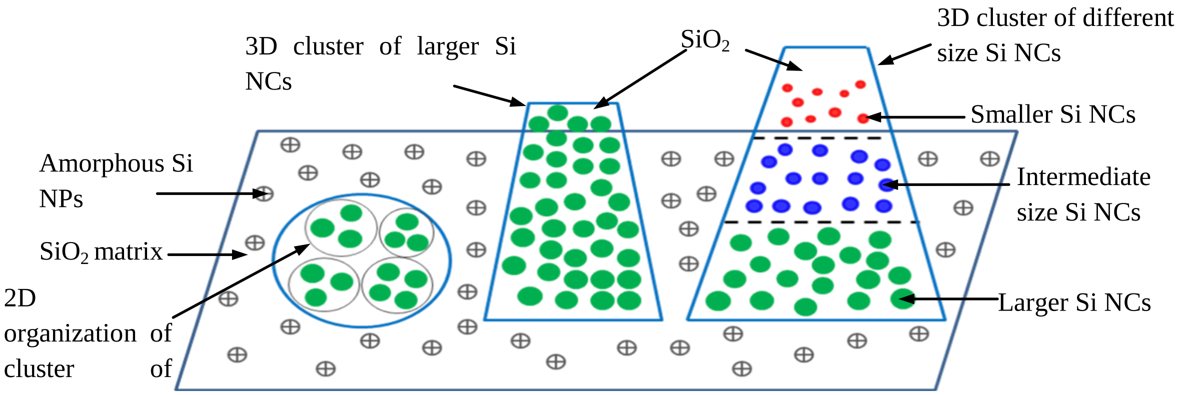

Fig. 3.4.13. Schematic of Si-SiO$_2$ nanocomposite film showing presence of 2D and 3D clusters of Si NCs embedded in SiO$_2$ matrix. Remaining film consist of amorphous Si NPs embedded in SiO$_2$. Line drawn in cluster showing stacking of different size Si NCs is guide to eye.

From the above discussion, we find that the grown NCp films have morphology as shown in the schematic (Fig. 3.4.13). Fig. 3.4.13 shows, organization of small clusters of Si-NCs in 2D (in plane) and big 3D clusters with different or same size Si NCs embedded in SiO_2 matrix. The rest of the film consists of amorphous Si NPs. The possible mechanism of these formations is discussed in the next sub section.

3.4.2.2. Formation of clusters of Si NCs embedded in SiO_2 matrix

It is quite intriguing to know that small clusters of Si NCs are closely organized in 2D or grows to become big 3D clusters, although the growth is carried out to be multilayer. To understand the origin of cluster formation of Si NCs in grown multilayer NCps, we have investigated single layer Si deposition on SiO_2 buffer layer (deposited on crystalline Al_2O_3 substrate with deposition time of Si-45 s). Raman mapping of single layer shows presence of crystalline Si only at particular sites (Fig. 3.4.14: structure marked with arrow). Further, as only HF phonons are observed it suggests presence of larger size Si NCs (> ~ 6 nm). Variation in Si phonon frequency and it’s line shape (asymmetric) in the structure (Fig. 3.4.14b & c) itself, suggests presence of different sizes of Si NCs in this structure/cluster. This suggests that clustering of Si NCs occurs in a single layer deposition itself. Raman mapping in corroboration with AFM performed at the same site show that cluster of type-1 with Gaussian intensity profile (Fig. 3.4.14e: size ~ 2.5 μm with height ~ 800 nm) are formed in a single layer. This indicates that it is intrinsic to basic growth mechanism of pulsed laser ablation (PLA). However, it is important to note that density of cluster observed in single layer deposition is much less then multilayer deposition, as observed by Raman mapping. It is important to note that in a single layer, size of cluster in optical, Raman and topography image is nearly same, whereas this is not the case for multilayer films as noted earlier.

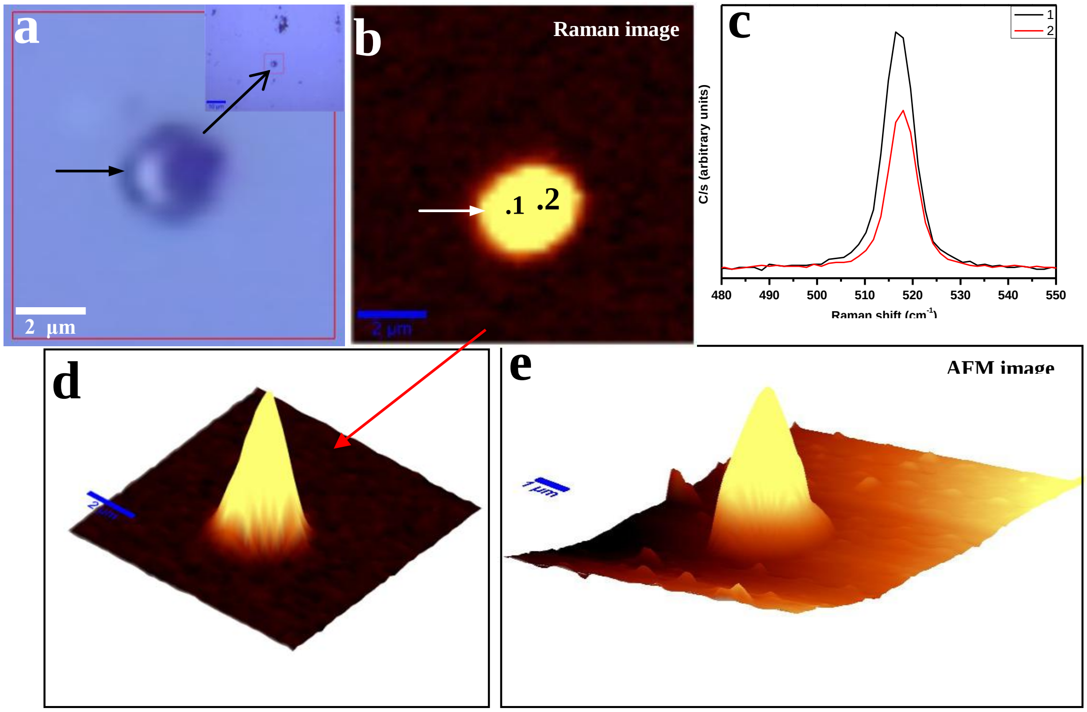

Fig. 3.4.14. a) Representative optical image of single layer of S-SiO$_2$, b) and c) corresponding Raman image and Raman spectra showing presence of HF phonons only, d) intensity pattern of Raman image (rotated by 90^0) and e) 3d AFM image (rotated by 90^0) showing one to one correspondence with Raman image.

Growth mechanism for the formation of NCs by PLA in the laser induced plume has been studied theoretically [246] as well as experimentally [247 - 252]. The size of NCs can be controlled by different laser parameters as fluence, wavelength, and pulse duration. In our case, Si-SiO$_2$ nanocomposites are grown by ablation of Si and SiO$_2$ targets, alternatively in PLD chamber using KrF laser beam (λ - 248 nm, pulse duration - 20 ns, repetition rate - 10 Hz) with a fluence of 2 J/cm^2. Crystalline Si particles of size ≥ 20 nm have been observed for these laser parameters, when deposition is performed in vacuum [248]. Further, the background gas pressure is also an important parameter, which influences the structure and morphology of the deposited material by affecting the collision rate of ablated species within the plume [249-252]. For similar laser, parameters, smaller particles (average size ~ 5 nm) have been obtained in the presence of helium background (~ 1 mbar) in the plume in gas phase and similar size particles condense and agglomerate on substrate [249-252]. Since, in the present case, growth is performed at background helium pressure of 10^{-1} mbar, Si NCs with size > ~ 6 nm can be formed in the ablated plume, which will get deposited at low energy sites on the substrate with buffer layer of SiO_2. Raman mapping (Fig. 3.4.14b & c) of single layer Si deposition on SiO_2 buffer layer shows variation in Si phonon frequency and it's asymmetric line shape suggesting that different sized Si NCs (6 -10 nm) are formed and clustered at particular sites. The fact that these Si NCs remained clustered without coalescence to form larger Si NCs even after annealing at 800 ^{o}C, suggests that they are indeed isolated by an insulating matrix of $SiO_{2.}$ This can happen if, SiO_2 buffer layer is being ruptured by high energy Si NCs during deposition, which is a finite possibility under these growth conditions. Thus, the cluster formation of Si NCs in SiO_2 surrounding may have been formed by embedding Si NCs from the plume. It is important to note that multilayer Si deposition leads to i) increase in density of clusters and ii) cluster arrangement in 2D and 3D and iii) observance of stacking of smaller (< ~ 4 nm), intermediate (~ 4 – 6 nm) and larger (> ~ 6 nm) size Si NCs. In multilayer deposition, increase in Si layers leads to increase in the density of Si NCs. Si NCs of forthcoming layer can either form another cluster on the existing cluster or they may find another low energy site to form another cluster at different spatial position. This can lead to three and two dimensional organization of clusters of Si NCs, respectively and increase in density of these clusters. In order to understand the third observation i.e. stacking of smaller, intermediate and larger Si NCs in descending order from top to bottom of the cluster, we have studied one unannealed multilayer NCp as the only possibility we could think of this stacking is due to annealing.

3.4.2.3. Study of growth mechanism leading to formation of smaller Si NCs

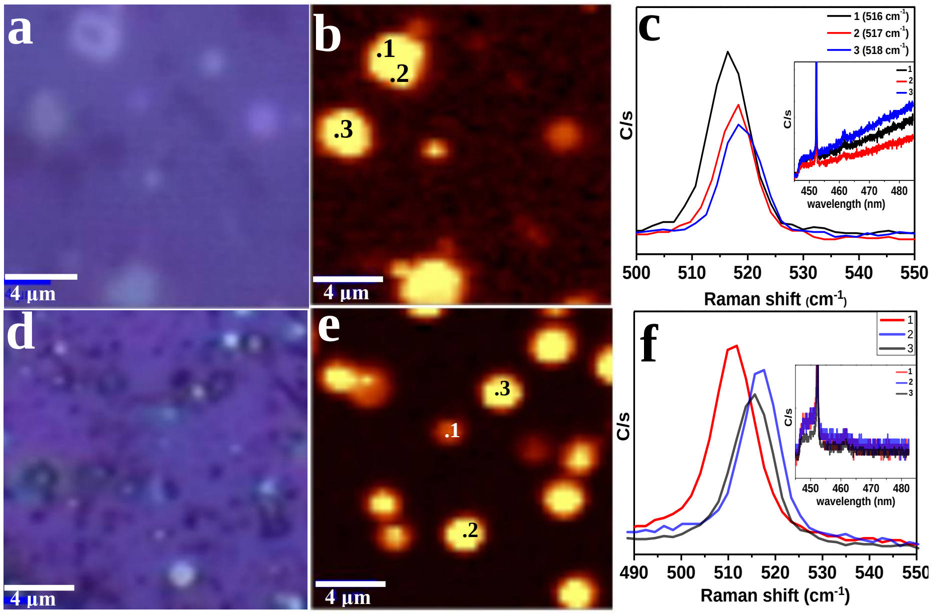

Fig. 3.4.15. a) Representative optical image of an unannealed NCp, b) and c) shows corresponding Raman image and Raman spectra, d) optical image of annealed sample e) and f) corresponding Raman image and Raman spectra. . Inset of Figure 3.4.15c & f shows full range spectra showing presence of defect PL in unannealed NCp.

Annealed (E2) and unannealed (E2U) NCps grown under same growth conditions (15 multilayers NCp with deposition time of Si is 90 s) are studied using Raman mapping. Raman mapping of an annealed NCp (E2) show observation of LF, IF and HF phonons suggesting presence of smaller, intermediate and larger Si NCs as noted above. However, Raman mapping of an unannealed (E2U) NCp (E2U), shows presence of Si phonon frequencies in the range ~ 516 - 519 cm^{-1} with FWHM ~ 8-10 cm^{-1} suggesting larger Si NCs with good quality are formed at room temperature itself (Fig. 3.4.15c). This is consistent with the understanding that Si-NCs are formed in plume itself, which then forms into clusters at low energy sites on the substrate. It is important to note that size of clusters observed in an unannealed NCp is quite large (5 - 6 µm) as compared to annealed NCps (1-2 μm). It is well known that clusters obtained in PLD are loosely bound clusters with dangling bonds, which can easily get separated on annealing, leading to smaller size clusters of Si NCs. Comparison of Raman mapping of an unannealed and an annealed NCp (Fig. 3.4.15c and Fig. 3.4.15f) show that after annealing at 800 ^{o}C, defect PL is significantly reduced (inset of Fig. 3.4.15f) compared to that of an unannealed NCp (inset of Fig. 3.4.15c), supports presence of dangling bonds in unannealed NCps. In an unannealed NCp, Raman signal corresponding to amorphous Si couldn't be observed in the rest of the region, due to the presence of large defect PL (inset of Fig. 3.4.15c) throughout the NCp, which is probably masking an amorphous Si Raman signal.

The above discussion suggests that room temperature PLD growth leads to formation of only larger Si NCs, whereas, annealing leads to formation of smaller and intermediate size Si NCs. Let us look at the possible reasoning for this. In the literature, we find that Stenger et al. have reported observance of simultaneously phonons ~ 500 cm^{-1} and 518 cm^{-1} from Si NCs (size ~ 4 nm : TEM), when SiOx is annealed at 1000 ^{o}C [136]. Li et al. have reported observance of Si phonon frequency ~ 495 cm^{-1}, when Si excess SiO_2 is annealed at 900 ^{o}C [118]. This suggests that higher temperature is required to form Si NCs from SiOx matrix because in the first step there will be formation of amorphous Si (~ 800 ^{o}C) and then crystalline Si (~ 1000 ^{o}C), whereas, in Si excess SiO_2, Si NCs are formed at relatively lower temperature. In our case, Si and SiO_2 are ablated alternatively, and thus it can be considered to be Si excess SiO_2. Therefore, there is a good possibility of formation of smaller size Si NCs in this case at lower temperature (800 ^{o}C). In a PLD chamber, heater is attached to the substrate holder, which means that the heat is getting transferred from bottom of the film to the top layer of the cluster. Further, SiO_2 being insulator, lesser heat will be transferred to the top of the cluster, suggesting that there is possibility of thermal gradient across the cluster. This thermal gradient can lead to formation of smaller size Si NCs at the top and intermediate size Si NCs in the middle of the cluster, leading to pyramid formation of different size Si NCs. Based on this understanding, absence of smaller size Si NCs in single layer Si deposition can also be correlated to presence of lesser amount of SiO_x at the surface i.e. there is not enough SiO_x to give rise to formation of different size Si NCs. Further, observance of smaller size Si NCs in annealed multilayer in some clusters can be correlated to presence of enough amount of SiO_x at the top in that particular clusters. This is consistent with the fact that AFM measurements are not possible for clusters showing LF phonons as noted above. This is also consistent with our attribution of LF phonons to be originating due to Si-O bonding environment at the surface of small Si NCs. This understanding further, explains the difference between size of cluster in Raman and optical image for stacking of i) smaller, intermediate and larger size Si NCs from bottom to top (Fig. 3.4.8 & 3.4.9) and ii) only larger Si NCs (Fig. 3.4.10). In the first case, presence of significant amount of $SiO_{x,}$ reabsorb light emitted from the bottom of the cluster leading to huge difference in optical and Raman image. Whereas, in the second case, lesser amount of SiOx is present and thus lesser emitted light will be reabsorbed. Therefore, comparatively lesser difference in size of cluster in Raman and optical image is observed.

Effect of annealing is also further studied for ten multilayer Si-SiO_2 NCps, annealed at different temperature (un annealed, 200 ^oC, 400 ^oC, 600 ^oC and 800 ^oC). All other growth conditions are kept same. Raman mapping is performed on these NCps, which shows that LF, IF and HF phonons are observed only in NCp annealed at 800 ^oC, whereas, in all other NCps, we could observe only HF phonons. Representative Raman mapping is shown for unannealed NCp

(E11: Fig. 3.4.16) and annealed at 400 ^{o}C (E13: Fig. 3.4.17). This supports our interpretation discussed above.

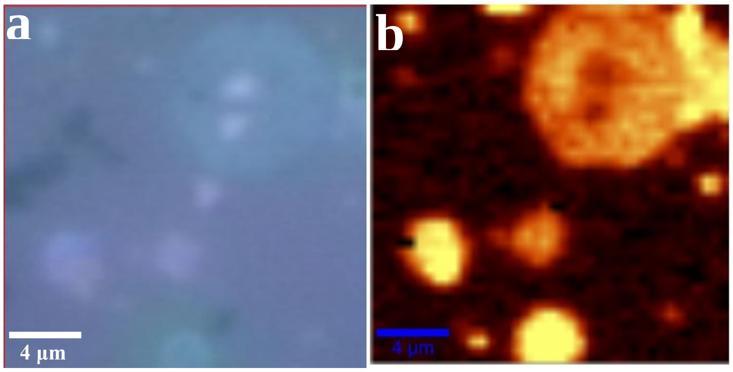

Fig. 3.4.16. a) Optical image and b) corresponding Raman image of unannealed Si-SiO$_2$ NCp shows presence of larger clusters.

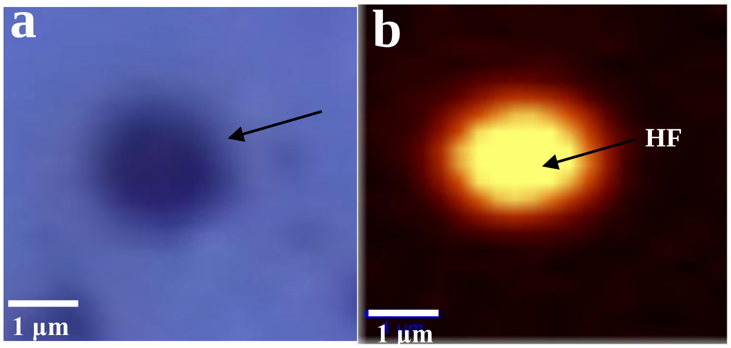

Fig. 3.4.17. a) Optical image and b) corresponding Raman image of Si-SiO$_2$ NCp annealed at 400 ^{o}C shows presence of smaller clusters.

To summarize, Raman mapping and AFM together are used to investigate and understand the morphology of Si-SiO$_2$ multilayer nanocomposites. Raman and AFM mapping together showed formation of different types of clusters of Si NCs in size and stacking in pulsed laser deposited Si-SiO$_2$ NCps. Further study of specially grown Si-SiO$_2$ NCps suggest formation of smaller Si NCs at the top due to annealing at 800 ^{o}C in Si rich SiO$_2$ and possible existence of thermal gradient in an insulating matrix of SiO_2. Whereas, larger Si NCs are formed in plume itself.

Thus, Raman mapping in corroboration with AFM has been used successfully to understand and describe the morphology of PLD grown Si-SiO_2 nanocomposite films. It is however, important to note that one needs to have proper understanding of the Raman spectra, in order to correlate it with AFM data in order to obtain unique information about the morphology of these nanocomposites, which is difficult to obtain by any other conventional techniques.

3.5. Size dependent interface bonding of Si nanocrystals: corroboration of Raman mapping and XPS study

In this section, we aim at establishing quantitative corroboration between Raman mapping and XPS studies for Si-SiO_2 NCps. In previous sections, we have attributed LF (495 - 510 cm^{-1}) phonons to vibration of Si-Si bonds at the surface of Si NCs in presence of oxygen in Si-SiO_2 NCps. Since, Raman spectroscopy is an indirect technique to study surface/interface, it is important to obtain similar information, independently using another experimental method. We have chosen to study size dependence of surface/interface for Si-SiO_2 NCps using XPS, as this has already been established for obtaining size dependent information of Si NCs in Si-SiO_2 NCps [225]. For Si-SiO_2 NCps, it has been predicted theoretically that for smaller Si NCs, Si=O bond forms at the interface leading to formation of Si^{3+} suboxides [222]. Further, increase in size of Si NCs leads to formation of only Si-O bonds leading to formation of Si^{2+} [222]. Thus, the flexibility of oxygen in establishing different coordination states at the surface of Si NCs can lead to variation in the Si–O bonds at the surface, which can be probed using XPS, wherein one measures the binding energy of core electron (photoelectric effect), which is sensitive to the bonding environment. For example, change in oxidation state (positive) of an element reflects in the change in binding energy (increase) of that element due to change in interaction of core electron and nucleus. However, it is important to note that the beam size in XPS (~ 1 cm x 1 cm) covers the full NCp and therefore, an average signal from XPS measurement needs to be corroborated with the statistical information obtained from the Raman mapping data. In order to do this, we choose those NCps which show contrast in Raman mapping results and thus results can be effectively corroborated with the XPS results. In this section, we have used Raman mapping in corroboration with absorption and XPS to study Si-SiO_2 i) 15 multilayers (E1-E6), ii) 10 multilayer (E7 (top layer SiO_2) and E8 (top layer Si)) and iii) single layer (Si/SiO_2: E9 (top layer Si) and E10 (top layer SiO_2)) nanocomposite film grown on crystalline Al_2O_3 substrate using PLD.

3.5.1. Corroboration of Raman mapping and XPS

Correlation of Raman mapping results and XPS data has been presented for NCp E1 and E7 in section 3.2. In the present section, we will study one to one correspondence between Raman mapping and XPS for all the NCps noted above. Further, results of XPS are corroborated with the understanding developed for observed morphology of these NCps.

3.5.1.1. Comparison in abundance of LF and IF phonons

i) E1- E6 Si-SiO_2 NCps (15 multilayer)

Raman image is generated using intensity of frequencies in the range 490 - 525 cm^{-1}. Representative Raman image is shown for NCp E4 (Fig. 3.5.1a). Raman mapping of NCps E1-E6 suggest abundant presence of smaller Si NCs in all the NCps (LF phonons). The percentage occurrence of LF phonons in these NCps (E1-E6) is summarized in histogram given in Fig. 3.5.8. Further, density of smaller Si NCs is less in NCp E6 as compared to other NCps. This is further investigated using XPS. XPS spectra of Si 2*p* core-level for E1-E6 NCps (Fig. 3.5.1) are fitted using Gaussian-Lorentzian line shape profile after standard linear background subtraction using XPS peak fit software [206]. The XPS spectra of Si-SiO_2 NCps are fitted by fixing the peak values of Si^0, Si^{1+}, Si^{2+}, Si^{3+} and Si^{4+} states at binding energy (B.E.) ~ 99.8, 100.5, 101.4, 102.4, and 103.4 eV, respectively, keeping intensity and width as variable parameters [225]. Fig. 3.5.1 shows XPS spectra of NCps E1 (Fig. 3.5.1b), E4 (Fig. 3.5.1c) and E6 (Fig. 3.5.1d). We find that the XPS spectra of NCps E1, E4 and E6 need to be deconvoluted into three chemical structures corresponding to Si^{4+}, Si^{3+} and Si^{2+}. Further, intensity (I) of Si^{3+} component is greater than Si^{2+} component (Fig. 3.5.1). The theoretical prediction that Si^{3+} suboxide is formed at the interface for smaller Si NCs [222] is also confirmed experimentally using XPS by Kim et al. [225]. Further, increase in size of Si NCs leads to observance of Si^{2+} (intermediate size) and Si^{1+} (larger size) suboxides. This suggests that higher ratio of Si^{3+} component as compared to Si^{2+}

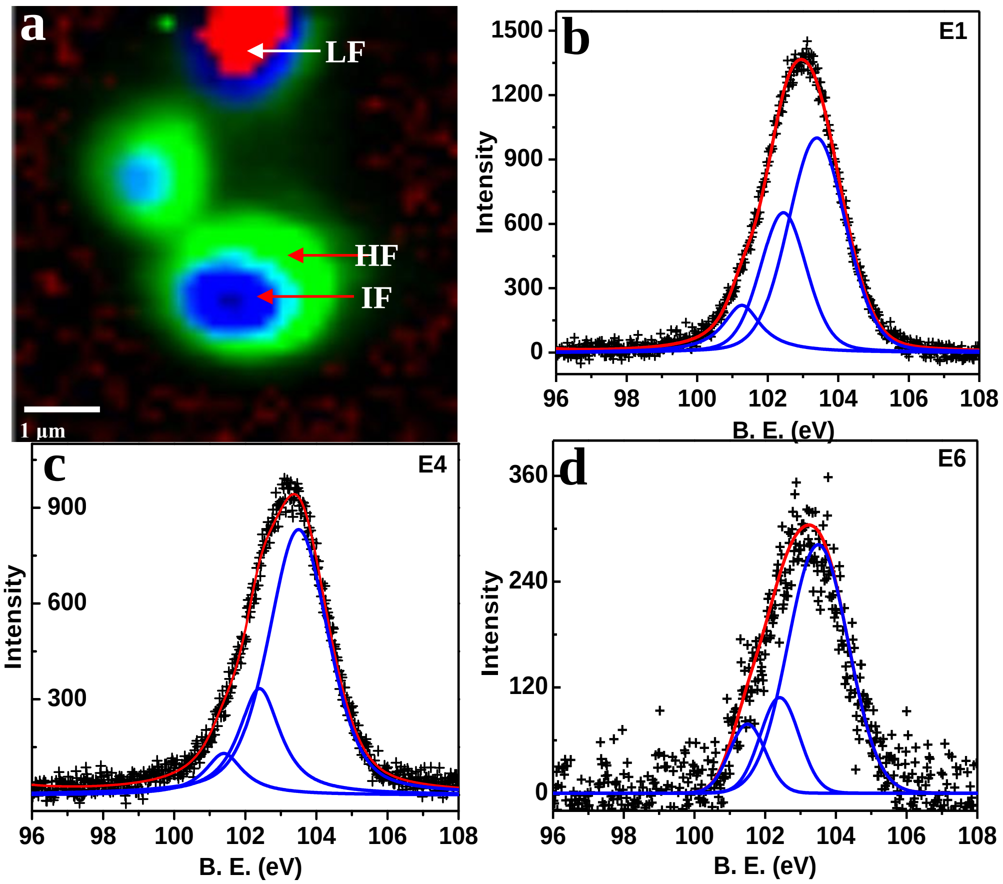

Fig. 3.5.1. a) Raman image showing LF, IF and HF phonons. XPS spectra of NCps b) E1), c) E4 and d) E6 shows difference in total intensity. Solid line (red color) is total fit to the raw data (+). Separate components are shown with blue line.

and/or Si^{1+} correspondence to smaller Si NCs. Higher ratio of Si^{2+} component correspondence to intermediate size Si NCs, whereas, higher ratio of Si^{1+} component correspondence to larger Si NCs. In our case, relative intensities (I) of Si^{3+} and Si^{2+} i.e. $I(Si^{3+})/I(Si^{2+}) > 1$ for NCps E1 - E5. Relative intensities of Si suboxide states are summarized in Fig. 3.4.8 for all NCps studied. This result is in agreement with the Raman mapping (Fig. 3.5.8), which shows abundant occurrence of LF phonons in all these NCps. It is interesting to note that $I(Si^{3+})/I(Si^{2+}) \sim 2.6$ for NCps E1-E5, whereas, for NCp E6, this ratio is ~ 1.8 suggesting decrease in number of smaller Si NCs. This is also in agreement with Raman mapping results (Fig. 3.4.2 & Fig. 3.5.8).

It is important to note that the total intensity of XPS spectrum decrease with the increase in deposition time of Si (Fig. 3.5.1b-d), indicating that total number of electrons reaching the detector decrease from NCp E1 to E6. In previous section, we have discussed the morphology of these NCps and showed that Si NCs are not homogenously distributed; instead they are clustered together at particular sites. Further, density of clusters increases with the increase in number of Si layers. This suggests that increase in deposition time of Si also leads to increase in density of Si NCs. Therefore, there is possibility that presence of clusters of Si NCs leads to scattering of electron from nearby surface and therefore we are not able to collect the signal from the whole surface, which is leading to decrease in intensity of XPS spectra from NCp E1 to E6.

ii) E7: Si-SiO_2 NCp (10 multilayers: SiO_2 as top layer)

Raman mapping of NCp E7 also shows clusters of Si NCs (Fig. 3.5.2). Further, Si phonon frequencies (495 - 519 cm^{-1}) in Raman spectra suggest formation of small, intermediate and large size Si NCs in this NCp too. These observations are consistent with the understanding developed from NCps E1-E6. It is important to note that, using 441.6 nm excitation, we have only observed IF phonons in the region where LF phonons are observed using 514.5 nm excitation. This suggest conversion of LF phonons to IF phonons. This is further checked by repeating the Raman mapping using 514.5 nm excitation (Fig. 3.5.2e) and we find that only IF and HF phonons are observed in the same cluster. This suggests that using 441.6 nm excitation, laser irradiation has lead to conversion of LF phonon to IF phonon i.e. easy manipulation as discussed in previous section.

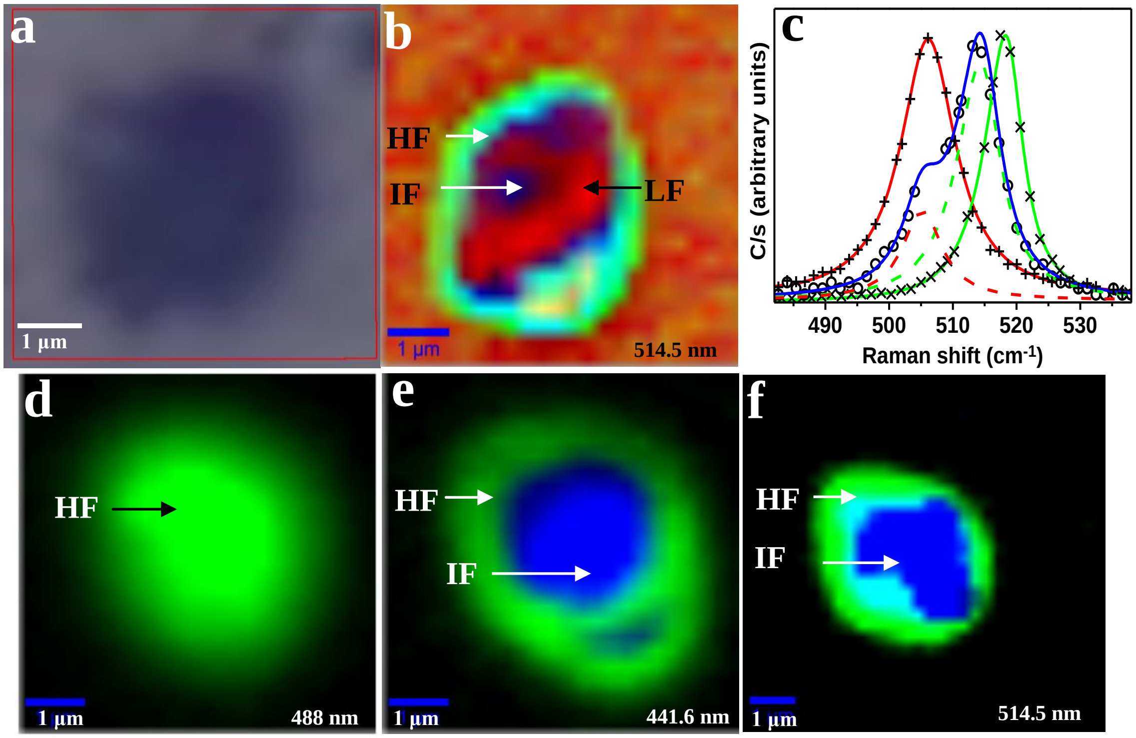

Fig. 3.5.2. a) Optical image of NCp E7, corresponding Raman image with excitations, b) 514.5 nm and c) Raman spectra showing LF, IF and HF phonons with 514.4 nm excitation. Raw data is shown with symbol and Solid line fit to the data. Raman image with excitations d) 488 nm and e) 441.6 nm and f) Raman image again created using 514.5 nm excitation.

Mainly three differences are observed in NCp E7 as compared to NCp E1-E6: 1) Rare presence (5%) of LF and IF phonons, although in the region where LF phonons are observed, percentage of occurrence of LF phonons is quite high (Fig. 3.5.2b), 2) Wavelength dependent

Raman mapping in corroboration with absorption spectroscopy suggests that LF and IF phonons are observed with laser wavelength of 514.5 and 441.6 nm (Fig. 3.5.2) and 3) Absence of Raman signal due to amorphous Si in the remaining region of NCp. This NCp is further investigated using XPS.

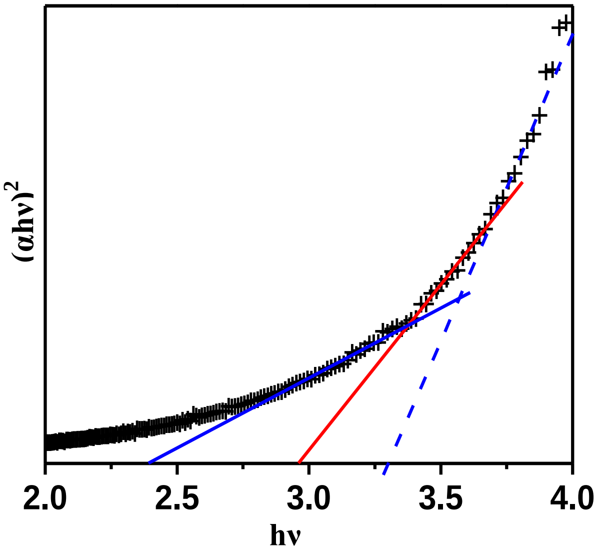

Fig. 3.5.3. $(\alpha h\nu)^2$ vs (hν) showing different band edges in NCp E7.

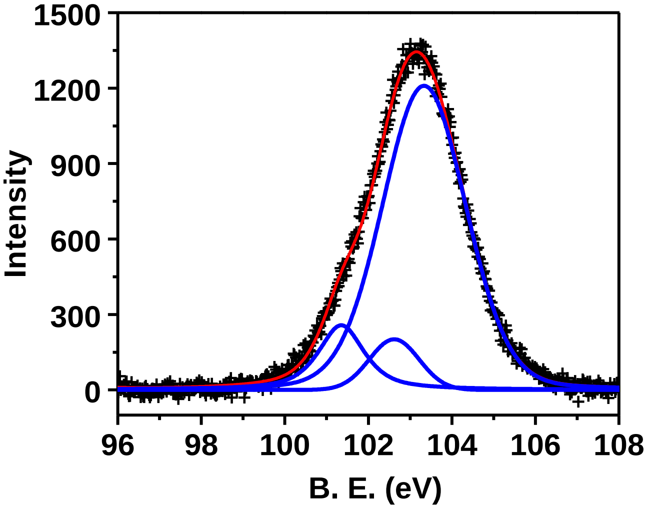

Fig. 3.5.4. XPS spectrum of NCp E7 showing presence of different suboxides. Solid line (red color) is total fit to the raw data (+). Separate components are shown with blue line.

By deconvoluting XPS spectrum of NCp E7, we find that three chemical structures corresponding to Si^{4+-2+} are observed in this NCp too (Fig. 3.5.4). Presence of Si^{3+} and Si^{2+} component in NCp E7 suggests presence of smaller and intermediate size Si NCs. However, $I(Si^{3+})/I(Si^{2+})$ ~ 0.6 for NCp E7, which is quite less, unlike higher ratio observed in NCps E1-E6. Therefore, XPS measurement on NCp E7 shows lesser intensity of Si^{3+} component, which in turn suggests lesser content of LF phonons in this NCp. This further suggests rare presence of smaller Si NCs as compared to NCps E1-E6, which is consistent with the observation of Raman mapping.

3.5.1.2. Comparison in presence of IF and HF phonons

i) E8: Si-SiO_2 NCp (10 multilayers: Si as top layer

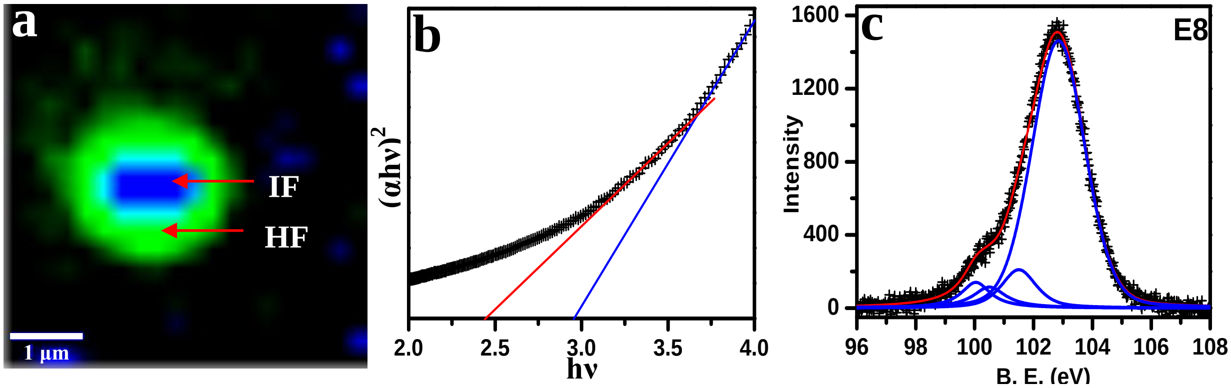

Fig. 3.5.5. a) Raman image showing presence of only IF and HF phonons, b) $(\alpha h\nu)^2$ vs (hν) showing different band edges and c) XPS spectrum of NCp E8. Solid line (red color) is total fit to the raw data (+). Separate components are shown with blue line.

Raman mapping of NCp E8 (Fig. 3.5.5) also show cluster of Si NCs at some places only as noted for NCps E1-E7. However, Raman mapping of NCp E8 shows Si phonon frequencies only in the range 510 - 519 cm^{-1}. This suggests that lowest frequency that can be observed in this NCp is ~ 510 cm^{-1}. This suggests presence of only intermediate and larger size Si NCs. Further, wavelength dependent Raman mapping shows observance of IF phonons only with laser wavelength of 514.5 nm. This is also supported with absorption spectroscopy, which shows observance of band edges ~ 2.43 eV and ~ 2.95 eV. The observed differences are understood to be due to the difference in top layer (Si), unlike in other NCps, wherein top layer is SiO_2 (E1-E7). In previous section, we have discussed the possibility of formation of smaller Si NCs in Si excess SiO_x (top layer: SiO_x) at 800 ^oC, which leads to observation of LF phonons (495 - 510 cm^{-1}). Observance of only IF and HF phonons in NCp E8 (top layer: Si) is consistent with this understanding of formation of smaller Si NCs in Si excess SiO_x. Absence of smaller Si NCs is further investigated using XPS. By deconvoluting XPS spectra of NCp E8, we find four chemical structures corresponding to $Si^{0-2+,4+}$ are observed (Fig. 3.5.5c). As we have noted above that Si^{3+} suboxides is observed for smaller size Si NCs, whereas, increase in size of Si NCs (intermediate and large size) leads to formation of only Si-O bonds leading to observance of Si^{2+} and Si^{1+} suboxides [225]. Presence of only Si^{1+} and Si^{2+} components in NCp E8 suggests absence of smaller Si NCs and presence of only larger and intermediate size Si NCs, respectively. This is also consistent with Raman mapping results, which show presence of only IF and HF phonons. Further, observance of Si^0 (~ 100 eV) is expected as the top layer is Si in this NCp. It is important to note that the observed B.E. for Si^0 is higher as compared to reported one (~ 99.78 eV). This positive shift in B.E. of core electron can be understood using it’s correlation with Si-Si bond length. For a given Si atom, the elongation of it’s bond length leads to decrease in local electron density at the center of the bond, which results in repulsion between electrons (valence and core electrons) of Si atom leading to higher B.E of core electrons. This suggests tensile strain in this NCp and is consistent with the tensile strain observed for intermediate size Si NCs as discussed in section 3.3.

ii) Monolayer Si-SiO_2 NCp: E9 (top layer: Si) and E10 (top layer: SiO_2)

Raman mapping for NCp E9 (Fig. 3.5.6) shows presence of clusters of only larger size Si NCs in both the NCps, as only HF phonons are observed. Sizes of silicon NCs that we have obtained from line shape fitting are ~ 9 nm. Observance of only HF phonons in wavelength dependent Raman mapping is well matching with the absorption spectra as we have observed band edge ~ 3 eV in $(\alpha h\nu)^2$ against (hν). We have discussed the Raman mapping of NCp E9 in previous section. Similar observations are made for NCp E10 (Fig. 3.5.7) i.e. cluster formation of larger Si NCs and observation of band edge ~ 3 eV in $(\alpha h\nu)^2$ against (hν). Further, in these two NCps also, we do not observe any signal due to amorphous Si.

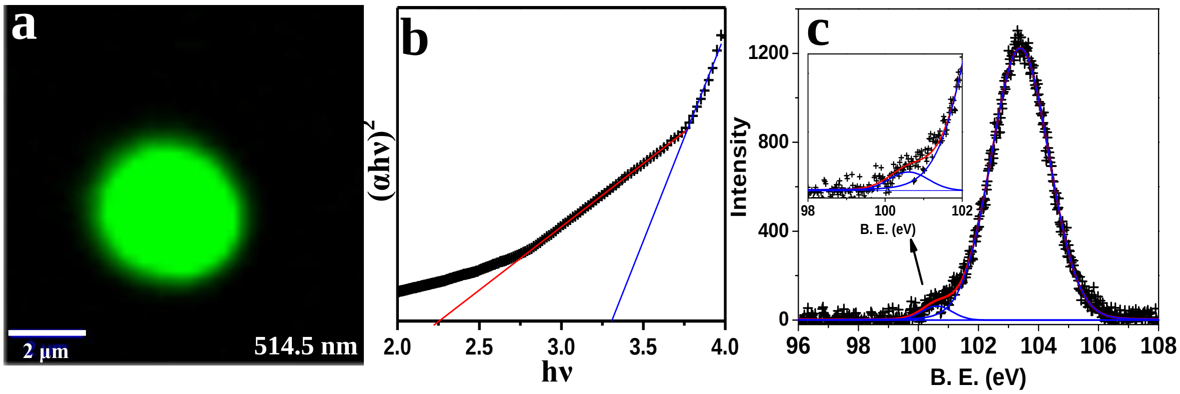

Fig. 3.5.6. a) Raman image with excitation source as 514.5 nm, b) $(\alpha h\nu)^2$ vs (hν) plot showing different band edges and c) XPS spectrum. Solid line (red color) is total fit to the raw data (+). Separate components are shown with blue line. Inset is shown for clarity of peak.

Deconvolution of XPS spectra for NCps E9 (Fig. 3.5.6c) and E10 (Fig. 3.5.7c) show chemical structure corresponding to $Si^{4+,1+}$ and Si^{4+}, respectively. Observance of Si^{1+} suggests presence of larger Si NCs in E9 NCp. Intensity of this component is quite less, which is expected as the density of Si clusters in single layer Si deposition is quite less compared to multilayer Si deposition as observed in Raman mapping. Further, we have only observed Si^{4+} component in NCp E10 as top layer is SiO_2 in this NCp.

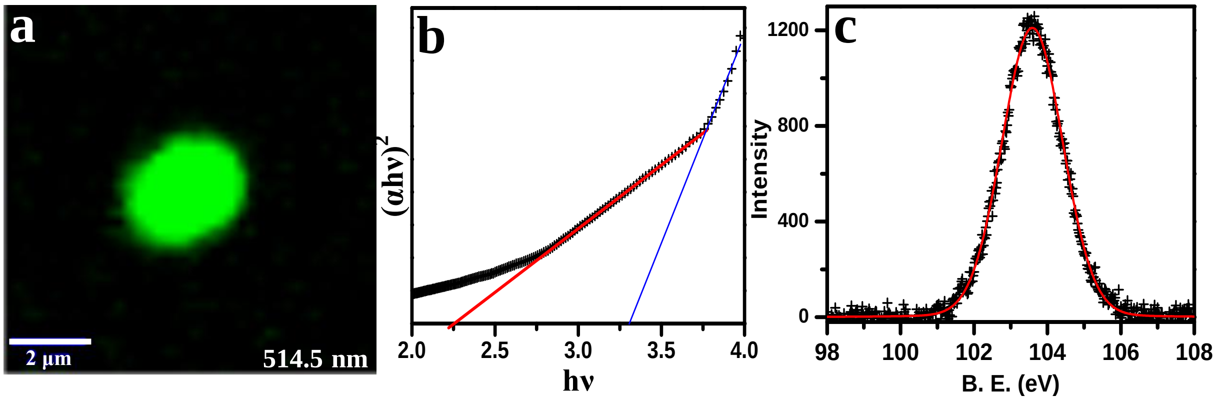

Fig. 3.5.7. a) Raman image with excitation source as 514.5 nm, b) $(\alpha h\nu)^2$ vs (hν) plot showing different band edges and c) XPS spectrum. Solid line (red color) is total fit to the raw data (+).

Raman mapping of NCps E7 - E10 shows absence of amorphous Si. These NCps are grown at different time with same growth parameters that were used for NCps E1 - E6, earlier. These differences observed may be related to higher laser power due to freshly filled laser.

3.5.2. Correlation of size and interface: Raman, absorption and XPS spectroscopy

One to one correspondence obtained between Raman mapping and XPS for all the NCps is presented as histogram in Fig. 3.5.8. Observed band edges are also noted for each sample in the histogram.

3.5.2.1. Correlation of band gap with size and interface

This histogram clearly suggests observance of Si^{2+} and Si^{3+} suboxide components with higher intensity in XPS, corresponding to higher content of IF and LF phonons in Raman mapping, respectively. Therefore, XPS results independently confirm our attribution of LF phonons to be originating from surface/interface of Si NCs in SiO_2 matrix. Further, corroboration of Raman mapping, absorption spectra and XPS for NCps E1-E10 suggests that direct band gap (edge) ~ 2.8 and 2.95 eV can be correlated to presence of smaller (< ~ 4 nm) and intermediate (~

<4 & < 6 nm) size Si NCs, respectively (Fig. 3.5.8). Since, Bohr exciton radius of Si is ~ 4.3 nm, strong and weak confinement of electrons is expected in smaller and intermediate size Si NCs, respectively. Based on the confinement of electron, expected direct band gap of Si NCs of size ~ 1 nm, 4 nm, 6 and 10 nm are calculated to be ~ 4.5 eV, 3.19 eV, 3.14 eV, 3.11 eV, respectively (bulk Si E_1 ~ 3.1 eV). However, our observation of lowering of this E_1 gap for smaller and intermediate size Si NCs is rather intriguing. In this regard, lowering of direct band gap in Si NCs is understood to be due to presence of oxygen in the matrix. Further, our result in corroboration with these calculation, thus suggest that it is not just the oxygen bonding but the bonding environment (Si-O or Si=O) also influence critically the direct band gap of Si-SiO_2 NCp. Thus, direct band gap for hydrogenated Si NCs follows the electron confinement, in which the diameter of NC is the principal quantity, whereas, in oxygen passivated Si NCs, both confinement and oxygen bonding environment play important roles. The type of oxygen bonding itself depends on the size of Si NCs and hence, absorption spectra, XPS and RM data can be well correlated to size of Si NCs in Si-SiO_2 NCps. Thus, systematic study of Si-SiO_2 NCps performed

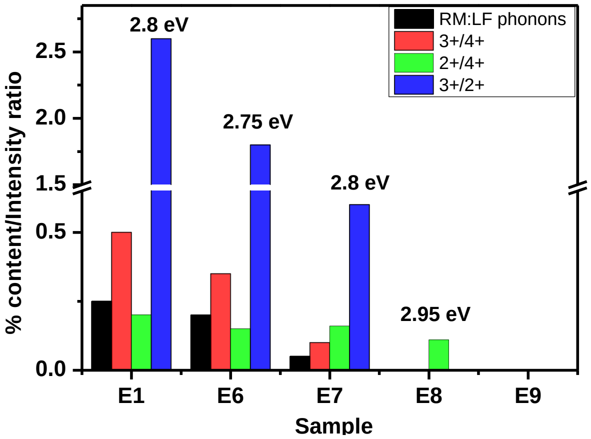

Fig. 3.5.8. Histogram comparing Raman mapping, absorption and XPS results.

using Raman mapping in corroboration with absorption and XPS spectroscopy has established the size dependent surface/interface of Si nanocrystals and it's implication on the band gap in these NCps.

3.5.2.2. Correlation of XPS with formation mechanism of nanocomposites

It is important to note that the escape depth of electron is nearly ~ 5-10 nm i.e. electrons present in 5 nm of surface will give rise to XPS signal. These NCps have ~ 20 nm thick SiO_2 layer deposited at the top, which is large as compared to escape depth of electron. This raises question on how we get such a good one to one correspondence of XPS with statistical information from Raman mapping data. In previous section, we have discussed the morphology and the plausible growth mechanism of Si-SiO_2 NCp, wherein Raman mapping of un-annealed and annealed NCps suggests formation of smaller Si NCs in Si excess SiO_2 at the top region. This understanding is also supported by absence of LF phonons in NCp E8 (Si top layer). Therefore, we are able to collect signal from interface of smaller Si NCs, because smaller Si NCs are formed at the top in the SiOx layer. This explains one to one correspondence between XPS and Raman mapping data for NCps studied.

In all these NCps, XPS data suggests that width increases with the increase in oxidation state from Si^0 (1.1 eV) to Si^{4+} (2 eV). We find that three effects mainly contribute to the measured width of the Si 2*p* core-level components: i) Structural disorder in the sample, ii) phonon broadening and iii) core-hole lifetime [253]. In Si-SiO_2 NCps, the transition lifetime decreases as we go from Si^0 to Si^{4+} due to charge transfer at the interface and thus increasing the natural width of the suboxide peak. Further, we have observed larger width of all the components viz Si^0 (1.1 eV), Si^{1+} (1.2 eV), Si^{2+} (1.3 eV), Si^{3+} (1.4 eV), Si^{4+} (2 eV) as compared to that reported Si-SiO_2 NCp [225]. We have observed larger width of LF and IF phonons in Raman spectra of Si-SiO_2 NCps, which is understood as due to variation in bonding environment at the surface of Si NCs. Further, geometry analysis of Si_{41} clusters, suggest variation in bond angle (Si-O-Si) and bond length (Si-Si) due to sp^3 and sp^2 hybridization at the surface of the cluster. Thus, variation in bonding environment can give rise to larger width of XPS spectra. Further,

To summarize, size dependent variation in surface/interface of Si NCs in single and multilayer Si-SiO_2 NCps studied using Raman mapping is well corroborated with XPS studies. Raman mapping and XPS on different NCps suggests that higher intensity of Si^{3+}, Si^{2+} and Si^{1+} suboxide states correspond to higher content of surface/interface (495 - 510 cm^{-1}), intermediate (511-514 cm^{-1}) and core (515 - 519 cm^{-1}) phonons for smaller (< ~ 4 nm), intermediate (~ 4 nm < 6 nm) and larger (~ > 6 nm) Si NCs, respectively. Thus, quantitative corroboration between Raman mapping and XPS found for all the NCps studied establish Raman microscopy/mapping of optical phonons as a standard tool to get information of surface/interface of smaller Si NC in Si-SiO_2 NCps. Important result of the corroboration of these data is that direct band gap ~ 2.8 and ~ 2.95 eV observed are attributed to smaller and intermediate size Si NCs, respectively and are understood to be due to interplay between confinement effect and bonding of oxygen at the interface of Si NCs in SiO_2 matrix.

3.6. Summary

In Si-SiO_2 NCps grown by PLD, large variation (495 - 519 cm^{-1}) in Si phonon frequencies is studied. Based on the line shape variation and behavior of Si phonons during specially designed laser irradiation experiment, Si phonon frequencies in the range 495 - 510 cm^{-1} and 515 - 519 cm^{-1} are attributed to the surface/interface of Si NCs and SiO_2 matrix and core of

Si NCs respectively. Further, Si phonons frequencies in the range 511 - 514 cm^{-1} are attributed to originate from intermediate size NCs where, both surface and core of Si NC contribute simultaneously. Stoke/anti-Stokes Raman spectroscopy and results of wavelength dependent Raman mapping in corroboration with absorption measurements show that resonance Raman scattering is crucial for the observance of interface phonons. Thus, large size distribution of Si NCs in these NCps is used advantageously to probe similarity and differences in them under certain experimental conditions. This understanding can also be used to obtain information of the interface and estimation of size in Si-SiO_2 NCps nondestructively and without needing any sample preparation. Further, this understanding in corroboration with AFM mapping is used to understand the morphology of Si-SiO_2 NCps, which suggests formation of cluster of Si NCs embedded in $SiO_{2,}$ although the growth is carried out to be multilayer. Raman and AFM mapping together showed that Si NCs are clustered in i) smaller clusters (~ 100 nm) organized closely in two dimensions (2D) and ii) a big (~ 2 μm) three dimensional (3D) isolated cluster. Raman mapping performed by varying the focal spot along the depth shows stacking of larger (> ~ 6 nm) to smaller sizes (< ~ 4 nm) Si NCs from bottom to top for some clusters. Further study of specially grown Si-SiO_2 nanocomposites to understand observed morphologies suggest, formation of smaller Si NCs at the top due to annealing at 800 ^{o}C in Si rich SiO_2 and possible existence of thermal gradient in an insulating matrix of $SiO_{2.}$ Whereas, larger Si NCs are formed in plume itself.

Further, in order to support the results obtained using Raman mapping, XPS measurements are performed on the NCps, which show distinct average Raman mapping data. XPS measurements showed observance of Si^{1+}, Si^{2+} and Si^{3+} suboxide states with higher intensity in the NCps corresponding to higher content of HF, IF and LF phonons in Raman mapping, respectively. Thus, quantitative corroboration between Raman mapping and XPS had been established for all the NCps studied.

Chapter 4

CdS-PVP nanocomposites

4.1. Introduction

Nanocomposite of semiconductor NCs and organic polymer matrix can effectively combine properties of both components to create a material with new unique properties [159, 160]. Polymers provide stability and processibility, keeping intact the optoelectronic properties of semiconductor NCs or enhancing it. In case of inorganic-organic NCps, lots of work has been done for NCs-block copolymer mixtures. It has been predicted theoretically as well as observed experimentally that the separation in block copolymers and interaction between NCs and block copolymers could be used to promote the ordering of NCs and thereby create highly organized hybrid materials [84-88] and is well established. However, for NCs-polymer NCps, whether the effect of interaction between the two constituents can also affect the formation of NCp is not well studied. We have chosen CdS-PVP NCps to investigate the effect of interaction between NCs and polymer on the formation and properties of NCp. CdS is a semiconducting material having unique optoelectronic properties, as it is possible to engineer the band gap over a wide spectral range (visible to UV). PVP matrix is chosen as monomers of PVP prefers to complex with many inorganic compounds and thus provide surface passivation.

Further, to find simple and cheap technique to grow inorganic-organic NCps with good control and being able to extend it to large scale production is one of the challenges in the field of NCps. Several chemical and physical routes have been used to fabricate semiconductor NCs, either in the form of powder or thin film [179-183]. However, inorganic-organic NCps are preferably grown using chemical techniques. Chemical bath deposition (CBD) [184-193] is one such simple route to grow thin film of NCs as well as NCps. Most of the literature shows that CdS-polymer NCps are grown using two-step process [184-190] i.e. CdS NCs are grown separately using either a chemical/physical process and then by some chemical process they are embedded in to a polymer matrix. This method is time and resource consuming. Here, we present one-step growth process, wherein growth of CdS NCs and formation of PVP matrix embedding them happens simultaneously. The process is therefore complex and need to be investigated systematically in order to gain control over the growth of such NCps. Herein, systematic study of CdS-PVP NCps by varying Cadmium acetate (Cd ion source), Thiourea (S ion source), PVP concentration, deposition time and heating/cooling cycles is discussed in section 4.2, which suggests co-operative growth mechanism for CdS-PVP NCp [254]. Further, we also find that very low concentration (100 times lower) of Cd^{2+}/S^{2-} ion sources show large differences in absorption and PL spectra as compared to NCps grown with higher concentration. In order to understand these differences, NCps are further studied using Raman, AFM and PL mapping, which clearly brings out differences in morphologies of these CdS-PVP NCps [255], wherein CdS NCs are embedded in i) thin film and ii) sphere of PVP for lower and higher concentration of Cd/S ion sources, respectively, as described in section 4.3. Further, we have discussed the effect of growth temperature on the collapse transition of PVP in section 4.4. Raman and AFM mapping along with XRD suggests that the collapse transition of PVP is not favored at 70 ^{o}C, which leads to opening (at 70 ^{o}C) and reformation (room temperature) of CdS-PVP NCp [256], which leads to band gap tuning of CdS NCs embedded in isolated PVP spheres, due to generation of stress during reformation of CdS-PVP NCp. These results obtained using Raman and AFM mapping data in corroboration with optical spectroscopies and electron microscopies, which gives insight into chemical, structural, crystalline and surface quality and it's correlation with morphology for CdS-PVP NCps are described in the following.

4.2. Insight into one-step growth of nearly monodispersive CdS nanocrystals embedded in PVP spheres

In this section, we discuss the optimization study of formation of CdS NCs embedded in a PVP matrix, grown using one-step CBD technique. We have used absorption, PL and diffuse reflectance spectroscopy in corroboration with SEM and TEM to study these NCps. Systematic study of variation in Cadmium acetate (Cd ion source), Thiourea (S ion source) and PVP concentration, deposition time, heating/cooling cycles, elucidates co-operative growth mechanism for one-step growth process for CdS-PVP NCps. Most of the literature shows that NCps are grown using two-step process [184-190]. In this two-step growth process, NCs are grown separately and are later incorporated in polymer matrix. Using this growth process, CdS-PVP NCps is relatively well studied. This growth process leads to formation of CdS NCs embedded in PVP thin film, which show huge size distribution (absorption edge) of CdS NCs. However, to the best of our knowledge, no systematic study has been performed for one-step growth of CdS-PVP NCp grown using CBD.

4.2.1. Growth: Chemical bath deposition

CdS-PVP NCps are grown using CBD technique. The ingredients used for this purpose are Cd-A, ThU and PVP. It is important to note here that for all depositions, molarity of Cd-A and ThU is taken to be same. For writing convenience, Cd-A & ThU concentration is written in molar (M) units and content of PVP is written in gram (g) for 100 ml of aqueous chemical bath. NCp grown with 1M: Cd-A & ThU concentration and 2g: PVP content, will be described hereafter as 1M, 2g. To study the growth of CdS NCs in PVP matrix from various angles, we have investigated,

(1) The effect of different molarities of Cd-A & ThU: Three different Cd-A & ThU concentrations 0.01, 0.5 and 1 M are used to study the growth. NCps are described as S1 (0.01 M, 4g), S2 (1 M, 2g), S3 (1 M, 4g), S4 (0.5 M, 2g), S5 (0.5 M, 4g)

(2) The effect of different quantity of PVP: quantity of PVP is varied from 0.05 g to 10 g (1.25 $*10^{-2}$ mM to 2.5 mM) in discrete steps for 0.5 M Cd-A & ThU. NCps are described as S6 (0.05g), S7 (0.1 g), S8 (10g)

(3) The effect of deposition time and heating/cooling process on growth is studied for 1 M, 2g. NCps are described as S2+ (1 M, 2g), S2H (1 M, 2g).

Total 40 NCps are prepared using different concentration of Cd-A & ThU, PVP quantity, heating/cooling cycles and depositions time. However, only those 10 NCps, for which data is presented in the thesis, are summarized in Table 4.2.1.

4.2.2. Systematic study of growth

In previous work [257], thin films of CdS were deposited using CBD technique. Two different molarities of the solution as 0.01 M and 0.02 M were used for optimization. SEM image showed particulate nature of surface for film grown using 0.02 M, while more uniformity is observed for 0.01 M CdS films. Absorption data also showed that films grown with 0.01 M concentration have lesser scattering losses as compared to films deposited using other molarity. Thus, basic characterization suggests that 0.01 M concentration leads to best quality films. Similar results have also been reported by other groups [174,179]. Based on the observation noted above, growth of CdS-PVP NCp is started with same CdS growth parameters, i.e. 0.01 M Cd-A & ThU. PVP content of 4 g in 250 ml of aqueous solution with stirrer is used (S1).

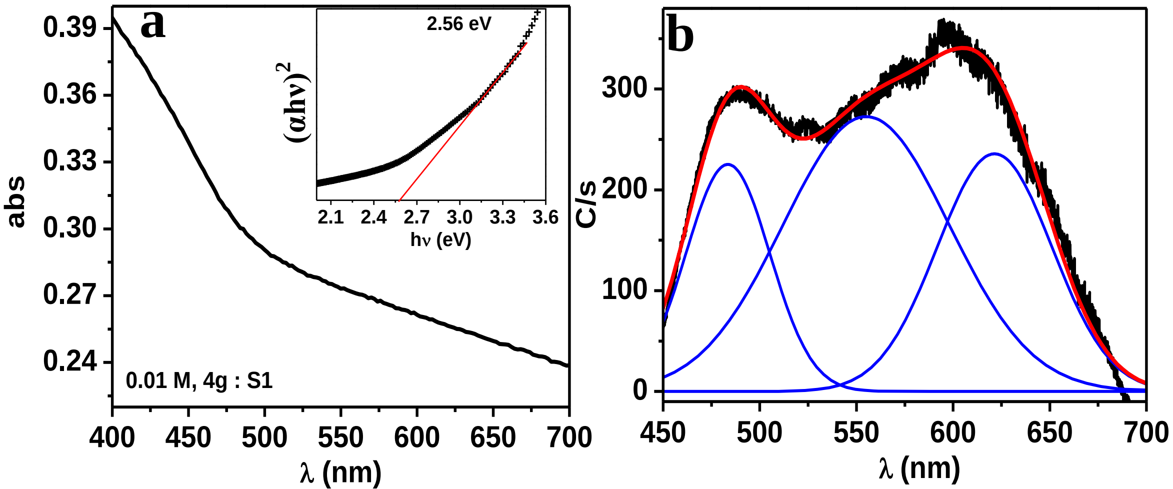

Fig. 4.2.1. a) Absorption spectrum of NCp S1 (0.01M, 4g), inset shows band gap calculation by plotting $(\alpha h\nu)^2$ against (hv) and b) corresponding PL spectrum showing peak related to band edge and defect. Cumulative fit (red solid line) to the raw data (black solid line) and separate Gaussian component are shown with solid blue lines.

Band gap of S1 NCp and size of CdS NCs are obtained from it's absorption spectrum (Fig. 4.2.1) as per formulism given in chapter 2 (equations-2.29-2.31). The average diameter of CdS NCs for S1 is calculated to be ~ 8 nm. Further, we find that the PL spectrum for S1 (Fig. 4.2.1b) can be fitted with minimum three Gaussian peaks, where, PL corresponding to band gap is ~ 483 nm (highest in energy) with FWHM ~ 50 nm and stronger defect PL peaks ~ 555 and 620 nm. The observed large defect PL suggests poor passivation of CdS NCs. It is important to note that we have observed interference fringes in PL spectra for λ > 500 nm. These fringes are observed in other samples (ZnO, CdZnS) too at similar positions. This suggests that observance of these fringes is related the optical elements used in Raman system. Formation of CdS NCs and it's crystalline quality is independently checked using Raman spectroscopy. Raman spectrum (Fig.

4.2.2) shows asymmetric line shape of CdS LO phonon ~ 300 cm^{-1}, which is red shifted as compared to LO phonons of bulk CdS ~ 303 cm^{-1} [179]. For NCs, quantum confinement of phonons leads to red shift, broadening and asymmetric line shape of phonons due to relaxation of Raman selection rule [153]. Observed asymmetric line shape and red shift of LO phonon from the bulk value along with blue shift in the band gap (band gap of bulk CdS is ~ 2.42 eV [179]), suggests formation of CdS NCs.

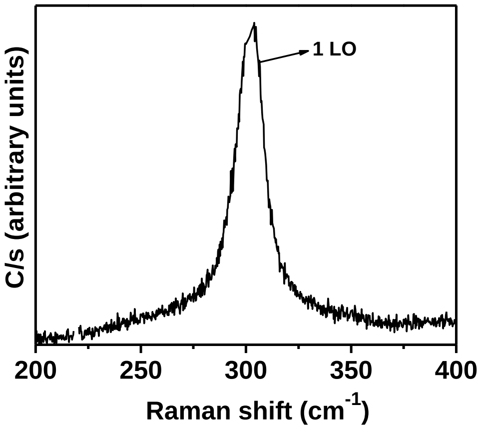

Fig. 4.2.2. Raman spectrum of sample S1 with 457.9 nm as excitation source showing 1LO phonon of CdS. This data is taken using RAMNAOR U1000, (Jobin Yvon, France) with CCD detector.

Since, this concentration of Cd-A & ThU (0.01 M) does not show desired quality, passivation and sizes of CdS NCs, therefore, we study the NCp growth with systematic variation of the bath parameters covering wide range. CdS-PVP growth is optimized using parameters like, 1) Cd-A & ThU concentration, 2) PVP quantity, and 3) heating/cooling and deposition time. Salient feature of this study is that, the growth of CdS - PVP NCp being co-operative in nature, and hence optimization of Cd-A & ThU concentration depends on the content of PVP in the chemical bath. For all NCps grown, we observe either an edge or a peak in absorption spectra. Absorption spectra of NCps grown with 0.5 M and 1 M concentration of Cd-A & ThU and PVP content of 0.05 g, 0.1 g, 2 g, 4 g (for 100 ml aqueous solution) show absorption peak for various growth conditions. Furthermore, SEM measurements show that sphere with sizes in the range 100 - 600 nm are formed in these NCps. However, for CdS-PVP NCp with 0.01 M Cd-A & ThU and 4 g PVP (250 ml aqueous solution), absorption spectra show band edge, irrespective of the variation in other growth conditions like sequence of addition, deposition time, heating etc. These observed differences for 0.01 M Cd-A & ThU are further investigated using Raman and AFM mapping and will be discussed in next section.

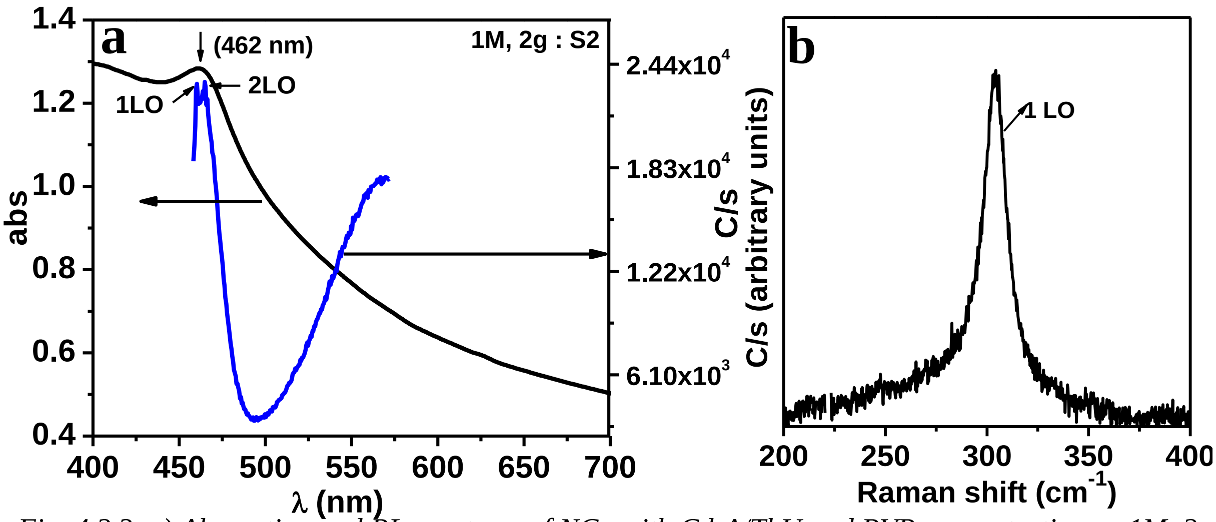

Fig. 4.2.3. a) Absorption and PL spectrum of NCp with Cd-A/ThU and PVP concentration as 1M, 2g (S2), b) Raman spectrum of the same NCp.

The observation of a peak in the absorption spectrum indicates formation of nearly monodispersive CdS NCs. To check, whether the absorption peak is due to band gap of nearly monodispersive CdS NCs, we have performed PL measurements on all NCps. Representative absorption and PL spectra are shown for NCp S2 (1M, 2g) in Fig. 4.2.3a. Band gap (Eg) is obtained by calculating the second derivative [258,259] of the absorption spectrum having peak

~ 2.68 eV (462 nm). The band gap from PL spectrum is obtained by fitting the lowest PL peak to a Gaussian. The band gap obtained is ~ 2.65 eV (468 nm, FWHM ~ 30 nm). This is in close agreement with the band gap obtained using the absorption spectrum. We find that the band gap values obtained from PL spectra are in close agreement with that obtained from absorption spectra (peak or band edge) for all NCps studied. The band gap obtained from PL spectrum is found to be within 2-6 nm lower in energy, due to band tailing effects. This confirms that the observed peak in absorption spectra is due to band gap of CdS NCs. Further, Raman spectrum of S2 (Fig. 4.2.3b) shows CdS LO phonon ~ 300 cm^{-1} having asymmetric line shape and FWHM ~ 13 cm^{-1}. This suggests formation of good crystalline quality CdS NCs as compared to NCp S1 (FWHM ~ 18 cm^{-1}).

It is important to note that the absorption spectrum show significant absorption even in the longer wavelength region (Fig. 4.2.3), following an absorption peak, which indicates scattering contribution at longer wavelengths. In order to investigate the scattering contribution, diffuse reflectance measurements are performed on all NCps. Diffuse reflectance spectroscopy is commonly used to obtain band gap of porous, powder NCps etc, where transmission measurements are not feasible [260,261]. The onset of the linear decrease in diffuse reflectance with increasing photon energy is taken as a measure of band gap [260]. Representative comparison of diffuse reflectance (R(D)) spectrum and absorption spectrum for NCp S2 is shown in Fig. 4.2.4a. It is important to note that, band gap observed using diffuse reflectance measurements is also in close agreement with that observed using absorption and PL spectroscopy measurements. Further, for powder samples, diffuse reflectance spectrum (DRS) shows nearly flat region at longer wavelengths followed by an abrupt decrease in reflectance (band gap). However, we observe either sloping (Fig. 4.2.4a) or near exponential curves at longer wavelengths manifesting the contribution of different type of scattering. Further, specular component (R(S)) shown in Fig. 4.2.4b is obtained by subtracting diffuse reflectance from the total reflectance, which shows flattening at longer wavelengths as expected.

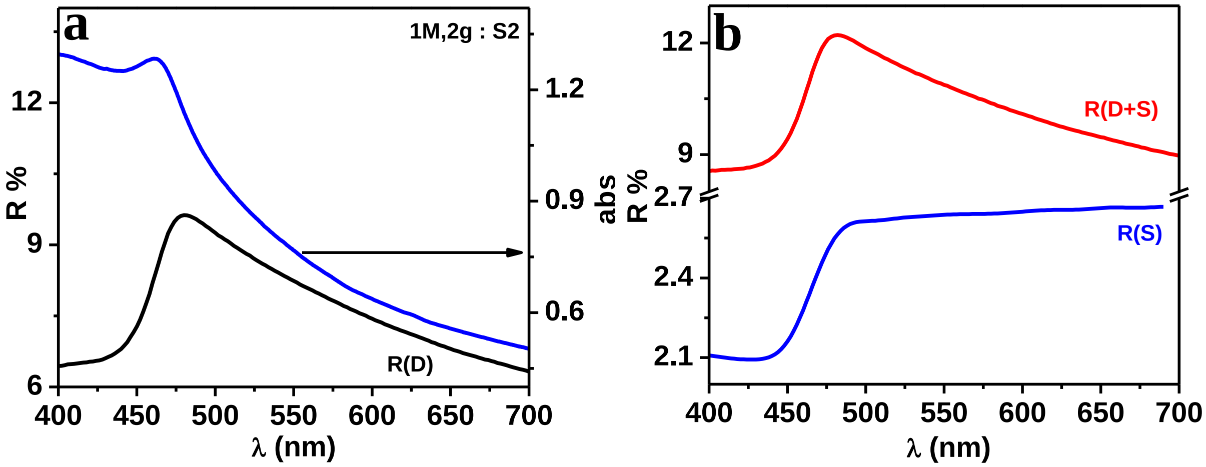

Fig. 4.2.4 a) Comparison of absorbance and diffuse reflectance (R(D)) for NCp S2 showing similar shape in the longer wavelength region and b) total reflectance (R(D+S)) and specular reflectance (R(S)) component.

The similar shape of absorption and DRS (Fig. 4.2.4a) in the longer wavelength region further confirms scattering contribution to the absorption spectrum. We find that DRS can be fitted using a polynomial in the longer wavelength region for S2. Taking this into consideration, absorption spectrum is deconvoluted using a Lorentzian and a polynomial, where, Lorentzian corresponds to the band gap absorption of nearly monodispersive CdS NCs and a polynomial corresponds to the contribution due to scattering of light (Fig. 4.2.5a).

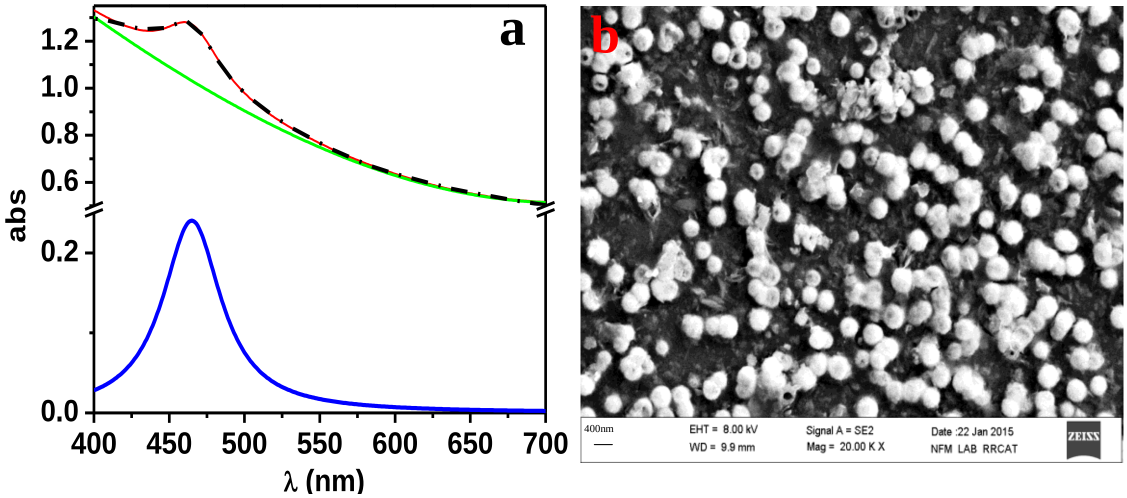

Fig. 4.2.5. a) A Lorentzian peak + a polynomial fit to the absorption spectrum for NCp S2. Solid line (red) show cumulative fit to raw data (dash dot line). Separate Scattering contribution (parrot color) and fitted absorption peak (blue color) are shown with solid line and b) SEM micrograph shows sphere sizes in the range ~ 200 - 300 nm.

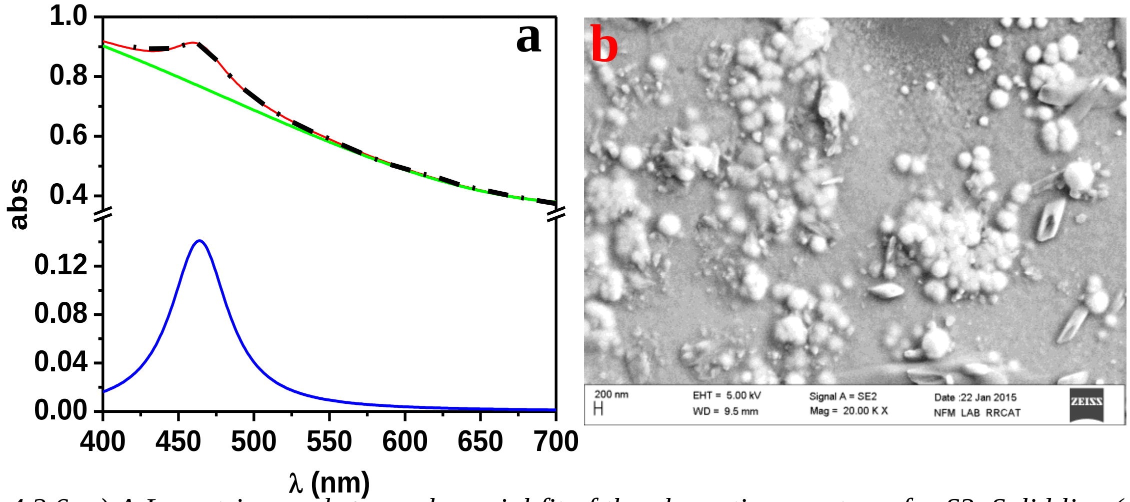

Fig. 4.2.6. a) A Lorentzian peak + a polynomial fit of the absorption spectrum for S3. Solid line (red) show cumulative fit to raw data (dash dot line). Separate Scattering contribution (parrot color) and fitted absorption peak (blue color) are shown with solid line and b) SEM micrograph shows sphere sizes in the range ~ 300 - 400 nm.

Taking diffuse reflectance spectra as a guide, we have deconvoluted all absorption spectra using a Lorentzian and a polynomial. Fitting parameters of a Lorentzian for all NCps are summarized in Table 4.2.1. Further, in order to elucidate the origin of this observed scattering contribution and find possible correlation with the morphology of NCps, NCps are investigated using SEM. It is well known that when the size of scatterer is very small as compared to incident wavelength, scattering efficiency goes as $1/\lambda^4$ whereas, when the size is of the order of incident wavelength, Mie scattering dominates. SEM micrograph of NCp S2 shows formation of spheres of sizes from 200 to 300 nm (Fig. 4.2.5b). Correlating this with scattering contribution obtained from deconvolution suggests that scattering of light (Rayleigh scattering ~ $1/\lambda^4$) due to spheres plays significant role in the absorption spectrum at longer wavelengths (Fig. 4.2.5a and b). Similar scattering contribution observed for NCp S3 (1M, 4g) at longer wavelengths is also consistent with the observation of sphere sizes in the range 300 - 400 nm for S3 (Fig. 4.2.6).

Further, for some NCps (S4 to S7), sphere sizes either lie in the range 300 - 600 nm or mainly structures formed on coagulation of spheres is found to be in this range of size. For these NCps, shape of absorption spectra and diffuse reflectance spectra is nearly a sloping straight line (at longer wavelengths) and consistently, deconvoluted scattering contribution shows flattening in the wavelength range 300 - 550 nm. This suggests dominance of Mie scattering in this case. Thus, the shape of absorption spectra is found to depend on both Rayleigh and Mie scattering contributions, which in turn depends on the sizes of spheres/structures observed in the NCp. Later in the section, we shall correlate the deconvoluted scattering contribution of the absorption spectra with morphology of the NCps. In the following, we discuss results obtained for growth under different bath parameters on the basis of understanding developed above.

Three Cd-A & ThU concentrations viz 0.01 M, 0.5 M and 1 M are used for the NCp growth and we observe very interesting results for two concentrations 0.5 M and 1 M. Absorption spectra for these NCps show presence of absorption peak, unlike for NCps grown using 0.01 M of Cd-A & ThU, which shows band edge. Observed difference may be related to the difference in morphology of these NCps. This will be discussed in detail in next section. Thus, two concentrations (0.5 and 1 M Cd-A & ThU) are studied under different growth conditions as discussed below.

4.2.2.1. Effect of Cadmium-Acetate &Thiourea concentration

Absorption spectra for NCps S2-S5 are shown in Fig. 4.2.7a. It is important to note that, shape of the absorption spectra in the longer wavelength region is different for NCps S4,S5 (0.5 M, 2 g & 4 g) as compared to NCps S2,S3 (1 M, 2 g & 4 g). Difference in scattering contribution obtained after deconvolution of absorption spectra is shown in Fig. 4.2.8. It shows flattening of scattering contribution in the wavelength range ~ 400-550 nm for NCps S4,S5, whereas, increase in scattering with decreasing wavelength for S2,S3 NCps. This observation is consistent with sphere sizes observed in SEM micrographs (Table 4.2.1), which suggests dominance of Mie scattering for NCps S4,S5, whereas Rayleigh scattering is dominant for NCps S2,S3.

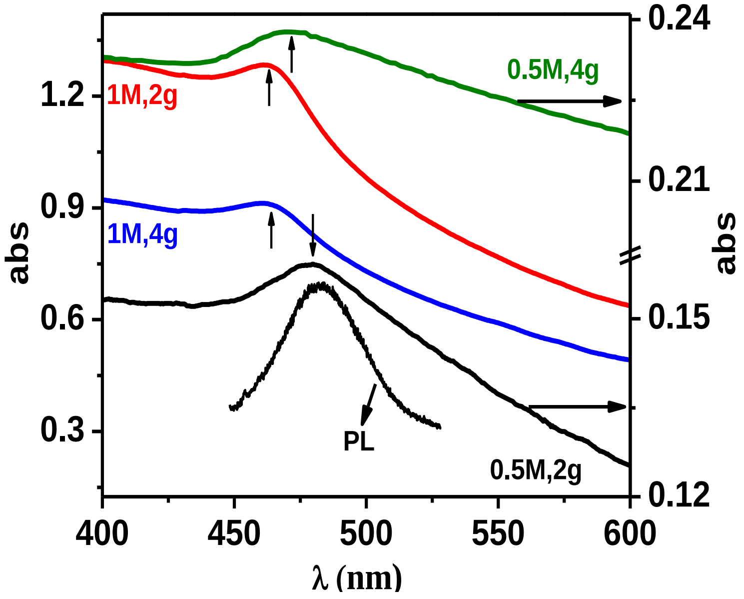

Fig. 4.2.7. Absorption spectra for 0.5 M and 1 M Cd-A/ThU concentration with 2g and 4g PVP content. Corresponding PL is also shown for 0.5M, 2g.

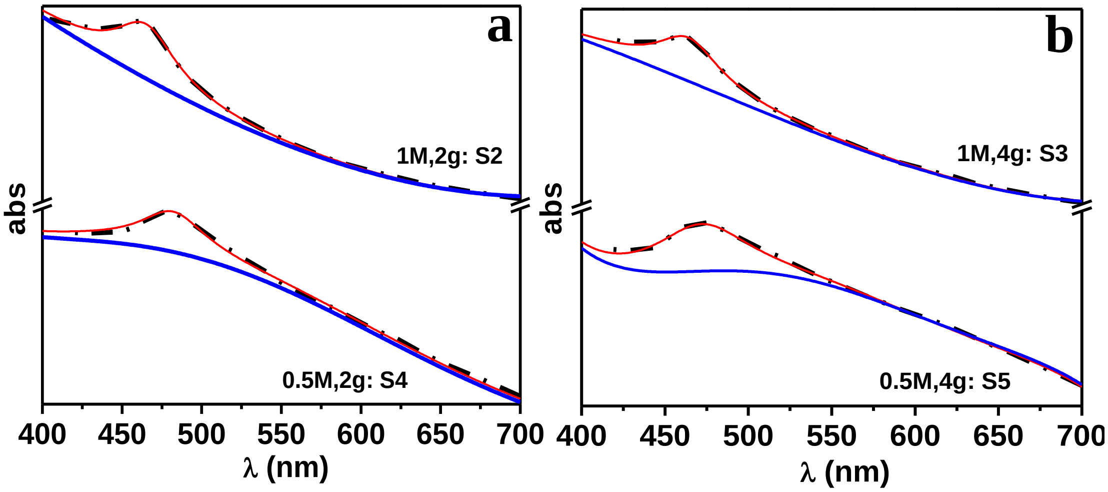

Fig. 4.2.8. a & b Fitted absorption spectra and difference in scattering background for 0.5 M and 1M Cd-A/ThU concentration with 2g and 4g PVP content. Solid line (red color) is fit to raw data (dot dash line). Solid line (blue color) shows scattering background.

Band gap and thus size of NCs is calculated from the deconvoluted absorption peak for S2-S5 (Fig. 4.2.9) using equations 2.29-2.31, as noted above. It is important to note that, irrespective of the growth conditions chosen or the amount of PVP taken (i.e. 2 g/4 g), 0.5 M concentration of Cd-A & ThU (S4, S5) leads to larger size CdS NCs (~ 7.5 nm: Table 4.2.1)) compared to that for 1 M Cd-A & ThU (S2, S3 ~ 6 nm: Table 4.2.1). This suggests that for larger molarity of Cd-A & ThU, smaller NCs are generated, irrespective of the variation of other bath parameters in the range specified above. This is not obvious, as one would expect faster growth of CdS with higher concentration of Cd-A & ThU (keeping the same amount of PVP) and hence larger CdS NCs. Further, Fig. 4.1.9 shows absorbance to be order of magnitude higher (Table 4.2.1) for NCps with 1 M to that of 0.5 M Cd-A & ThU concentration, suggesting larger density of CdS NCs for S2 and S3. This is in accordance with higher concentration of Cd-A & ThU in the chemical bath, although it is much larger than change in the concentration. These two observations suggest co-operative growth mechanism for the CdS-PVP NCp growth and are discussed in more detail in theory corroboration part (sub sub section 4.2.2.5).

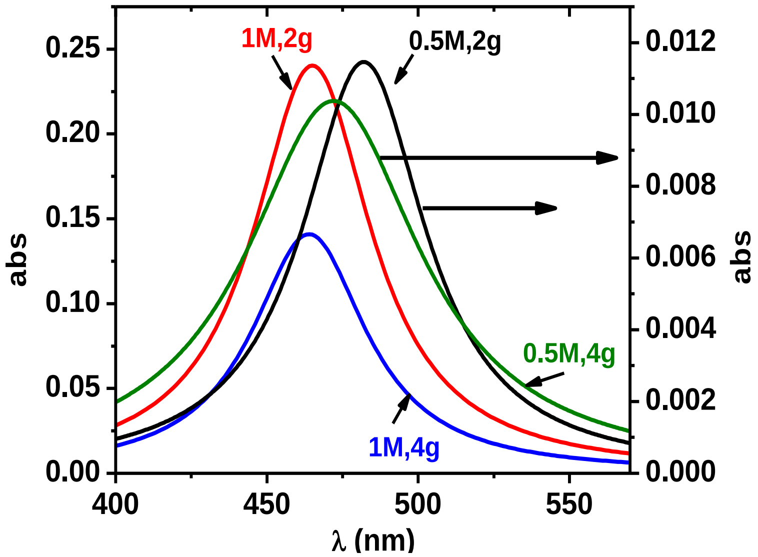

Fig. 4.2.9. Comparison of absorption peak for S2-S5 NCps.

Although, scattering contribution can be corroborated with size of spheres observed in SEM micrographs, it is important to note here that sizes of CdS NCs as calculated using absorption spectra are in the range of 6 - 8 nm. This is in contrast with sphere sizes observed in SEM i.e. 100 to 600 nm. To elucidate this difference and understand morphology of these NCps, one NCp is further investigated using TEM in the following.

4.2.2.2. Size of CdS NCs: consistency of absorption spectroscopy, SEM and TEM

As noted earlier in SEM micrographs, sphere sizes for different NCps are different and lie in the range 100 - 600 nm, whereas, absorption spectra suggest size of CdS NCs to be in the range of 6 - 8 nm. This led us to believe that these white spheres may be polymer spheres and

CdS NCs of sizes ~ 6 - 8 nm may be dispersed in the darker region. To check this, we have performed EDS measurements on these NCps. We find rather intriguing result that the appropriate stoichiometric ratio for Cd and S is obtained in the region of white spheres and not in the darker region. The only possibility, we could think of is that smaller size CdS NCs are embedded in these spheres and these spheres are PVP spheres. To further look into this, we have performed TEM measurement on one NCp S2+ (1 M, 2 g). This NCp is grown by allowing NCp S2 to remain in the chemical bath for additional 24 hrs at room temperature. NCp S2+ is chosen for TEM measurement, because absorption and PL spectra (Fig. 4.2.10a) show sharp band gap related peak and SEM micrographs (Fig. 4.2.10b) show uniform and large density of spheres. For TEM measurement, one white sphere is chosen and is looked into with high resolution. Since, electron beam in TEM is needed to cross lot of polymer and CdS material, TEM imaging is very difficult to achieve for a sphere and the image obtained is at the edge of the sphere. *The TEM image (Fig. 4.2.10c) shows near monodispersivity of the CdS NCs along with consistency of size*

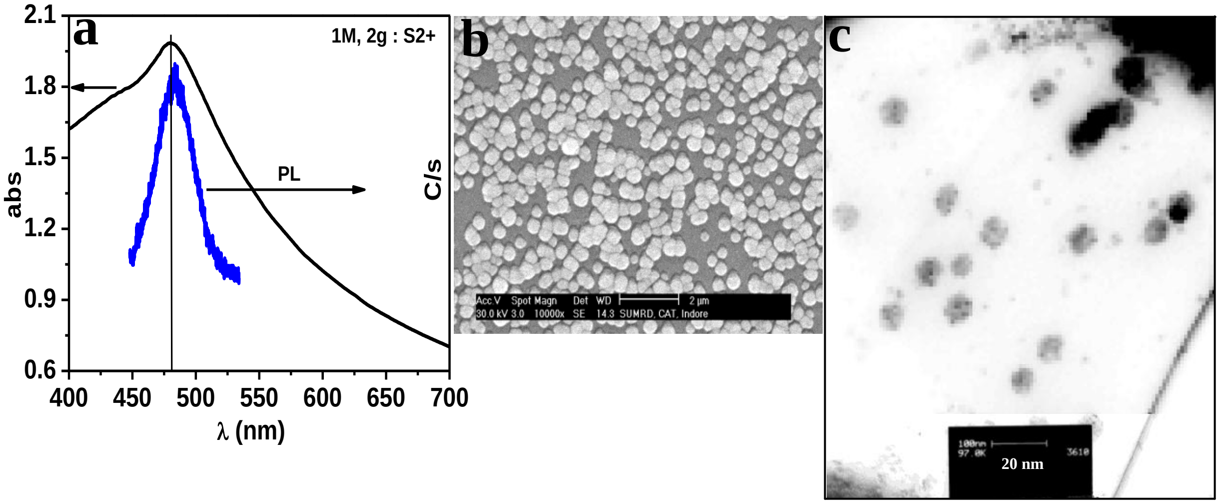

Fig. 4.2.10. a) Absorption and PL spectra of NCp with Cd-A/ThU and PVP concentration as 1M,2g (S2+), b) corresponding SEM image and c) TEM image of the same NCp.

(~ 8 nm) obtained from the absorption spectrum. This establishes the fact that, we have achieved the growth of nearly monodispersive spherical CdS NCs embedded in a polymer, wherein, polymer itself is taking the morphology of a sphere. Thus, our study suggests change in conformation of PVP i.e. form two dimensional planar structure to three dimensional sphere formation. It is interesting to understand, why PVP is conformed to this morphology and will be discussed in the theory corroboration part (sub sub section 4.2.2.5).

4.2.2.3. Effect of PVP concentration

To study the effect of PVP quantity, we have chosen 0.5 M concentration of Cd-A & ThU and PVP quantity viz 0.05 g (S6), 0.1 g (S7), 2 g (S4), 4 g (S5) and 10 g (S8) are used. Absorption spectra for all NCps are shown in Fig. 4.2.11, which shows absorption peak for all NCp except S8, wherein absorption edge is observed. For NCps, wherein absorption peak is observed, deconvolution of the absorption spectra (Fig. 4.2.12) show flattening of scattering contribution in all NCps, suggesting dominance of Mie scattering. Deconvolution of the absorption spectra show flattening of scattering contribution in the range ~ 400 - 500 nm in S6 and S7, suggesting dominance of Mie scattering. SEM micrographs show PVP spheres sizes ~ 100 - 200 nm, however, micrograph shows that large density of structures of the size ~ 400 - 500 nm are formed due to coagulation of PVP spheres, which are responsible for the Mie scattering observed. Consistent with higher density of structures it shows maximum absorbance (Table 4.2.1) for NCp S7. Further, observation of flattening of scattering contribution in the wavelength range ~ 400 - 550 nm for NCps S4, S5 is consistent with sphere sizes observed in SEM micrographs (Table 4.2.1).

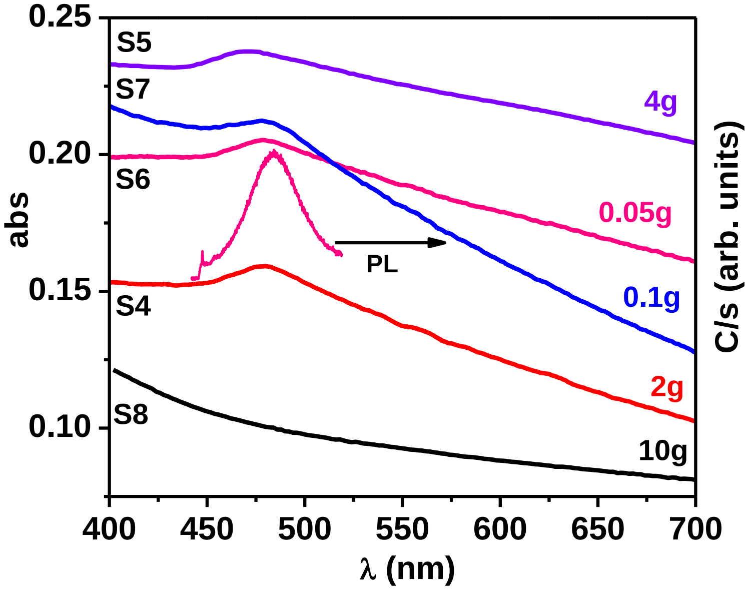

Fig. 4.2.11. Absorption spectra of NCps with Cd-A & ThU concentration as 0.5 M and different contents of PVP as 0.05 g (S6), 0.1 g (S7), 2 g (S4), 4 g (S5) and 10 g (S8). Corresponding PL spectrum is shown for NCp S6.

Narrow absorption peaks (Fig. 4.2.13) observed for all the NCps (except for PVP-10 g) suggest the formation of nearly monodispersive CdS NCs. Further, absorption spectra show that almost similar NC sizes (~ 8 nm: Table 4.2.1) are formed for NCps with PVP quantity of 0.05 - 2 g, whereas smaller size (~ 7 nm: Table 4.2.1) CdS NCs are observed for NCp with PVP content of 4 g. This can be understood by considering that higher quantity of PVP i.e. 4 g, will lead to faster growth of PVP restricting the development of larger CdS NCs by capping. However, similar sizes of CdS NCs for 0.05 to 2g PVP quantity are rather surprising. For NCp S8, absorption edge is observed and thus band gap is obtained from $(\alpha h\nu)^2$ v/s (hν) plot to be ~ 2.44 eV (508 nm).

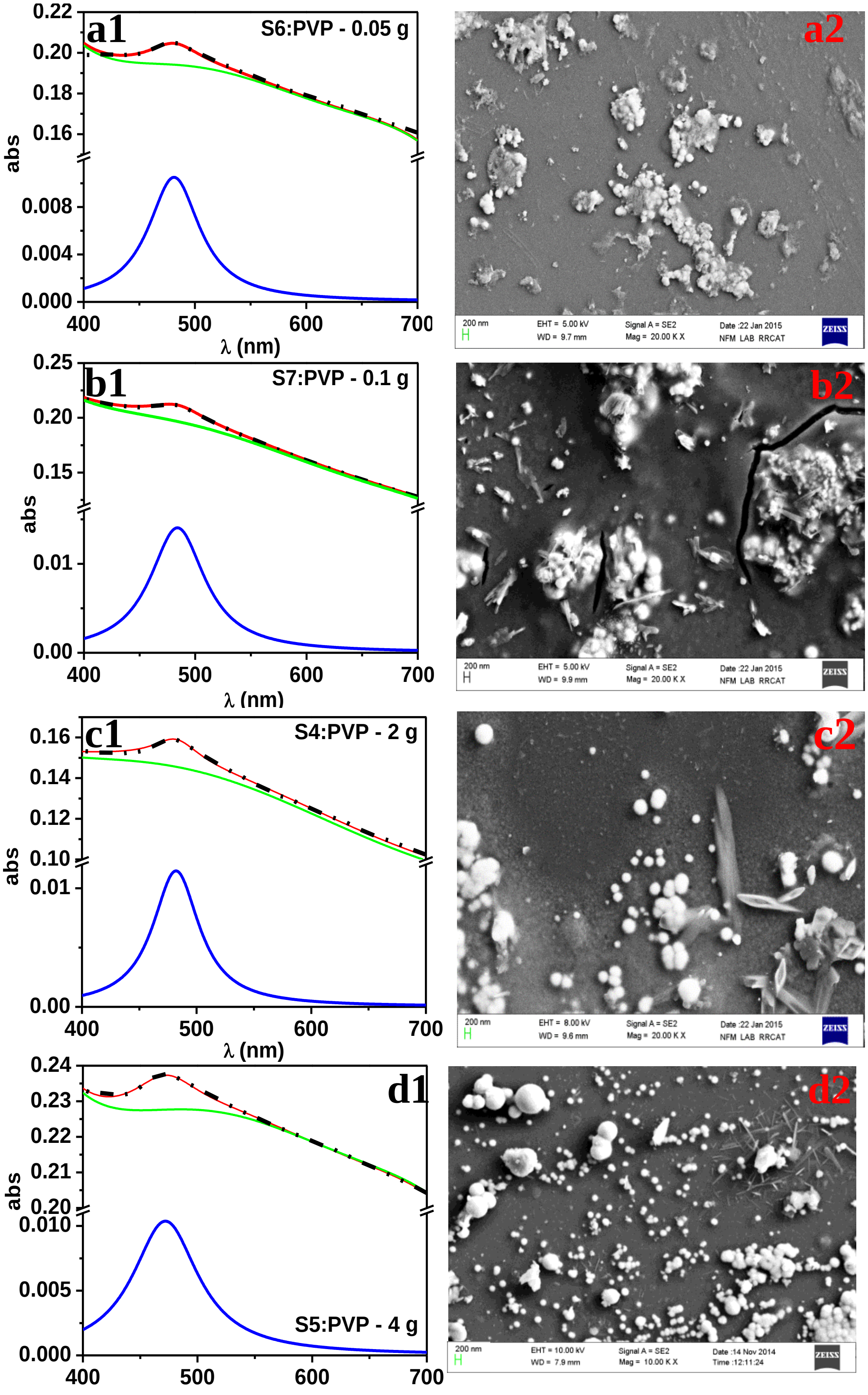

Fig. 4.2.12. Deconvoluted absorption spectra for NCp S7, S6, S4 and S5 (noted in the figure), which shows flattening of scattering background and corresponding SEM micrographs.

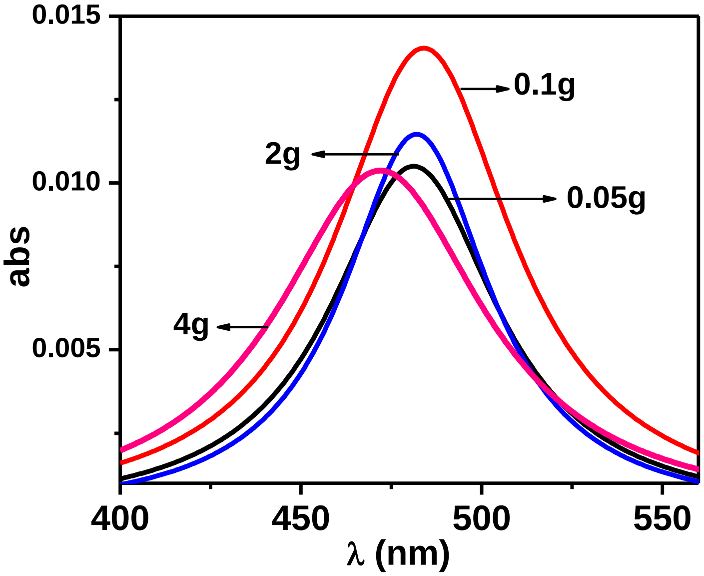

Fig. 4.2.13. Absorption peak obtained after the removal of scattering contribution from observed absorption spectra for NCps with Cd-A & ThU concentration as 0.5 M and different contents of PVP as noted in the Fig. 4.2.13.

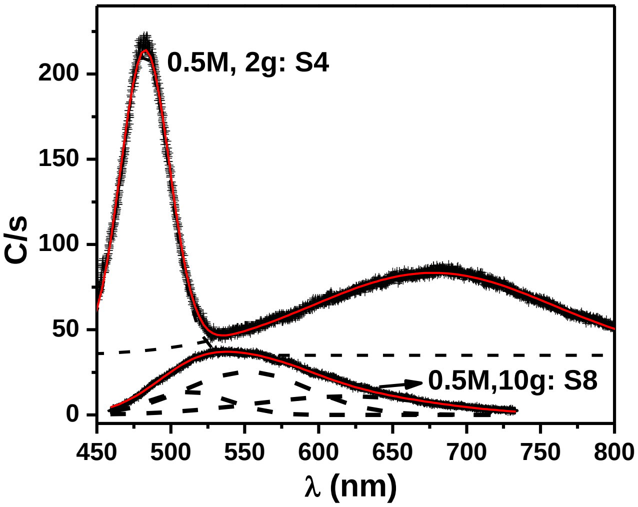

Fig. 4.2.14. Comparison of PL spectra for S4 and S8 NCps. PL spectrum for S4 (PVP: 2g) is shifted in y-axis by 35 C/s to enhance the clarity. Cumulative fit to raw data (+) is shown with solid red line. Separate Gaussian components are shown with dash line.

It is important to note that PL spectrum of S8 (showing absorption edge) is fitted using minimum required (three) Gaussian peaks ~ 509 nm, 550 nm, and 620 nm (Fig. 4.2.14). PL peak

~ 509 nm corresponds to the band gap transition, whereas, stronger PL peaks ~ 550 nm and 620 nm corresponds to defect PL. For comparison, Fig. 4.2.14 show PL spectrum of the S4 (0.5M, 2g: absorption peak), which can be fitted using two Gaussian peaks. For this NCp, intensity of the defect PL (peak ~ 680 nm) is much less as compared to the intensity of band gap PL (~ 483 nm). Similar observations are made for all the NCps, which show absorption peak for the band gap transition. This suggests that in these NCps, CdS NCs are better passivated, whereas, non-radiative transitions are dominant in case of NCps showing absorption edge.

4.2.2.4. Effect of deposition time and preheating

To understand the effect of deposition time and temperature of the chemical bath on the growth of NCp, total eight NCps are studied. The as grown (growth: 40 hours (RT)) NCps (S2-S5) are taken and rest of the NCps are further allowed to grow for 24 hour in chemical bath (S2+ - S5+) at room temperature. In the next step, the same chemical bath is subjected to heating at ~ 70 ^{0}C for 2 hours and then allowed further growth in the chemical bath for 36 hrs (S2H - S3H) at room temperature. Representative absorption spectra of NCp S2, S2+ and S2H are shown in Fig. 4.2.15. Deconvoluted absorption peaks show increase in size of CdS NC size from ~ 6 nm (S2) to 11 nm (S2H). Larger absorbance observed for NCp S2+ (Fig, 4.2.15a-c and Table 4.2.1) is consistent with increased density of PVP spheres as observed in SEM micrographs (Fig. 4.1.15d-f). Further, SEM micrographs show that on heating, non-uniformity in polymer sphere sizes increases (~ 200 - 600 nm: Table 4.2.1). Absorption spectra show increase in width of absorption peak from 50 nm (S2) to 90 nm (S2H) (Table 4.2.1) indicating larger size distribution of CdS NCs or degradation of crystalline quality. Both the observations together suggest that these growth conditions lead to non-uniformity in sizes of both CdS NCs and PVP spheres. Heating the bath has also led to decrease in absorbance (Table 4.2.1). Such a large variation in size and density of PVP spheres and CdS NCs after heating indicates reformation of PVP spheres and thus CdS-PVP NCps. This is further investigated and is discussed in detail in section 4.4.

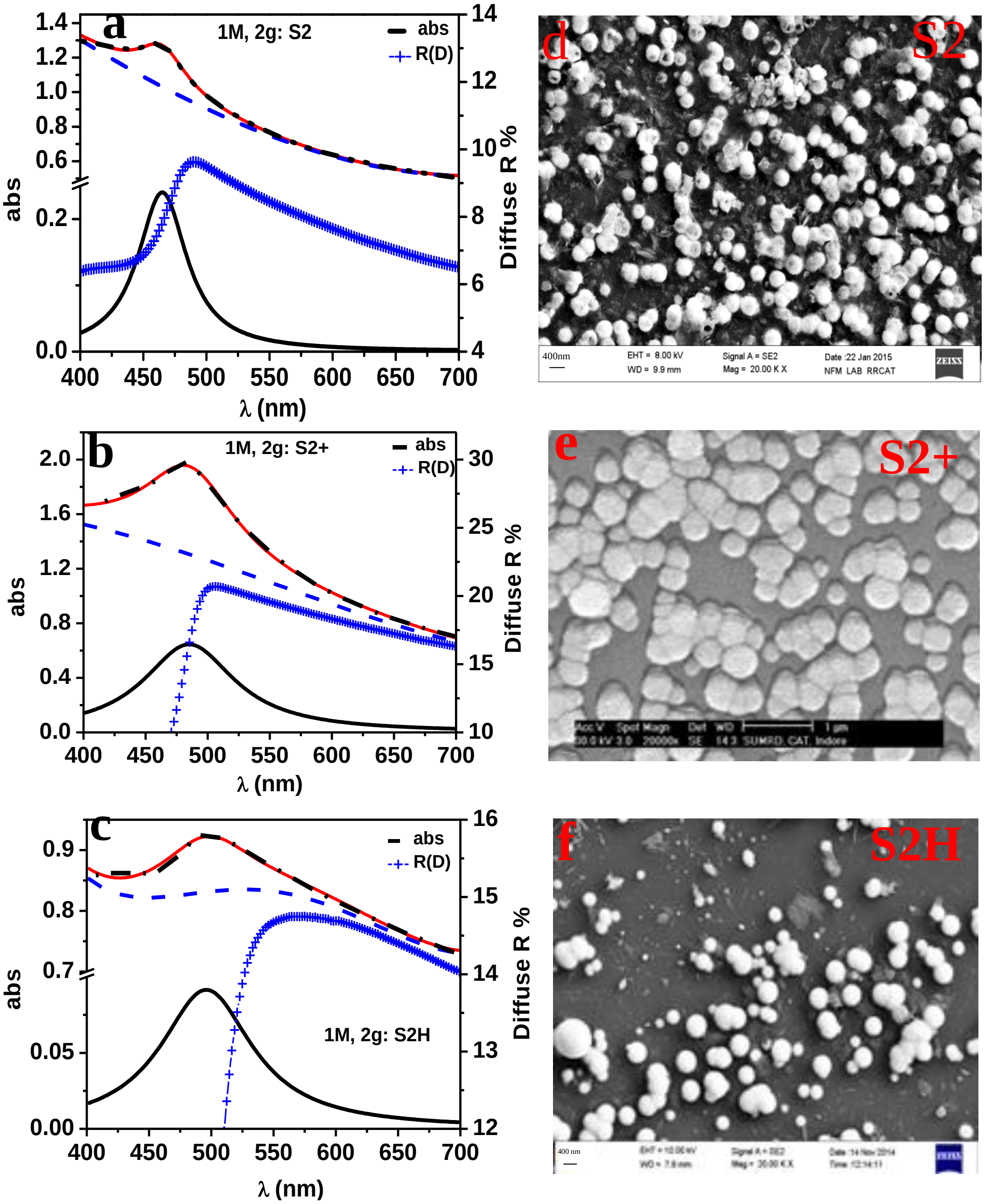

Fig. 4.2.15. Deconvoluted absorption spectrum and diffuse reflectance spectrum for NCp. a) S2, b) S2+ and c) S2H. Cumulative fit (red color) to raw absorption data (dash dot) and separate component (black line and dash line) are shown. Diffuse reflectance spectra are shown with line + symbol (+) and 7d-f) corresponding SEM images for these NCps.

Fig. 4.2.15a-c shows difference between R(D) spectra for these three NCps. This difference in scattering contribution to absorption spectra with change in growth conditions can also be well correlated to PVP sphere sizes observed (S2: 200 - 300 nm (Fig. 4.2.15d), S2+ : 400 - 500 nm (Fig. 4.2.15e) and S2H: mainly 200 - 600 nm (Fig. 4.2.15f)) in these NCps. It is to be noted that onset and center of diffuse reflectance edge, matches with corresponding band gaps obtained from sharp and broad absorption peaks, respectively. Although, Fig. 4.1.15 is scaled to show only part of diffused reflectance spectra, it is to be noted that onset of edge in DRS matches with absorption peak for S2+, where there is uniformity in CdS NCs.

4.2.3. Theory corroboration

There are quite a few observations in this set of experiments, which can be termed as unusual, since they cannot be explained using simple and common reasoning. In the quest of understanding these observations, we looked for possible explanation in the existing literature related to modeling of growth. The qualitative corroboration obtained from the literature is given below.

1. *Observation:* One expects CdS NCs to be embedded in two dimensional polymer matrix in CBD grown films. However, SEM and TEM results show that CdS NCs are embedded in PVP with CdS - PVP NCp taking the morphology of a sphere.

A collapse of a polymer in a solvent or in the presence of NCs, leading to formation of globules has been explained in terms of effective mediated attraction between the side chains monomers due to NCs-polymer [84]. Diamant et al. have shown that not only interaction between particle/molecule and polymer, but also intra-polymer interactions have an important role as well in partial collapse of the polymers [85]. Recently, in PVP–Mn doped CdS NCp, attractive interaction between PVP and CdS i.e. C = O→Cd^{+2} is observed [262,263]. This attractive interaction between CdS NCs and monomers leads to collapse of a polymer into a globule formation i.e. conformation of polymer to a sphere embedded with CdS NCs. Further, it may be noted that the concentration of polymer and NCs is also a determining factor for condition of partial collapse of polymer and this will be discussed in next section.

2. *Observation:* Our absorption data indicates decrease in size of CdS NCs for higher concentrations of Cd-A & ThU (0.5 and 1M) while keeping PVP concentration (2g/4g) same.

Cao et al. has reported DFT for a coarse-grained model of block copolymer-nanoparticle mixtures and predicts that well-organized structures can be effectively controlled by adjusting the polymer-particle interaction [86] and thus this is the main parameter controlling the structure/morphology. This interaction can be changed with change in concentration of PVP & or Cd/S ions, temperature. Variations in these parameters can give rise to different size of CdS NCs and different morphology of CdS-PVP NCps as noted earlier. Further, in complex mixtures of polymers and nanoparticles, it is not simply the ordering of the polymers that effect the spatial organization of the particles; the particles in fact affect the self-organization of the copolymers [84]. In our case, it is only polymer and hard spheres (nanoparticles) and probably therefore no self organization of polymers are observed. However, there are evidences of co-operative growth mechanism of NCp of PVP and CdS hard spheres like i) lower size Cd/S NCs in higher concentration of Cd/S ion source which depends on relative PVP concentration, while conserving the total amount of CdS in the film as observed in our case, ii) Change in size of CdS NC occurs only for certain PVP content when Cd-A & ThU is kept constant and PVP content is varied, etc.

3. *Observation*: While changing the ratio of Cd/S ions and PVP, we observe that there is optimum concentration of PVP for fixed concentration of Cd/S ions, to have a narrow size distribution of NCs.

Thompson et al. [87] and Balazs et al. [88] using combination of self consistent field theory and DFT have predicted that in NCp, only NCs having sizes in a particular range will form. This is because, NCs are solid and thus polymer chains must stretch around these NCs, which causes a loss in conformational entropy and thus require extra energy. Further, this loss will be larger for larger NCs and thus larger energy is required to include these NCs. Therefore larger NCs will not be included in the bulk of the polymers as it is not favored thermodynamically. Also the process of formation and dissolution of NCs is an equilibrium process and thus smaller particles may be dissolved. This will lead to monodispersity in size of NCs within polymers as is observed in our case.

Thus, our experimental observations in corroboration with existing growth simulation studies suggests that co-operative growth mechanism leads to collapse of PVP, which in turn thermodynamically favors inclusion of only nearly monodispersive CdS NCs.

In view of the above discussion it is interesting to note the following:

i) Stirring leads to size distribution, although it may be homogenous as reported [185]. This suggests that if additional kinetic energy is provided, it allows larger size NCs to be included in polymer matrix thus leading to larger size distribution.

ii) 0.5-1 M Cd-A & ThU and 2-4g PVP gives rise to most interesting set of nearly monodispersive CdS NCs. Indicating suitable co-operative growth and polymer collapse conditions for these NCps.

iv) *Elashmawi* et al. have also reported decrease in crystallite size, with increase in Cd/S ion concentration with Cd/S ion concentration ~ 0.6, 1.2, 2.4 M (similar to our case). However, their observed size of CdS NCs and calculated size from absorption spectra shows inconsistency, probably as the spheres observed in TEM has been identified as CdS NCs, instead of polymer embedded with CdS NCs as is shown by us [193].

Table 4.2.1. Growth conditions, peak position (band gap), peak width, area under the curve and corresponding size of CdS NCs and PVP spheres are summarized for all NCps.

			PVP +H_2O + Cadmium acetate + Thiourea	Absorption spectra : band gap and absorbance obtained from fitting		Size of CdS NCs (~ nm) calculated from band gap	SEM: PVP sphere size (~ nm)
NCp	Cd-A/ThU (M)	PVP (g)	Growth conditions	Peak/Edge Position (width) nm	Area under the curve		
S1	0.01	4	70 ^{0}C : 3 hrs	482 (Edge)	___	8.0	
S2	1	2	RT : (40 hrs)	463.5 (50)	22.5	6.2	200-300
S3	1	4	-do-	463.9 (46)	10	6.3	300-400
S4	0.5	2	-do-	482 (50)	0.89	8.0	300-600
S5	0.5	4	-do-	472 (70)	1.14	7	200-600
S6	0.5	0.05	-do-	481 (56)	0.9	8	100-200
S7	0.5	0.1	-do-	483 (60)	1.29	8.3	100-200
S8	0.5	10	-do-	510 (Edge)	___	32	
S2+	1	2	(S2) + (24 hrs)	482 (80)	68	8.2	400-500
S2H	1	2	(S2+) + (70 ^{0}C (1.30 hr) + 36 hrs)	495 (90)	15	11	200-600

To summarize, systematic study of one-step CBD grown CdS-PVP NCps suggests that co-operative growth mechanism plays an important role in the formation of these NCps. While, this method eliminates an additional step for growth of NCps, we find that complexity of the process actually led to better control on the growth i.e. formation of nearly monodispersive CdS NCs. Further, it is important to note that these CdS-PVP NCps have shown stability as we have not observed any changes in the absorption spectra and SEM images over ~10 years.

Based on the understanding developed, co-operative nature of growth for CdS-PVP NCp using CBD is further investigated using Raman and AFM mapping and will be discussed in next section.

4.3. Effect of relative concentration of Cd/S ion source and PVP on the morphology

In the previous section, we have discussed the results of absorption, PL and diffuse reflectance spectroscopy along with SEM data, which gives important insight into the inclusion of nearly monodispersive (absorption peak) CdS NCs in PVP sphere for 0.5 and 1 M Cd-A/ThU. However, PL and absorption spectra of NCps grown with 0.01 M Cd-A/ThU concentrations are significantly different.

Controlled synthesis of inorganic NCs-polymer NCp requires a good understanding of the influences of polymer chemical structure and its interactions with NCs. Further, question whether and how the morphology of composite materials can be effectively manipulated by changing the parameter of polymers such as its chain length or the characteristics of NCs such as their size and concentration of NCs is of current interest. As noted in the previous section the differences observed in absorption and PL spectra for S1 (0.01M, 4g{0.4 mM}) and NCp S2 (1M, 2g{0.5 mM}) may be related to morphology of the NCps, we further investigate this using Raman, AFM and PL mapping. Raman and AFM mapping on same sites, suggests that CdS NCs are mainly embedded in thin film of PVP for lower Cd/S ion concentration (0.01 M), whereas, sphere formation of PVP is observed for larger Cd/S ion concentration (1 M). This observed difference in morphology is corroborated with the existing growth modeling on NCps and is also used to explain the differences observed in absorption, PL and Raman spectra.

4.3.1. Study of co-operative growth: Raman mapping

To study co-operative growth mechanism using Raman mapping, we have chosen five

NCps: S1-S5. In the first part, we have studied the effect of interaction between CdS and PVP on the morphology of NCp. Further, effect of different relative concentration of Cd-A/ThU (0.5, 1 M) and PVP (2g, 4g) on the CdS NCs embedded in PVP spheres.

4.3.1.1. Effect of interaction between CdS and PVP on the morphology

In order to understand the difference observed in NCp S1 and S2 as noted in last section, we have performed GIXRD on these NCps to know, if structure plays any role in the same, along with Raman, PL and AFM mapping as discussed below.

Raman and AFM mapping

i) S1: 0.01 M, 4g (0.4 mM: PVP)

GISXRD data for S1 NCp is shown in Fig. 4.3.1a (INDUS BL-12). Position (2θ) and FWHM of each peak is estimated using Gaussian line shape, which shows diffraction peaks centered ~ $2\theta = 20.91^0$, 22.96^0. A comparison of the measured XRD data with JCPDS data (No. 751546 (C) & 772306 (H)) shows that peak exclusive to hexagonal ($2\theta = 20.91^0$) as well as cubic phase (~ $2\theta = 22.96^0$) is observed in this NCp. This suggests the formation of both cubic and hexagonal phase. Further, comparison of observed data with that of JCPDS data shows that both the planes are shifted towards lower 2θ values suggesting higher d (interplanar spacing) values. Interplanar distance $d = \lambda/2\sin\theta$, thus obtained, is used to estimate the strain = $(d - d_{hkl})/d_{hkl}$, where, d_{hkl} is the tabulated value of interplanar distance for (hkl) plane [264]. Positive values of strain suggest elongation in the planes, whereas negative value of strain suggests presence of compression. We find that the order of strain is ~ 0.02 and ~ 0.03 in cubic and hexagonal phase, respectively. Further, the calculated size of CdS NCs estimated from GIXRD data using the Scherrer formula [265] comes out to be ~ 40 nm, which is quite large as compared to size obtained using absorption spectrum (~ 8 nm). This is due to noted FWHM (~ 0.2^0) being underestimated due to presence of background (inset of Fig. 4.3.1a) and thus leading to overestimated size of NCs. Further, SEM is performed to study the morphology of this NCp. SEM image (Fig. 4.3.1b) of this NCp suggests presence of rarefied PVP spheres of size ~ 100 nm. This indicates that lower concentration of Cd/S ion source leads to formation of rarefied PVP spheres, which is further studied.

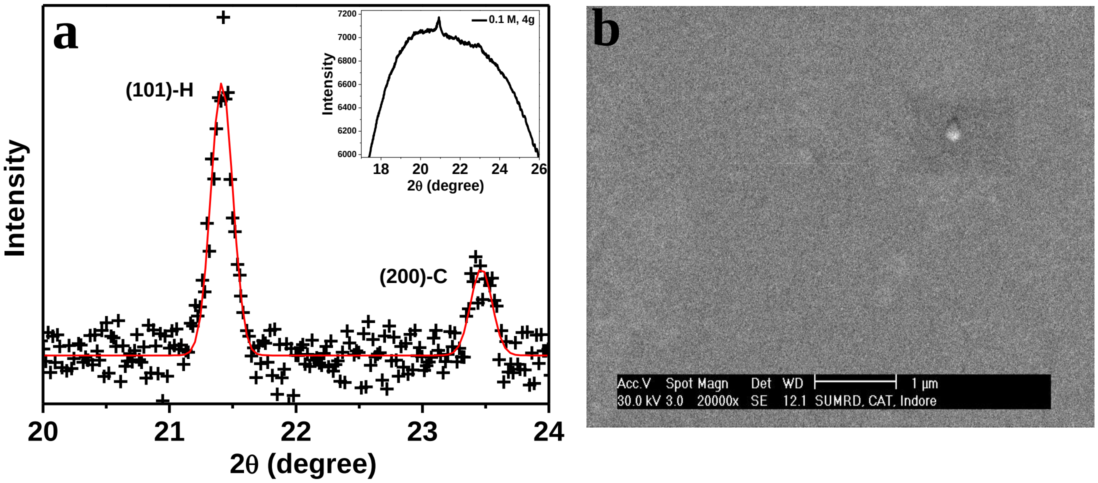

Fig. 4.3.1. a) GISXD pattern of NCp S1 showing formation of both cubic and hexagonal phase and b) SEM image showing rarefied PVP sphere. Inset shows presence of large background.

Optical image of S1 NCp created using microscope shows the presence of rarefied isolated white and black structures. Raman mapping is performed on the selected area at many places. Representative Raman image (10*10 μm^2 with step size ~ 0.1 μm, acquisition time ~ 3s) created using intensity of frequencies in the range 292-305 cm^{-1} is shown in Fig. 4.3.2b. This range is chosen because, while performing Raman spectroscopy measurements at spatially different positions, we observed variation in CdS LO phonon frequency from 295-303 cm^{-1}. Raman image and corresponding Raman spectra show observance of Raman signal corresponding to CdS over the whole mapping region (Fig. 4.3.2 b & c). Observed red shift of

LO phonon of CdS in the range 300 - 302 cm^{-1} and asymmetric line shape suggests existence of different size CdS NCs. Although, Raman line shape is found to be asymmetric, PCM fit to the line shape is not feasible due to presence of PL background. Further, there is variation in FWHM in the range 17 - 20 cm^{-1} over different region, indicating variation in crystalline quality of CdS NCs. In order to check the surface passivation of CdS NCs, PL mapping is performed, which shows variation in position of PL peak related to band gap suggesting size distribution of CdS NCs over different region of the NCp (Fig 4.3.2 d). Further, the FWHM of band gap related peak is ~ 50 nm. PL mapping shows defect PL in the range ~ 620 - 630 nm suggesting presence of

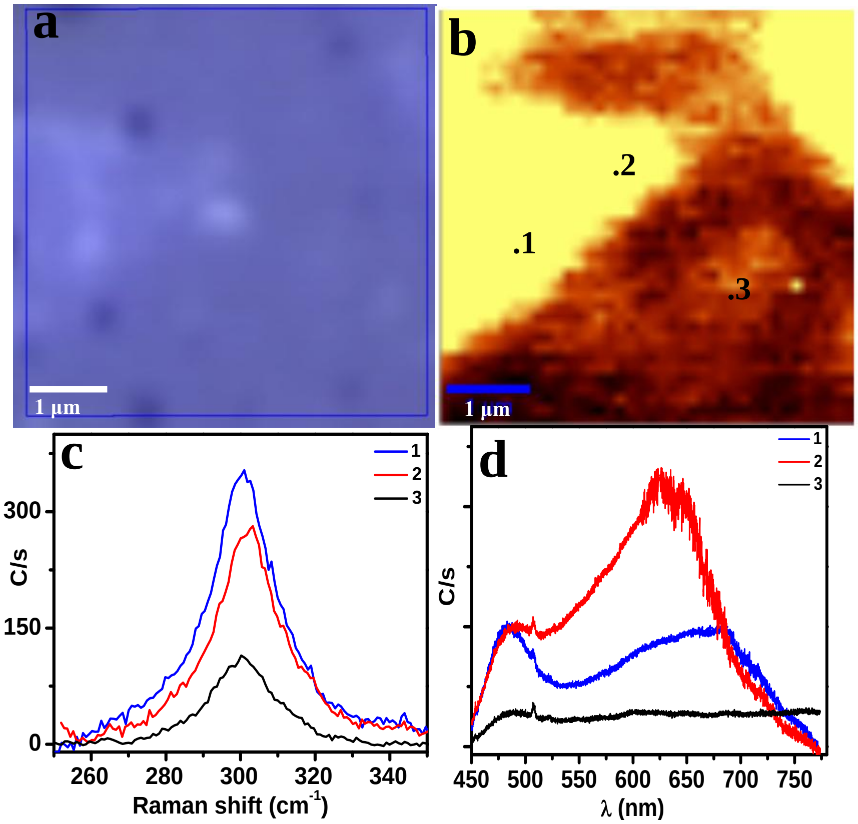

Fig. 4.3.2. a) Optical image of NCp S1 showing rarefied isolated PVP spheres, b) corresponding Raman image of the marked area, c) Raman spectra and d) PL spectra at marked positions show variation in Raman and PL peak position.

sulfur vacancies [266]. Also variation in intensity of defect PL over different region of the film (Fig. 4.3.2d) is observed. In most of the regions, intensity of defect PL is larger or comparable to intensity of band gap related PL peak. This suggests that CdS NCs formed in this NCps are not passivated properly.

Raman and PL mapping suggests presence of CdS NCs over whole region of the NCp. Further, SEM image as well as optical image suggests rarefied PVP spheres. This indicates the possibility that CdS NCs are embedded in PVP, wherein PVP is mainly taking the morphology of thin film. In order to know about the morphology of this NCp, AFM measurements (step size ~ 160 Å) are performed on the same region that is chosen to perform Raman mapping (Fig. 4.3.3). Topography image suggests no sphere like formation, however Raman mapping shows presence of CdS NCs (abs edge: size ~ 8 nm) over the whole region. Thus, Raman and AFM mapping suggests that lower concentration of Cd/S ion source leads to formation of CdS NCs, which are mainly embedded in thin film of PVP. We shall like to note that the black structures observed in these NCps shows Raman signal corresponding to graphite.

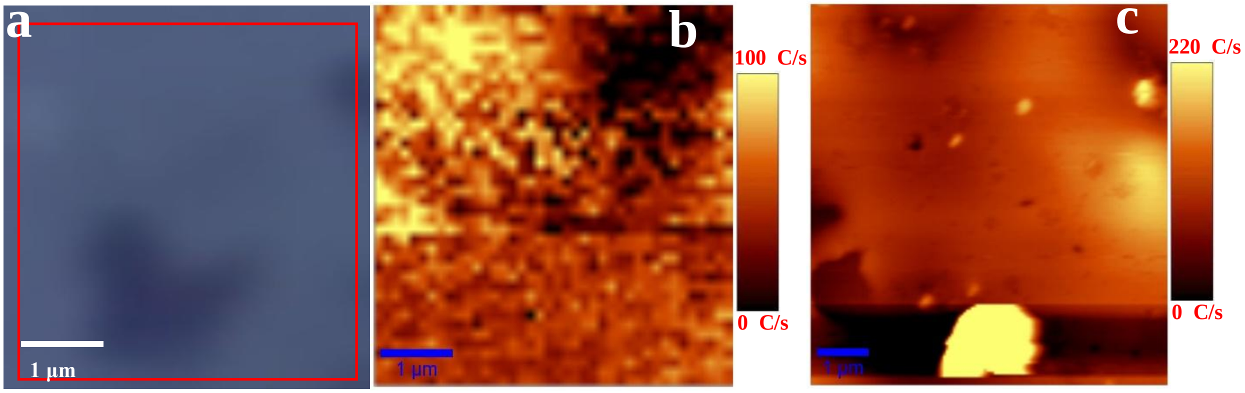

Fig. 4.3.3. a) Optical image created using 50 x objective, b) Raman image and c) topography image of the marked area in optical image.

In the above, we have discussed Raman and AFM mapping data of S1 NCp and interpreted that CdS NCs are embedded in thin film of PVP as sphere formation of PVP is not observed. It can also happen that only CdS NCs are formed at the substrate and not PVP film. However, previous study performed [257] as well as literature suggests that [174,179] with 0.01 M concentration of Cd-A/ThU, good crystalline and optical quality CdS thin should be formed with the growth conditions used. However, our absorption data suggests that CdS NCs of size ~ 8 nm (Table 4.2.1) are formed in this S1 NCps, which can happen if there is another source restricting the growth of CdS i.e. PVP. Since, sphere formation of PVP is not observed; only other possibility considered is thin film formation of PVP. This understanding is further corroborated with the existing theory and will be discussed later in this section.

ii) <u>S2: 1 M, 2g (0.5 mM: PVP)</u>

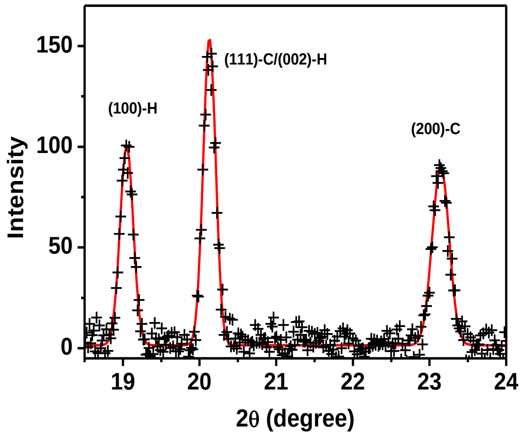

Fig. 4.3.4. GISXRD spectrum of NCp S2 showing peaks corresponding to both hexagonal and cubic structure.

GIXRD pattern of S2 NCp is shown in Fig. 4.3.4. Position (2θ) and FWHM of each peak estimated using Gaussian line shape, shows diffraction peaks centered ~ 2θ = 19.04^0, 20.13^0 and 23.15^0. A comparison of the measured XRD data with JCPDS data (No. 751546 (C) & 772306

(H)) shows that peak exclusive to hexagonal ($2\theta = 18.93^0$) as well as cubic phase (~ $2\theta = 23.36^0$) is observed in our NCps, whereas peak ~ 20.19^0 corresponds to both hexagonal and cubic phase. This suggests the formation of both cubic and hexagonal phase. Further, comparison of observed data with that of JCPDS data shows that hexagonal plane is shifted towards higher 2θ values suggesting lower d (interplanar spacing) values, whereas cubic plane is shifted towards lower 2θ values, which suggests compressive strain (~ 0.006) along hexagonal plane and tensile strain (~ 0.006) along cubic plane.

Optical image (Fig 4.3.5a) of S2 NCp suggests presence of isolated white PVP spheres. Raman mapping is performed on these spheres at many places. Representative Raman image (2*2 μm^2 with step size ~ 0.1 μm, acquisition time ~ 3s) created using intensity of frequencies in

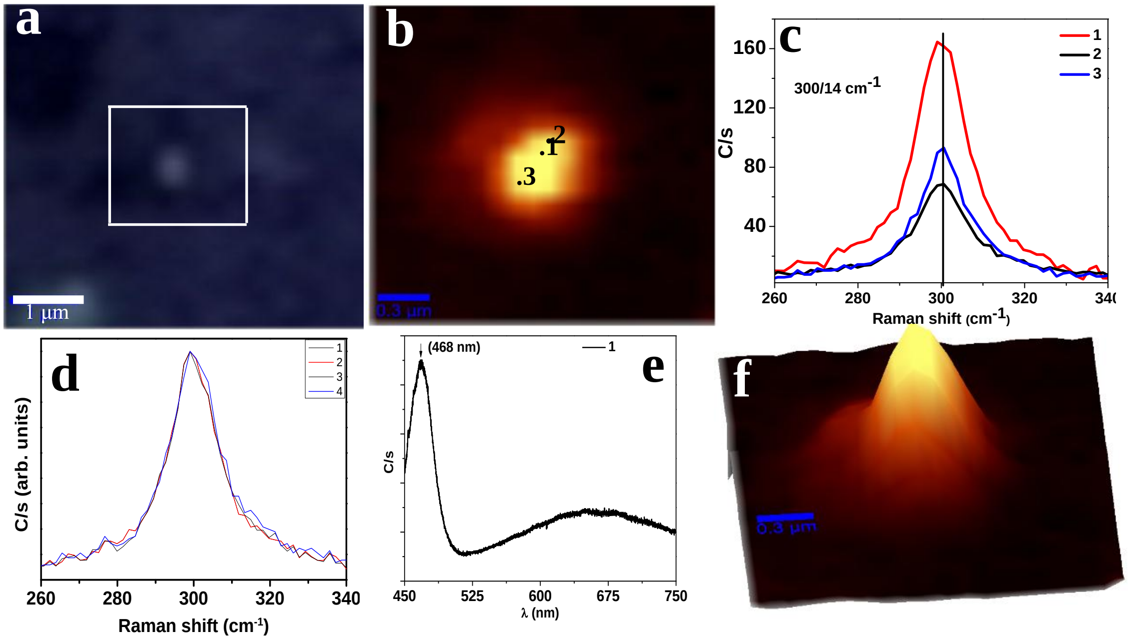

Fig. 4.3.5. a) Optical image of NCp S2, b) Raman image, c) corresponding Raman spectra at marker positions showing no change in LO phonon except intensity, d) Normalized Raman spectra at spatial different points showing no change in FWHM, e) PL spectrum and f) three dimensional Raman intensity intensity profile.

the range 292 - 305 cm^{-1} is shown in Fig. 4.3.5b. We observe asymmetric line shape of red shifted LO phonons ~ 300/14 cm^{-1} across this isolated PVP sphere (Fig. 4.3.5c) in the bright region. In the rest of the region, no Raman signal corresponding to CdS can be observed with this acquisition time as well with higher acquisition time. This shows that CdS NCs are present in the PVP spheres only. Further, PL spectrum (Fig. 4.3.5e) suggests that intensity of defect PL is quite less as compared to band gap related PL (~ 468 nm). Thus, Raman and PL data shows that CdS NCs are of better crystalline quality and are better passivated as compared to CdS NCs formed in S1 NCp. It is important to note that we have not observed any change in Raman (line shape, frequency, FWHM) and PL (peak position) spectra of CdS NCs embedded in one isolated PVP sphere (Fig. 4.3.5d) of size ~ 0.3 µm, where Raman data is taken in steps of 0.1 µm (Fig. 4.3.6). However, these parameters vary from one PVP sphere to other PVP sphere. This indicates presence of nearly monodispersive CdS NCs inside one PVP sphere. However, size of PVP sphere is less as compared to spatial resolution of the system (~ 0.4 µm). Thus, in order to find

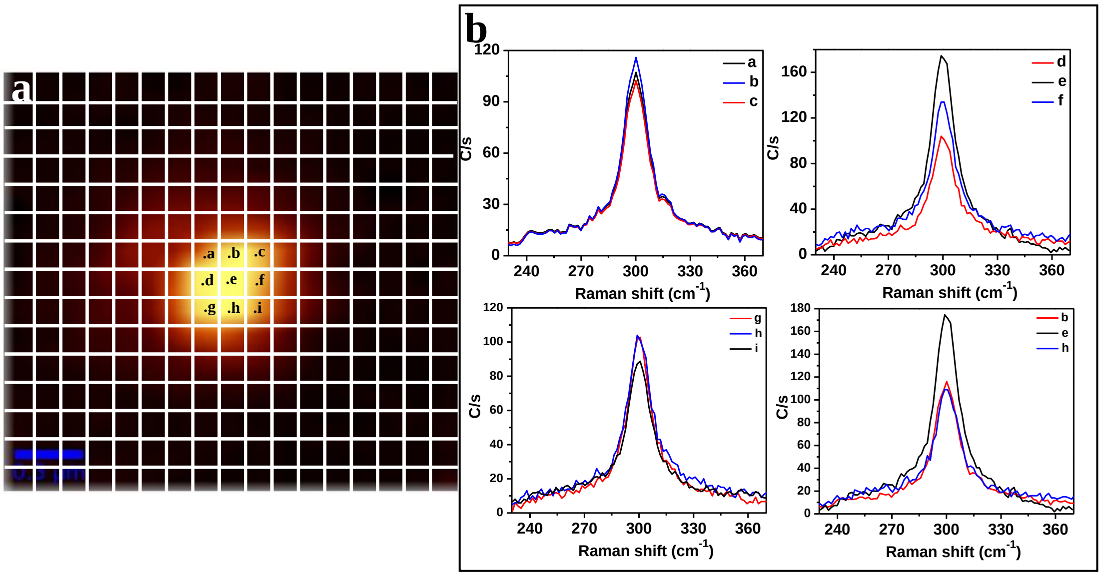

Fig. 4.3.6. a) Raman image of NCp S2, wherein array is formed with step size of 0.1 µm, b) corresponding Raman spectra for all the positions marked in Raman image.

out, whether these observations are due to presence of nearly monodispersive CdS NCs or because the size of PVP sphere is less than the spatial resolution of the system, we have performed Raman mapping in the region where we have observed two closely placed PVP spheres (ref: Annexure 4.3.1).

Raman mapping of two closely spaced PVP spheres (Fig. A4.3.1) shows variation in Raman and PL peak position and line shape at step size of ~ 0.1 μm, which shows that the observed spatial resolution is better. This is understood to be due to decrease in actual laser intensity, which reaches CdS NCs inside the PVP sphere because of scattering of light from the PVP sphere. Thus, only the highest intensity of Gaussian beam gives measureable Raman signal in Raman mapping leading to observance of better spatial resolution than expected. Therefore, from the Raman mapping data, one can say that nearly monodispersive CdS NCs are embedded in isolated PVP sphere. This is consistent with the observed absorption peak in the absorption data.

In order to know about the sizes of PVP spheres, AFM measurements (step size ~ 160 Å) are performed on the same region that is chosen to perform Raman mapping. One to one correspondence is observed between optical, Raman and AFM image (Fig. 4.3.7). Topography image shows presence of isolated PVP spheres (Fig. 4.3.7c & d). Raman mapping suggests presence of CdS NCs in these PVP sphere and black structures only. Further, AFM measurements show that size of isolated PVP spheres is ~ 200 - 300 nm.

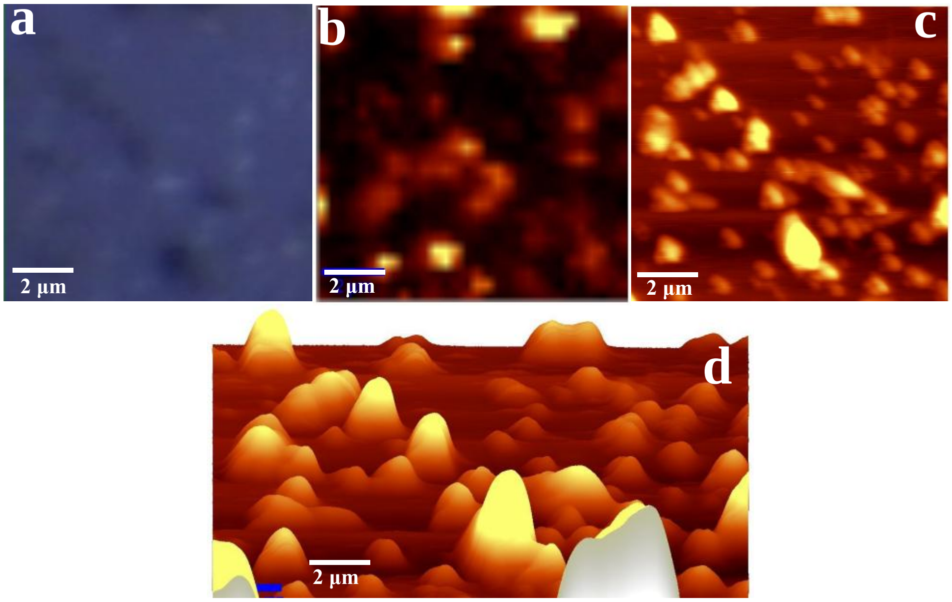

Fig. 4.3.7. a) Optical image, corresponding b) Raman image, c) AFM image of NCp S2 and d) 3D profile of topography image showing presence of spheres.

Thus, Raman and AFM mapping data of NCp S1 and S2 suggest two different morphologies of CdS-PVP NCps, i) thin film formation of PVP and ii) sphere formation of PVP. Further, sphere formation of PVP leads to inclusion of only nearly monodispersive CdS NCs of better crystalline quality with better passivation, whereas, this thin film formation of PVP leads to broad size distribution in CdS NCs with relatively poor crystalline quality and surface passivation. Both these NCps are grown at room temperature. Since, concentration of PVP is similar for both the NCps, lower concentration of Cd/S ion source is expected to give smaller size CdS NCs and one would expect larger size distribution for larger Cd/S concentration. However, our observations suggest the opposite behavior. The only difference between these two NCps seems to be the relative ratio of Cd/S ion source and PVP, which is expected to lead the observed differences. It may be important to recall that the spherical morphology of PVP has led to near monodispersivity of CdS NCs. This further emphasizes the fact that co-operative growth mechanism plays an important role in deciding the morphology of these NCps. The collapse of polymer in presence of NCs has been modeled as already discussed in last section. Further, corroboration of our experimental result with the predictions of growth modeling studies [89,267] is discussed in the following.

Theory Corroboration

Simulation on growth modeling suggests that the collapse of polymer depends on 1) attractive interaction between NCs and polymer and 2) concentration of NCs [89]. The collapse of polymer happens when polymer undergoes a sharp change from an extended, low density state to a high density collapsed accompanied by a corresponding sharp increase in density of NCs absorbed within the polymer [89,267], which means that the collapse transition of polymer is a first-order phase transition. This transition occurs as a competition between NC-polymer attraction, which tends to shrink the polymer chain and repulsion between side chains of monomers of a polymer, which tends to expand it. Indeed, the evidence of attractive interaction between Cd^{2+} ion of CdS NCs and C=O of PVP is reported [262] and later it is also predicted using DFT [263]. This suggests that the attractive interaction between CdS NCs and PVP as well as high density of CdS NCs leads to formation of PVP spheres, which can overcome the repulsion of side chains at room temperature for S2 NCp. This can also be seen from three dimensional intensity profile of Raman image (Fig. 4.3.5f), which shows Gaussian profile of isolated PVP sphere embedded with CdS NCs. Monte Carlo simulations performed by Antypov et al. [267] show that the attraction between NC and polymer leads to collapse of polymer, with volume absorption of high density NCs, as is observed in Raman mapping (Fig. 4.3.5f). This further suggests that high density of CdS NCs is leading to sphere formation of PVP sphere.

Further, theoretically it is predicted that change in density of NCs by three times can lead to differences in the morphology of NCp, wherein they have take polymer containing 100 monomers [89]. In S1 NCp, lesser concentration of Cd/S ion source is expected to give lesser density of CdS NCs compared to S2, which is also supported by absorption spectra. Thus, one can say that the lower density of CdS NCs does not fulfill the collapse condition for PVP. Thus, high density of CdS NCs leads to formation of PVP sphere as is observed for 1 M Cd-A/ThU concentration for 2g PVP content, whereas, low density of NCs (i.e. low concentration of Cd-A/ThU (0.01 M) as compared to PVP content (4g)) will mainly lead to thin film formation of PVP. Thus, corroboration of Raman and AFM mapping with theoretical predication suggests that density of CdS NCs is an important factor affecting the morphology of CdS-PVP NCps. Further, in previous section, we have discussed that formation of PVP sphere thermodynamically favors inclusion of only nearly monodispersive CdS NCs. Since, NCs are embedded in high density PVP spheres; they are better passivated in S2 NCp as compared to S1 NCp. These two NCps are further studied using Attenuated total reflectance-Fourier transform Infrared spectroscopy **(**ATR-FTIR) measurements to get further information about interaction between two constituent components, which are leading to very different morphologies in these cases as discussed below.

Fourier transforms Infrared spectroscopy

We have performed attenuated total reflectance-Fourier transform Infrared spectroscopy (ATR-FTIR [268]) on these chosen NCps. IR spectra give information of various functional groups within a molecule and the vibrations related to specific bonds thus reflect effect of surrounding environment. FTIR for CdS-PVP NCp can give direct evidence of the change in interaction between CdS NCs and PVP in case of thin film or sphere formation of PVP. FTIR measurements in transmission mode were not feasible due to presence of absorbing glass substrate. Therefore, ATR-FTIR measurements were performed on these NCps, in here IR beam is directed into a crystal of relatively higher refractive index as compared to sample. The IR beam is totally internally reflected at the crystal/sample interface. Because of its wave-like properties, the light is not reflected directly by the boundary surface but from the sample. The fraction of light reaching into the sample i.e. it's penetration depth depends on the incident wavelength, incident angle, the refractive indices of the ATR crystal and the sample. In the spectral regions where the sample absorbs energy, the wave is attenuated. After several internal reflections, the IR beam exits the ATR crystal and is directed to the IR-detector. In case of polymer-metal hybrid materials, the interaction between functional groups of polymer such as NH_2, -CO-, etc and Cd^+, Ga^+, Mn^+ ions etc. is expected. For example, in PVP, the C=O groups show a prominent peak at ~ 1650 cm^{-1} in FTIR spectrum [269]. This characteristic peak is used to explore the interaction between PVP and metal ions. The shift in the peak towards lower wave number is attributed to bond weakening as a result of bond formation between O atom and Cd ion, which eventually passivate the NC surface.

ATR-FTIR spectroscopy measurements are performed in the region 600 – 1800 cm^{-1}. Comparison of FTIR spectra (Fig. 4.3.8a) for glass substrate and NCps suggest presence of signal from substrate too. After the removal of this background (FTIR of substrate), we have plotted the spectra (Fig. 4.3.8b) in the range 1550 - 1750 cm^{-1} in order to study the effect of interaction between CdS and PVP on the C=O of PVP for two NCps S1 and S2. It is important to note that FTIR background is nearly flat in this region.

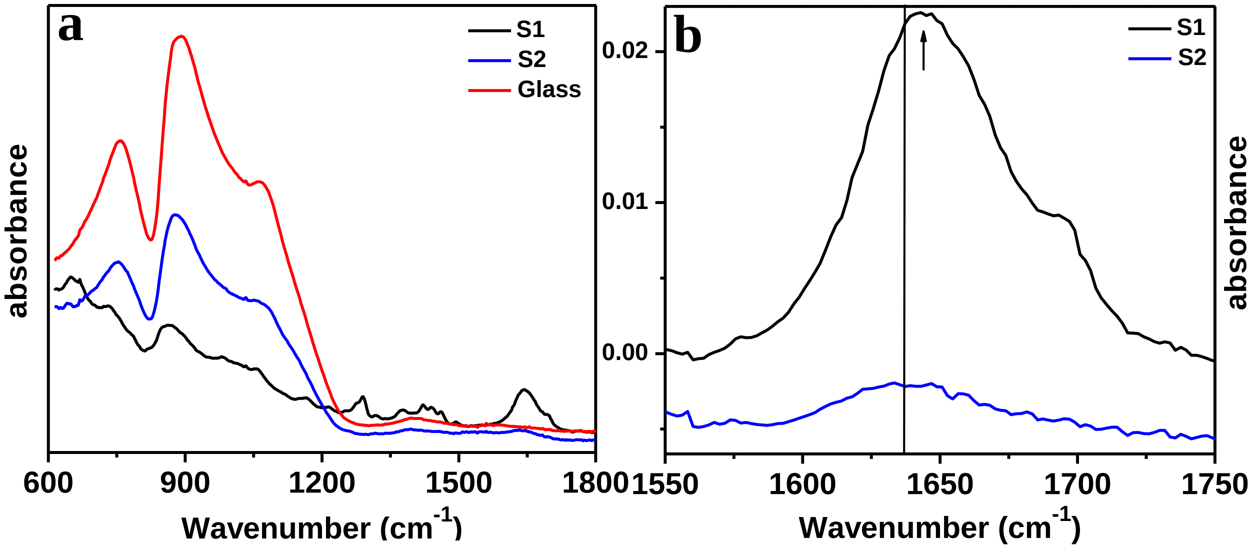

Fig. 4.3.8. a) ATR-FTIR spectra of S1 (black line), S2 (blue line) and plain glass substrate (red line) and b) ATR-FTIR spectra obtained after removing the substrate background for S1 and S2 NCps.

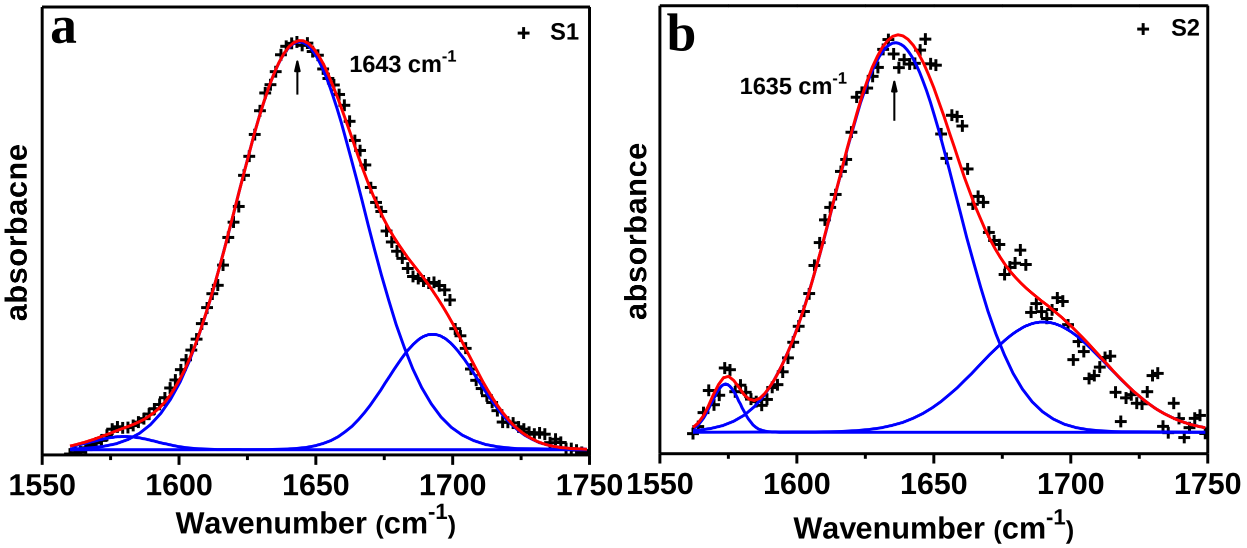

Fig. 4.3.9. ATR-FTIR spectra of NCps a) S1 and b) S2. Solid line (red) is fit to raw data (+) and separate Gaussian peaks are shown by blue solid line.

FTIR spectra of the both the NCps are well fitted using Gaussian function (Fig. 4.3.9), which suggests presence of large distribution in the bonding environment. Comparison of spectra for S1 and S2 NCps (Fig. 4.3.9) suggests that in the both the NCps, peak corresponding to C=O is red shifted as compared to that reported for pure PVP (~ 1650 cm^{-1}), manifesting interaction between CdS NCs and PVP. Further, we find that the observed red shift is larger in S2 (~ 1635 cm^{-1}) as compared to S1 (~ 1643 cm^{-1}). Since, observed red shift suggests interaction between NC and PVP, the greater peak shift reveals stronger interaction [270] between CdS and PVP. Therefore, FTIR results suggest stronger interaction between CdS NCs and PVP in S2, which is consistent with our understanding developed that the strength of total interaction between CdS NCs and PVP is large due to large density of CdS NCs, which is leading to sphere formation of PVP. Whereas, strength of total interaction is weaker for lesser density of CdS, which is giving rise to thin film formation of PVP. It is important to note that the intensity of absorption peak is large in S1 as compared to S2. This is understood as in S1 NCp, there is continuous film of PVP, whereas, isolated PVP sphere are observed in S2 leading to decrease in cross section. Another peaks observed ~ 1575 cm^{-1} and ~ 1693 cm^{-1} in both NCps corresponds to graphite and amide group of PVP, respectively

4.3.1.2. Effect of relative concentration on size and passivation of CdS nanocrystals embedded in PVP spheres

Change in concentration of Cd/S ion source

We have studied the effect of change in concentration of Cd-A/ThU from 0.5 to 1 M for 2g/4g PVP. Absorption spectra show decrease in band gap of CdS NCs with the decrease in Cd-A/ThU concentration from 1 M (Eg ~ 463 nm) to 0.5 M (Eg ~ 482 nm). XRD measurements in both these sample suggests presence of both cubic and hexagonal phase. Further, we find compressive strain (~ 0.006) in hexagonal plane and tensile strain (~ 0.006) along cubic plane. This suggests that decrease in band gap of CdS NCs for 0.5 M Cd-A/ThU can be correlated to increase in size of NCs (~ 8 nm). Further, AFM measurements in agreement with SEM results show increase in variation in sizes of PVP spheres (from 200-300 nm to 300-600 nm) with decrease in Cd-A/ThU concentration (Figure 4.3.10 c & g). This suggests that increase in size of CdS NCs leads to increase in size of PVP spheres. This is expected as the polymer sphere has to increase its volume in order to accommodate larger NCs, which is leading to increase in size of PVP sphere [87,88].

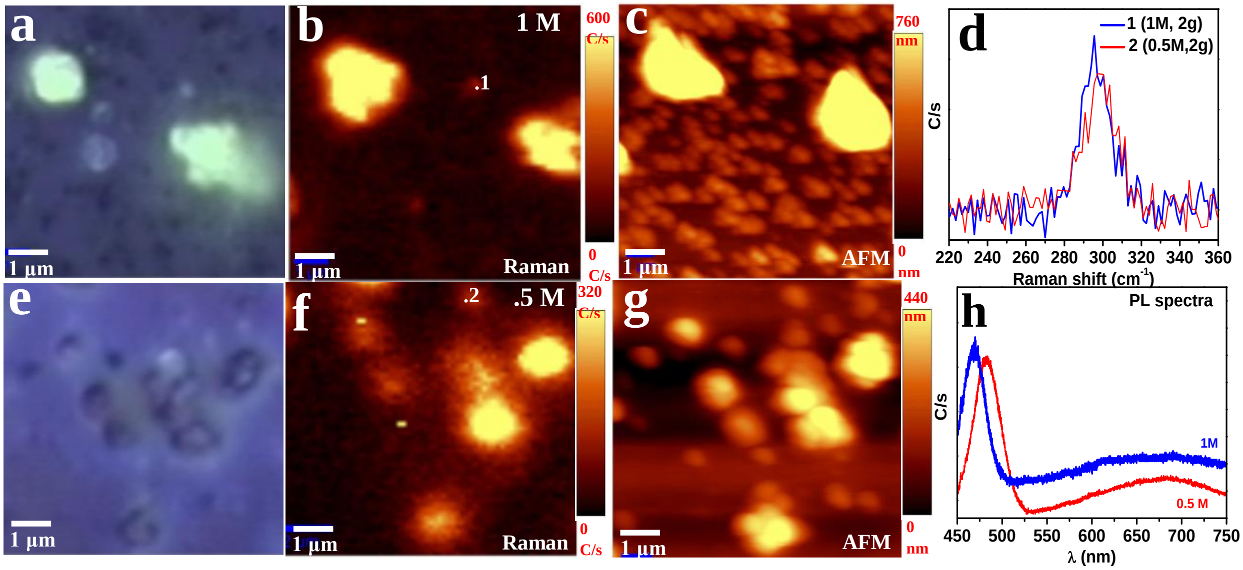

Fig. 4.3.10. Optical image, Raman image and corresponding AFM image for NCps S2 (a, b & c) and S4 (e, f & g). d) Raman spectra and h) PL spectra at marked positions.

For 0.5 M concentration of Cd-A/ThU we have observed sizes of PVP spheres in the range 300 - 600 nm. Comparison of Raman and PL mapping of isolated PVP sphere with size ~ 300 nm show that smaller CdS NCs (band gap PL ~ 468 nm) are embedded for 1M Cd-A/ThU concentration (Fig. 4.3.5) compared to that for and 0.5 M concentration (band gap PL ~ 482 nm: Fig. 4.3.11). FWHM in smaller CdS NCs is expected to be larger due to confinement effects, however, it is smaller (~14 cm^{-1}) compared to that for larger NCs (~ 17 - 22 cm^{-1}), which suggests that smaller CdS NCs are of better crystalline quality. Further, Raman and PL mapping shows variation in FWHM (~ 17 - 22 cm^{-1}) of LO phonon as well as variations in intensity of defect PL across one PVP sphere in NCp S4 (0.5 M). At some spatial positions, intensity of defect PL is comparable to intensity of band gap PL. This suggests that larger CdS NCs embedded in similar size PVP sphere (~ 300 nm) are of degraded crystalline quality and passivation.

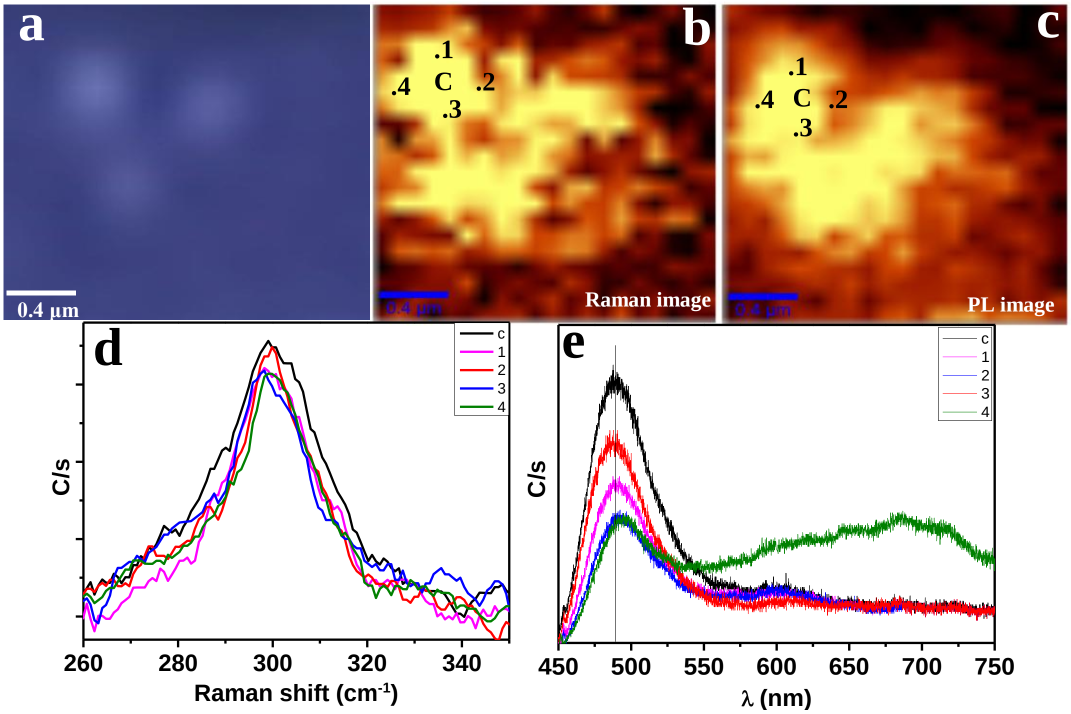

Fig. 4.3.11. a) Optical image shows three isolated PVP spheres, b) corresponding Raman image, c) PL image, d) & e) Raman and PL spectra on the marked positions.

Raman and PL mapping (Fig. 4.3.12) of PVP sphere of size ~ 600 nm (S4: 0.5 M) shows variation in size of CdS NCs as there is variation in frequency of LO phonon in the range ~ 298 – 300 cm^{-1} and variation in position of band gap related PL (band gap PL varies in the range 492 - 499 nm). FWHM of LO phonon also varies in the range 16 - 22 cm^{-1} across this isolated PVP sphere. Comparison of PL mapping at two different size PVP spheres (size ~ 300 nm (Fig. 4.3.11) and 600 nm (Fig. 4.3.12) shows that smaller CdS NCs (band gap PL ~ 484 nm) are embedded in smaller PVP sphere, whereas large NCs (band gap PL varies in the range 492 - 499 nm) are embedded in larger sphere. PL mapping shows that the CdS NCs of different sizes are randomly dispersed within the PVP sphere. Also for larger PVP sphere, intensity of defect PL is larger as compared to that in smaller sphere suggesting poor passivation. Thus Raman mapping in corroboration with PL mapping shows that smaller NCs embedded in small PVP spheres are of better crystalline quality and are better passivated as compared to larger CdS NCs embedded in larger PVP spheres. This suggests that size of PVP sphere depends on the size of CdS NCs, which in turn further affects the crystalline quality and passivation of CdS NCs i.e. co-operative mechanism plays an important role in the growth of CdS-PVP NCps.

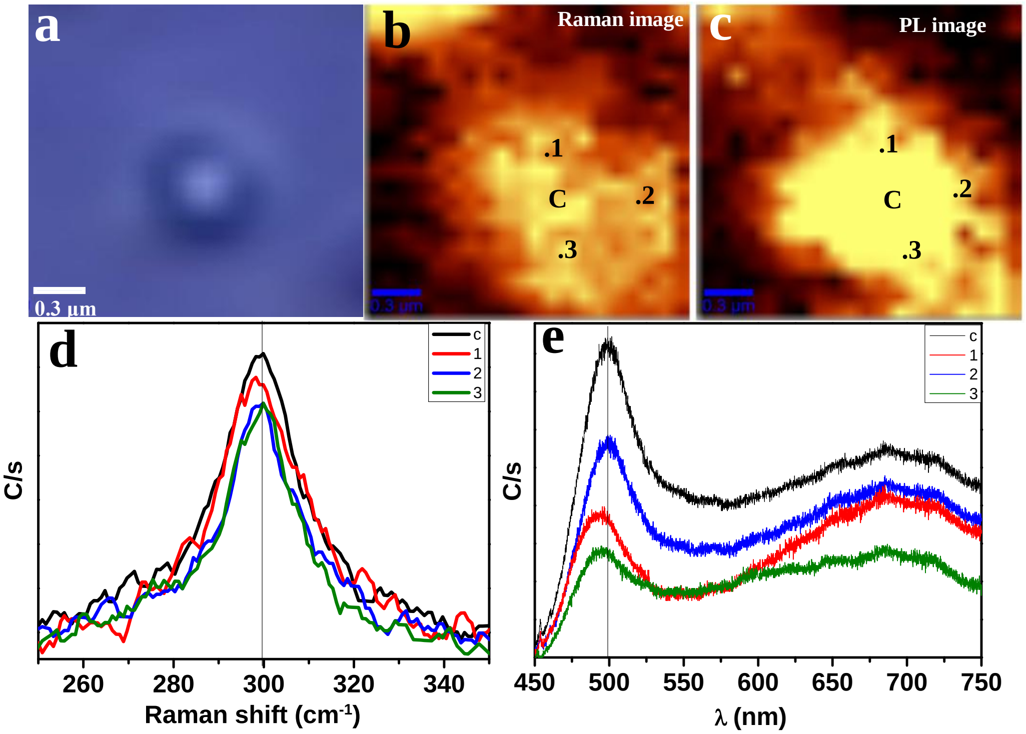

Fig 4.3.12. a) Optical image showing isolated PVP sphere ~ 600 nm, b) corresponding Raman image, c) PL image, d) & e) Raman and PL spectra on the marked positions.

Change in size of CdS NCs as well as PVP sphere occurs simultaneously when, concentration of Cd-A/ThU relative to PVP is varied. This suggests that the growth mechanism is co-operative in nature. In addition, absorption spectroscopy, Raman, PL and AFM mapping show that smaller and larger sizes CdS NCs are included respectively in smaller and larger PVP spheres. Further, smaller size CdS NCs are of better crystalline quality and better passivated. This is understood as surface area is larger for larger CdS NCs and hence, passivation of all the dangling bonds is thermodynamically less favored, as polymer has to wrap around a NC. It also shows that for different relative ratio of Cd-A/ThU and PVP concentration, the same PVP sphere size gives different size of CdS NCs. Further, for the same NCp, when the PVP sphere size increase from 300 nm to 600 nm, it is observed that there is corresponding increase in size of CdS NCs from ~ 8 nm to ~ 12 nm. This is consistent with the results [267] obtained from growth simulation studies, which suggests increase in size of polymer sphere due to increase in szie of NC.

Change in concentration of PVP

We have studied the effect of concentration of PVP from 2g to 4g for Cd-A/ThU concentration of 0.5 & 1 M. Absorption spectra suggest similar size (~ 6 nm) CdS NCs in both these NCps. PL mapping also suggests that similar size CdS NCs are formed with the increase in PVP content from 2g (1 M Cd-A/ThU: band gap PL ~ 468 nm) to 4g (1 M Cd-A/ThU: band gap PL ~ 468 nm). Mapping (Fig. 4.3.13) results show that CdS NCs of similar size embedded in PVP spheres show poor passivation when growth is done using larger PVP content. Further, density and non-uniformity in PVP spheres size increase with the increase in PVP content. Both these results are consistent with our understanding that passivation of CdS NCs in case of sphere comes from conformation of the PVP, whereas CdS NC in PVP thin film are passivated by miscelle formation with PVP on surface of a NC. The later will have stronger dependence of passivation of NCs on PVP concentration.

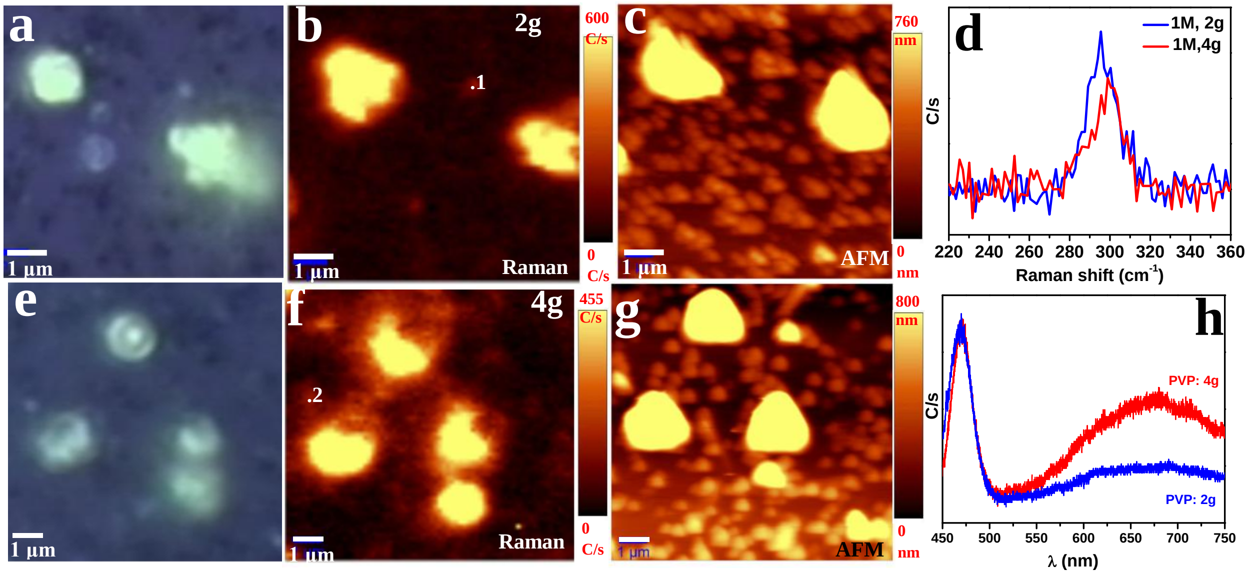

Fig. 4.3.13. Optical image, Raman image and corresponding AFM image for NCps S2 (a, b & c) and S3 (e, f & g). d) Raman spectra and h) PL spectra at marked positions.

To summarize, Raman and AFM mapping investigation of CdS-PVP NCps on same selected sites suggest that CdS NCs are embedded in PVP sphere and thin film of PVP for higher and lower concentration of Cd/S ion source, respectively. Sphere formation of PVP is understood to be due to larger density of CdS NCs, which is leading to stronger strength of interaction. ATR-FTIR spectroscopic measurements also support this understanding developed.

4.4. Effect of preheating of chemical bath on the morphology

In this section, we have used Raman and AFM mapping as a local probe in corroboration with average results obtained using XRD, to study the effect of heating the chemical bath on the growth of CdS-PVP NCps. In the earlier section (4.2), we have studied that on heating the chemical bath at 70 ^{0}C and further allowing the growth at room temperature in the chemical bath for 36 hrs (S2H:table 4.2.1), we found increase in size of CdS NCs as well as PVP spheres. This is difficult to explain, as CdS NCs are already embedded in PVP spheres and new PVP spheres may be formed, but the data suggests modification of existing CdS NCs and PVP spheres. In the present section, we have used Raman, PL and AFM mapping to understand this reformation of PVP spheres with larger size CdS NCs on preheating of chemical bath. Two NCps S2 and S3 are studied for the effect of increase in bath temperature. These two NCps are further kept at room temperature in same chemical bath for 36 hrs with preheating at 70 ^{0}C for 2 hrs and are referred as S2H (Table 4.2.1) and S3H.

4.4.1. Study of strain tuning of band gap

Before going into the discussion of S2H and S3H, we shall discuss Raman and AFM mapping for S2 and S3 NCps in further detail.

4.4.1.1. Growth at room temperature

Optical image of both these NCps show the presence of yellowish green coagulated structures and white PVP spheres. Here, we will discuss the mapping of coagulated structures. Representative Raman image of the chosen area (10*10 μm^2 with step size ~ 0.1 μm, acquisition time - 0.5 s) is created using intensity of frequencies in the range 292-305 cm^{-1} (Fig. 4.4.1b) to include the observed variation in CdS LO phonon frequency from 295-300 cm^{-1} at spatially different positions. Raman spectra show asymmetric line shape of phonons with frequencies varying in the range 295-300 cm^{-1} within one coagulated structure (Fig. 4.4.1). This suggests presence of CdS NCs of different sizes/stress in coagulated structures. Further, CdS NCs embedded in isolated PVP spheres (Fig. 4.3.5: FWHM ~ 14 cm^{-1}) are of better crystalline quality as compared to embedded in coagulated structures (Fig. 4.4.1: FWHM ~ 20 cm^{-1}). In the previous section, we have shown that nearly monodispersive CdS NCs are embedded in one isolated PVP spheres. However, parameters for CdS NCs i.e. frequency of phonon, it's FWHM changes from one sphere to another sphere. This can explain the variation observed in coagulated structures.

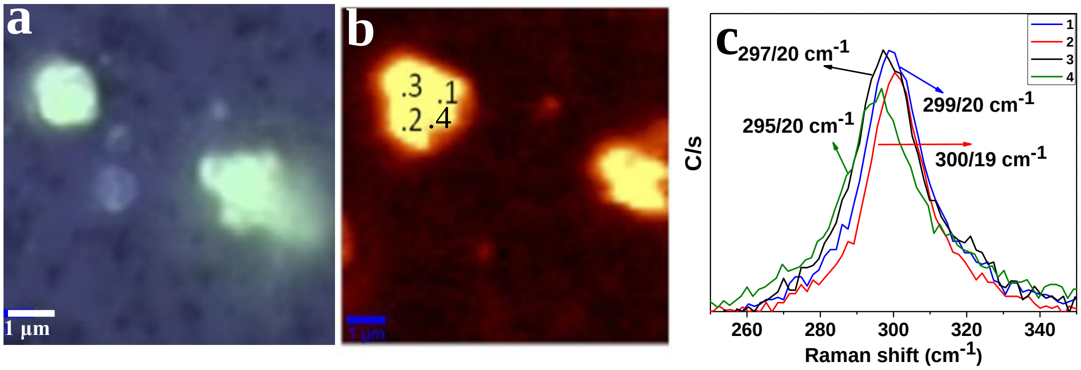

Fig. 4.4.1. a) Optical image of NCp S2, b) Raman image and c) corresponding Raman spectra of marked positions in Raman image showing variation in LO phonon.

After performing the Raman mapping once, we observe the diminishing of yellowish green color in the optical image. To check, whether laser heating is destructive in the present case, we have performed Raman mapping twice at chosen area consecutively. Raman mapping shows similar Raman image as obtained earlier (Fig. 4.4.2b & d). However, laser exposure has caused quenching of defect PL as observed in optical image (Fig. 4.4.2a & c) and Raman spectra

(Fig.4.4.2e). This suggests that laser annealing has caused reductions in the surface defects. This is further checked by performing time series PL spectroscopic measurements at similar power density that is used to perform Raman mapping. This measurement shows reduction of defect PL within a time span of 90s and after that we do not observe any change in the spectra (Fig. 4.4.2f).

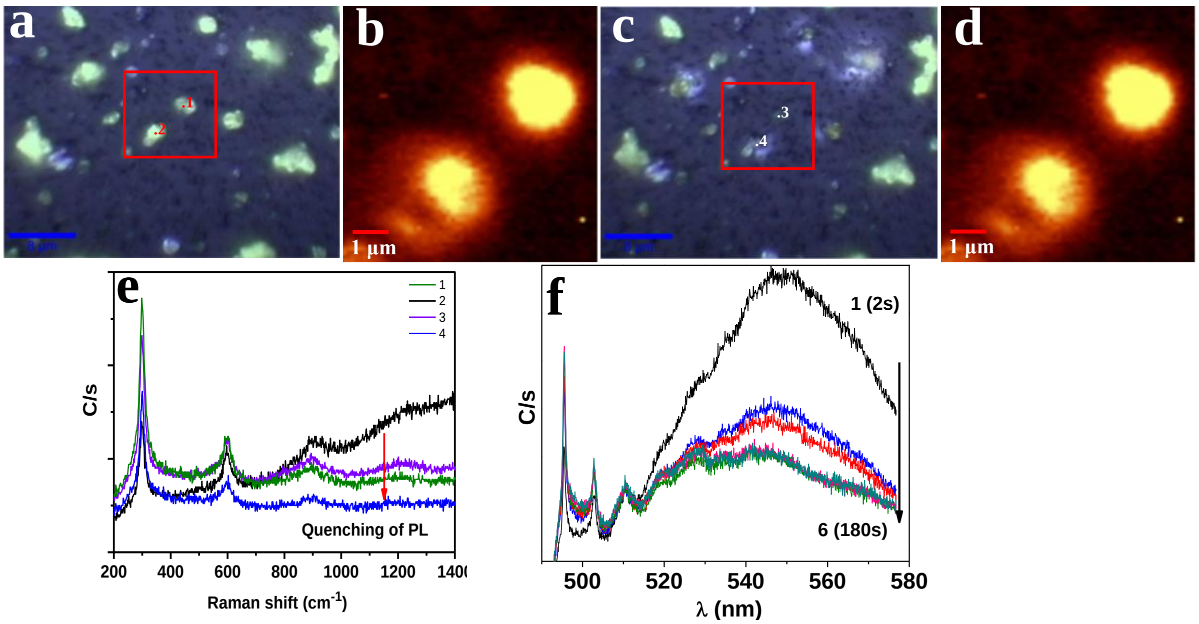

Fig. 4.4.2. a) Optical image, b) corresponding Raman image of marked area in (a), c) optical image after repeating the measurements again on the same area, d) corresponding Raman image of same area and e) Raman spectra showing quenching of PL after performing Raman mapping. f) Time series PL spectra showing reduction in defect PL.

In order to know about the sizes of PVP spheres, AFM measurements are performed on the same region that is chosen to perform Raman mapping. One to one correspondence is observed between Raman image and AFM topography (Fig. 4.4.3). Topography image shows presence of large coagulated PVP structures and isolated PVP spheres of different sizes (Fig. 4.4.4c). Size of isolated PVP spheres (200 - 300 nm) observed from AFM measurements are in accordance with SEM observation.

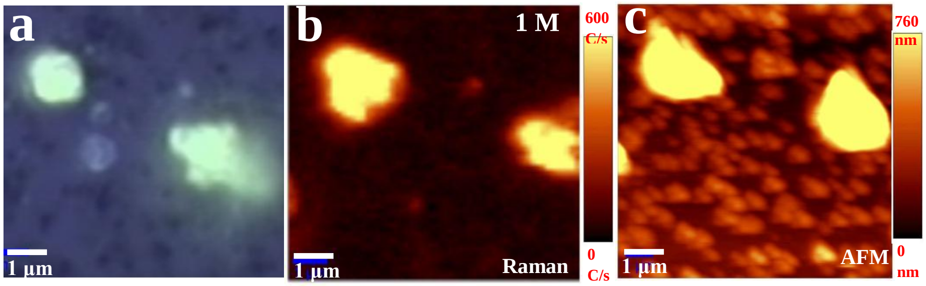

Fig. 4.4.3. Optical image, Raman image and corresponding AFM image for NCp S2.

Further, as discussed in the previous section, the GISXRD data of S2 NCps (Fig. 4.4.4), which suggests presence of both hexagonal and cubic phase. Further, comparison of observed data with that of JCPDS data shows that hexagonal plane is shifted towards higher 2θ values suggesting lower d (interplanar spacing) values, whereas cubic plane is shifted towards lower 2θ values. Using this, we find compressive strain (~ 0.006) in hexagonal plane and tensile strain (~ 0.006) along cubic plane. Presence of two phases can lead to the observance of stress.

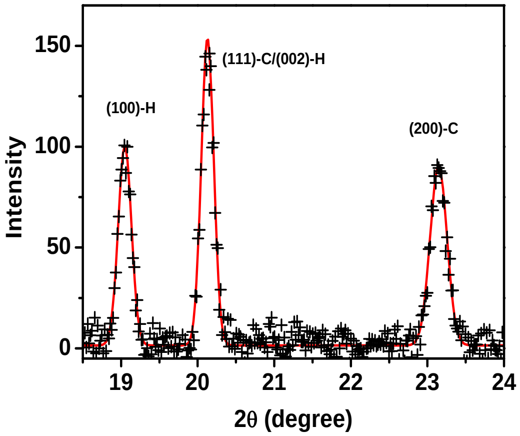

Fig. 4.4.4. GISXRD spectrum of NCp S2 showing peaks corresponding to both hexagonal and cubic structure.

4.4.1.2. Growth at room temperature after preheating at 70 ^{0}C

Optical image of these two NCps (S2H and S3H) suggests that coagulation has decreased considerably for these two NCps compared to S2 and S3. Representative optical image is shown for NCp S2H (Fig. 4.4.5a). Here, larger PVP sphere with size varies mainly from 0.5 - 0.7 µm have formed. Optical image (Fig. 4.4.5a), Raman image (Fig. 4.4.5b) and topography (Fig. 4.4.5c) image for NCp S2H show presence of two types of PVP spheres -1) isolated PVP spheres (~ 0.5 - 0.7 µm): type-I and 2) dimer: type II. Raman (Fig. 4.4.5b) and AFM mapping (Fig. 4.4.5c) performed on the same site show phonons ~ 298 and 300 cm^{-1} for isolated and dimer PVP sphere, respectively. Red shift observed in type I structure as compared to type II structure suggests either smaller size CdS NCs or presence of tensile stress. This is further studied using GIXRD measurements as discussed in the following.

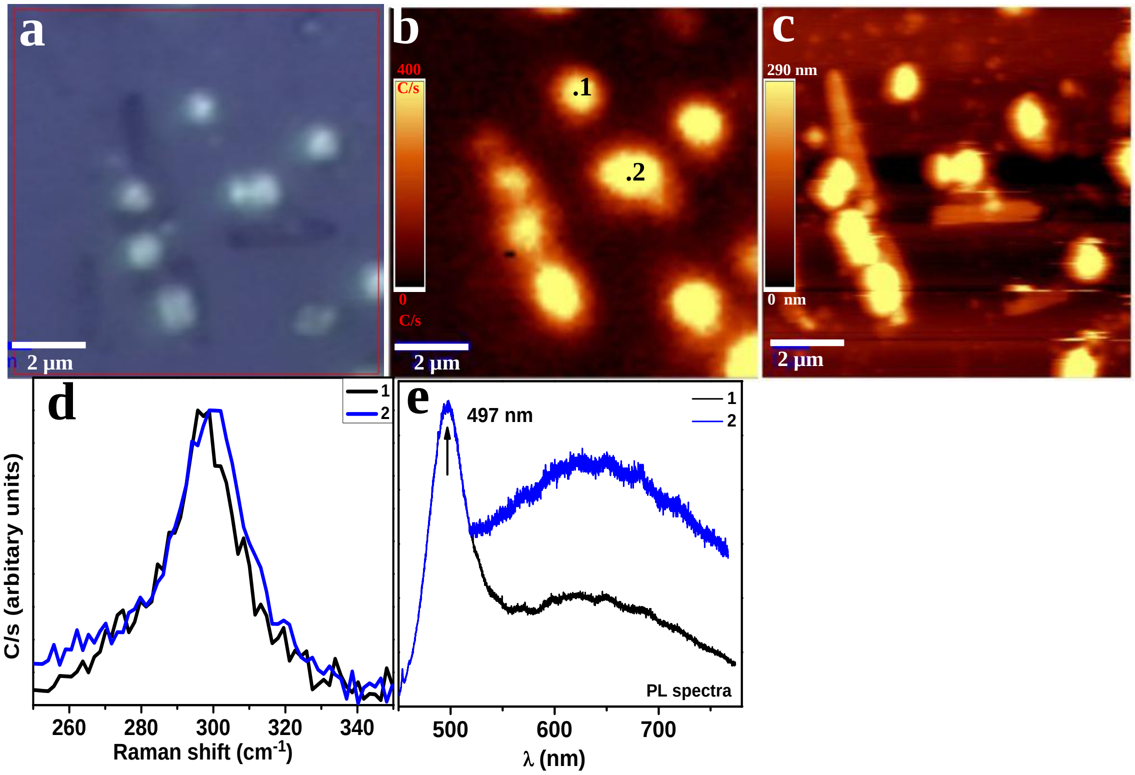

Fig. 4.4.5. a) Optical image of NCp S2H showing decrease in coagulation, b) Raman image, c) AFM image showing one to one corresponds between optical, Raman and AFM image, d) Normalized Raman spectra of marked positions showing difference in position of LO phonon and e) PL spectra at similar positions.

GISXRD data (Fig. 4.4.6) for NCp S2H and S3H shows diffraction peaks centered ~ 2θ = 21.48^0 (101 (H)). GISXRD pattern shows peak exclusive to hexagonal (2θ = 21.48^0) phase of CdS NCs. This shows the formation of dominantly hexagonal phase of CdS NCs in both the NCps, which suggests heating the chemical bath has led to formation only hexagonal phase of CdS NCs, which is stable phase of CdS. Further, it is interesting to note that a strong peak/shoulder at lower 2θ is observed in both the NCps suggesting presence of some region i.e. some of CdS NCs are under tensile strain ~ 0.006 and ~ 0.007 for NCps S2H and S3H, respectively. Taking Young's modulus ~ 62 GPa (of bulk [271]), we find that stress comes out to be ~ 0.3 GPa.

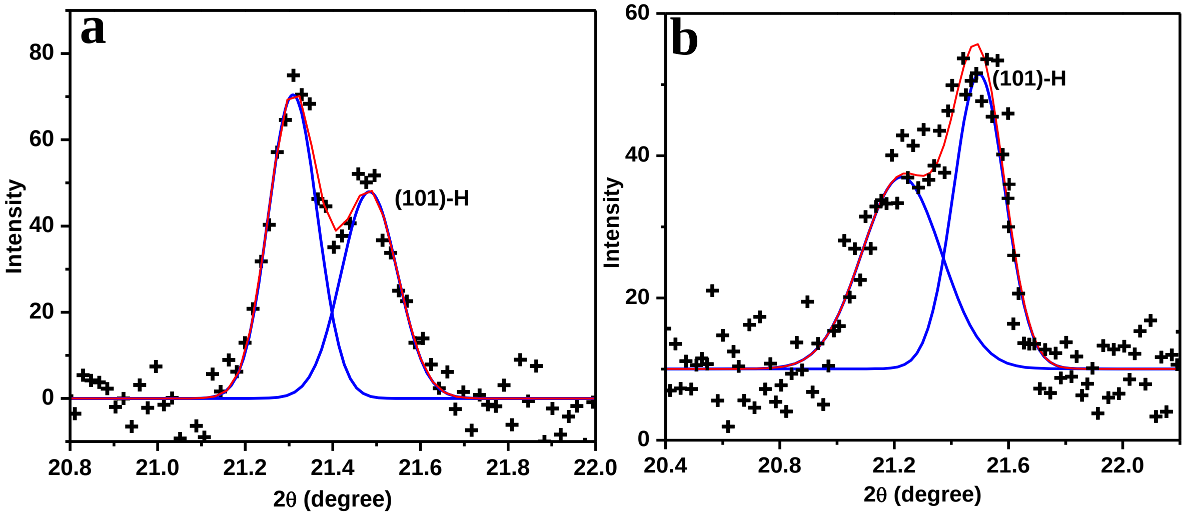

Fig. 4.4.6. a) GISXD pattern showing presence of only hexagonal phase for NCps a) S2H (1 M, 2g) and b) S3H (1M, 4g).

This order of stress leads to Raman shift ~ 1.8 cm^{-1} [272]. This suggests that observed Raman shift ~ 298 cm^{-1} from type I PS sphere may be due to presence of tensile stress indicating that the actual phonon frequency (inclusive of confinement effect) is ~ 300 cm^{-1} for both type I and type II spheres. Further, the stress will also change band gap [273] of CdS NCs. Stress ~ 0.3 GPa will lead to change in band gap ~ 0.12 meV. PL spectra of type I and type II structures are well fitted using three Gaussian peaks (Fig. 4.4.7). Strong band gap related peak for both the structures is observed ~ 497 nm. Further a sharp peak ~ 522 nm and 533 nm is also observed for type I and type II structures, respectively. Further, difference between these two band gaps observed is ~ 0.1 meV for type I sphere, similar with the calculated value using GIXRD data. This confirms that the observed stress is the reason for red shift of Raman spectra for type I w.r.t type II structures.

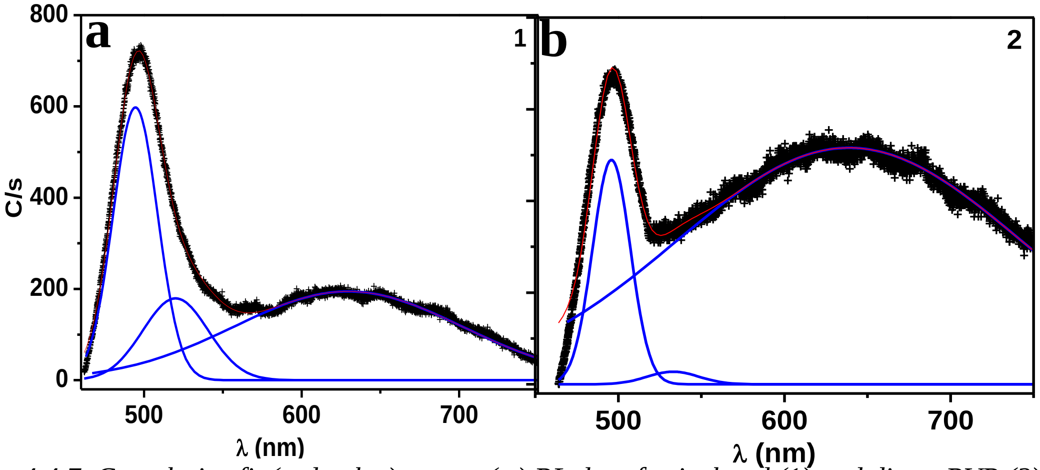

Fig. 4.4.7. Cumulative fit (red color) to raw (+) PL data for isolated (1) and dimer PVP (2) spheres. Separate Gaussian components are shown with solid line (blue color).

We have also performed Stokes/anti-Stokes Raman measurements (using 514.5 nm excitation) in these two types of structures. Intensity ratio of Stokes to anti-Stokes (I_S/I_{AS}) is nearly 1 (sharp resonance) for NCs embedded in isolated PS whereas, $I_S/I_{AS} > 1$ for two coagulated PSs (Fig. 4.4.8). This suggests presence of resonance Raman scattering in case of CdS NCs embedded in isolated PSs, which can be corroborated to the band gap peak ~ 522 nm observed in these structures. This band gap peak is closer to excitation source (514.5 nm) used for the Raman study. Thus, Raman and PL in corroboration with GIXRD suggest stress related band gap tuning resulting in resonance Raman scattering for CdS NCs embedded in type I structures. In the following, we shall analyze these results in perspective of NCps growth on heating of chemical bath.

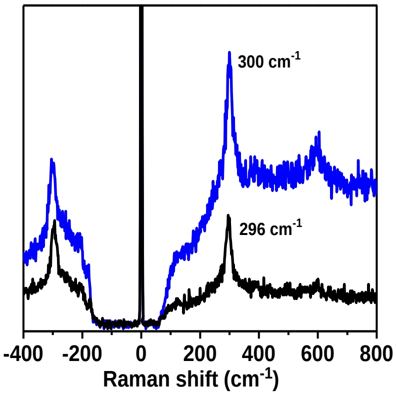

Fig. 4.4.8. Stokes/anti-Stokes Raman spectra for type I (black color) and type 2 (blue color) structures, performed using 514.5 nm excitation.

Raman and AFM mapping suggest conversion of coagulated structures in S2 to isolated PVP spheres in S2H after heating. This suggests that this growth condition has led to reformation of PVP spheres. Theoretically, it has been observed that heating at this temperature leads to disruption of water-polymer and nanocrystal-polymer bonds [274] indicating unfavorable condition for collapse transition of PVP. Thus this growth conditions can lead to opening of PVP spheres when heated at 70 ^{0}C and subsequent room temp growth will lead to reformation of PVP spheres. Similar observations are also made for NCp S3H. However, comparison of three dimensional topography images for NCp S3H (Fig. 4.4.9d) and S2H (Fig. 4.4.9e) suggests that the isolated PVP spheres show nearly Gaussian profile, whereas, dimmers show flat at the top. For S3H NCp, mainly flat shape is observed at the top suggesting that mainly dimmers of PVP spheres are formed, whereas, in NCp S2H, isolated spheres are of high density. This could be due to larger density of PVP spheres in S3 leading to more dimer formations in S3H. Further, from the above discussion, one can say that tensile strain for CdS NCs embedded in isolated PVP spheres on growth after heating gets relaxed on dimmer formation.

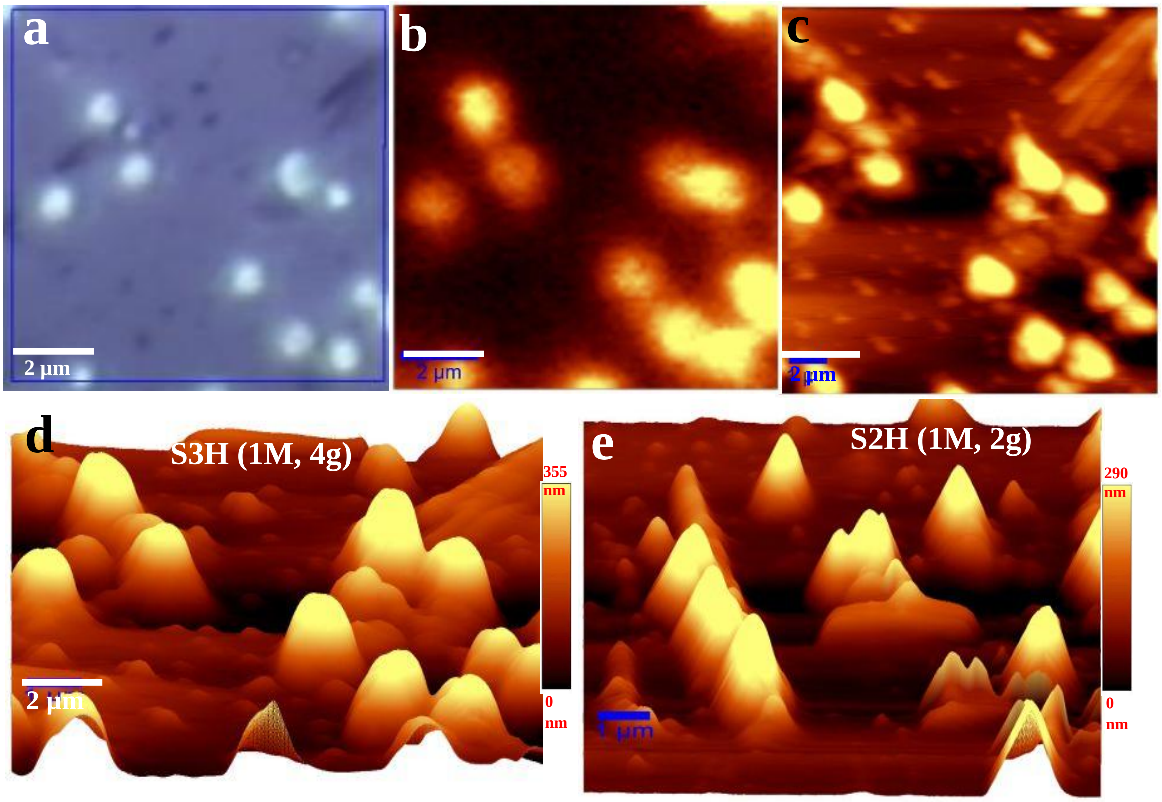

Fig. 4.4.9. a) Optical image of NCp S3H, corresponding b) Raman and c) topography image. Comparison of 3D topography image of d) S3H and e) S2H suggests larger density of dimmers in S3H NCp.

ATR-FTIR spectroscopy: Comparison for S2 and S2H

Comparison of IR spectra for NCps S2 and S2H (Fig. 4.4.10) suggest presence of two peak ~ 1618 cm^{-1} and 1650 cm^{-1} corresponding C=O in S2H, wherein peak ~ 1618 cm^{-1} is red shifted from it's normal value (~1650 cm^{-1}). This can be corroborated with the observation of two peaks corresponding to normal and stressed CdS NCs in XRD data. Peak observed ~ 1618 cm^{-1} corresponding to C=O is more red shifted in NCp S2H compared to that in S2 (~ 1635 cm^{-1}). Tensile strain in CdS NCs weakens the Cd-S bond, which will lead to corresponding strengthening of C-O bond of PVP, which is connected to Cd. This will lead to more red shift of C-O bond for S2H as compared to S2. An additional peak ~ 1650 cm^{-1} suggests presence of some region wherein C=O bond is unperturbed. This can be correlated to dimer structures consistent with larger defect PL indicating dangling bonds of CdS NCs.

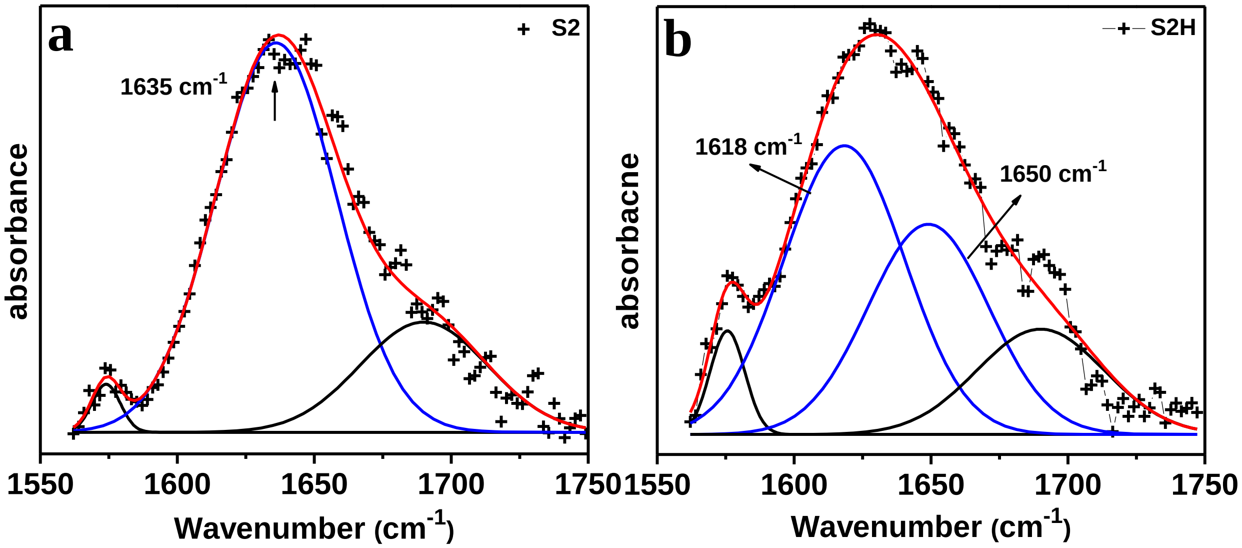

Fig. 4.4.10. ATR-FTIR spectra of NCps, a) S2 and b) S2H. Solid line (red) is fit to raw data (+) and separate Gaussian peaks are shown by blue (relevant) and black solid line.

To summarize, it is found that this collapse transition of PVP is not favored at 70 ^{o}C and thus it leads to opening (at 70 ^{o}C) and reformation (room temperature) of purely hexagonal phase CdS in PVP spheres leading to formation of only isolated and dimmer PVP structures. Stronger resonance Raman scattering for CdS NCs embedded in isolated PVP structures is observed due to stress related band gap tuning.

4.5. Summary

We have chosen to study CdS-PVP NCps to investigate the effect of interaction between CdS NCs and PVP on the formation and properties of NCp. Systematic study of variation in bath parameters elucidated co-operative growth mechanism, which leads to formation of only nearly monodispersive CdS NCs embedded in PVP spheres. Further, Raman and AFM mapping investigation on same selected sites on CdS-PVP NCps show that CdS NCs are embedded in PVP sphere and thin film of PVP for higher and lower concentration of Cd/S ion source, respectively. This observation is understood in the light of existing growth modeling on NCps, which predicts that the larger density of CdS NCs leading to stronger attractive interaction between NCs surface and polymer can facilitate collapse of polymer i.e. sphere formation of PVP under specific conditions, which in turn thermodynamically favor inclusion of nearly monodispersive NCs. This understanding is further supported with ATR-FTIR measurements. Raman and AFM mapping in corroboration with GIXRD data suggests that the collapse transition of PVP is not favored at 70 ^{o}C i.e. heating the chemical bath leads to opening of PVP spheres and reformation (room temperature) of CdS-PVP NCp. Heating the chemical bath has also lead to formation of two types of PVP spheres, i) isolated and ii) dimer. Raman and AFM mapping in corroboration with XRD data suggest presence of residual tensile stress in CdS NCs embedded in single PVP sphere as compared to the dimer, which leads to observance of resonance Raman scattering of CdS NCs due to stress related band gap tuning.

It is interesting to note that CdS NCs embedded in PVP matrix has shown promising and better NLO property as compared to bare CdS NCs as well as CdS NCs embedded in other polymer matrices [174] because of better crystalline quality and better passivation of CdS NCs.

Chapter 5

Conclusion

Raman spectroscopy/mapping is used as a local probe to study semiconductor nanocomposites (NCps) i.e. semiconductor nanocrystals (NCs) embedded in a matrix. Further, the understating developed using Raman mapping is used in corroboration with atomic force microscopy (AFM) mapping to get unique information about the morphology of NCps studied, which is difficult to obtain by any other conventional technique. In NCps, properties can depend not only on the individual components used, but may also depend on the interaction between NCs and matrix. Although, this interaction is expected to be weak, it is considered interesting to see, if they can have significant contribution in the formation and properties of NCps. We have studied two NCps, i) Si-SiO$_2$ NCps and ii) CdS-polyvinyl pyrrolidone (PVP) NCp. In the former case, ceramic matrix is an oxide of the same semiconductor, whereas, in the second case, organic matrix provides complete heterogeneous structure. The interaction between semiconductor NCs and matrix is expected to be quite different for these two cases. This study is expected to elucidate the role played by range of interactions between two weakly interacting constituent components of NCPs on their formation and properties.

i) Si-SiO$_2$ nanocomposites

To go back in history, the UV-visible PL in porous Si, Si NCs and specifically Si NCs embedded in SiO$_2$ matrix has been area of intense research activity. The debate is still going on whether, quantum confinement or surface plays a major role in the observance of UV-visible PL. Parallel to this, we find similar debate about Si phonon variation in Raman spectra of Si NCs in Si-SiO$_2$ NCps. For Si-SiO$_2$ NCps grown using different techniques, different groups have reported different Si phonon frequencies in the range 495 - 519 cm^{-1}. In this range of Si optical phonons, origin of high frequency ($\geq$ 515 cm^{-1}) Si phonons is well understood to be due to phonon confinement in Si NCs. However, understanding of origin lower frequencies ~ 500 cm^{-1}

is far from satisfactory. We have investigated six Si-SiO_2 multilayer NCps using Raman mapping, which shows Si optical phonons in the range 495 - 519 cm^{-1} in each NCp studied. The large distribution in Si phonon frequencies is used advantageously to compare their behavior with respect to each other under same experimental conditions. Based on the line shape, whole range Si phonons are broadly separated into three different regions as, i) 495 - 510 cm^{-1} (low frequency - LF) phonons with Lorentzian line shape, ii) 515 - 519 cm^{-1} (high frequency - HF) phonons with asymmetric line shape and iii) 511 - 514 cm^{-1} (intermediate frequency - IF) phonons with asymmetric line shape. Our study elucidates that LF phonons originate from the smaller size NCs, where phonon frequency is governed by dominant surface/interface effect and HF phonon originates from core of larger size Si NCs, where frequency is governed by the confinement effect. Further, IF phonons originate from intermediate size Si NCs, wherein both core and surface/interface phonons contribute. It is found that the contribution of core and surface/interface phonon depends on size of the Si NC.

To understand the origin of whole range Si optical phonons, Raman spectroscopy monitored local laser irradiation experiment is performed at the desired frequency. In this five step experiment, changes in Raman spectra were measured, while laser irradiation was kept ON and OFF for certain durations. To avoid any perturbation due to laser heating, this experiment is performed at low laser power density ~ 2-5 kW/cm^2. This power density is chosen based on the laser heating study reported in literature for Si NCs embedded in insulating matrix. On the basis of line shape variation and behavior of Si optical phonons during the laser irradiation experiment, LF Si phonons in the range 495 - 510 cm^{-1} are attributed to originate from the surface/interface of Si-SiO_2 for smaller Si NCs (< ~ 4 nm). The phonon frequency variation in the range 495 to 510 cm^{-1} is attributed to variation in local SiO_x environment seen by Si-Si bonds at the surface of the Si NC. HF Si phonons in the range 515 - 519 cm^{-1} originate from core of larger Si NC (~ 6 - 10 nm). Consistently, our study further elucidates that IF Si phonons (~ 511 - 514 cm^{-1}) originate from intermediate size Si NCs (~ 4 to 6 nm) wherein, both surface/interface and core of Si NC contribute simultaneously. Further, during the laser irradiation, the contribution of core increases with the increase in size of Si NC, which self-consistently explain our attribution of these phonons. In a collaborative work, Raman spectra is calculated for Si_{41} cluster by Dr. C. Kamal (ISUD, RRCAT), which show dominant contribution of Si atoms vibrating at the surface of the cluster and thus support our understanding developed from the experiment. This shows that the interface between Si NCs and SiO_2 matrix plays important role in Raman spectra and surface/interface phonon contribution is dominant for smaller Si NCs. It is important to note that we have observed larger Raman signal coming from surface/interface of Si-SiO_2 compared to that from core of Si NCs, which is difficult to appreciate because of low scattering volume (width ~ 10 Å) of the surface/interface. This is further investigated using wavelength dependent Raman mapping in corroboration with absorption measurements, which elucidate that resonance Raman scattering is crucial for the observance of surface/interface phonons, whereas, core phonons show non resonant behavior. This understanding is consistent with the observation of such a strong signal from surface/interface of Si-SiO_2. Further, observed absorption edge ~ 3.1 eV in all NCps corresponds to direct band gap of Si, whereas absorption edges ~ 2.5 eV and 2.9 eV are related to surface/interface of Si-SiO_2 NCp originating from smaller size NCs. This suggests that the electronic band structure is different for smaller Si NCs, because surface/interface effects are dominating. Thus, we find that the occurrence of surface/interface phonons depends on, i) size of Si NC and ii) excitation wavelength. This understanding can be used to explain the Raman data variation reported in the literature in different Si-SiO_2 NCps over a decade, as different groups have used different excitation wavelength, although they have observed similar size Si NCs embedded in SiO_2 matrix.

During the laser irradiation experiment, laser energy can either lead to correction of bonds or heating effect. Results of this experiment suggests that used laser energy (low laser power density) leads to more crystalline Si-Si bonding environment i.e. correction of bonds at the surface/interface for smaller Si NCs, whereas, no measurable changes are observed for larger Si NCs. This can be understood as the interface is porous i.e. incoherent for smaller Si NCs embedded in SiO_2 matrix due to presence of large density of dangling bonds, whereas interface tends to become coherent as the size of NC increases. Thus, low laser energy in laser irradiation experiment is used for correction of surface/interface for smaller Si NCs. Further, it is important to note that if enough time is given, LF phonon gets converted to IF phonon, which in turn gets converted to HF phonon on laser irradiation.

NCps also plays an important role in third generation photovoltaic devices. These devices employ multiple optical gaps in a single device to increase the efficiency of single band gap device. Further, Si NCs embedded in SiO_2 matrix are also used preferably in metal-oxide-semiconductor (MOS) memory devices compared to thin film Si/SiO_2. Our study suggests observance of multiple optical gaps in Si-SiO_2 NCp and the understanding developed can be gainfully used to manipulate and characterize Si-SiO_2 NCp, simultaneously for photovoltaic and MOS device applications.

The understanding developed using Raman mapping in corroboration with AFM mapping is further used to get unique information about morphology of Si NCs embedded in $SiO_{2.}$ Raman and AFM mapping shows that Si NCs are clustered in i) smaller clusters (~ 100 nm) organized closely in two dimensions (2D) and ii) a big (~ 2 μm) three dimensional (3D) isolated cluster, although the growth is carried out to be multilayer (Si/SiO_2). Raman mapping performed by varying the focal spot along the depth shows stacking of larger (> ~ 6 nm) to smaller sizes (< ~ 4 nm) Si NCs from bottom to top. To understand formation of these observed morphologies in Si-SiO_2 NCps, additional NCps with specific growth parameters/conditions are grown and studied in view of the above understanding. Raman and AFM mapping of a single layer suggest that larger Si NCs are formed in the plume itself and cluster formation occurs at the substrate. Thus, various types of cluster formations in multilayer growth can be understood as Si NCs of next layer will either sit on the existing cluster or it may find another low energy site to form another cluster at different spatial position, thereby increasing either size of a cluster or number density of clusters. Further, Raman mapping of an unannealed Si-SiO_2 NCps suggests formation of smaller Si NCs at the top due to annealing at 800 ^{o}C in Si rich SiO_2 and possible existence of thermal gradient in an insulating matrix of SiO_2. This suggests that although higher temperature is required to form Si NCs from SiOx matrix because in the first step there will be formation of amorphous Si (~ 800 ^{o}C) and then crystalline Si (> 1000 ^{o}C), whereas, in Si excess SiO_2, Si NCs are formed at relatively lower temperature.

Earlier, we have discussed the use of Raman mapping to probe the effect of size dependence of surface/interface on Raman spectra of Si-SiO_2 NCps. Size dependence of interface for Si-SiO_2 NCps has already been established using XPS in the literature. Thus, size dependence of surface/interface using Raman mapping can be independently corroborated using XPS. The beam size in XPS (~ 1 cm x 1 cm) covers the full sample, therefore, an average signal from XPS measurement needs to be corroborated with the statistical information obtained from the Raman mapping data. In order to do this, we have chosen samples which show average contrast in Raman mapping results regarding size of Si NCs. XPS measurements show observance of Si^{1+}, Si^{2+} and Si^{3+} suboxide states with higher intensity in the NCps corresponding to higher content of HF, IF and LF phonons in Raman mapping, respectively. Although, we have observed one to one correspondence between Raman mapping and XPS, it is important to note that the escape depth of electron is nearly ~ 5-10 nm i.e. electrons present at surface will give rise to XPS signal. However, these NCps studied have ~ 20 nm thick SiO_2 layer deposited at the top, which is large as compared to escape depth of electron. The observed one to one corroboration can however be explained with the understanding that smaller Si NCs are formed in Si excess SiO_2 top layer during annealing at 800 ^oC.

ii) CdS - PVP nanocomposites

CdS NC is chosen for the study, as it is considered an important optoelectronic material, due to the possible band gap engineering over a wide spectral range (visible to UV). PVP matrix is chosen as monomers of PVP prefers to complex with many inorganic compounds and thus provide surface passivation. In case of inorganic-organic NCps, lots of work has been done for NCs-block copolymer NCps, which suggests that the separation in block copolymers and interaction between NCs and block copolymers could be used to promote the ordering of NCs. However, for NCs-polymer NCps, whether the effect of interaction between the two can also lead to ordering is the aim of this study. We have chosen to study CdS-PVP NCps to investigate the effect of interaction between NCs and polymer on the formation of NCp. Our study suggests that in CdS-PVP NCps grown using one-step chemical bath deposition(CBD) process, the interaction between Cd^+ ion at the surface of CdS nanocrystal and PVP monomers give rise to collapse of polymer, which leads to inclusion of nearly monodispersive CdS nanocrystals embedded in PVP spheres.

Systematic study of variation in Cadmium acetate (Cd-A: Cd^+ ion source), Thiourea (ThU: S^- ion source), PVP concentration, deposition time and heating/cooling cycles elucidated co-operative growth mechanism for one-step CBD grown CdS-PVP NCp. The observation of a peak in the absorption spectrum indicates formation of nearly monodispersive CdS NCs. However, observed significant absorption even in the longer wavelength region, following an absorption peak, indicates scattering contribution at longer wavelengths from these NCps. The observed scattering contribution in absorption spectra is separated by using diffuse reflectance spectra as a guide. This scattering contribution is understood as occurring due to Rayleigh and Mie scattering, which is in turn correlated with spheres/structures seen in SEM micrographs. Deconvoluted absorption peak in corroboration with SEM and TEM show that nearly monodispersive CdS NCs (size ~ 6 - 10 nm) are embedded in PVP sphere (size ~ 100 - 600 nm). This observation is understood in the light of existing growth modeling on NCps, which predicts that the attractive interaction between NCs surface and polymer can facilitate collapse of polymer i.e. sphere formation of PVP under specific conditions. Further, only similar size NCs will be included in polymer spheres, as inclusion of larger NCs is not favored thermodynamically and smaller NCs may get dissolved. Thus, interaction between CdS NCs and PVP monomers leads to formation of PVP sphere with inclusion of nearly monodispersive CdS NCs of better crystalline quality and passivation.

Further, Raman and AFM mapping investigation on same selected sites on CdS-PVP NCps show that CdS NCs are embedded in i) PVP sphere and ii) thin film of PVP for different relative concentration of Cd-A/ThU to PVP. We find that for fixed PVP content, larger concentration of Cd/S (0.5 M &1 M) ion source (larger density of CdS NCs) leads to formation of PVP sphere, whereas, thin film of PVP is observed in case of lower concentration of Cd/S

(0.01 M) ion source. This suggests growth condition is favorable for collapse transition of PVP in first case, but not in the second case, consistent with the theoretical predictions reported. --- predicts that the morphology of NCp depends on the interaction between NCs and polymer as well as density of NCs. Further, three dimensional Raman intensity profile of isolated PVP, which suggests volume absorption of large density of CdS NCs, is also expected from growth modeling studies. This understanding is further supported with ATR-FTIR measurements, which shows stronger interaction between CdS NCs and PVP for larger concentration of Cd/S ion source, which leads to sphere formation of PVP. Further, it is found that smaller CdS NCs of better crystalline quality and better passivation are embedded in smaller PVP spheres. This is understood as larger energy is required for PVP to stretch over larger NCs while forming a spherical morphology, which can leave more dangling bonds at the surface of CdS NCs.

Further, Raman and AFM mapping in corroboration with XRD data suggests that the collapse transition of PVP is not favored at 70 ^{o}C i.e. heating the chemical bath leads to opening of PVP spheres and reformation (room temperature) of CdS-PVP NCp. Further, XRD data shows formation of both cubic and hexagonal phases for NCps grown at room temperature, whereas, chemical bath heated at 70 ^{o}C leads to NCps with only stable hexagonal phase of CdS NCs. Heating the chemical bath has also lead to formation of two types of PVP spheres, i) isolated and ii) dimer. Raman and AFM mapping in corroboration with XRD data suggest presence of residual tensile stress in CdS NCs embedded in single PVP sphere as compared to the dimer, which leads to observance of resonance Raman scattering of CdS NCs due to stress related band gap tuning.

Thus, one-step growth of CdS-PVP NCp using CBD is found to be co-operative in nature. An interaction between CdS NCs and PVP leads to different morphology of NCp, depending on their relative concentrations; in here it is defined by initial Cd/S ion source to PVP concentration in the chemical bath. While, this method eliminates an additional step for growth of NCps, we find that complexity of the process actually leads to better control on the growth i.e. formation of nearly monodispersive CdS NCs of better crystalline quality and better passivation. This is expected to enhance the non-linear optical (NLO) properties of CdS NCs, which are useful for optical limiting devices.

In both NCps studied, we find that the weak interaction between constituent parts i.e. semiconductor nanocrystal and matrix plays an important role in determining the morphology as well as properties of nanocomposites.

Future scope

To probe nearly monodispersive Si and CdS NCs with sizes in the range 2 – 7 nm using Triple stage Raman spectrometer, in order to develop one to one correlation between confined acoustic and optical phonons. Further, in case of Si-SiO$_2$ NCps, one to one correlation between confined acoustic phonon, optical phonon and PL spectrum can also explain the variation observed in PL spectra of these NCps. This is because, we believe that the variation in Raman and PL spectra are interconnected and correlation of the two is already established for studied NCps. In case of CdS-PVP NCp, wherein CdS NCs are embedded in thin film of PVP, it has been reported that this NCp give better NLO property as compared to bare CdS NCs as well CdS NCs embedded in other polymers because of better crystalline quality and better passivation. Our study suggests that CdS NCs embedded in PVP spheres are of better crystalline quality and passivation compared to CdS NCs embedded in thin film of PVP. Thus, it would be interesting to study NLO property for these two different morphologies.

Annexure

3.2.1. Phonon confinement Model

For a bulk crystal, conservation of momentum requires Raman scattering of only optical phonons near the centre of the Brillouin zone (**q** ~ 0). This is because in the Raman scattering experiment, the magnitude of scattering vector is $2\boldsymbol{k_0}\sin(\theta/2)$, where $\boldsymbol{k_0}$ is the wave vector of the incident light and θ is the scattering angle. Thus, the maximum value of the scattering vector could be $2\boldsymbol{k_0}$ (corresponding to the backscattering geometry), which has a value ~ 5×10^4 cm^{-1} for visible light. Hence, the wave vector probed by this techniques is much smaller than the wave vector **q** of the full phonon dispersion curve, which extends up to the boundary of the Brillouin zone ($\mathbf{q}/a$ ~ 10^8 cm^{-1}, where a is the lattice parameter). This **q** ~ 0 selection rule is essentially a consequence of the infinite periodicity of the crystal lattice. Thus, for bulk crystals, Raman spectrum is a symmetric line with Lorentzian line shape with a FWHM, which can be related to phonon lifetime. For NCs, due to lack of long range order, the **q** vector selection rule does not apply and the range of **q** vectors having their wave vectors non-zero are also accessible. As crystallite gets confined in one, two or three dimensions, translational symmetry breaks in the direction of confinement. This leads to relaxation of **q** ~ 0 selection rule as uncertainly in **q**, $\Delta q \sim 1/d$ (confinement) and one can sample $\mathbf{q} \neq 0$ (~1/d). Here the allowed values of **q** are $\mathbf{q} \alpha 1/d$, where d is the diameter of the particle. Hence, for smaller particle, there will be contribution from higher q's and thus leading to the observed red shift, asymmetric line and broadening of optical phonon as explained by phonon confinement model (PCM) by Campbell and Fauchet [153].

Consider a spherical nanoparticle of diameter d. A plane-wave-like phonon wave function cannot exist within the particle because the phonon cannot propagate beyond the crystal surface. Thus a weight function was introduced W ($\mathbf{r}$, L), which decays to a very small value close to the boundary. The wave function of phonon for infinite crystal,

$$\Phi\,(\mathbf{q}_0, \mathbf{r}) = u\,(\mathbf{q}_0, \mathbf{r})\, e^{-i\mathbf{q}_0 \cdot \mathbf{r}} \tag{A3.2.1}$$

For confined phonon, wave function is

$$\Psi\,(\mathbf{q}_0, \mathbf{r}) = W(\mathbf{r}, L)\; u\,(\mathbf{q}_0, \mathbf{r})\, e^{-i\mathbf{q}_0 \cdot \mathbf{r}} \tag{A3.2.2}$$

$$\Psi\,(\mathbf{q}_0, \mathbf{r}) = \Psi'\,(\mathbf{q}_0, \mathbf{r})\; u\,(\mathbf{q}_0, \mathbf{r}) \tag{A3.2.3}$$

Expanding

$$\Psi'(\mathbf{q}_0, \mathbf{r}) \;=\; \int C(\mathbf{q}_0, \mathbf{q})\, e^{i\mathbf{q} \cdot \mathbf{r}} d^3q$$

Where,

$$C\,(\mathbf{q}_0, \mathbf{q}) = \frac{1}{(2\pi)^3} \int \Psi'\,(\mathbf{q}_0, \mathbf{r})\, e^{-i\mathbf{q} \cdot \mathbf{r}} d^3r \tag{A3.2.4}$$

The particle (nanocrystal) phonon wave function is a superposition of plane waves with $\mathbf{q}$ vectors centered at $\mathbf{q}_0$. It was seen that the Gaussian weight function was best suited as compared to other functions and thus

$$W\,(\mathbf{r}, d) = \exp(-\alpha r^2/L^2) \tag{A3.2.5}$$

Therefore,

$$C\,(\mathbf{q}_0, \mathbf{q}) = \exp\{-L^2(\mathbf{q} - \mathbf{q}_0)^2/4\alpha\} \tag{A3.2.6}$$

Where the value of α decides how rapidly the wave function decays as one approaches the boundary. Value of $\alpha = 8\pi^2$ was used by Campbell. This gives for $\mathbf{q}_0 = 0$

$$|C\,(0, \mathbf{q})|^2 = \exp\{-L^2(\mathbf{q})^2/16\pi^2\} \tag{A3.2.7}$$

First order Raman spectrum is then given by

$$I(\omega) = \int \frac{|C(0,\mathbf{q})|^2 d^3q}{(\omega-\omega(\mathbf{q}))^2+(\Gamma_0/2)^2} \qquad \text{A3.2.8}$$

Where, $\omega(\mathbf{q})$ is the phonon dispersion curve and Γ_0 is the natural line width of the zone-center optical phonon in the bulk. Line shape will be different when confining in one direction or two directions because integration depends on the dimension of confinement (Fig. A3.2.1).

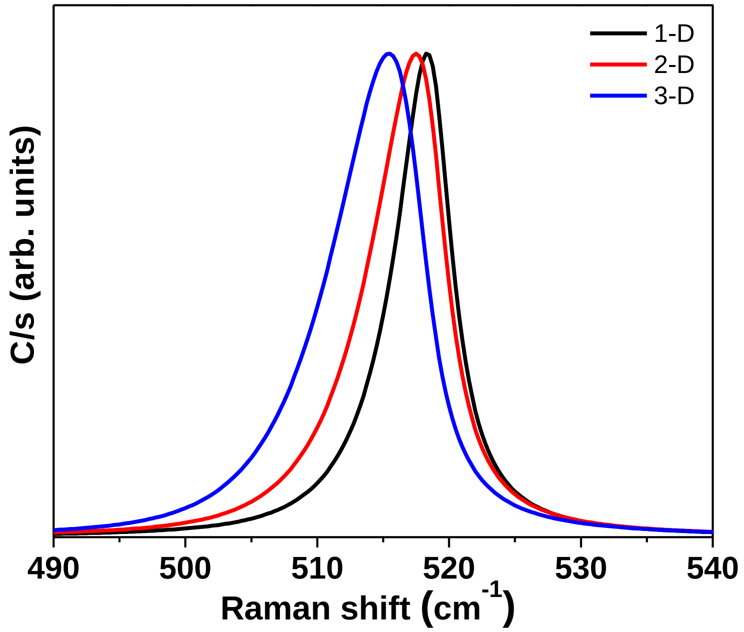

Fig. A3.2.1. Calculated line shape for one dimensional (1-D), two dimensional (2-D), three dimensional (3-D) phonon confinement.

As crystallite gets confined in one, two or three dimensions, translational symmetry breaks in the direction of confinement. This leads to relaxation of $q = 0$ selection rule as uncertainly in q, $\Delta q \sim 1/d$ (confinement) and one can sample $q \neq 0 \sim 1/d$. This leads to sampling of acoustic phonons $q \neq 0 \sim 1/d$, (ω_{cap}~10-50 cm^{-1}), which can be observed in Raman spectroscopy. As size decreases, in addition to confinement, surface to volume ratio increases and this makes observation of surface phonons possible.

3.2.2. Spatial resolution: Raman mapping of Si-SiO$_2$ nanocomposites

While performing Raman mapping, we have observed variation in frequency, FWHM and line shape of Si optical phonon at step size of 0.15 μm. This suggests betterment in spatial resolution because the calculated spatial resolution is ~ 0.5 μm. This is further looked into. Raman mapping is performed on 4 * 4 μm^2 area with step size of ~ 0.15 μm and thus, an array of area 0.15 * 0.15 μm^2 is created over the Raman image (Fig. A3.2.2a). Fig. A3.2.2b shows corresponding Raman spectra at marked positions showing variation in LO phonon (frequency, line shape) and it's FWHM at a step size of ~ 0.15 μm across one structure (Fig. A3.2.2), which suggests that the observed resolution is better. TEM micrographs [158] show presence of isolated particles with separation between two particles is ~ 100 nm. This suggests that the observed betterment in spatial resolution is due to two factors, 1) separation between two particles is ~ 0.1 μm and 2) central part of Gaussian beam profile is giving the significant signal during Raman mapping.

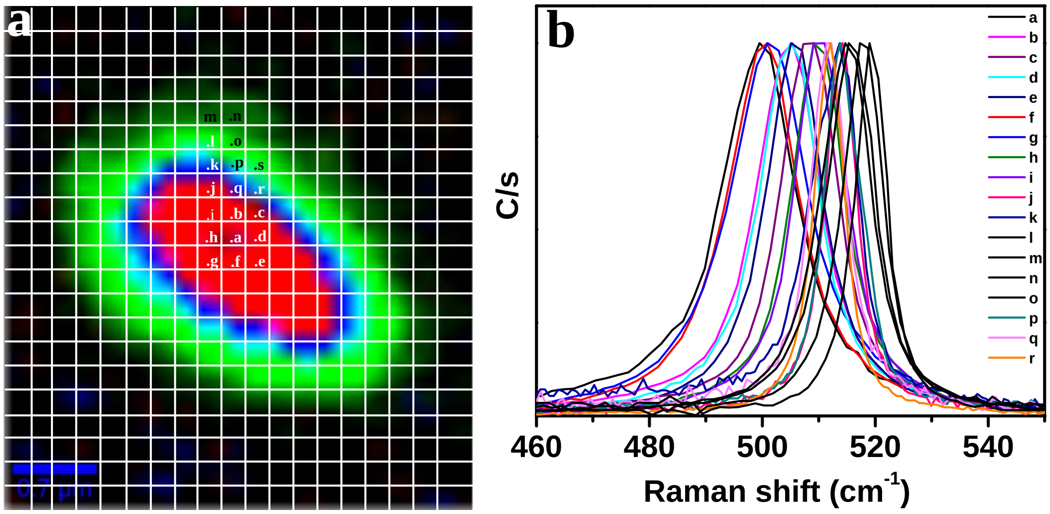

Fig. A3.2.2. a) Raman image of Si-SiO$_2$ NCps, wherein array is formed with step size of 0.15 μm and b) corresponding Raman spectra for all the positions marked in Raman image.

3.2.3. Calculation of Raman spectra of Si cluster (Si_{41})

First, optimized geometric structure of Si cluster is obtained and then the optimized structures are employed to perform calculations of Raman spectra. DFT [231] based electronic structure calculations with bulk-like tetrahedral coordination, using Amsterdam Density Functional (ADF) code [232] are carried out. Two possible terminations for Silicon atoms present at the surface of the cluster, namely (a) oxygen and (b) hydrogen atoms are considered, in order to avoid the dangling bonds. The former termination is used to mimic the Si cluster/SiO_2 interface. The calculations of ground state properties have been carried out by using triple-ξ Slater-type orbital (STO) basis set with two added polarization functions (TZ2P basis set of ADF basis set library) [232] along with generalized gradient approximation (given by Perdew-Burke-Ernzerhof (PBE) [232]) exchange-correlation (XC) functional. The geometric structures of the cluster with the two above mentioned terminations, and with bulk-like initial positions, are fully relaxed using the BFGS technique until the norm of the energy gradient and energy attain values less than 10^{-4} au and 10^{-6} au respectively. The optimized geometric structure of Si_{41} cluster is obtained with two different terminations like $Si_{41}O_{42}H_{24}$ and $Si_{41}H_{60}$.

For the calculation of Raman spectra of these optimized geometric structures, linear response theory within TDDFT is used, which is implemented in RESPONSE module of the ADF code [233]. The intensity of Raman spectra is calculated by estimating the first derivative of the polarizability with respect to normal coordinates. The same TZ2P basis set is used for the calculations of polarizability. It is well known that for performing calculations of response properties within TDDFT, it is required to use approximate forms for the XC potential at two different levels. At the first level, standard PBE XC potential for the calculation of ground-state Kohn-Sham orbitals and their energies are used. The second level of approximation is needed for

XC kernel which determines the XC contribution to the screening of applied fields and for this we use the reasonably accurate adiabatic local density approximation (ALDA).

3.3.1. Removal of interference fringes from absorption spectra (Si-SiO_2)

Absorption spectra of all NCps show interference fringes (Fig. 3.3.13). It is well known that when an un-polarized (combination of *p and s-polarized light*) light passes through a thin film with the thickness comparable to that of wavelength of light, wave reflected from upper and lower surface interfere constructively and destructively leading to observance of interference fringes [243]. During the growth, SiO_2 is used as buffer layer leading to SiO_2/Al_2O_3 interface. Since the refractive index of these materials is different, interference fringes in the absorption spectra are observed. The interference fringes free absorption data can be obtained by measuring the absorption at Brewster angle (instead of normal incidence) using *p-polarized light* [243]. Due to transverse nature of electromagnetic field and according to intensity of radiation emitted from a dipole, *p-polarized light* will not be reflected if the angle of incidence is given by [243]

$$\theta_B = \text{arc tan}\,(n_2/n_1) \qquad \text{A3.3.1}$$

This equation is known as Brewster **law**, and θ_B is Brewster angle. Here, n_1 and n_2 is the refractive index SiO_2 (~ 1.5) and crystalline Al_2O_3 (~ 1.7), respectively. Brewster angle comes out to be ~ 50^0. One can clearly see the disappearance of interference fringes in the absorption spectrum when the p-polarized light falls at ~ 55^0 on the NCp (Fig. A 3.3.1).

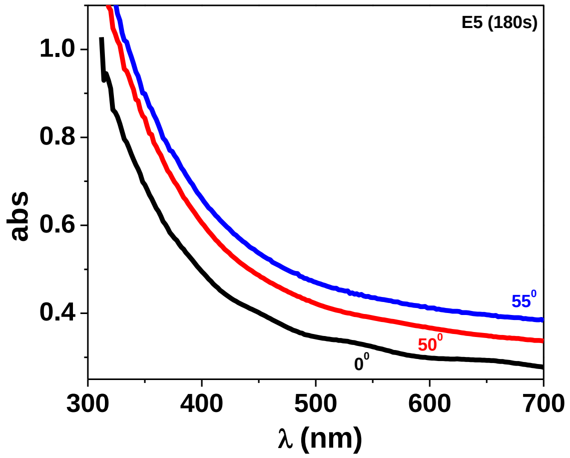

Fig. A3.3.1. Absorption spectra of E5 measured at different angles using p-polarized light.

4.3.1. Spatial resolution: Raman mapping of CdS-PVP nanocomposites

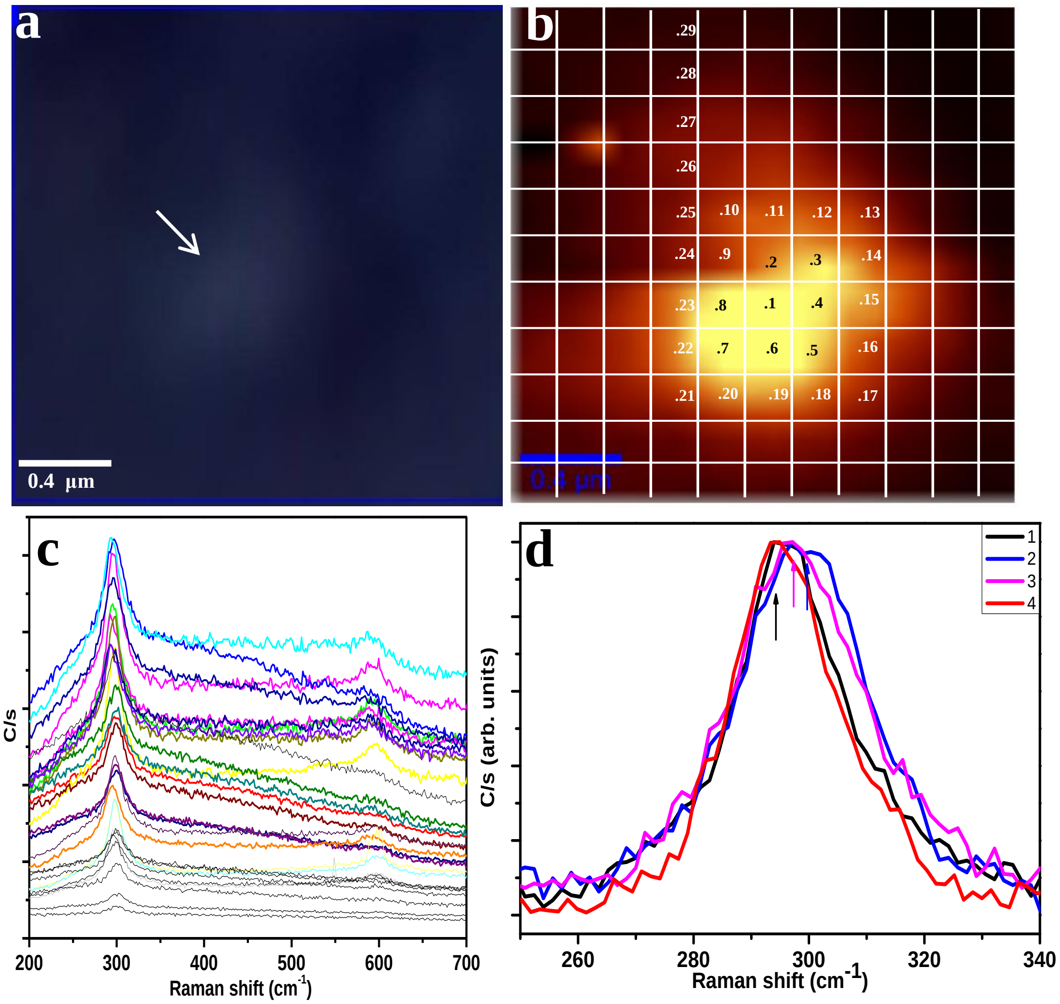

Fig. A4.3.1. a) optical image, b) Raman image of NCp S3, wherein array is formed with step size of 0.1 µm, c) corresponding Raman spectra for all the positions marked in Raman image and d) Raman spectra for four marked positions showing variation in Raman spectra at step size of 0.1 µm.

Raman mapping is performed on 2 * 2 µm^2 area with step size is 0.1 µm. Therefore, we have created an array of area 0.1 * 0.1 µm^2 over the whole Raman image (Fig. A4.3.1b). Fig. A3.3.1c shows corresponding Raman spectra at marked positions showing variation in PL over different arrays. Further, Raman spectra near the boundary of two different PVP spheres i.e. at four adjacent arrays suggest variation in phonon frequency (from 295 to 300 cm^{-1}), FWHM (from 16 - 18 cm^{-1}) and PL at a step size of ~ 0.1 µm as shown in Fig. A4.3.1d. This clearly shows observed betterment in spatial resolution (~ 0.1 µm) as the expected resolution is ~ 0.4 µm. This betterment in spatial resolution is observed because of presence of scattering of light due to presence of PVP sphere (as also observed in absorption spectra), while focusing the laser on this region (Fig. A4.3.2). Scattering of light (Rayleigh cross section α d^6/λ^4) from the PVP sphere leads to decrease in the intensity and thus very less intensity is available for inelastic scattering. In this case, only central part of Gaussian beam profile with highest intensity gives Raman signal leading to better spatial resolution than expected. Therefore, Raman mapping of isolated PVP spheres show presence of nearly monodispersive CdS NCs in the sphere, in agreement with the absorption spectroscopy results.

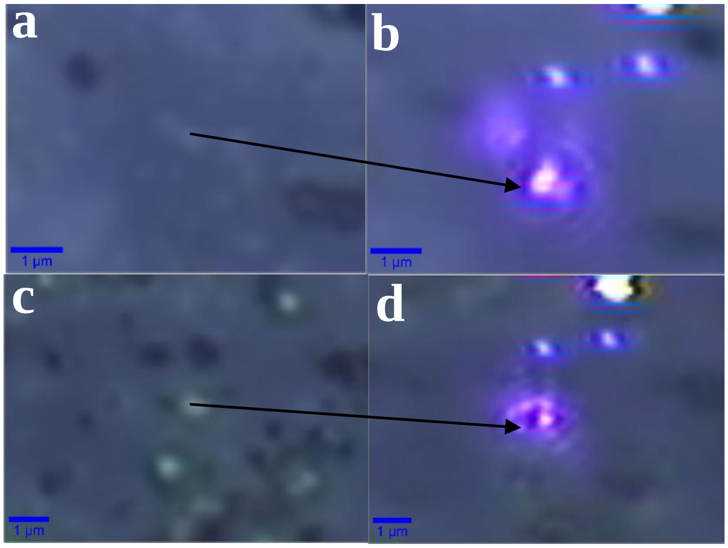

Fig. A4.3.2. a) Optical image, b) laser focused at the PVP sphere (~ 0.3 µm) marked with arrow, c) Optical image, b) laser focused at the PVP sphere (~ 0.6 µm) marked with arrow.

References

[1] P.Y. Yu, M. Cardona, “Fundamentals of Semiconductors, Graduate Springer-Verlag Berlin Heidelberg” (2010).

[2] A. Volta, Phil. Trans. R. Soc. **72**, 237 (1782).

[3] M. Faraday, Phil. Trans. R. Soc. **123**, 507 (1833).

[4] A. E. Becquerel, Comptes Rendus de l'Academie des Sciences **9**, 711 (1839).

[5] W. Smith, J. of the Soc. Telegraph Engineers **2**, 31 (1873).

[6] F. Braun, Annalen der Physikt und Chemie **153**, 556 (1874).

[7] A. Schuster, Philosophical Magazine **48**, 251 (1874).

[8] G. L. Pearson and W. H. Brattain, Proc. of the IRE December 1794 (1955).

[9] B. Yugang Sun and J. A. Rogers, Adv. Mater. **19**, 1897 (2007).

[10] J. Singh “Electronic and Optoelectronic Properties of Semiconductor Structures ”Cambridge University Press (2003).

[11] D. M. Chapin, C. S. Fuller, and G. L. Pearson, J. Appl. P hys. **25**, 676 (1954).

[12] S. Xiao and S. Xu, Critical Reviews in Solid State and Materials Sciences **39**, 277 (2014).

[13] O. Masala and R. Seshadri, Annu. Rev. Mater. Res. **34**, 41 (2004).

[14] A.P. Alivisatos, Endeavour **21**, 56 (1997).

[15] B. H. Kim, M. J. Hackett, J. Park, and T. Hyeon, Chem. Mater. **26**, 59 (2014).

[16] M. A. El-sayed, Acc. Chem. Res. **37**, 326 (2004).

[17] RTO Lecture Series, EN-AVT-**129**, (2005).

[18] G. Y. Jing, H. L. Duan, X. M. Sun, Z. S. Zhang, J. Xu, Y. D. Li, J. X. Wang, and D. P. Yu, Phys. Rev. B **73**, 235409 (2006).

[19] P. Sharma, S. Ganti, and N. Bhate, Appl. Phys. Lett. **82**, 535 (2003).

[20] S. Kan, T. Mokari, E. Rothenberg and U. Banin, Nature Materials **2**, 155 (2003).

[21] H. Chen , X. Kou , Z. Yang , W. Ni and J. Wang, Langmuir **24**, 5233 (2008).

[22] W. E. Buhro and V. L. Colvin, Nature Materials **2**, 138 (2003).

[23] B. Wiley, Y. Sun and Y. Xia, Acc. Chem. Res. **40**,1067 (2007).

[24] F. J. Heiligtag and M. Niederberger, Materials Today **16**, (2013).

[25] G. S. Tanwar, R. Saharan and Dr. G. S. Tanwar, International Journal of Computer Applications **1**, (2010).

[26] R. E. Howard, W. J. Skocpol and L. D. Jackel, Ann. Rev. of Mater. Science, **16**, 441 (1986).

[27] O. E. Semonin, J. M. Luther and M. C. Beard, Material Today **15**, 508 (2012).

[28] R. Kumar , O. Al-Dossary, G. Kumar and A. Umar, Nano-Micro Lett. **7**, 97 (2015).

[29] R. H. Baughman, A. A. Zakhidov and W. A. de Heer, Science **297**, 787 (2002).

[30] X. Duan, Y. Huang, Y. Cui, J. Wang and C.M. Lieber, Nature **409**, 66 (2001).

[31] E. O. Odoh and A. S. Njapba, Advances in Physics Theories and Applications **46**, 26 (2015).

[32] F. Kreupl, A.P. Graham, G.S. Duesberg, W. Steinhogl, M. Liebau, E. Unger and W. Honlein, Microelectronic Engineering **64**, 399 (2002).

[33] P. Colomban, J. Nano Res. **8**, 109 (2009).

[34] P. Sciau, C. Mirguet, C. Roucau, D. Chabanne and M. Schvoerer, J. Nano Res. **8**, 133 (2009).

[35] K. Wang, “Nanomaterials: from Interfacial Characteristics to Device Applications” (2011) McMaster University.

[36] B. Nowack, H. F. Krug and M. Heigh, Environ. Sci. Technol. **45**, 1177 (2011).

[37] M. Faraday, Philos. Trans. R Soc. Lond. **147**, 145 (1857).

[38] C. Gerber and H. P. Lang, Nature nanotechnology **1**, (2006).

[39] K. Kalyanasundaram, et al., Angew. Chem. Int. Ed. **20**, 987 (1981).

[40] A. Henglein, Ber. Bunsen-Ges. **86**, 301 (1982).

[41] R. Rossetti, et al., J. Chem. Phys. **80**, 4464 (1984).

[42] B.L. Cushing, V.L. Kolesnichenko and C.J. O’Connor, Chem. Rev. **104**, 3893 (2004).

[43] S. Suresh, Nanoscience and Nanotechnology **3**, 62 (2013).

[44] J.J. Luo and I.M. Daniel, Compos. Sci. Technol . **63**,1607 (2003).

[45] W. A. Badawy, J. Advanced Research **6**, 123 (2015).

[46] J. Z. Zhang, J. Phys. Chem. Lett. **4**, 2975 (2013).

[47] L. Shao, Y. Gao and F. Yan, Sensors **11**, 11736 (2011).

[48] J. L. West and N. J. Halas **5**, 285 (2003).

[49] Z. Han, F. Qiu, R. Eisenberg, P. L. Holland and T. D. Krauss, Science **338**, 1321 (2012).

[50] A. Das, Z. Han, M. G. Haghighi and R. Eisenberg, PNAS **110**, (2013).

[51] U. Resch-Genger, M. Grabolle, S. Cavaliere-Jaricot, R. Nitschke and T. Nann, Nature Methods **5**, 763 (2008).

[52] J. V. Frangioni, Curr. Opin. Chem. Biol. **7**, 626 (2003).

[53] M. Bruchez, M. Moronne, P. Gin, S. Weiss and A. P. Alivisatos, Science **281**, 2013 (1998).

[54] X. Michalet, F. F. Pinaud, L. A. Bentolila, J. M. Tsay,S. Doose, J. J. Li, G. Sundaresan, A. M. Wu, S. S. Gambhir and S. Weiss, Science **307,** 538 (2005).

[55] I. L. Medintz, H. T. Uyeda, E. R. Goldman and H. Mattoussi, Nature Mater. **4,** 435 (2005).

[56] A. Y. Nazzal, L. Qu, X. Peng and M. Xiao, Nano Lett. **3**, 819 (2003).

[57] D. Beydoun, R. Amal, G. Low and S. McEvoy, J. of Nanoparticle Research **1**, 439 (1999).

[58] K. Maeda and K. Domen, J. Phys. Chem. C **118**, 7851 (2014).

[59] C. Liu, F. Li, L. P. Ma and H. M. Cheng, Adv. Mater. **22**, E28 (2010).

[60] T. Fang , J. G. Duh and S. R. Sheen, J. Electrochem. Soc. **152**, A1701 (2005).

[61] N. C. Li, C. J. Patrissi, G. L. Che and C. R. Martin, J. Electrochem. Soc. **147**, 2044 (2000).

[62] L. J. Fu, H. Liu, C. Li, Y. P. Wu, E. Rahm, R. Holze and H. Q. Wu, Solid State Sci. **8**, 113 (2006).

[63] Y. G. Wang , Y. R. Wang, E. J. Hosono , K. X. Wang and H. S. Zhou , Angew. Chem., Int. Ed. **47**, 7461 (2008).

[64] R. Liu, J. Duay and S. B. Lee, ACS Nano **4**, 4299 (2010).

[65] H. X. Zhang, C. Feng, Y. C. Zhai, K. L. Jiang, Q. Q. Li and S. S. Fan, Adv. Mater. **21**, 2299 (2009).

[66] R. Liu and S. B. Lee, J. Am. Chem. Soc. **130**, 2942 (2008).

[67] H. Zhang , G. P. Cao, Z. Y. Wang, Y. S. Yang, Z. J. Shi and Z. N. Gu, Nano Lett. **8**, 2664 (2008).

[68] L. L. Beecroft and C. K. Ober, Chem. Mater. **9**, 1302 (1997).

[69] S. Baksi and S. Biswas, The Scitech Journal **1**, (2014).

[70] A. Du , Y. Hau Ng, N. J. Bell, Z. Zhu, R. Amal and S. C. Smith, J. Phys. Chem. Lett. **2**, 894 (2011).

[71] S. B. Kondawar, S. P. Agrawal, S. H. Nimkar, H. J. Sharma and P. T. Patil, Adv. Mat. Lett. **3**, 393 (2012).

[72] S. S. Varghesea, S. Lonkara, K. K. Singh, S. Swaminathan and A. Abdala, Sensors and Actuators B: Chemical **218**, 160 (2015).

[73] A. Leela, M. Reddy, S. R. Gowda, M. M. Shaijumon and P. M. Ajayan, Adv. Mater. **24**, 5045 (2012).

[74] Y. Li, A. Rizzo, R. Cingolani and G. Gigli Microchimica Acta **159**, 207 (2007).

[75] M. A. Green *Proc. SPIE* 8981, “Physics, Simulation, and Photonic Engineering of Photovoltaic Devices III, 89810L” (2014).

[76] S. W. Song, Y. Jeong and S. Kw, IEEE J. of Selected Topics in Quantum Electronics **21**, 4 (2015).

[77] G. Dong, H. Wang, G. Chen, Q. Pan and J. Qiu, Froiters in Materials **2**, (2015).

[78] D. Crespy, M. Bozonnet and M. Meier, Angewandte Chemie **47**, 3322 (2008).

[79] R. Soulairol and F. Cleri, Solid State Sciences **12**, 163 (2010).

[80] K Seino, F Bechstedt and P Kroll Nanotechnology **20**, (2009) 135702 & ref. therein.

[81] N. Daldosso, M. Luppi, S. Ossicini, E. Degoli, R. Magri, G. Dalba, P. Fornasini, R. Grisenti, F. Rocca, L. Pavesi, et al., Phys. Rev. B **68**, 085327 (2003).

[82] F. Djurabekova and K. Nordlund, Phys. Rev. B **77**, 115325 (2008).

[83] M. Houssa, G. Pourtois, M. Caymax, M. Meuris, M. M. Heyns, V. V. Afanas’ev and A. Stesmans, Appl. Phys. Lett. **93**, 161909 (2008).

[84] P. G. de Gennes, J. Phys. Lett. **37**, 59 (1976).

[85] H. Diamant and D. Andelman, Macromolecules **33**, 8050 (2000).

[86] D. Cao, J. Wu, J. of Chem. Phys. **126**, 144912 (2007).

[87] R. B. Thompson, V. V. Ginzburg, W. M. Matsen and A. C. Balazs, Macromolecules **35**, 1060 (2002).

[88] A. C. Balazs, T. Emrick and T. P. Rusell, Science **314**, 1107 (2006).

[89] M. G. Opferman, R. D. Coalson, D. Jasnow and A. Zilman, Phys. Rev. E **86**, 031806 (2012).

[90] C. V. Raman and K.S. Krishnan, Nature **121**, 502 (1928).

[91] M. Born and E. Wolf, "Principles of optics, Cambridge University press" (2002).

[92] L. Opilik, T. Schmid and R. Zenobi, Annu. Rev. Anal. Chem. **6**, 379 (2013).

[93] V. S. Y. Lin, K. Motesharei, K. P. S. Dancil, M. J. Sailor and M. R. Ghadiri, Science **278**, 840 (1997); J. Harper and M. J. Sailor, *Anal. Chem.* **68**, 3713 (1996).

[94] B.Hamilton, Semicond. Sci. Technol. **10**, 1187 (1995).

[95] S. Xiao and S. Xu, Critical Reviews in Solid State and Materials Sciences **39**, 277 (2014).

[96] M. J. Sailor, J. L. Heinrich, J. M. Lauerhaas and P. V. Kamat, Studies in Surface Science and Catalysis **103**, 209 (1996).

[97] V. V. Doan, and M. J. Sailor, Science **256**, 1791 (1992).

[98] L. T. Canham, Appl. Phys. Lett. **63**, 337 (1993).

[99] H. Wu, G. Zheng, N. Liu, T. J. Carney, Y. Yang and Y. Cui Nano Lett. **12**, 904 (2012).

[100] T. Yoshinobu, H. Ecken, A. B. M. Ismail, H. Iwasaki, H. Luth and M. J. Schoning, Electrochim. Acta. **47**, 259 (2001).

[101] L.T. Canham, Nanotechnology **18**, 185704 (2007)

[102] L. T. Canham, Appl. Phys. Lett. 57, 1046 (1990).

[103] A. G. Cullis and L. T. Canham, Nature **353**, 335 (1991).

[104] S. M. Prokes, Appl. Phys. Lett. **62**, 3244 (1993).

[105] J. L. Gole, F. P. Dudel, D. Grantier and D. A. Dixon, Phys. Rev. B 56, 2137 (1997).

[106] M. V. Wolkin, J. Jorne, P. M. Fauchet, G. Allan and C. Delerue, Phys. Rev. Lett. **82**, 197 (1999).

[107] L. Pavesi, L. Dal Negro, C. Mazzoleni, G. Franzo and F. Priolo, Nature **408**, 440 (2000).

[108] L. Khriachtchev, M. Räsänen, S. Novikov and J. Sinkkonen, Appl. Phys. Lett. **79**, 1249 (2001).

[109] S. Takeoka, M. Fujii and S. Hayashi, Phys. Rev. B **62**, 16820 (2000).

[110] D. Nesheva, C. Raptis, A. Perakis, I. Bineva, Z. Aneva, Z. Levi, S. Alexandrova and H. Hofmeister, J. Appl. Phys. **92**, 4678 (2002).

[111] E. Lioudakis, A. Othonos, G. C. Hadjisavvas, P. C. Kelires, and A. G. Nassiopoulou, Physica E **38**, 128 (2007).

[112] C. Garcia, B. Garrido, P. Pellegrino, R. Ferre, J. A. Moreno, J. R. Morante, L. Pavesi, and M. Cazzanelli, Appl. Phys. Lett. **82**, 1595 (2003).

[113] Y. Kanemitsu, T. Ogawa, K. Shiraishi and K. Takeda, Phys. Rev. B **48**, 4883 (1993).

[114] C. Ternon, C. Dufour, F. Gourbilleau and R. Rizk, Eur. Phys. J. B **41**, 325 (2004).

[115] B. G. Fernandez, M. Lopez, C. Garcia, A. Perez-Rodriguez, J. R. Morante, C. Bonafos, M. Carrada and A. Claverie, J. Appl. Phys. **91**, 798 (2002).

[116] Y. Kanemitsu, H. Uto, Y. Masumoto, T. Matsumoto, T. Futagi and H. Mimura, Phys. Rev. B **48**, 2827 (1993).

[117] I. F. Crowe, M. P. Halsall, O. Hulko, A. P. Knights, R.M. Gwilliam, M. Wojdak and A. J. Kenyon J. Appl. Phys. **109**, 083534 (2011)

[118] G. H. Li, K. Ding, Y. Chen, H. X. Han and Z. P. Wang J. Appl. Phys. **88**, 1439 (2000)

[119] A. N. Mikhaylov, A. I. Belov, A. B. Kostyuk, I. Yu. Zhavoronkov, D. S. Korolev, A. V. Nezhdanov, A. V. Ershov, D. V. Guseinov, T. A. Gracheva, N. D. Malygin, E. S. Demidov and D. I. Tetelbaum, Physics of the Solid State **54**, 368 (2012).

[120] J. Bornacelli, J. Alejandro, R. Esqueda, L. R. Fernández and A. Oliver, J. Nanotechnology **2013**, 736478 (2013).

[121] O. L. Bratus, A. A. Evtukh, O. S. Lytvyn, M. V. Voitovych, V. O. Yukhymchuk, Semiconductor Physics, Quantum Electronics & Optoelectronics **14**, 247 (2011).

[122] C. Bonafos, M. Carrada, N. Cherkashin, H. Coffin, D. Chassaing et al., J. Appl. Phys. **95**, 5696 (2004).

[123] Y. Q. Wang, R. Smirani and G. G. Ross, Nanotechnology **15**, 1554 (2004).

[124] S. Guha, S. B. Qadri, R. G. Musket, M. A. Wall and T. Shimizu-Iwayama J. of Appl. Phys. **88**, 7 (2000).

[125] A. A. Sirenkoa, J. R. Fox, I. A. Akimova, X.X. Xia, S. Ruvimov and Z. Liliental-Weber, Solid State Comm. **113**, 553 (2000).

[126] G. Zatryb, A. Podhorodecki, X. J. Hao, J. Misiewicz, Y. S. Shen and M. A. Green, Nanotechnology **22**, 335703 (2011).

[127] G. Zatryb, A. Podhorodecki, J. Misiewicz, J. Cardin and F. Gourbilleau, Nanoscale Research Letts. **8**, 40 (2013).

[128] P. Mishra and K. P. Jain, Materials Science and Engineering B **95**, (2002).

[129] T. Ye-Liao, Z. Yu-Hua, Z. Jun, X. Chun-Lai, C. Bu-Wen, W. Qi-Ming and X. Jun Chin. Phys. B **21**, 077402 (2012).

[130] C. Ternon, F. Gourbilleau, X. Portier, P. Voivenel and C. Dufour Thin Solid Films **419**, 5 (2002).

[131] V. Paillard, P. Puech, M. A. Laguna, R. Carles, B. Kohn and F. Huisken, J. Appl. Phys. **86**, 1921 (1999).

[132] G. Faraci, S. Gibilisco, P. Russo, A. R. Pennisi, G. Compagnini, S. Battiato, R. Puglisi and S. L. Rosa, Eur. Phys. J. B **46**, 457 (2005).

[133] L. Khriachtchev, M. Räsänen and S. Novikov Appl. Phys. Letts. **88**, 013102 (2006).

[134] M. J. Konstantinovic, S. Bersier, X. Wang, M. Hayne, P. Lievens, R. E. Silverans and V. V. Moshchalkov, Phy. Rev. B **66,** 161311(R) (2002).

[135] Li Wei-Long, J. Rui, L. Ming, C. Chen, X. Chang-Qing, Z. Chen-Xin, L. Hao-Feng, Z. Pei-Wen, Y. Tian-Chun, Chin. Phys. Lett. **26**, 046801 (2009).

[136] I. Stenger, B. Gallas, B. Jusserand, S. Chenot, S. Fisson, and J. Rivory Eur. Phys. J. Appl. Phys. **44**, 51 (2008).

[137] T. Arguirov, T. Mchedlidze, M. Kittler, R. Rölver, B. Berghoff, M. Först and B. Spangenberg, Appl. Phys. Letts. **89**, 053111 (2006).

[138] Y. Q. Wang, G. L. Kong, W. D. Chen, H. W. Diao, C. Y. Chen, S. B. Zhang and X. B. Liao, Appl. Phys. Letts. **81**, 22 (2002).

[139] S. Hernández, P. Pellegrino, A. Martínez, Y. Lebour, B. Garrido, R. Spano, M. Cazzanelli, N. Daldosso, L. Pavesi, E. Jordana and J. M. Fedeli. J. Appl. Phys. **103**, 064309 (2008).

[140] Ma Zhixun et al., Science in China **43**, 4 (2000).

[141] Y. Duan, J. F. Kong and W. Z. Shen, J. of Raman Spectroscopy **43**, 756 (2011).

[142] T.Okada, T. Iwaki, K. Yamamoto, H. Kasahara and K. Abe, Solid State Commun. **49**, 809 (1984).

[143] H. Kohno, T. Iwasaki, Y. Mita and S. Takeda, J. of Appl. Phys. **91**, 5 (2002).

[144] C. Meier, A, Gondorf, S. Lüttjohann, A. Lorke and H. Wiggers, Physica E **32**, 155 (2006).

[145] P. Mishra and K. P. Jain, Phys. Rev. B, **64**, 073304 (2001).

[146] H. S. Mavi, B. G. Rasheed, A. K. Shukla, S. C. Abbi and K. P. Jain, J. Phys. D: Appl. Phys. **34**, 292 (2001).

[147] C. M. Hessel, J. Wei, D. Reid, H. Fujii, M. C. Downer and B. A. Korgel, J. Phys. Chem. Lett. **3**, 1089 (2012)

[148] F.Fang, W. Zh ang, J. Sun, N. Xu, J. Zhu, Z. Ying and J. Wu, J. Mater. Res. **24**, 7 (2009).

[149] T. Seto, T. Orii, M. Hirasawa and N. Aya, Thin Solid Films **437**, 230 (2003).

[150] J. R. Rani, V. P. Mahadevan Pillai, R. S. Ajimsha, M. K. Jayaraj and R. S. Jayasree, J. Appl. Phys. **100**, 014302 (2006).

[151] M. Nishida J. Appl. Phys. **99**, 053708 (2006).

[152] Z. Zhou, L. Brus and R. Friesner, Nano Lett. **3**, 163 (2003).

[153] I. H. Campbell and P. M. Fauchet, Solid State Comm. **58**, 739 (1986).

[154] H. S. Mavi, S. Prusty, A. K. Shukla, S. C. Abbi, Thin Solid Films **425**, 90 (2003).

[155] S. Go, H. Bilz and M. Cardona, Phys. Rev. Letts. **34**, 581 (1975).

[156] J. Zi, Phys. Rev. B **55**, 15 (1997).

[157] S. K. Arguirova, Tz. Arguirov, D. WoL Wframm and J. Reif, J. Appl. Phys. **94**, 8 (2003).

[158] A. Chaturvedi, M. P. Joshi, E. Rani, A. Ingale, L. M. Kukreja and A. K. Srivastava J. of Luminescence **154**, 178 (2014).

[159] J. Kao, K. Thorkelsson, P. Bai, B. J. Rancatore and T. Xu, Chem. Soc. Rev. **42**, 2654 (2013).

[160] J. Jordan, K. I. Jacob, R. Tannenbaum, M. A. Sharaf and I. Jasiuk, Mater. Sci. Eng. A **393**, 1 (2005).

[161] E. Coronado, J. R. Galan-Mascaros, et al, Nature **408**, 447 (2000).

[162] F. Croce, G. B. Appetecchi, L. Persi and B. Scrosati, Nature **394**, 456 (1998).

[163] T. J. Pinnavaia, Science **220**, 365 (1983).

[164] Y. Wang, and N. Herron, Science **273**, 632 (1996).

[165] J.G. Winiarz, L. M. Zhang, M. Lal, C. S. Friend and P. N. Prasad, J. Am. Chem. Soc. **121**, 5287 (1999).

[166] S.N. Sidorov, et al., J. Am. Chem. Soc. **123**, 10502 (2001).

[167] T.C. Merkel, B.D. Freeman, R.J.Spontak, Z. He, I. Pinnau, P. Meakin, and A. J. Hill, Science **296**, 519 (2002).

[168] C. Joly, M. Smaihi, L. Porcar and R. D. Noble, Chem. Mater. **11**, 2331 (1999).

[169] R. A. Potyrailo, A. A. Leach, Appl. Phys. Lett. **88**, 134110 (2006).

[170] Y. Zou, D. Li and D. Yang Nanoscale Research Letters **6,** 374 (2011).

[171] H. Li, X. Gui, C. Ji, P. Li, Z. Li, L. Zhang, E. Shi, K. Zhu, J. Wei, K. Wang, H. Zhu, D. Wu and A. Cao Nano Res. **5**, 265 (2012).

[172] J. N. Freitas, A. S. Gonçalve and A. F. Nogueira, Nanoscale **6**,6371 (2014).

[173] S. T. Navale, A. T. Mane, M. A. Chougule, N. M. Shinde, J. H. Kim and V. B. Patil, RSC Adv. **4**, 44547 (2014).

[174] C. Jing, X. Xu, X. Zhang, Z. Liu and J. Chu, J. Phys. D: Appl. Phys. **42**, 075402 (2009).

[175] R. E. Schwerzel, K. B. Spahr, J. P. Kurmer, V. E. WoodJerry and A. Jenkins, J. Phys. Chem. A **102**, 5622 (1998).

[176] H. Du, G. Q. Xu, W. S. Chin, L. Huang and W. Ji, Chem. Mater. **14**, 4473 (2002).

[177] F. Haaf, A. Sanner and F. Satruab, Polymer Journal **14**, 143 (1985).

[178] W. Feng, H. Tao, Y. Liu and Y. Liu, J. Mater. Sci. Technol. **22**, (2006).

[179] K. M. Gadave, S. A. Jodgudri and C. D. Lokhande, Thin Solid Films 245, 7 (1994).

[180] C. Nascu, V. Vomir, I. Pop, V. Ionescu and R. Grecu, Mater. Sci. Eng. B **41**, 235 (1996).

[181] R. S. Mane and C. D. Lokhande, Mater. Chem. Phys. **65**, 1 (2000).

[182] J. Valenta, J. Dian, K. Luterová, I. Pelant, J. Buršík and D. Nižňanský, Physica Status Solidi (a) **184**, R1 (2001).

[183] N. M. Huang, C. S. Kan, P. S. Khiew and S. Radiman, J. of Mater. Sci. **39**, 2411 (2004).

[184] M. Pattabi, B. Saraswathi and A. K. Manzoor, Materials Research Bulletin **42**, 828 (2007).

[185] S. Peretz, B. Sava, M. Elisa and G. Stanciu, J. of Optoelectronics and Advanced Materials **11**, 2108 (2009).

[186] D. S. Yoo, S. Y. Ha, I. G. Kim, M. S. Choo, K. Kim and E. S. Lee, New Physics: Sae Mulli **61**, 680 (2011).

[187] R. S. Patil, C. D. Lokhande, R. S. Mane, T. P. Gujar and S. H. Han, J. of Non- Crystalline Solids **353**, 1645 (2007).

[188] F. Antolini, M. Pentimalli, T. Di Luccio, R. Terzi and M. Schioppa, Materials Letters **59**, 3181 (2005).

[189] L. Pedone, E. Caponetti, M. Leone, V. Militello, V. Pantò, S. Polizzi and M. L. Saladino, J. of Colloid and Interface Science **284**, 495 (2005).

[190] E.J. Tang, S.Y. Dong, Colloid Polym. Sci. **287**, 1025 (2009).

[191] H. Du, G. Q. Xu and W. S. Chin Chem. Mater. **14**, 4473 (2002).

[192] Y. Lin, J. Zhang, E. H. Sargent, and E. Kumacheva, Appl. Phys. Lett. **81**, 3134 (2002)

[193] I. S. Elashmawi, A. M. Abdelghany and N. A. Hakeem, J Mater Sci: Mater Electron **24**, 2956 (2013).

[194] D. B. Chrisey and G. K. Hubler, “Pulsed Laser Deposition of thin films” New York: John Wiley & Sons (1994).

[195] B. A. Ezekoye, P.O. Offor, V. A. Ezekoye and F. I. Ezema, Int. J. of Scientific Research **2**, 452 (2013).

[196] P. Bruesch, “Phonons: Theory and Experiment I, Springer-Verlag Berlin Heidelberg” (1982).

[197] R. Shankar, “Principle of Quantum Mechanics” Springer (2008).

[198] P. Bruesch, “Phonons: Theory and Experiment II, Springer-Verlag Berlin Heidelberg” (1982).

[199] A. Zoubir, “Raman Imaging: Techniques and Applications” Springer-Verlag Berlin Heidelberg (2012).

[200] K. S. Birdi, “Scanning Probe Microscopes: Applications in Science and Technologies” CR Press (2003)

[201] M. Fox, “Optical Properties of Solids” Oxford University Press (2001).

[202] Y. Wang and N. Herron Phys Rev B **42**, 7253 (1990).

[203] P. J. Goodhew, “Electron microscopy and analysis” John Humphreys and Richard Beanland. 3rd. London : Taylor & Francis (2000).

[204] C. Kittel, “Introduction to Solid State Physics” John Wiley & Sons (2007).

[205] C. C. Chusei and D. W. Goodman, Encyclopedia of Physical Science and Technology **17**, 921 (2002).

[206] R.W. M. Kwok ⟨http://www.phy.cuhk.edu.hk/ surface/xpspeak/⟩.

[207] L. Pavesi, L. D. Negro, C. Mazzoleni, G. Franzo and F. Priolo, Nature **408**, 23 (2000).

[208] G. Conibeer, et al., Thin Solid Films **511**, 654 (2006).

[209] E. C. Cho, M. A. Green, G. Conibeer, D. Song, Y. H. Cho, G. Scardera, S. Huang, S. Park, X. J. Hao, Y. Huang and L. V. Dao, Advances in OptoElectronics **2007**; 69578 (2007).

[210] M. Hamasaki, T. Adachi, S. Wakayama and M. Kikuchi, J. Appl. Phys. **49**, 3987 (1978).

[211] L. A. Nesbit, Appl. Phys. Lett. **46**, 38 (1985).

[212] F. Wang, D.M. Wolfe, C.L. Hinkle and G. Lucovsky, J. of Non-Crystalline Solids **227–230**, 507 (1998).

[213] Ekta Rani, Alka A. Ingale, A. Chaturvedi, C. Kamal, D. M. Phase, M. P. Joshi, A. Chakrabarti, A. Banerjee and L. M. Kukreja, J. Raman Spectrosc. **47**, 457 (2016).

[214] Ekta Rani, Alka A. Ingale, A. Chaturvedi, M. P. Joshi and L. M. Kukreja. Appl. Phys. Lett. **107**, 163112 **(**2015).

[215] Ekta Rani, Alka A. Ingale, A. Chaturvedi, M. P. Joshi and L. M. Kukreja submitted in J. of Alloys and Compounds **672**, 403 (2016).

[216] Ekta Rani, Alka A. Ingale, D. M. Phase, A. Chaturvedi, M. P. Joshi and L. M. Kukreja submitted in Appl. Phys. Letts: Under review.

[217] J.H. Parker, JR., D. W. Feldman and M. Ashkin, Phys. Rev. B **155**, 712 (1967).

[218] G. Dolling and R. A. Cowley, Proc. Phys. Soc. **88**, (1996).

[219] S. K. Gupta and P. K. Jha, Solid State Commun. **149**, 1989 (2009).

[220] C. Hong-Shan, Ji Sheng-Fu, N. Jian-Zhong, X. Bao-Han, L. Shu-Ben, Acta Phys Chim Sin **15**, 454 (1999).

[221] D. E. Yılmaz, C. Bulutay and T. Cagin, Phys. Rev. B **77**, 155306 (2008).

[222] G. Hadjisavvas and P. C. Kelires, Phys. Rev. Letts. **93**, 226104 (2004).

[223] M. Ippolito, S. Meloni and L. Colombo, Appl. Phys. Lett. **93**, 153109 (2008).

[224] M. Roussel, E. Talbot, P. Pareige and F. Gourbilleau, J. Appl. Phys. **113**, 063519 (2013).

[225] S. Kim, M. C. Kim, S. H. Choi, K. J. Kim, H. N. Hwang and C. C. Hwang, Appl. Phys. Lett. **61**, 103113 (2007).

[226] D. E. Yilmaz, Ph. D Thesis, Bilkent University Turkey (2009).

Title :”On the strain in Silicon nanocrystals".

[227] T. R. Hart, R. L. Aggarwal and B. Lax, Phys. Rev. B **1**, 2 (1970).

[228] G. Faraci, S. Gibilisco and A. R. Pennisi, Phys. Rev. B **80**, 193410 (2009).

[229] F. Laplant, G. Laurence, and D. Ben-Amotz, Applied Spectroscopy **50**, 1034 (1996).

[230] G. Lucovsky, A. Banerjee, B. Hinds, B. Claflin, K. Koh and H. Yang J. Vac. Sci. Technol. B **15**, 1074 (1997).

[231] P. Hohenberg and W. Kohn, Phys. Rev. **136**, B864 (1964). W. Kohn, L. J. Sham, *ibid.* **140**, A1133 (1965).

[232] E. J. Baerends, J. Autscbach, A. Berces, et al. Amsterdam Density Functional, Theoretical Chemistry, Vrije Universiteit, Amsterdam, URL http://www.scm.com.

[233] J. P. Perdew, K. Burke and M. Ernzerhof, Phys. Rev. Lett. **77**, 3865 (1996).

[234] T. Nikitin and L. Khriachtchev, Nanomaterials **5**, 614 (2015).

[235] X. L. Wu, G. G. Siu, S. Tong, X. N. Liu, F. Yan, S. S. Jiang, X. K. Zhang and D. Feng, Appl. Phys. Lett. **69**, 4 (1996).

[236] H. Xia, Y. L. Wang, W. Zang, X. N. Liu, et al., J. Appl. Phys. **78**, 11 (1995).

[237] J. H. Shima, S. Imb and N. H. Choa, Appl. Surface Science **234**, 268 (2004).

[238] S. Hayashi and H, Kanamori, Phys. Rev. B **26**, 12 (1982).

[239] Q. Jiang, Z. Zhang and J. C. Li, Acta Mater. **48**, 4791 (2000).

[240] M. Green, “*Third Generation Photovoltaics: Advanced Solar Energy, Conversion,* (Eds: T. Kamiya, H. Venghaus, B. Monemar, Y. Yamamoto), Springer-Verleg, Berlin, p. 59-66 (2003).

[241] S. Yang, W. Li, B. Cao, H. Zeng, and W. Cai, J. Phys. Chem. C 115, 21056 (2011).

[242] D. E. Yılmaz, C. Bulutay and T. Çağın, Appl. Phys. Lett. **94**, 191914 (2009).

[243] T. Li, J. Kanicki, W. Kong and F. L. Terry Jr., J. Appl. Phys. 88, 10 (2000).

[244] A. En Naciri, P. Miska, A.-S. Keita, Y. Battie, H. Rinnert, and M. Vergnat, J. Nanoparticle Research **15**, 1538 (2013).

[245] M. F. Cerqueira, T.V. Semikina, N. V. Baidus, and E. Alves, Int. J. Materials and Product Technology **39**, 195 (2010).

[246] W. Marine, L. Patrone, B. Luk'yanchuk and M. Sentis, Appl. Surf. Sci. **154**, 345 (2000).

[247] N. Suzuki, T. Makino, Y. Yamada, T. Yoshida and O. Seinosuke, Appl. Phys. Lett. **76**, 1389 (2000).

[248] W. O. Siew, S. S. Yap, C. Ladam, Ø. Dahl, T. W. Reenaas and T. Y. Tou, Appl. Phys. A **104**, 877 (2011).

[249] R. F. Wood, K. R. Chen, J. N. Leboeuf, A. A. Puretzky and D. B. Geohegan, Phys. Rev. Lett. **79**, 1571 (1997).

[250] D. B. Geohegan, A. A. Puretzky, G. Duscher and S. J. Pennycook, Appl. Phys. Lett. **72**, 2987 (1998).

[251] D. B. Geohegan, A. A. Puretzky, G. Duscher and S. J. Pennycook, Appl. Phys. Lett. **73**, 438 (1998).

[252] T. Makino, N. Suzuki, Y. Yamada, T. Yoshida, T. Seto and N. Aya, Appl. Phys. A **69**, S243 (1999).

[253] P. S.Bagus, E. S.Ilton and C. J.Nelin Surface Science Reports **68**, 273 (2013).

[254] Ekta Rani, Rahul Aggarwal, Alka A Ingale, K. Bapna, C. Mukherjee, M. K. Singh, P. Tiwari and A. K. Srivastava, J. of Mater. Sci. **51**, 1581 (2016).

[255] Ekta Rani, Alka A Ingale, A. K. Sinha et al. to be submitted

[256] Ekta Rani, Alka A Ingale, A. K. Sinha et al. to be submitted

[257] V. Shukla, M. Mittal, A. A. Ingale Proceedings of DAE- Solid state Physics symposium, Amritsar **49**, 538 (2004).

[258] S. Kus, Z. Marczenko, N. Obarski, Chern Anal **41**, 899 (1996).

[259] M. P. Horvath, R. A. Copeland, M. W. Makinen, Biophys J **77**, 1694 (1999).

[260] P. D. Fochs, Proc Phys Soc B **69**, 70 (1956).

[261] M. Nowak, B. Kauch, P. Szperlich, Rev Sci Instrum **80**, 046107 (2009).

[262] P. Verma, G. S. Manoj, A. C. Pandey, Physica B 405, 1253 (2010).

[263] A. M. Abdelghany, E. M. Abdelrazek, D. S. Rashad, Spectrosche Acta A 130, 302 (2014).

[264] A.K. Sinha, R.K. Gupta and S.K. Deb, Appl Phys A **108**, 607 (2012).

[265] B.D. Cullity and S.R. Stock, Elements of X-Ray Diffraction, Prentice-Hall Inc. (2001).

[266] A. Veamatahau, B. Jiang, T. Seifert, S. Makuta, K. Latham, M. Kanehara, T. Teranishid and Y. Tachibana, Phys.Chem.Chem.Phys. **17**, 2850 (2015).

[267] D. Antypov and J. A. Elliott, Macromolecules **41**, 7243 (2008).

[268] F. M. Mirabella, Jr., Practical Spectroscopy Series; Internal reflection spectroscopy: Theory and applications, Marcel Dekker, Inc.; Marcel Dekker, Inc., 1993, 17-52.

[269] L. Saravanan, S. Diwakar, R. Mohankumar, A. Pandurangan and R. Jayavel, Nanomater. nanotechnol. **1**, 42 (2011).

[270] W. Tu, X. Zuo and H. Liu, Chinese Journal of Polymer Science **26**, 23 (2008).

[271] M. Gaith and I. Alhayek, Rev. Adv. Amter. Sci. **21**, 183 (2009).

[272] R. J. Briggs and A. K. Ramdas, Phys. rev. B **13**, 5518 (1976).

[273] W. Yin, S. Chen, J. Yang, Y. Yan and S. Wei, Appl. Phys. Letts. **96**, 221901 (2010).

[274] Jung-Chul An "Synthesis, characterization, and kinetic studies of ionizing radiation-induced intra- and inter-cross linked poly (vinyl pyrrolidone) nanohydrogels" (2007).